Electroanalysis of Single Nanoparticles via Particle-electrode Collision Processes

Thesis submitted for D. Phil Physical & Theoretical Chemistry

YIGE ZHOU

SUPERVISOR: PROF. R. G. COMPTON

SEPTEMBER 2012

Contents

Abstract

This thesis begins with the investigation of size- and density-effects of AgNP arrays in voltammetry, including the study of size-dependent adsorption behavior by observing thallium underpotential deposition on AgNPs, and surface coverage effects of AgNP modified electrodes in voltammetry showing the transition from convergent to linear diffusion.

The main focus of this thesis is next presented: the electroanalysis of nanoparticles (NPs) studied via their impacts with an electrode via both indirect (*i.e*. electrocatalytic) and direct electrochemical measurements. The study first realises the direct detection and sizing of silver NPs (AgNPs) using anodic particle coulometry (APC). This theme is then extended to gold and nickel NPs, aggregation studies and the measurement of sticking coefficients. Furthermore, the determination of nanoparticle concentration is realised by measurement of the flux to electrodes.

In contrast to APC, electrode-particle impacts using surface tagged NPs provide a non-destructive way of sizing the NPs from the charge associated with one monolayer of "tag". In addition to tagged NPs, underpotential deposition and bulk deposition of metal onto single AgNPs are also observed as part of the studies of indirect electrochemical measurement. Finally the charge transfer kinetics of the oxidation of silver and nickel nanoparticles is studied.

Acknowledgements

This thesis would not have reached its present form without the help and support of many generous people whose names will not fit into a single Acknowledgement section. I just mention those people whose contribution is obvious.

My first debt of gratitude has to go to my supervisor Professor Richard Compton for giving me such an opportunity to work in this prestigious group and for his guidance, support, and inspiration over the past three years. Both his strictness and kindness make all the novel results presented in this thesis possible. His enthusiasm and sharp insight in research has made himself a charming scientist and has set a great example for me in my future career.

I would like to extend my thanks to Dr. Fallyn Campbell for helping me get my research started and Dr Neil Rees for providing valuable help and advice on the major part of my work. Neil's smartness, kindness and humor can always smooth away the difficulties I encountered in research. He may have already forgotten it, but the 1500 - word email he sent to me at 2 a.m. teaching me how to outstand from a research group of more than 20 students, will be remembered forever.

I want to say thank - you to other group members, especially to Min, Emma, Danu, Mat, Jane, Eduardo, Justin, Lin, Qian, Ying, Yao and Stephen, and to those who have left the group - Leigh, Barbara, Juan, Luis, Thomas, Baptiste, Chaopeng and Rui, for all your help and support and for making my doctoral study full of sunshine. To Danu, Jane, Eduardo and Lin, for every joke and gossip we shared at lunch time. To Baptiste for the constant delicious home-made desserts you brought to lab. To Min and Emma for all the

girls' chats and laughters without Neil's presence.

I would like to express my gratitude to St John's College for the generous Kendrew Scholarship that supports my study and life in Oxford, and also for providing me a home, good food and the opportunity of meeting many nice friends.

Last but not least, I would like to give my sincere thanks to my beloved parents. Thanks for their unconditional love, support and sacrifice. Every lonely and weak moment in Oxford I always had them standing at my back although we were physically thousands of miles away. Their every wrinkle and gray hair create the only Doctor Zhou in the family. I owe them everything and I believe that the Doctor title is the best present to them for the return of their whole-hearted love for all these years.

Chapter 1

Introduction to Electrochemistry

Electrochemistry is the branch of chemistry concerned with the interrelation of electrical and chemical effects. This introductory chapter outlines the fundamental principles underpinning the study of electrochemistry, with respect to electrochemical equilibrium, electrochemical cells, mass transport, electrode kinetics, voltammetry at microelectrodes and commonly used electroanalytical techniques.

1.1 Electrochemical equilibrium

1.1.1 Introduction to electrochemical equilibrium

An electrochemical equilibrium can be established by inserting a metal, for example a platinum wire, into a solution containing $K_4Fe(CN)_6$ and $K_3Fe(CN)_6$, as illustrated in Figure 1.1.

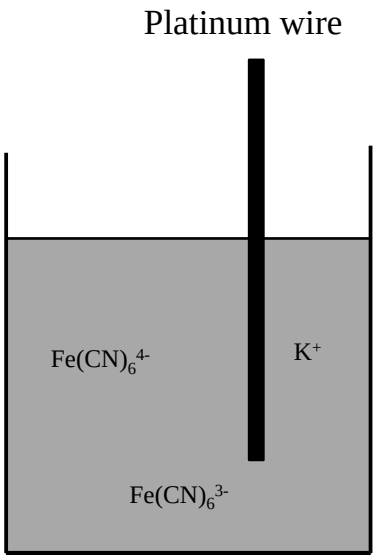

Figure 1.1: A platinum wire in a solution of $K_4Fe(CN)_6$ and $K_3Fe(CN)_6$.

In the cell an electron might leave the platinum wire and join an $Fe(CN)_6^{3-}$ in the solution, forming $Fe(CN)_6^{4-}$. Alternatively an $Fe(CN)_6^{4-}$ close to the electrode might give up its electron to the wire turning into $Fe(CN)_6^{3-}$. In practice both events take place and the following equilibrium is established at the surface of the platinum wire shortly after its insertion to the solution:

$$Fe(CN)_6^{3-}(aq) + e^- \rightleftharpoons Fe(CN)_6^{4-}(aq). \tag{1.1}$$

Under equilibrium, the rate at which $Fe(CN)_6^{3-}$ gains electrons from the metal elec-

trode is equal to that at which $Fe(CN)_6^{4-}$ gives up electrons. Once a dynamic equilibrium is attained, no further net charge is possible but there is a charge separation between the electrode and the solution, which is the origin of the electrode potential established on the metal electrode. Changes in the electron energies in this process are shown in Figure 1.2 as a function of the equilibrium.

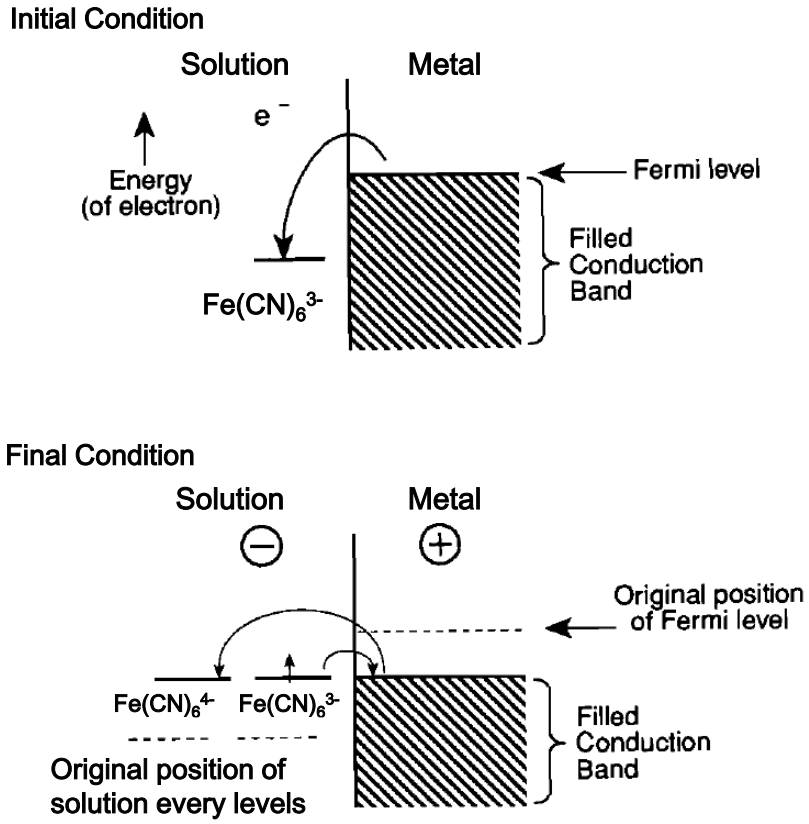

Figure 1.2: The energy of electrons in the ions in solution and in the metal before and after the establishment of equilibrium.

1.1.2 The Nernst Equation

In order to account for both chemical and electrical energies, a new quantity, the electrochemical potential, $\overline{\mu_A}$, of a species A

$$\overline{\mu_A} = \mu_A + z_A F \phi, \tag{1.2}$$

where z_A is the charge on the molecule A, μ_A is the chemical potential of species A, F is the Faraday constant, and $z_A F\phi$ indicates the electrical energy of A. When this equation is attained under constant temperature (T) and pressure (P), a balance will be obtained between the electrochemical potentials of the reactants and the products. For example we have considered in (1.1), it follows

$$\overline{\mu}_{\mathrm{Fe(CN)}_6^{3-}} + \overline{\mu}_{e^-} = \overline{\mu}_{\mathrm{Fe(CN)}_6^{4-}}, \tag{1.3}$$

at equilibrium. Combining equation (1.2) and equation (1.3) allows us to expand this expression to obtain the Nernst equation for single electrode-solution interface.

$$\phi_m - \phi_s = \frac{\Delta\mu^0}{F} + \frac{RT}{F} ln\left(\frac{[\mathrm{Fe(CN)}_6^{3-}]}{[\mathrm{Fe(CN)}_6^{4-}]}\right) \tag{1.4}$$

where ϕ_m -ϕ_s ($\Delta\phi_{m/s}$) indicates the potential drop across the electrode/solution interface, $\Delta\mu^0 = \mu^0_{\mathrm{Fe(CN)}_6^{3-}} + \mu_{e^-} - \mu^0_{\mathrm{Fe(CN)}_6^{4-}}$, which is a constant at a given T and P.

For a general one-electron redox process as shown in (1.5)

$$Ox + \mathrm{e}^- \rightleftharpoons Red, \tag{1.5}$$

the Nernst equation can be written in its more general form, in concentration of the species, as

$$E = E^0 + \frac{RT}{F} ln\frac{[O]}{[R]}, \tag{1.6}$$

and in terms of activities of the species, as

$$E = E^0 + \frac{RT}{F} ln\frac{(a_{ox})}{(a_{red})}. \tag{1.7}$$

The Nernst equation can be used to determine the equilibrium potential of a half-cell in an electrochemical cell based on the concentration/activities of the chemical species

involved and the standard potential, E^0.

1.1.3 Standard electrode potentials and formal potentials

The standard electrode potential, abbreviated as E^0, is the measure of individual potential of a reversible electrode at standard state, which is with solutes at an effective concentration of 1 mol dm^{-3}, and gases at a pressure of 1 atm. It is conventional to quote the system potential (couple or half-cell) against the standard hydrogen electrode (SHE), also known as normal hydrogen electrode (NHE) whose standard potential is 0V. Tabulated values of standard electrode potentials for typical reactions are very easy to be found in electrochemical literatures. "Standard electrode potential" is also commonly written as "standard reduction potential".

Standard potentials refer to standard states. Very dilute solutions can be assumed ideal and calculations using standard potentials are then reasonably accurate without activity coefficient corrections. But for more concentrated solutions of more than about 0.01 M, activity coefficients are unknown. A device for avoiding this is the formal potential, E^0_f, defined as the potential of the half-cell when the concentration quotient of the Nernst equation equals 1.

As we know, the concentration of species in solution can be related to the activity by (14.8)

$$a_A = \gamma_A[A], \tag{1.8}$$

where a_A is the activity of species A, γ_A is the activity coefficient and $[A]$ is the concentration. Considering the Fe^{3+} / Fe^{2+} couple, the Nernst equation gives

$$E = E^0{}_{Fe^{3+}/Fe^{2+}} + \frac{RT}{F} ln \frac{a_{Fe^{3+}}}{a_{Fe^{2+}}}, \tag{1.9}$$

or

$$E = E^{0}_{Fe^{3+}/Fe^{2+}} + \frac{RT}{F} ln \frac{\gamma_{Fe^{3+}}}{\gamma_{Fe^{2+}}} + \frac{RT}{F} ln \frac{[Fe^{3+}]}{[Fe^{2+}]} \tag{1.10}$$

Thus when the concentrations of Fe^{3+} and Fe^{2+} are equal, the formal potential is

$$E^{0}_{f} = E^{0}_{Fe^{3+}/Fe^{2+}} + \frac{RT}{F} ln \frac{\gamma_{Fe^{3+}}}{\gamma_{Fe^{2+}}} \tag{1.11}$$

Therefore

$$E = E^{0}_{f} + \frac{RT}{F} ln \frac{[Fe^{3+}]}{[Fe^{2+}]} \tag{1.12}$$

The value of E^{0}_{f} differs between media, based on the ionic strength and relative complexing abilities. The value of the standard potential for half-reactions and cells are obtained by measuring the formal potential value over a range of ionic strength and extrapolating to zero ionic strength, where activity coefficients approach unity.

1.2 Electrical double layer and Faradaic/non-Faradaic processes

1.2.1 Electrical double layer

A charged surface, or an electrode in contact with an electrolyte will attract ions of opposite charge and repel like charge, thus an ion atmosphere in the immediate vicinity of the surface is established. This is referred to as the electric double layer and the solution side of the double layer is thought to be made up of several layers. Models describing the structure of the double layer have been proposed by Helmholz, Gouy and Chapman, and Stern.

The layer closest to the electrode, the inner layer, contains solvent molecules and sometimes specifically adsorbed ions or molecules. This layer is also called the compact, Helmholz, or Stern layer. The locus of the electrical centers of the specifically adsorbed

ions is called the inner Helmholtz plane (IHP). The specific adsorption of molecules causes a reduced charge density required in the solution double layer to compensate for the electrode charge.

The locus of centers of the nearest solvated ions approaching the electrode is called the outer Helmholtz plane (OHP). The interaction of the solvated ions with the charged electrode is essentially independent of the chemical properties of the nonspecifically adsorbed ions. These ions are distributed in a three-dimensional region called the diffuse layer, which extends from the OHP to the bulk solution. A schematic representation of the double-layer region is shown in Figure 1.3.

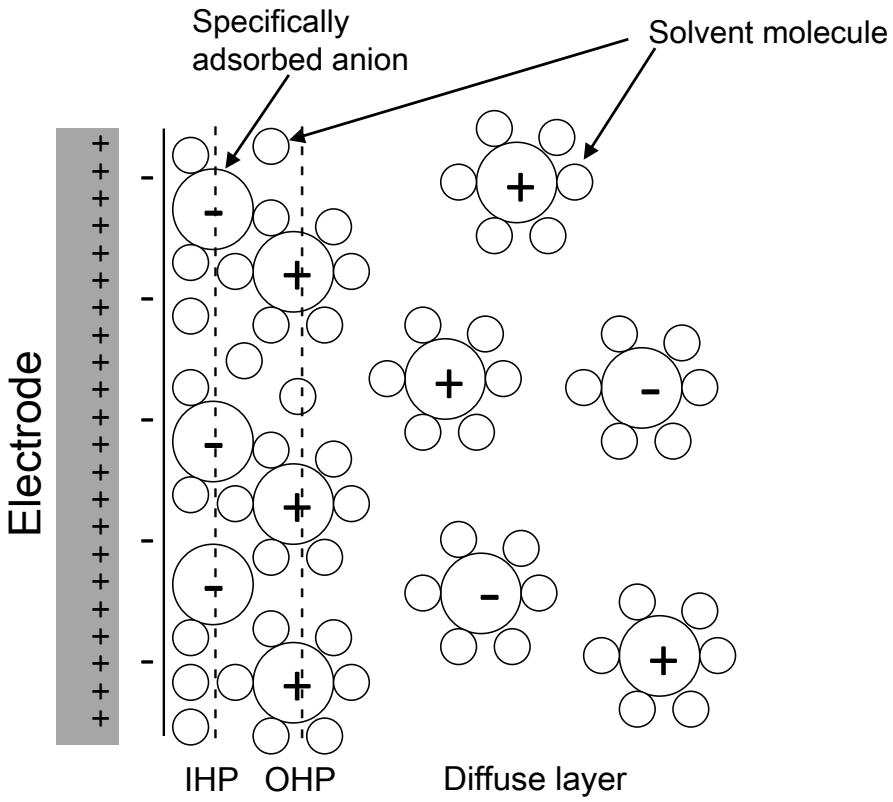

Figure 1.3: A schematic representation of the double-layer region.

1.2.2 Faradaic and non-faradaic process

There are two types of processes occurring at electrodes. One kind comprises reactions in which electrons are transferred across the electrode-solution interface that causes oxidation or reduction to occur. Such reactions can be governed by Faraday's law, which is, the amount of chemical reaction caused by the flow of current is proportional to the amount of electricity passed. Thus they are called faradaic processes. Electrodes at which faradaic processes occur are sometimes called charge-transfer electrodes.

Under some conditions, there are no charge transfer reactions occurring at a given electrode-solution interface because such reactions are thermodynamically or kinetically unfavorable. However, processes such as adsorption and desorption can occur, and the structure of the electrode-solution interface can change with changing potential or solution composition. These processes are called non-faradaic processes. Although no changes exist across the interface, external currents can flow, in the form of charging currents. The positive side of non-faradaic processes is that the capacitance can be used for energy storage.

When electrode reactions take place, both faradaic and non-faradaic processes will happen. Although the former are usually the primary concern in the investigation of an electrode reaction, the effects of the latter must be taken into account to further understand the charge transfer and associated reactions.

1.3 Electrochemical cells

1.3.1 Types and definitions of electrochemical cells

An electrochemical cell is a device that is capable of deriving electrical energy from chemical reactions or facilitating chemical reactions through electrical energy. Electrochemical cells where faradaic currents are flowing are classified into galvanic and electrolytic cells.

A Galvanic cell is an electrochemical cell where a redox reaction takes place spon-

taneously at the electrodes when they are connected by a conductor. These cells are often employed to convert chemical energy into electrical energy.

An electrolytic cell is an electrochemical cell that undergoes a redox reaction when the applied external voltage is greater than the open-circuit potential. These cells are frequently used to carry out desired chemical reactions by consuming electrical energy.

In this thesis, we will focus on electrolytic cells. As reactions occurring at only one of the electrodes are concerned, treatment is simplified by concentrating on only one-half of the cell at a time. An electrolytic half-cell includes chemical changes accompanying faradaic reactions at electrodes in contact with electrolytes. The electrode where reductions occur is called a cathode and the one where oxidations occur an anode. A current in which electrons flow from the electrode to a species in solution across the interface is a cathodic current, while if electrons flow from a species to the electrode it is an anodic current.

1.3.2 Three electrode set up within an electrolytic cell - the need for a counter electrode

The simplest approach to the measurement of current/voltage characteristics involves the use of two electrodes. One is termed a working electrode (WE) where the reaction occurs and the other is a reference electrode (RE) which provides a fixed potential so that the potential drop between the WE and the solution is precisely defined. Consider a potential, E, applied between a WE and a RE, then

$$E = (\phi_m - \phi_s) + iR - (\phi_{RE} - \phi_s). \tag{1.13}$$

In this equation, $\phi_m - \phi_s$ is the potential drop or driving force at the WE/solution interface. $\phi_{RE} - \phi_s$ is the potential drop at the RE/solution interface and is fixed by RE. R is the solution resistance between the electrodes and iR describes the potential drop in

solution. When i is very tiny, for example in microelectrode studies the term iR can be neglected. Since $(\phi_{RE} - \phi_s)$ is fixed, equation (1.13) can be simply reduced to

$$E = (\phi_m - \phi_s) + \text{constant.} \tag{1.14}$$

Therefore, changes in the applied potential, E, are directly reflected in the driving force, $\phi_m - \phi_s$, and the simple two-electrode arrangement is perfectly acceptable. However, with larger electrodes, iR is no longer negligible. In this situation, changes in E would cause unknown changes in iR as well as altering $\phi_m - \phi_s$, so that the latter would no longer be controlled.

To circumvent this problem it is usual to introduce another electrode, an auxiliary or counter electrode (CE) in addition to the other two, thus a three-electrode set up is formed. In this arrangement, the current is passed between WE and CE. CE can be any convenient one, such as a platinum wire/mesh or a cheap carbon rod, because its electrochemical properties do not affect the behavior of the electrode of interest. It is usually chosen to be an electrode that does not produce substances by electrolysis that will reach WE surface and cause interfering reactions there.

1.3.3 Working electrode (WE)

The working electrode (WE) is the electrode in an electrochemical system at which the reaction of interest occurs. Depending on whether the reaction at the electrode is a reduction or an oxidation, the working electrode can be referred to as either cathodic or anodic. The material of the working electrode strongly influences the voltammetric response. Common materials include mercury, noble metals such as gold, silver or platinum, and inert materials such as carbon (glassy carbon (GC) or pyrolytic carbon). The choice of electrode material is determined by two primary factors: the redox behavior of the target analyte and the background current over the potential region of interest. In addition, it is also important to consider the potential window, electrical conductivity, mechanical

properties, reproducibility of the electrode surface, cost and toxicity.

1.3.4 Reference electrode (RE)

The reference electrode (RE), as mentioned above, provides a stable and reproducible potential that is independent of sample composition, against which the potential of WE can be compared. The standard half-cell potentials of all aqueous redox couples are given with respect to the standard hydrogen electrode (SHE), the primary reference electrode. However, SHE has its drawbacks and is sometimes inconvenient to use, requiring hydrogen gas and a specially prepared platinum wire electrode. The platinum surface is easily poisoned and other electrode processes can compete with the H^+/H_2 couple and in turn interfere with the electrode potential. Therefore other reference electrodes are used as alternatives with the calomel electrode and silver/silver chloride (Ag/AgCl) electrode particularly common.

Saturated calomel electrode (SCE)

The calomel electrode comprises a column of liquid mercury, contacting insoluble dimercury (I) chloride (known traditionally as 'calomel'). Both contact an aqueous solution of chloride ions, usually in the form of KCl. The calomel electrode can be represented in shorthand notation as follows:

$$Cl^-(aq)|Hg_2Cl_2(s)|Hg(l) \tag{1.15}$$

The half-cell reaction is

$$Hg_2Cl_2(s) + 2e^- \rightleftharpoons 2Cl^-(aq) + 2Hg(l) \tag{1.16}$$

The standard potential refers to unit activity for all species, including Cl^-. In practice it is often convenient to use saturated KCl solution instead in a few KCl crystals in the

electrode to maintain the saturation. In this case Cl^- concentration is able to keep constant and the preparation of KCl of exactly known concentration from time to time is avoided. The potential of the saturated calomel electrode (SCE) is 0.244 V at 25 °C versus SHE.

Silver/silver chloride (Ag/AgCl) electrode

The silver/silver chloride (Ag/AgCl) electrode comprises a silver wire coated with a porous layer of silver chloride. The almost insoluble AgCl layer can be formed on the surface of the Ag wire by electro-oxidation of the wire in a solution containing chloride ions such as KCl solution. The coated wire is then dipped into a fresh KCl solution. The Ag/AgCl electrode is represented as

$$Cl^-(aq)|AgCl(s)|Ag(s), \tag{1.17}$$

which leads to the half-cell reaction

$$AgCl(s) + e^- \rightleftharpoons Ag(s) + Cl^-(aq) \tag{1.18}$$

In the Ag/AgCl electrode there is no liquid mercury or Hg_2Cl_2 paste to deal with so is more rugged than the calomel electrode. The Ag/AgCl electrode is easily miniaturised and is thus convenient for many biological applications. The potential of a saturated Ag/AgCl electrode is 0.197 V at 25 °C versus SHE.

1.3.5 The need for supporting electrolyte

Supporting electrolyte is essential for an electrochemical cell. The addition of excess background electrolyte acts to compress the potential drop to within 10-20 Angstroms of the working electrode surface. The fact that electron transfer between the electrode and the solution phase species takes place by quantum mechanical tunneling implies that the species we investigate must be located within a similar distance of the electrode surface.

'Frumkin correction' is necessary when experiments are conducted in poorly conducting electrolytes to account for potential drop over greater distances. The concentration of the electrolyte is normally taken as 100 times more than the electroactive species to suppress migration effects, decrease resistance and maintain a constant ionic strength. Supporting electrolytes may be inorganic salts, mineral acid or buffer.

1.4 Mass transport

In general, the current for a simple electrode reaction, $Ox + e^- \rightleftharpoons Red$, is determined by the rates of processes such as:

1. Mass transfer (e.g., of Ox from the bulk solution to the electrode surface).
2. Rate of electron transfer at the electrode.
3. Chemical reactions preceding or following the electron transfer.
4. Other surface reactions, such as adsorption, desorption, or crystallisation.

In the following sections of this introductory chapter the first two factors will be discussed in more depth.

Mass transport is the net movement of material from one location to another arising due to differences in electrical or chemical potential between the locations. In order for electrolysis to proceed the reactant molecules must be transported from the bulk solution to the electrode interface, and the products will diffuse away from the electrode surface. As the overall reaction rate will be controlled either by the kinetics of electron transfer or by the rate of mass transport, it is anticipated that when reactions occur rapidly, mass transport effects may play an important role in the electrochemical dynamics of a system. There are three significant transport processes involved in an electrochemical cell: diffusion, convection and migration. Below we will discuss each of the process in a little more detail.

1.4.1 Migration

The external electric field that exists at the electrode/solution interface as a result of the drop in electrical potential between the two phases is capable of exerting an electrostatic force on charged species and thereby inducing the movement of ions to or from the electrode. This movement is known as the process of migration and is likely to accompany electrochemical reactions. Migration often takes place in bulk solution where concentration gradients are generally small.

The interplay of migration and electrolysis will result in a complex physical transport process which is difficult to control or interpret. The effect of this on a charge transfer process at an electrode surface is a change in the concentration of ionic species in the vicinity of the electrode and in turn a change in the electrical potential in the solution. As a result, the electric field near the electrode is also altered. Consequently the migratory fluxes and the rate of mass transport of the electroactive species will be changed, making the interpretation of experimental data difficult.

In order to eliminate migration effects experimentalists normally add to the solution a high concentration of background electrolyte that is both chemically and electrochemically inert. The effect of the high concentration of background electrolyte is to maintain electrical neutrality throughout the interfacial region with the exception of the very tiny region immediately adjacent to the electrode. The addition of excess background electrolyte eliminates the build up of the electric fields in the solution as the reactions proceed. As we have mentioned above, in order to neglect the migratory mass transport effects, calculations have shown that a concentration of background electrolyte approximately 100 times that of the reactant species is required.

1.4.2 Convection

Convection is due to the mechanical force that acts on a solutions. Convection can be classified as natural convection or forced convection. Natural convection arises from thermal

gradients and/or density differences within the solution. Thermal gradients may result from the exo- or endo-thermicity of a given process while differences in density result directly from the electrode reactions. Natural convection is a significant perturbation in electrolysis with electrodes of mm or larger sizes and is generally undesirable as it is difficult to predict.

Forced convection is achieved by external forces such as gas bubbling, pumping, or stirring. This technique can be used to swamp any contributions from natural convection to ensure reproducibility in experiments. In particular, forced convection has well-defined hydrodynamic behavior that enables quantitative description of the flow and the prediction of the pattern of mass transport to the electrode.

1.4.3 Diffusion

Diffusion arises from uneven concentration distributions and will take place from high to low concentration, which is, down the concentration gradient.

Fick's 1st Law

At a given point, x, there will be a diffusive flux which is quantified by Fick's 1st Law:

$$j = -D\frac{\partial c}{\partial x}, \tag{1.19}$$

where j is the flux (mol cm^{-2} s^{-1}), $\frac{\partial c}{\partial x}$ is the local concentration gradient at a given point x, and D is the diffusion coefficient (cm^2 s^{-1}) whose magnitude typically lies in the range of 10^{-6} to 10^{-5} cm^2 s^{-1} in aqueous solution. Diffusion coefficient is strongly temperature sensitive, often following Arrhenius type relationships:

$$D = D_\infty exp\left(\frac{-E_a}{RT}\right), \tag{1.20}$$

where D_∞ is the hypothetical value of D at an infinite temperature and E_a (kJ mol^{-1}) is an activation energy for diffusion.

The measured current is directly proportional to the flux as shown by the following equation:

$$i = nFAj, \tag{1.21}$$

where n is the number of electron transfer, A is the electrode area.

What is worth noting is that Fick's 1st Law presumes that the flux is driven solely by concentration gradients within the solution without taking into account the gradient of electric fields. For the case that the diffusion species is charged (e.g., ions) the effect of the external electric fields is significant. In normal voltammetric practice however, the presence of sufficient background electrolytes eliminates the effect of the electric fields.

Fick's 2nd Law

Fick's 2nd Law can be derived from the first law. Consider an infinitesimal volume element of unit cross-sectional area and thickness dx, the change in concentration at a given location x is given by the difference in the flux in and out of the volume element:

$$\frac{\partial c}{\partial t} = \frac{J(x) - J(x + \partial x, t)}{dx} = -\frac{\partial J}{\partial x}. \tag{1.22}$$

Differentiating equation (1.19) we get

$$\frac{\partial J}{\partial x} = -D\frac{\partial^2 c}{\partial x^2} \tag{1.23}$$

and in turn the expression of how the concentration of a species at point x varies with time

$$\frac{\partial c}{\partial t} = D\frac{\partial^2 c}{\partial x^2}, \tag{1.24}$$

which is Fick's 2nd Law in one dimension. In three dimensions the appropriate expression

is given below as

$$\frac{\partial c}{\partial t} = D\left(\frac{\partial^2 c}{\partial x^2} + \frac{\partial^2 c}{\partial y^2} + \frac{\partial^2 c}{\partial z^2}\right) \tag{1.25}$$

This expression can be adapted for disc electrodes with cylindrical coordinates or spherical coordinates when dealing with spherical or hemispherical electrodes.

The Cottrell equation

The Cottrell equation was first considered by Cottrell to solve the problem which in modern parlance constitutes 'potential step chronoamperometry at a planar macroelectrode'. It describes the change in electrical current with respect to time in a controlled potential experiment such as chronoamperometry. Specifically it describes the current response when the potential is a step function. The change of the current is due to the depletion of material near the electrode surface with time as a potential is applied.

The Cottrell equation is expressed as follows:

$$I = \frac{nFA\sqrt{D}c^*}{\sqrt{\pi t}}, \tag{1.26}$$

where n is number of electrons transferred, A is the electrode area and c^* is the bulk concentration of the electroactive species. The Cottrell equation describes the case for a planar electrode but can also be derived for cylindrical and spherical geometries by using the Laplace operator and boundary conditions in conjunction with Fick's 2nd Law. The equation shows that the current decays to zero with a dependence that is inversely proportional to the square root of time.

Figure 1.4 shows the depletion of material near the electrode surface as experiment progresses. The zone of depletion is known as the diffusion layer of the electrode. The electroactive species have to diffuse across this layer to reach the electrode and react. The diffusion layer will become thicker as time progresses and both the rate of diffusion and and the current will decrease.

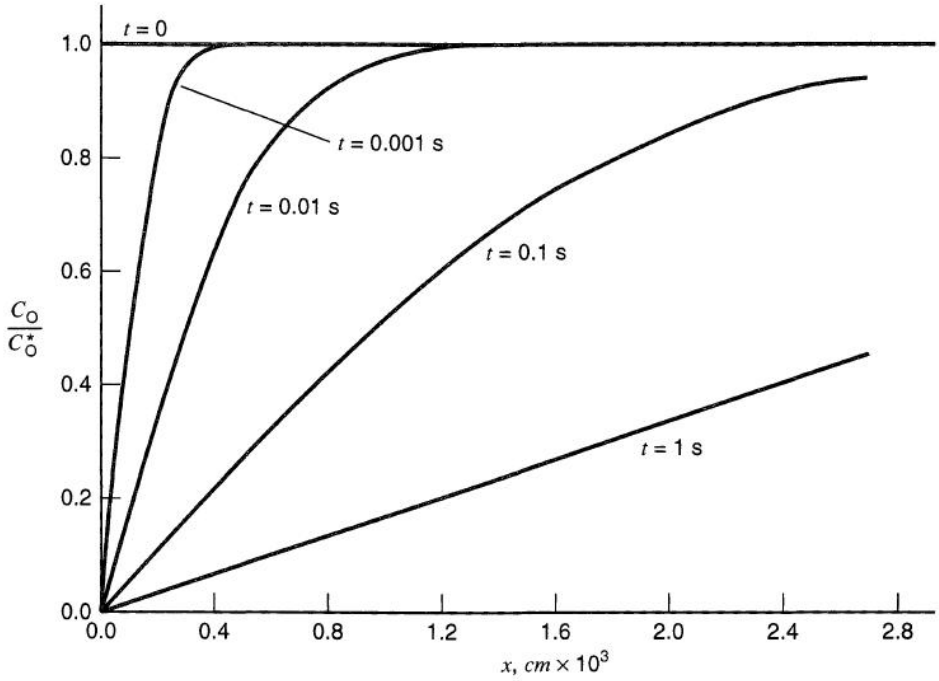

Figure 1.4: Concentration profiles at varying times after the start of a Cottrell experiment. $D = 1 \times 10^{-5}$ cm^{2}s^{-1}. $\frac{C_O}{C_O^*}$ is ratio of the concentration at the electrode surface to bulk concentration.

The Nernst diffusion layer

When a potential step is applied to a system, it is predicted that the current will depend on the reciprocal of the square root of time for up to a few seconds. However, at very short times the current due to the Faradaic processes is obscured by 'charging current', thus this dependence does not exist. At long time, the experimentally measured currents tend to reach a steady value rather than falling to zero as predicted by the Cottrell equation. This is consistent with Figure 1.5 from which we can see that the bulk solution is well mixed beyond a critical distance, δ, from the electrode, so that the concentration of elecroactive material is maintained constant. The mixing in the bulk solution is due to natural convection induced by density differences.

At the zone close to the electrode, the natural convection dies away. This zone, specifically between $x = 0$ and $x = \delta$, is the so-called diffusion layer. Since the change in concentration only takes place in this zone, diffusional transport is then operative in this

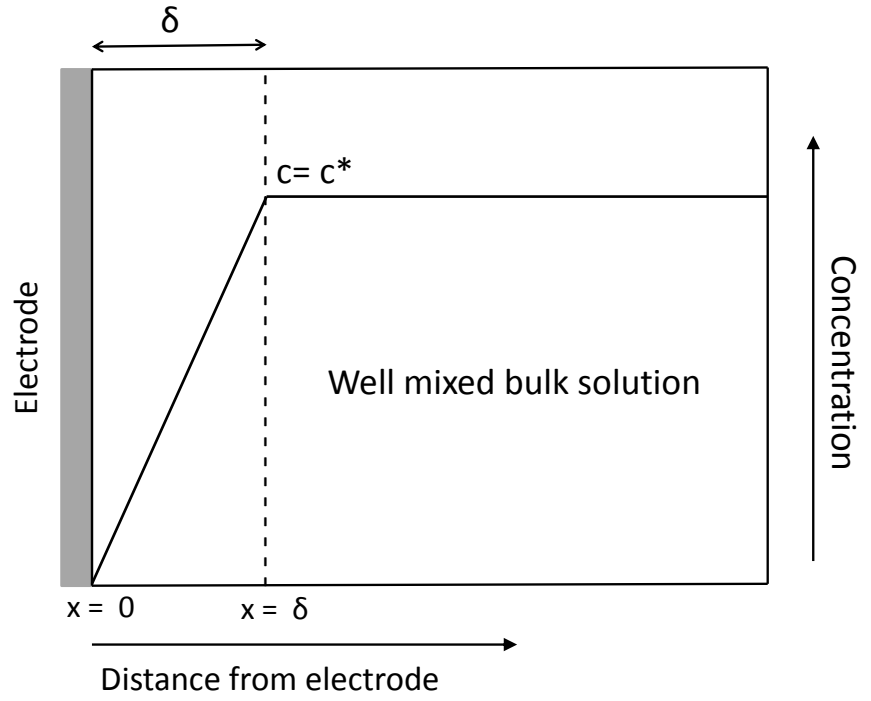

Figure 1.5: The Nernst diffusion layer model.

region described by Fick's 1st Law:

$$j = D\frac{\partial c}{\partial x} = \frac{Dc^*}{\delta}. \tag{1.27}$$

The corresponding current is

$$I_{ss} = \frac{nFADc^*}{\delta} = nFAm_T c^* \tag{1.28}$$

and

$$m_T = \frac{D}{\delta}, \tag{1.29}$$

where m_T is the mass transport coefficient (cm s^{-1}).

It is worth noticing that the Nernst diffusion layer is a simplified model. However, it is still helpful and insightful in experimental practice. For a diffusion-only model, it is important to restrict the timescale of the experiment so that the concentration changes are

confined to a distance significantly closer to the electrode surface than δ.

The Cottrell equation predicts that the limiting current falls with time. In contrast, a limiting current is attained in the case of the Nernst diffusion layer when the concentration decays from the the bulk value c^* to zero over the distance of the diffusion layer, δ from the electrode surface. The limiting current is shown in equation (1.28).

1.5 Electrode kinetics

Consider a simple one-electron transfer process:

$$A + e^- \underset{k_a}{\overset{k_c}{\rightleftharpoons}} B. \tag{1.30}$$

k_c and k_a represent the first-order heterogeneous rate constants for the forward (reductive) and backward (oxidative) electron transfer reactions, respectively. The net flux of the above process can be expresses as

$$j = k_c[A]_0 - k_a[B]_0, \tag{1.31}$$

where $[A]_0$ and $[B]_0$ are the bulk concentrations of the electroactive species.

In an analogous manner to chemical rate processes, electron transfer reactions can be described using the transition state model. This model views the reduction reaction of A to B as occurring via a path which involves an energy barrier to overcome. The summit of the energy barrier is called the transition state. Transition state theory predicts the rate of the reduction reaction (k_c) to be

$$k_c = Aexp\left(\frac{-\Delta G_c^{\ddagger}}{RT}\right). \tag{1.32}$$

$\Delta G_c^{\ddagger}$ is termed the standard free energy of activation and A is known as 'frequency factor' accounting for the rate of collision of the electroactive molecules with the electrode

surface. Similarly, the rate of the reduction reaction (k_a) can be expressed as

$$k_a = Aexp\left(\frac{-\Delta G_a^{\ddagger}}{RT}\right). \tag{1.33}$$

1.5.1 The Butler-Volmer equation

The Butler-Volmer equation is one of the most fundamental relationships in electrochemical kinetics and underpins most current interpretations of electrode kinetics. It describes how the electrical current, or reaction rate constant for an electrode depends on the electrode potential, considering that both a cathodic and anodic reaction can occur on the same electrode. For a typical one electron transfer system shown in equation (1.30), the rate constants k_c and k_a will be potential dependent. The cathodic reduction is expected to predominate at relatively negative electrode potentials whilst the anodic oxidation does so at relatively positive potentials.

The Butler-Volmer equation can predict the precise way in which k_c and k_a depend on potential. The most convenient forms of its expression are given below as:

$$k_c = k^0 exp\left[\frac{-\alpha F(E - E_f^0)}{RT}\right] \tag{1.34}$$

and

$$k_a = k^0 exp\left[\frac{+\beta F(E - E_f^0)}{RT}\right] \qquad (\beta = 1 - \alpha), \tag{1.35}$$

where k^0 is the standard electrochemical rate constant (cm s^{-1}) and is a measure of the rate of the redox couple. A reaction with a large value of k^0 will achieve equilibrium rapidly while the one with a small value will be sluggish. α and β are both known as transfer coefficients and provide a measure of the symmetry of the energy barrier. The value of the transfer coefficient normally lies between zero and unity, and for an experiment where kinetic data is collected over a relatively narrow potential range the value will remain

constant. $\alpha \rightarrow 0$ indicates that the transition state will be reactant like while α close to unity implies a product like transition state in a reduction.

1.5.2 The Tafel Law

According to the Butler-Volmer equation, the net flux (mol cm^{-2} s^{-1}) of a simple one-electron process described in equation (1.30) is:

$$j = k^0 exp\left[\frac{-\alpha F(E - E_f^0)}{RT}\right][A]_0 - k^0 exp\left[\frac{+\beta F(E - E_f^0)}{RT}\right][B]_0. \tag{1.36}$$

The net flux is a balance between the reduction current and the oxidation current. At extreme potentials, for example, $E \gg E_f^0$ or $E \ll E_f^0$ it is possible to neglect one of the terms, Accordingly, for an electrochemical reduction of A to B

$$A + e^- \rightarrow B \tag{1.37}$$

$$j = k^0 exp\left[\frac{-\alpha F(E - E_f^0)}{RT}\right][A]_0, \tag{1.38}$$

whilst for an electrochemical oxidation reaction

$$B + e^- \rightarrow A \tag{1.39}$$

$$j = k^0 exp\left[\frac{+\beta F(E - E_f^0)}{RT}\right][B]_0. \tag{1.40}$$

Assuming that $[A]_0$ and $[B]_0$ are not substantially altered from their constant bulk values, the Tafel equation can be written as

$$ln|I_{red}| = -\frac{\alpha FE}{RT} + constant \tag{1.41}$$

and

$$ln|I_{ox}| = \frac{\beta FE}{RT} + constant \tag{1.42}$$

Therefore, from a plot of $ln|current|$ against $potential$ it is possible to obtain the value of the transfer coefficient α or β.

1.5.3 Marcus theory

Marcus theory is another model to explain electron transfer kinetics. It was originally formulated to deal with outer sphere electron transfer reactions, for example, the reduction of Fe^{3+} to Fe^{2+}, where Fe^{3+} and Fe^{2+} only change in their charge with one electron transferred. Later Marcus theory was extended to include inner sphere electron transfer contributions, in which a change of distances of geometry in the solvation or coordination shells of the two species is taken into account. A typical example is the electrochemical reduction of $Fe(H_2O)_6^{3+}$ to $Fe(H_2O)_6^{2+}$ where Fe-O distances are different. Marcus Theory has provided a physical model for understanding the energetic control on electron transfer as well as a means of its calculations by relating the standard heterogeneous rate constant to a reorganisation energy.

1.6 Voltammetry at microelectrodes

In this section we will discuss the diffusion mode of microelectrodes and the corresponding change in the scope of voltammetric studies.

1.6.1 Spherical or hemispherical electrode

The current-time response resulting at a planar macroelectrode was discussed previously as

$$I \propto \frac{1}{\sqrt{t}} \tag{1.43}$$

The same exercise for a spherical or hemispherical electrode is essential to understand microelectrode behaviour. By solving Fick's 2nd Law of diffusion in spherical coordinates and applying the boundary conditions for potential step chronoamperometry, we can deduce the flux of reactant at the electrode surface:

$$j = Dc^* \left(\frac{1}{\sqrt{D\pi t}} + \frac{1}{r_e} \right), \tag{1.44}$$

where r_e is radius of spherical or hemispherical electrode. It is insightful to consider the short-time and long-time limits of equation (1.44).

1. At the short-time limit,

$$j = \frac{c^* \sqrt{D}}{\sqrt{\pi t}}. \tag{1.45}$$

Since $\sqrt{D\pi t} \ll r_e$. Under this condition, the diffusion layer is small compared to the radius of the spherical electrode, resulting in approximate linear diffusion.

2. At the long-time limit,

$$j = D\frac{c^*}{r_e} \tag{1.46}$$

or

$$I = 4\pi r_e DFc^* \quad \text{(sphere)} \tag{1.47}$$

$$I = 2\pi r_e DFc^* \qquad \text{(hemisphere)}. \tag{1.48}$$

The diffusion modes for both cases are illustrated in Figure 1.6

At long-time limit, a steady-state current or flux is established. This result does not conflict with the the Cottrell equation. In the case of spherical diffusion, because the

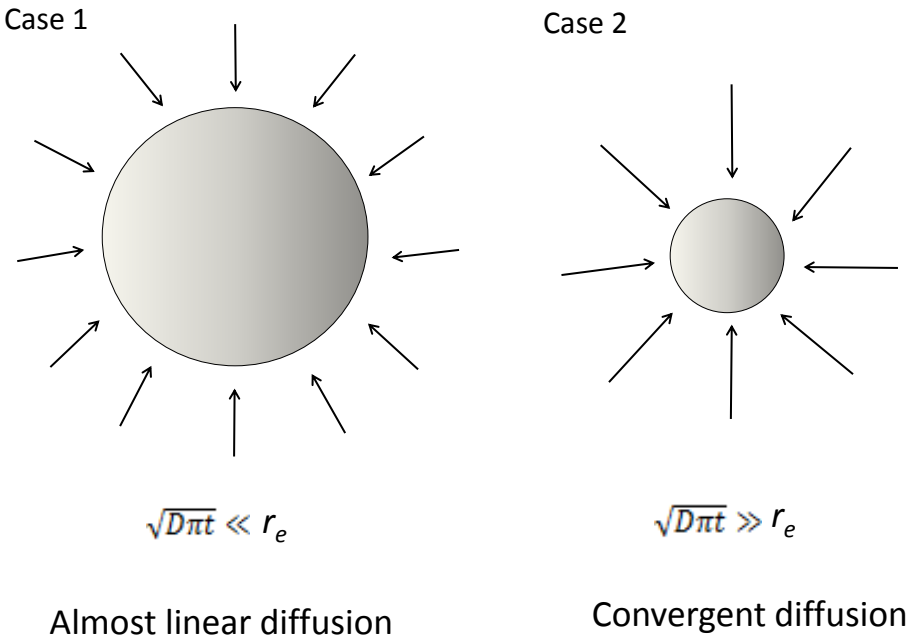

Figure 1.6: Two cases of diffusion to a sphere.

diffusion layer thickness will expand as the electrolysis continues so that its 'surface area' will increase. Thus more and more electroactive species will be met as time proceeds and will 'feed' the constant diffusion gradient at the electrode surface once steady-state is attained. From equation (1.44) it is obvious that the steady-state current tends to dominate for electrodes with small r_e. That is to say, a steady-state current is rapidly established at a microelectrodes of spherical or hemispherical geometry with the flux being greater with decreasing size of the electrode.

1.6.2 Microdisc electrodes

In the previous sections we have discussed the current-time transients resulting from potential steps at both a macro planar electrode and a spherical or hemispherical electrode. Similarly, dealing with Fick's 2nd Law in cylindrical coordinates and considering the relevant boundary conditions, we obtain the steady-state flux at any radius, r, on the disc electrode (radius r_e)

$$j = \frac{2}{\pi} \frac{c^* D}{\sqrt{r_e^2 - r^2}}. \tag{1.49}$$

At long times the current tends to reach a steady-state value, which is

$$I = 4nFc^* Dr_e. \tag{1.50}$$

As is predicted by equation (1.49), the flux at the disc edge is infinite, although in practice the electrode kinetics must be finite so this is never exactly true. The current flowing at the edge nevertheless dominates the steady state current. The transient is calculated as:

$$I = 4nFc^* Dr_e f(\tau), \tag{1.51}$$

where τ is the dimensionless time with its value $\tau = 4Dt/{r_e}^2$. For short times when $\tau < 1$,

$$f(\tau) = \left(\frac{\pi}{4\tau}\right)^{1/2} + \frac{\pi}{4} + 0.094\tau^{1/2} + \ldots \quad , \tag{1.52}$$

whilst at long times when $\tau > 1$,

$$f(\tau) = 1 + 0.71835\tau^{-1/2} + 0.005626\tau^{-3/2} - 0.00646\tau^{-5/2} + \ldots \quad . \tag{1.53}$$

It follows that at very short times the current can be expressed as

$$I = 4nFc^* Dr_e \left(\frac{\pi}{4\tau}\right)^{1/2} \tag{1.54}$$

$$I = \frac{nFA\sqrt{D}c^*}{\sqrt{\pi t}} \tag{1.55}$$

where $A = \pi {r_e}^2$. This result is simply consistent with Cottrell equation for planar diffusion implying that the diffusion to the microdisc electrode surface is effectively planar, or linear. Thus at these short times, the diffusion layer thickness is thin compared with the electrode size. At longer times, the decay of current is less rapid than what the Cottrell

equation predicts because the convergent diffusion also contributes to the current. The diffusion layer at long times approaches hemispherical geometry. Here $f(\tau) \rightarrow 1$, so that $I = 4nFc^*Dr_e$ as shown in equation (1.50).

1.6.3 Voltammetry: micro vs. macro

From the earlier part of this section we can summarise that at both a microdisc electrode or a spherical/hemispherical electrode, Cottrellian behavior can be seen at short times but the current tends to reach a steady-state value at longer times. We also notice that for both cases the steady-state current is only proportional to electrode radius, showing a convergent diffusion mode. With the decrease of the electrode size, the current density is greater, the material transport becomes faster, and the timescale to reach steady-state is shorter.

As we have mentioned in previous chapters, at a large planar electrode, the potential step leads to a Cottrellian decay to zero current. It is similarly the case that in voltammetry a peak-shaped response is seen at a macroelectrode under linear sweep conditions. The fall off of the current is a result of the depletion of material near the electrode surface so that the current is controlled by diffusion. In contrast, the current shown on the microelectrode voltammetry does not decay to zero but reaches a steady-state value at long times. Accordingly, if the applied potential is scanned at a sufficiently slow rate, no peak current is displayed at microelectrode. The comparison of the voltammetry of micro- and macro-electrodes is shown in Figure 1.7.

1.6.4 Shoup-Szabo expression

In section 1.6.2 a general current-time transient has been deduced in equation (1.51). Experimetalists can measure D and either c^* or n using this equation provided the third parameter is known. The Shoup and Szabo expression makes it possible.

The Shoup and Szabo expression is obtained empirically and correctly predicts the

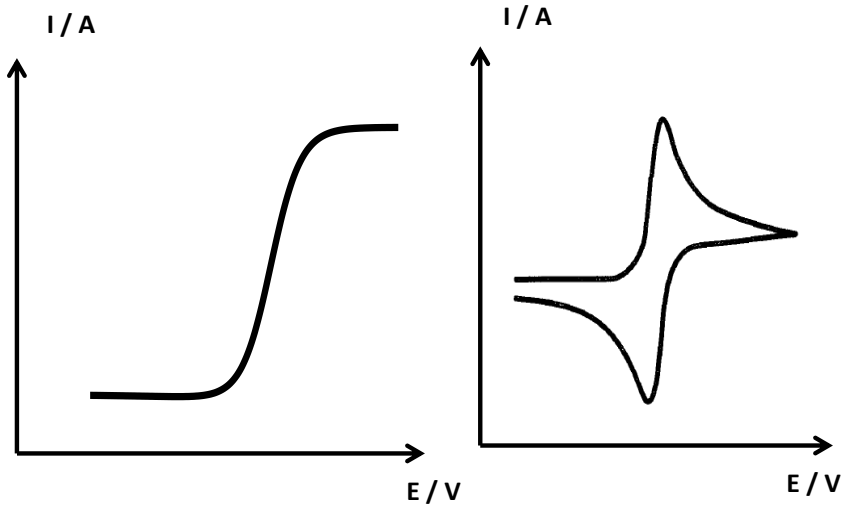

Figure 1.7: Voltammetry at a micro- (left) and a macro-electrode (right) at slow scan rates.

current over the entire time domain with a maximum error of less than 0.6%. The expression is as followed:

$$f(\tau) = 0.7854 + 0.8863\tau^{-1/2} + 0.2146exp(-0.7823\tau^{-1/2}). \tag{1.56}$$

It follows from equations (1.51) and (1.56) that it is possible to best-fit the measured transient to give simultaneously optimum values of D and nc^*, provided that the measured experimental data is of high quality. So if n or c^* are known, the third parameter may be deduced.

1.7 Cyclic voltammetry

The main used electroanalytical techniques presented in this thesis are cyclic voltammetry (CV) and chronoamperometry. As the latter has been covered in previous sections, we will focus on the the introduction of the former in this section.

Cyclic voltammetry (CV) is a type of potential dynamic electrochemical measurement and is the most common electroanalytical technique employed. In the CV experiment, a

potential is applied to the working electrode, which changes with time, according to a triangular potential waveform as shown in Figure 1.8. The experiment records the plot of current vs. potential which is known as a voltammogram. CV can be used to provide information on the system of interest, such as the kinetics of heterogeneous electron transfer and the thermodynamics of redox reactions and of adsorption processes.

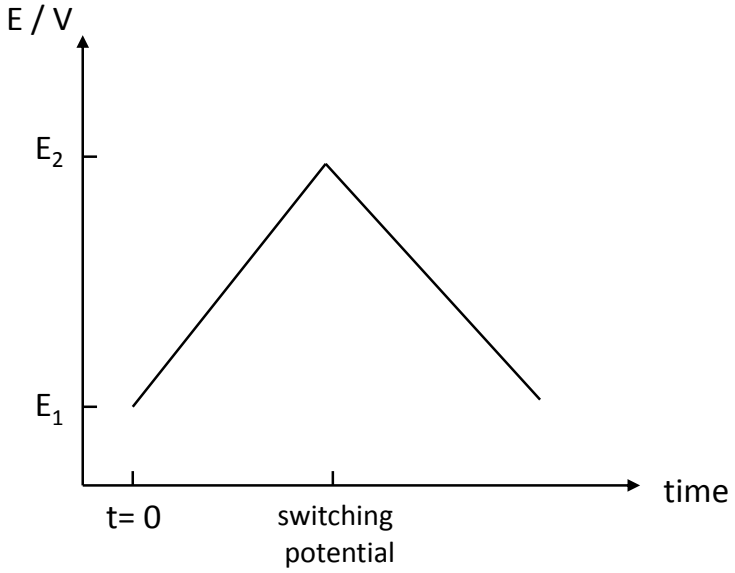

Figure 1.8: A triangular potential waveform.

Depending on the relative rates of electron transfer and mass transport to the electrode, a reversible, quasi-reversible or irreversible voltammogram is observed. Figure 1.9 shows typical reversible, quasi-reversible and irreversible voltammetry at a microelectrode obtained by varying the value of the standard electrochemical rate constant k^0, keeping all the other variables constant.

For a fully reversible A/B redox couple the peak current (i_p) can be given by the Randles-Sevčík equation:

$$i_p = (2.69 \times 10^5) n^{3/2} A c^* D^{1/2} \upsilon^{1/2} \qquad \text{at 298K,} \tag{1.57}$$

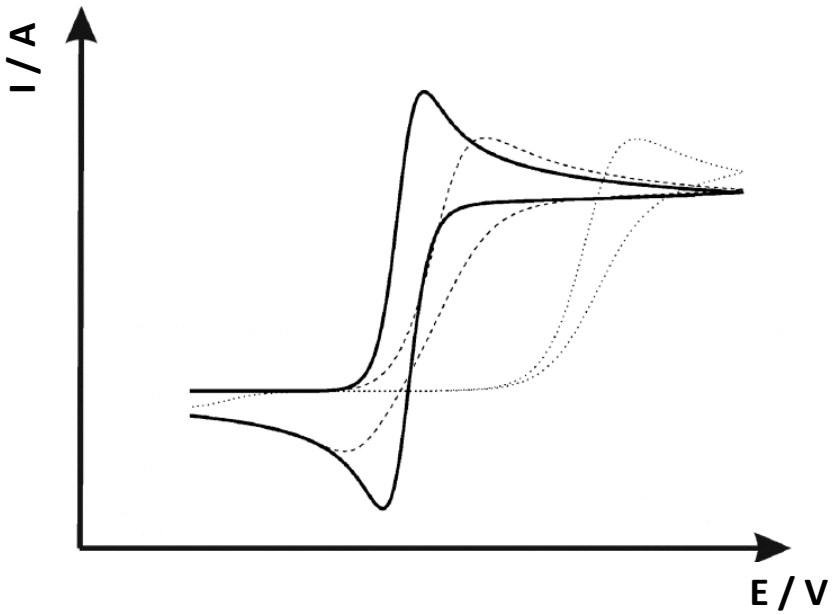

Figure 1.9: Examples showing reversible (solid line), quasi-reversible (dashed line) and irreversible (dotted line) voltammogram at a microelectrode.

where υ is the scan rate (V s^{-1}).

Irreversible and quasi-reversible systems display sluggish electron transfer. The voltammogram of these cases is normally distinguished by the wider peak-peak separation and the reduced magnitude of each peak. The peak current (i_p) of an irreversible electrode process can be predicted by a modified Randles-Sevčík equation: [1–7]

$$i_p = (2.99 \times 10^5)(n\alpha)^{1/2} A c^* D^{1/2} \upsilon^{1/2} \qquad \text{at 298K.} \tag{1.58}$$

Bibliography

[1] R. G. Compton and C. E. Banks. *Understanding Voltammetry, 2nd Edition*. World Scientific, Singapore, 2008.

[2] A. J. Bard and L. R. Faulkner. *Electrochemical Methods: Fundamentals and Applications, 2nd edn.* John Wiley & Sons, Inc., New York, 2001.

[3] A. C. Fisher. *Electrode Dynamics*. Oxford University Press, Oxford, 1996.

[4] P. H. Rieger. *Electrochemistry, 2nd Edition*. Chapman & Hall, New York, 1994.

[5] R. G. Compton and G. H. W. Sanders. *Electrode Potentials*. Oxford University Press, Oxford, 1996.

[6] J. Wang. *Analytical Electrochemistry, 2nd Edition*. Wiley-VCH, New York, 2001.

[7] C. M. A. Brett and A. M. O. Brett. *Electrochemistry: Principles, Methods, and Applications*. Oxford University Press, Oxford, 1993.

Chapter 2

Electrochemistry with metal nanoparticles

In this chapter I aim to give an overview of electrochemistry with nanoparticles with sections corresponding to various electrochemical characteristics of nanometallic particles and their practical applications. The introduction gives a brief idea of the basics of colloidal particles together with an overview of the related literature. Subsequently, typical synthesis procedures of common metal nanoparticles with regards to silver, gold and nickel, are discussed. The electrochemistry with metal nanoparticles is then reviewed in the areas of electroanalysis, electrocatalysis and single nanoparticle-electrode impacts (the main focus of the thesis) and finally a summary and some perspectives are given.

2.1 Introduction

Colloid chemistry is an important discipline to both science and technology [1, 2]. The electrical behavior of colloidal dispersions in solution classically encompasses colloidal nanoparticles with surface charges which act as stabilizers, repelling the nanoparticles from aggregating. The causes of the surface charges are from adsorption of small ions, surfactants, or polyelectrolytes and are also responsible for the electrokinetic properties of the colloidal nanoparticles.

Colloids, or metal sols, have long been known and taken use of, dating back to ancient techniques for imparting colors to glass. In the middle of 19th Century that such colorations are scattering phenomena was eventually qualitatively explained by Michael Faraday by proposing that the ruby red color of gold colloid is the consequence of its small particle size [3]. Since then small metallic particles have been the subject of scientific and technological interest. A large number studies of both theoretical and experimental work have been carried out to understand the basic characteristics of the electronic, optical, chemical and mechanical properties of metallic nanoparticles [4–6, 6–11]. At the beginning of the 20th century Mie made seminal contributions to correlate quantitatively the changes in the optical properties with the size of the particles, thereby placing our understanding of the optical coloration and absorbance spectra of metal nanoparticles onto a quantitative level [4].

Metal colloids and semiconductor colloids not only exhibit the same surface ionic charging and electrokinetic properties as other colloids, but also are able to act as electron donors and acceptors. This is an important distinction from the other colloids that was recognised by Henglein [12] and Grätzel [13] in their early work dealing, respectively, with electron storage on Ag nanoparticles during pulse radiolysis and with photocatalytic water reduction in the presence of colloidal Pt. The metal nanoparticles were aptly referred to as colloidal micro-/nano-electrodes which have been extensively used in the study of electrochemistry.

Electrochemistry has been inherently associated with nanoscience and nanotechnology and many electrochemical phenomena occur in size regimes that are very small. Petrii and Tsirlina reviewed the effects of size on diffusion kinetics, electrical double layer at the interface, elementary act of charge transfer and phase formation [14]. At the same time, an excellent account of the double layers, optical and electrochemical properties associated with metal colloids was given by Mulvaney [15]. Willner has reviewed the area of nanoparticle based functionalization of surfaces and their applications [9–11]. Recently Welch and Campbell [16, 17] concluded in their reviews unique advantages of nanoparticles over macroelectrodes when used for electroanalysis: enhancement of mass transport, catalysis, high effective surface area and control over electrode microenvironment.

This chapter is devoted to electrochemistry with nanoparticles. First, a general introduction and main synthesis procedures of metal nanoparticles with regards to silver, gold and nickel, the three nanoparticles used in the thesis, are discussed. Electrochemistry with metal nanoparticles is then reviewed in the areas of nanoparticle modified electrode, electroanalysis, and electrocatalysis. The electrochemistry of single metal nanoparticles is mentioned and finally a summary and some perspectives are given.

2.2 Synthesis of metal nanoparticles

2.2.1 Silver

Silver has the highest electrical conductivity of all metals and is highly stable. It is an ideal material for the construction of electrodes [18]. Silver is known for its catalytic properties, for example, to catalyse the decomposition of H_2O_2, and is an important material in the electroanalytical determination of a variety of analytes such as halides, toxic compounds, organic compounds and biomolecules. Over the last decades silver has been engineered into nanoparticles with sizes of 1 to 100 nm. The maximisation of the total surface area

of the nanoparticles leads to the highest values of the activity to weight ratio. As their properties can be distinctly different from that of the bulk metal, AgNPs have attracted much attention and have found applications in diverse areas, including catalysis [19], medicine [20], electronics [21], optics [22], and biotechnology and bioengineering [23]. Furthermore, nowadays AgNPs are very well known for the use as antibacterial/antifungal agents in a diverse range of consumer products [24].

In recent years, the most typical method of colloidal AgNP preparation is by chemical reduction of a silver salt in the presence of a protecting/stabilizing agent. This is commonly performed in an aqueous surfactant polymer solution as the composition of the reaction mixture can be very easily altered to employ different reducing and capping agents to obtain AgNPs. Typically used stabilizing agents include citrate, oleate, humic acid and cetyl trimethylammonium bromide (CTAB) [25–28]. Some uncommon stabilizing agents include the lipopeptide biosurfactant surfactin [29] and α-cyclodextrin [30]. In this thesis, the procedure for the preparation of AgNPs is taken from the work of Pyatenko *et al*. [25] using citrate as both the reducing agent and the stabilizer. Some alternative solution methods of preparation for colloidal AgNPs have included the use of biomolecules and microwave heating [31].

Electrodeposition is a unique process that produces nanoparticles with controlled size, morphology and the composition. It is simple, fast, inexpensive, and among the most familiar binder-free techniques. The advantage of this technique is that the nanoparticles get directly attached to the substrate and the characteristics of the nanoparticles can be controlled by adjusting the operating conditions and bath chemistry. The synthesis of AgNPs via electrodeposition method is typically by applying a pulsed or constant potential [32]. In addition, NPs of various sizes can be obtained by stripping of a Ag film with different durations of the applied striping potential. Furthermore, it is also possible to electrochemically deposit Ag-DNA hybrid NPs, by the addition of DNA to the deposition solution as a template [33].

2.2.2 Gold

Gold is also an efficient conductor of electricity and is known for its malleability and ductility. AuNPs have received great interest due to their attractive electronic, optical, and thermal properties as well as catalytic properties and potential applications in the fields of physics, chemistry, biology, medicine, and material science and their different interdisciplinary fields [34, 35].

As the high surface energy of AuNPs can make them extremely reactive, they can also suffer heavy aggregation. Thus, special precautions have to be taken to avoid their aggregation or precipitation in the processes of AuNPs production. Similar to AgNPs, AuNPs are typically prepared by chemical reduction of the corresponding transition metal salts in the presence of a stabilizer which binds to their surface to impart high stability and rich linking chemistry and provide the desired charge and solubility properties. Some of the commonly used methods include protection by self-assembled monolayers, the most popular being citrate [36] and thiol-functionalised organics [37];encapsulation in the H_2O pools of reverse microemulsions [38]; and dispersion in polymeric matrixes [39].

Although the synthesis of AgNPs has made great progress, problems on how to control the size, monodisperse, morphology and surface chemistry of AuNPs are still very challenging. Recently, designing novel protectors for AuNPs have been the focus of the research. The recent advances include the synthesis of biomolecule protected AuNPs [40, 41], green agent protected AuNPs [42, 43], polymer protected AuNPs [44, 45], and dendrimer protected AuNPs [46, 47]. AuNPs synthesised using the above methods have been put into wide application such as nanosensor, biosensor, catalysis, nanodevice and nanoelectrochemistry [40, 42, 44, 46].

AuNPs can also be produced using electrodeposition techniques. El-Deab and coworkers used a potential step electrolysis method to deposit AuNPs on a glassy carbon electrode [48]. Ma *et al*. employed the cyclic voltammetric technique to deposit AuNPs on to an indium tin oxide (ITO) electrode [49]. Furthermore, constant current electrolytic

method is also used for AuNPs production [50]. Apart from the metal nanoparticles, the preparation of composites of metal particles and conducting polymers with core-shell structure has also been reported [51, 52].

Another way to synthesize AuNPs is via electroless deposition. The typical examples of this methods are: electroless reduction of $AuNa(S_2O_3)_2$ by L-ascorbic acid onto a GCMS substrate [53]; silver-catalysed electroless deposition in SBA-15 [54]; $KAu(CN)_2$ and $HAuCl_4$ based electroless gold coating. In recent researches AuNPs have been produced to form nano-composite with other supporting materials or by template synthesis. For example, Kobayashi has deposited AuNPs electrolessly on polystyrene spheres [55] and on silica spheres [56]. Batchelor-McAuley *et al*. reported the electroless deposition of AuNPs on multi-walled carbon nanotubes (MWCNTs) [57]. The template synthesis of AuNPs by electroless deposition was reported to form AuNPs integrated nanotube arrays [58].

2.2.3 Nickel

Nickel is a hard and ductile metal and is a possible alternative to expensive noble metals such as platinum, palladium and silver, often used as cathode materials in fuel cells and capacitors. Ni nanoparticles (NiNPs) have attached much attention because of their use in numerous practical applications, such as magnetic materials, conducting materials and catalysts.

Various synthetic methods have been reported to prepare NiNPs in aqueous solution. Couto reported a modified polyol synthesis of small NiNPs using $NiCl_3$ as precursor, $NaBH_4$ as reducing agent and PVP stabilising agent [59]. A variety of surfactantless synthesis of NiNPs have also been proposed, including the work of utilizing hydrazine [60], and high-temperature synthesis [61]. Note that NiNPs are quite easily oxidised, thus it can be advantageous to coat them with a layer of carbon to protect them against oxidation of the surface, as well as to maintain the nanocrystralline properties and magnetism.

Alternative approaches to the synthesis of NiNPs include thermal decomposition of nickel organometallic precursor in alkylamines [62]; reduction of nickel salt in polyethylene glycol (PEG) [63]; pulsed-laser deposition in alumina matrix [64]; microwave irradiation by reduction of nickel precursor [65]; and electroless plating methods [66, 67].

2.3 Metal nanoparticle-modified electrodes for electroanalysis

Electroanalysis is one of the best methods for detecting species in solution, especially aqueous solution, both quantitatively and qualitatively. The advantages of electroanalysis over other detection techniques are its low cost, ease of use, accuracy and reliability. Common analytical techniques employed in electroanalysis include cyclic voltammetry (CV), chronoamperometry, differential pulse voltammetry, linear sweep voltammetry and stripping voltammetry.

Compared to the corresponding bulk materials, nanoparticles (NPs) have attracted intense interest for their unique optical, magnetic, electronic and chemical properties and have been exploited in many areas of electrochemistry, from analysis through catalysis, corrosion science and energy production/storage devices. With particular regards to electroanalysis, as is mentioned in Introduction, Welch *et al*. [16] and Campbell *et al*. [17] concluded unique advantages to the use of a nanoparticle-modified electrode when compared to a macroelectrode. They are: high effective surface area, enhanced mass transport, catalytic activity, improved selectivity, higher signal-to noise ratio and unique optical properties. The use of NPs also provides control over the local microenvironment which can be highly advantageous when incorporating sensitive or biological material into a system. In the following section I will explain in detail the above advantages with particular attention to mass transport and catalytic properties.

As is discussed by Compton *et al*. [68], the size of the electrode affects the mass trans-

port of redox active species to and from the electrode surface and the bulk solution, which, in turn, influences the observed electrochemical response. They assume the voltammetry to perform in stagnant solution and consider a simple electrochemically and chemically reversible one-electron transfer process between the electrode and species A in solution to form the product B in solution:

$$\mathrm{A} + e^- \rightleftharpoons \mathrm{B}. \tag{2.1}$$

The diffusion of A from bulk solution to the electrode is described by Fick's first and second laws of diffusion, given in one dimension by equations (2.2) and (2.3), respectively:

$$j = -D\frac{\partial C}{\partial x} \tag{2.2}$$

$$\frac{\partial C}{\partial t} = D\frac{\partial^2 C}{\partial x^2} \tag{2.3}$$

where j is the flux (mol cm^{-2} s^{-1}), D the diffusion coefficient (cm^2 s^{-1}) and C the concentration (mol cm^{-3}).

At a macroelectrode, the diffusion of A to the electrode or B from the electrode surface is planar and the current response is typically described as 'diffusion limited'. At the edge of the macroelectrode, the diffusion to or from the edge is effectively to a point, therefore the flux, j, and hence the rate of mass transport, is correspondingly larger and diffusion becomes convergent. This 'edge effect' is negligible at a macroelectrode, but the convergent diffusion to the edges of the electrode becomes increasingly significant as the dimensions of the electrode are decreased. When the dimensions of the electrode are decreased to nanoscale, the diffusion to the nanoelectrode is almost totally convergent. However, the authors also pointed out that non-Fickian diffusion effects may be observed below a threshold of NPs radius of 10 nm, where the continuum description starts to fail. Convergent diffusion to NPs electrode provides the benefit of enhanced mass transport,

and in turn means that the current density at these individual electrodes is greater than at a macroelectrode.

The enhanced mass transport at NPs also modify the appearance of the voltammetric signal due to the increased mass transport overpotential. Conversely, the catalytic properties of some NPs can cause a decrease in the overpotential needed for a reaction to become kinetically viable, producing voltammetry which appears more reversible than that displayed by the corresponding macroelectrode [16].

Of course cost considerations are important when constructing an electrode for real use. NPs modification of an inexpensive substrate material can lead to a larger surface area-to-volume ratio for the expensive metal and in turn lower the cost of the electrode. The large effective surface area may also cause a larger number of active sites and often a higher signal-to-noise ratio.

2.3.1 Voltammetry of NP modified electrode

As is mentioned above, convergent diffusion to NPs electrode provides the benefit of enhanced mass transport, which in turn means that the current density at these individual electrodes is greater than at a macroelectrode. However, the absolute current measured is much smaller due to the much smaller size of single nanoparticle (NP). Therefore various strategies have been taken to overcome this problem, by fabricating nanoband array electrodes, or NPs modified electrodes [69, 70]. The next two chapters of this thesis will focus on the voltammetry of NP modified electrode in terms of the effect of size and coverage of NPs in voltammetry. In the following section we will give an introduction to NP modified electrodes and also an overview of recent research advances in this area.

Simm *et al*. illustrated the effect of nanoparticle size (hemispherical, radius r) within an array on peak current and compared it to that of a macroelectrode (disc, radius $R = 1$ cm) [71]. For low coverages the response reflects the sum of the individual nanoparticles responses whereas for large coverages the diffusion fields overlap and ultimately linear

diffusion to the entire NP modified electrode results.

However, Simm *et al*. and Compton *et al*. [68] also stated that in practice it is difficult to achieve diffusion independence. Instead, the diffusion layers surrounding each nanoparticle in the array often overlap to varying extents with the diffusion layer surrounding their neighbours. This lack of diffusional independence can actually be taken as advantageous [68]. For example, the overlap of neighbouring diffusion layers within the array can be sufficiently large that diffusion to the entire array becomes planar, or almost planar. Under this circumstance, the nanoparticle array electrode behaves as if it were a macroelectrode. As such, one can construct nanoelectrode arrays that behave as if they were a macroelectrode of the same material as the nanoparticles used to construct the array, whilst only requiring a fraction of the amount of material required to make such a macroelectrode. This is particularly economic in practical sensor designs, as most metal electrodes are made using expensive metals such as platinum, gold, etc.

Next let's look at the voltammetry of NP (array) modified electrode. We consider first the voltammetric response of a single spherical NP sitting upon a planar electrode, assuming electrolysis occurs only at the NP surface. Streeter [72] simulated this problem and demonstrated the correlation between the voltage scan rate and the shape of the voltammetry. They considered a simple one electron reduction process of A to B and the response was shown to be a function of the dimensionless sweep rate (σ),

$$\sigma = \left(\frac{F}{RT}\right)\left(\frac{\upsilon r^2}{D}\right), \tag{2.4}$$

where υ is the voltage scan rate (V s^{-1}), r is the nanosphere radius and D is the diffusion coefficient of species A and B, assumed to be equal. Typical responses are shown in Figure 2.1 for scan rates σ of 10^{-3}, 1 and 10^{3}. Note that for sufficiently slow scan rate a steady-state current is established; with the increasing of the scan rate the diffusion layer becomes increasingly compressed and a peak-shaped voltammetry is shown.

When electrodes are modified with a sufficient coverage of NPs such that their diffu-

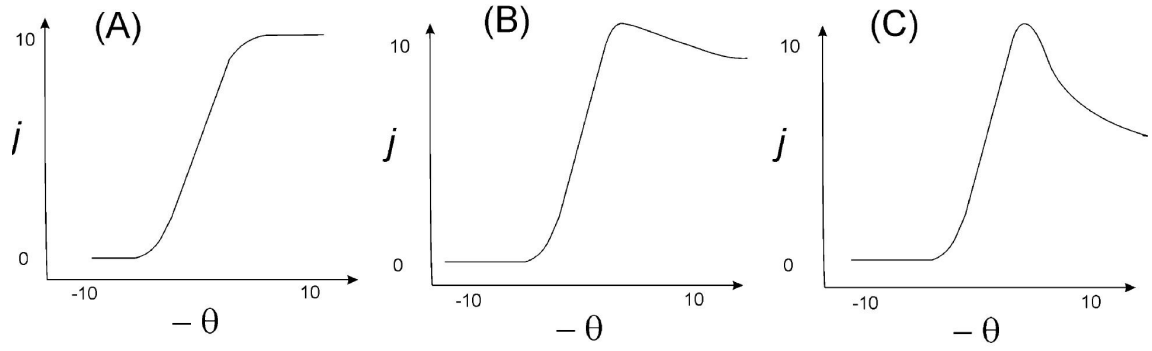

Figure 2.1: The voltammetric behaviour simulated for the reversible electron transfer at a spherical particle. Scan rate (σ) 10^{-3} (a), 1 (b) and 10^{3} (c)

sion layers interact, the current per NP is reduced from that predicted for isolated NPs. In particular, four cases of behaviour can be identified [73], as summarised in Figure 2.2. Over short time scales, the NPs are isolated so that diffusion is initially linear and a peak-shaped voltammetry can be obtained (case 1). Case 2 describes convergent diffusion at two adjacent but diffusionally independent NPs and it gives a steady-state voltammetry. Over longer time scales, the diffusion zones for adjacent NPs overlap, leading to less efficient mass transport (case 3). At long times, diffusion occurs linearly over the entire assembly and peak-shaped voltammetry reemerges. The corresponding voltammetry is shown in Figure 2.3. The four cases of diffusion mode will be restated and detailed in Chapter 4.

Recently, investigations have been done into the effect of NP size and coverage on voltammetry and whether or not the electrode kinetics changed between the macroscale and the nanoscale. Campbell *et al*. [70] studied H_2O_2 reduction at a silver NP (AgNP) array, which has shown that the voltammetric trace for H_2O_2 reduction will vary with both NP size and the extent of surface coverage. A decrease in NP size causes a negative shift in the peak potential (the change in the mass-transport regime, planar to convergent), whereas increasing coverage causes a positive shift (diffusion layers of neighbouring NPs becoming more heavily overlapping, tending towards linear diffusion to and from the electrode surface). Furthermore, they observed similar transfer coefficients between mac-

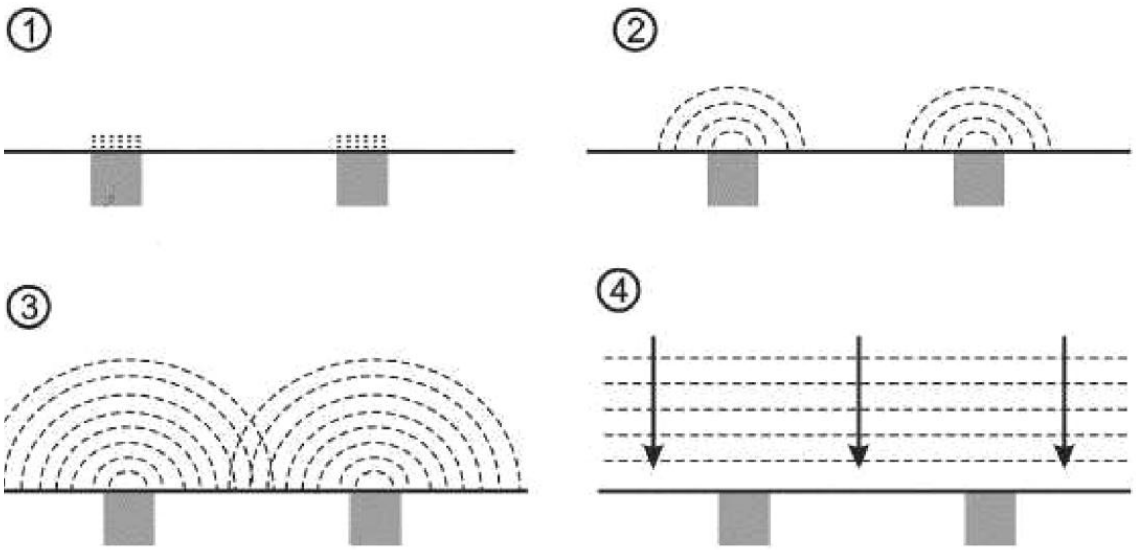

Figure 2.2: (1) Linear diffusion to each nanoparticle. (2) convergent diffusion to each nanoparticle. (3) Overlapping diffusion zones. (4) Overall linear diffusion.

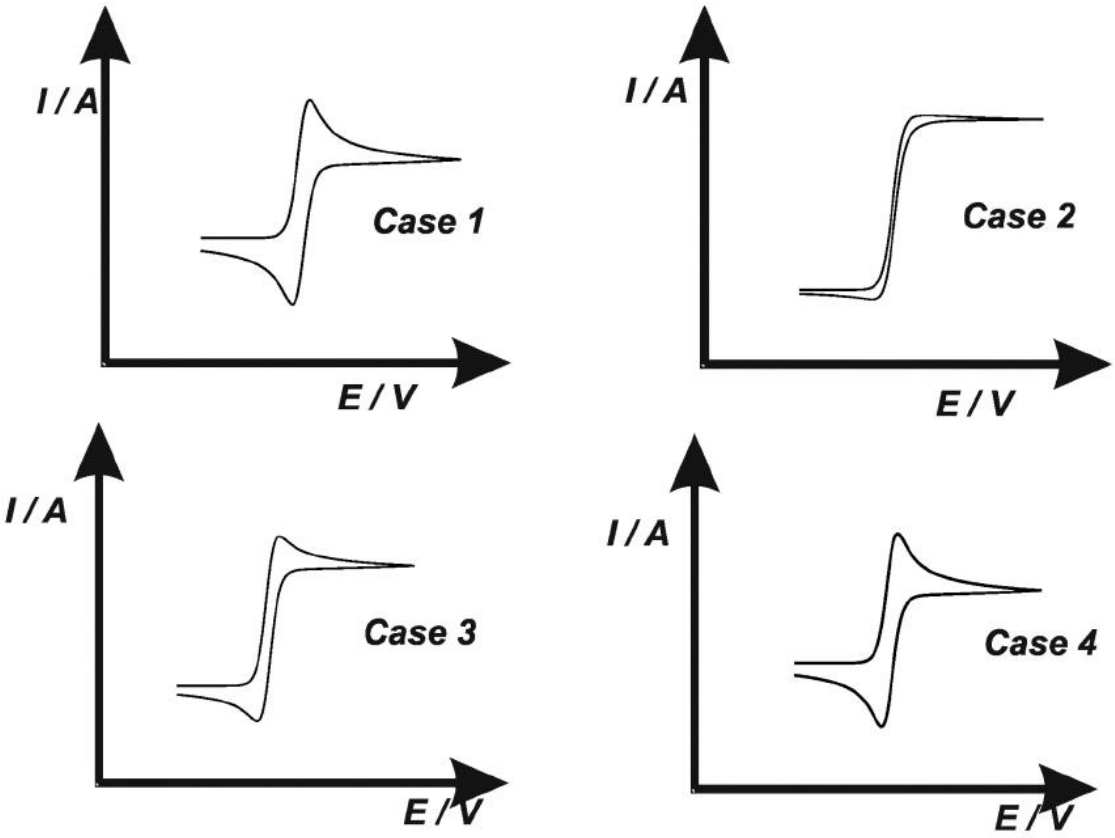

Figure 2.3: Typical voltammetric responses obtained for case 1, case 2, case 3 and case 4 at varying scan rate.

roelectrode and NP array. In contrast, for the reduction of protons at AgNPs arrays, both the rate constant and the transfer coefficient changed markedly between the two electrode types [74].

Later, Campbell *et al*. [75] investigated the altered electrode kinetics reported at the bulk Ag macroelectrode and at AgNP arrays for the reduction of 4-nitrophenol. They found out that the NP arrays displayed significantly altered electrode kinetics from that obtained at the Ag macroelectrode, therefore inferring a change in the mechanism of the rate-determining step for the reduction of 4-nitrophenol between the macro- and nano-scales.

Meanwhile, as will be fully discussed in Chapter 4, Zhou and co-workers [76] have found the shape and size of voltammograms obtained on AgNP modified electrodes to be extremely sensitive to the NP coverage, reflecting the transition from convergent to planar diffusion with increased coverage. They also found a linear relationship between the apparent rate constant and the degree of surface coverage. The extrapolation gives a value close to that recorded experimentally for the silver macroelectrode, showing that by increasing the NP density the electrode kinetics tend towards those of a macro-disk electrode.

The apparent size-dependent adsorption behaviour of AgNPs towards the underpotential deposition (UPD) of a selection of heavy metals was investigated by Campbell and Zhou [77, 78], considering the UPD of thallium, lead and cadmium at AgNP arrays. For all three heavy metals, distinctive UPD behaviour is observed at large NPs and bulk Ag electrodes but no obvious UPD feature recorded at NPs below 50 nm diameter.

Additionally, NP size effects have been simulated by Ward Jones *et al*. [79] for the anodic stripping voltammetry of various sizes of AgNPs and have been compared with experimental data.

In the following sections an overview will be given for NPs modified electrodes and their used in electroanalysis, depending on commonly used modification methods.

2.3.2 Electrochemical deposition of metal NPs

Electrochemical deposition is a powerful method to construct metal NP modified electrodes. As the nucleation and growth of metal NPs occur directly on a conducting surface during electrolysis, the attachment of metal NPs should be strong enough and the conducting between the base and the NPs should be good enough. However, careful controls of the electrolysis conditions are needed for preparing NPs with uniform size and controlled densities since the electrolysis reaction does not tend to proceed uniformly.

Glassy carbon (GC) electrodes are the most used substrate electrodes for electrochemical deposition of metal NPs. Finot *et al*. [80] reported gold nanocrystals deposited electrochemically on GC substrates and showed that the particle size, density, and surface texture can be controlled by varying the deposition conditions. El-Deab *et al*. [81] reported the control over the loading of AuNPs on GC for the electrochemical reduction of oxygen, by changing the concentration of $AuCl_4^-$ and the deposition time. Furthermore, they reported the control of crystallographic orientation of AuNPs on GC in the presence of two different additives (cysteine and iodide ions). The direct electron transfer of copper-zinc superoxide dismutase was realised.

The potential step method was used to electrodeposit AuNP onto GC electrode which has been utilised for an anodic stripping voltammetric analysis of As(III) in 1 M HCl by Dai *et al*. [82]. In addition, a flow analysis electrochemical system for the detection of As(III) has been developed using an AuNPs-modified GC electrode prepared with a similar electrodeposition by Majid *et al*. [83].

In addition to AuNPs, AgNPs were reported to be electrodeposited on a GC electrode, and were utilised for the electrocatalytic reduction of benzyl chloride [84]. Palladium NPs (PdNPs) could also be prepared on GC by simple electrochemical deposition process and showed the effectiveness in the detection of catecholamines in the presence of ascorbic acid by differential pulse voltammetry [85]. Further, Aoun and Taniguchi [86] reported the direct electrocatalytic oxidation of glucose in alkaline solution using electrochemic-

ally deposited platinum NPs (PtNPs).

Indium tin oxide (ITO) is another substrate devoted for the electrochemical deposition of metal NPs. Dai and Compton [87] reported the preparation of AuNPs modified ITO film coated glass electrodes for the first time through direct electrochemical deposition from acidic solution containing 0.1 mM $HAuCl_4$. The resulting surfaces were characterised with AFM and utilised for the detection of As(III).

Besides the commonly used Au precursor $AuCl_4^-$, Wang *et al*. [88] reported the direct electrodeposition of AuNPs onto ITO using a $KAu(CN)_2$ phosphate buffer solution by a cyclic voltammetric mode. The as-prepared AuNPs deposited ITO coated glasses were used for the immobilisation of superoxide dismutase, which realised direct electron transfer and for the detection of a superoxide anion. They also reported the applications of the same electrodes in the electrocatalytic oxidation of glucose [89], the construction of a horseradish peroxidase-based hydrogen peroxide sensor [90], and the amperometric detection of morphine [91].

Recently, Toghill *et al*. [92] reviewed the modification of boron doped diamond (BDD) electrodes with electrodeposition from metal salts to obtain metal NPs (such as Au, Ag, and Pt NPs) modified BDD electrodes, and their use in electroanalysis. As a new substrate, a carbon ionic liquid electrode was reported as a support to form a PdNP array electrode by electrodeposition [93]. This electrode was applied to O_2 reduction, H_2O_2 oxidation, and the oxidation of formaldehyde.

2.3.3 Modification of chemically prepared metal NPs

Another approach to prepare metal NP modified electrodes is via chemical preparation of metal colloids followed by immmobilisation of the NPs onto substrate electrode. Before modification, chemically synthesised metal NPs in solutions are grown to have a well-controlled shape and size that can be modified or attached onto the electrode surfaces. This contrasts with the electrochemical deposition method where size and shape control

is hard. However, some functional bindings of metal NPs are necessary for fixation on the electrode surfaces, though metal NPs might be modified on the electrode just by simple drop-casting method in some cases [94]. Thus many researches have been carried out to the interfacial nanoarchitectures of metal NPs to prepare metal NPs modified electrode.

The use of bridging reagents, or linker molecules, is a well-known approach. For example, 3-mercaptopropyl-trimethoxysilane (MPTMS), 3-aminopropyltrimethoxysilane (APTMS) or related compounds can be utilised to attach AuNPs onto the surfaces of glass, ITO or SiO_2 due to the bonding ability of the silanol group and the affinity of the -SH or $-NH_2$ group toward AuNPs [95, 96]. AuNPs attached with the APTMS linker have been reported for the construction of further Au nanostructuring on glass [97], SiO_2 [98] and ITO electrode [99]. However, the organic moiety and the alkyl-chain length of the linker molecules can hinder the electron-transfer reactions. Thus the drawbacks of organic components should be kept in mind when evaluating the performances of the modified electrodes under the view of electron transfer.

In addition to linker molecules, capping reagents also affect the electron transfer efficiency and electrocatalytic properties of metal NPs. For example, the Brust-Schiffrin method [100] is a breakthrough to prepare very small thiol-capped AuNPs with uniform size. However, the thiol capping is too strong to allow good electrochemical results [101], raising the importance of the selection of different capping agents for the better performance of metal NPs modified electrode.

Successful electrochemical results have been obtained after removal of the capping layer. For example, after heat removal of the capped decanthiol at 300°C, Au [102], Au-Pt alloy [103], and bimetallic Au-Ag NPs [104] modified carbon electrodes showed excellent electrocatalytic activity towards the oxidation of glucose. In addition, Chen and co-workers [105] prepared Fe-Pt alloy NPs modified Au electrode for the electrooxidation of formic acid after removal of capping agents oleylamine and oleic acid in an ultraviolet zone chamber.

2.3.4 Metal NPs integrated nanoarchitectures

While electrochemically and chemically derived metal NP modified electrodes are summarised above, metal NP integrated nanoarchitectures have been developed. In particular, carbon nanocomposites such as carbon nanotubes (CNTs) and graphene have led to interesting applications.

Dai *et al*. [106] reported the electroless plating of AuNPs onto the surfaces of GC microspheres followed by wiring up the modified spheres using multiwalled carbon nanotubes (MWCNTs) in a film on a GC electrode. The as-obtained nanostructure showed equivalent voltammetric behaviour to As(III) reduction as an Au film macrodisk electrode but only used about 1% of its material. In recent progress, Qu *et al*. [107] reported the electrochemical fabricaton of Au, Ag, Pt or Pd NPs with a diameter of 40-60 nm using a MWCNTs/GC electrode and investigated the electrocatalytic activity of thus-formed nanocomposites.

AgNPs decorated CNTs have attracted attention of many researchers. Tsai's group [108, 109] prepared AgNPs in MWCNT-modified ITO electrode using Nafion which was applied to a surface-enhanced Raman scattering chemical sensor. It has also been reported that in the presence of carboxy group functionalised or poly-grafted CNTs, AgNPs were *in situ* electroreduced from $AgNO_3$ solution. The resulting AgNPs/CNTs nanohybrids were then drop cast on a gold electrode and used as a non-enzymatic hydrogen peroxide sensor [110, 111].

Other metal NPs such as Pd and Pt NPs have also been extensively studied. Chen *et al*. [112] reported the modification of the carboxyl group functionalised CNTs with PdNPs. The prepared nanostructure was then fixed on a GC electrode with Nafion and applied to a novel non-enzymatic sensor for glucose. PtNPs were reported to be electrochemically deposited on a MWCNT/Nafion coated GC electrode using cyclic voltammetry method and used for methanol oxidation [113].

Layer-by-layer assembly method provides a route for preparing integrated nanoar-

chitectures. AuNP/MWCNTs thin film was fabricated using this technique and applied to the electrooxidation of methanol. Crespilho *et al*. [114] reported a unique layer-by-layer approach for constructing nanostructured membranes composed of polyamidoamine dendrimers, AuNPs, redox mediator, and poly(vinylsulfonic acid) [115].

Graphene, a single atomic layer of graphite, has fascinated the scientific community in less than ten years due to its large thermal conductivity, excellent mechanical properties, large surface area and very high electronic conductivity. Unlike rolled structured CNTs, graphene is a two-dimensional planar sheet with an open structure; hence both sides of graphene can be utilised for supporting catalysts. Therefore it is expected to be a promising catalysts carrier. Many trials have been done to fabricate metal NPs decorated graphene [116, 117], such as chemical reduction, chemical vapor deposition (CVD), and high temperature treatment. The prepared NPs/graphene was put into application of electrocatalysis of methanol and glucose. However, these methods have their drawbacks such as being time or labour consuming, and may not be environmentally friendly. Xia's group [118] pioneered a novel method of one-step electrochemical reduction to fabricate graphene supported Pt NPs. This method is green, fast and economic and the obtained material showed superior electrocatalytic property towards the oxidation of methanol.

In addition to CNTs and graphene, other materials were also used to support metal NPs. Baron *et al*. summarised in their review metal NPs deposited onto carbon microspheres and their use for electroanalysis [119]. Colloidal spheres of TiO_2 [120] and polymer [121] have been used for the assembly of PtNPs and Au/Pt NPs. In the area of template synthesis, a porous anodic alumina template was used to fabricate AuNPs integrated nanotubes by electroless deposition [58] found the application in non-enzymatic electrooxidation of glucose.

2.4 Metal nanoparticles for electrocatalysis

The use of metal NPs for electrocatalysis has been well documented [122–124] since early 1970's. Improving the performance of electrochemical devices has driven the research on the use of NPs for electrocatalysing various reactions with the aim of using them in the construction of fuel cells, sensors, and batteries. Since vast reviews on this topic are already available, we only summarise recent literature here on the use of NPs with regards to the electrooxidation of methanol, electroreduction of oxygen, electrocatalysis of other reactions, and application to batteries and capacitors.

2.4.1 NPs for electrocatalytic oxidation of methanol

Studies on the electrocatalytic oxidation of CO and methanol have attracted massive attentions from researchers of both electrochemistry and catalysis [125]. The most commonly used catalysts for methanol oxidation belong to the platinum (Pt) group. For example, Pt NPs have been modified onto the boron-doped diamond electrodes [126] towards achieving electrocatalysis of methanol oxidation. The high dispersity inside the nano-honeycomb matrix and the high surface area of the NPs lead to very good electrocatalytic properties. However, one major disadvantage associated with these catalysts is that they tend to get poisoned by the CO-like intermediates formed during the catalytic processes. Various trials have been done to solve this problem with the most common one being the use of Pt-M alloy NPs (M is another metal). The mechanism of some binary systems has been reported: decomposition of methanol occurs only on platinum atoms while the other metal atoms provide active oxygen-containing species for removing poisoning intermediates such as adsorbed CO [127, 128].

Yao *et al*. [127] have prepared highly dispersed Pt-Ru NPs with different atomic ratios supported on carbon nanotubes (CNTs). Their electrocatalytic activity towards methanol oxidation strongly depends on the atomic ratio of Pt to Ru. The higher the concentration of Pt in the binary system is, the greater the electrocatalytic activity will be. Zhong and

co-workers [128] have deposited Au-Pt alloy on a GC electrode surface by the exchange-crosslinking-precipitation route and applied the obtained material for methanol oxidation in alkaline media. Recently, Liu and co-workers [129] reported a new synthesis of Pt-Re alloy NPs with controlled size, dispersion and composition by a capping agents-based method. The as-prepared Pt-Re alloy NPs showed high activity for methanol electrooxidation.

In addition to Pt based alloys, less noble metal NPs such as copper-palladium (Cu-Pd) and silver-palladium (Ag-Pd) NPs have also been explored as catalysts for methanol oxidation in alkaline media [130]. However, in these studies the alloying process causes deterioration in the performance compared to pure palladium clusters. Most recently, Hu *et al*. [131] reported hollow Pd-Cu alloyed nanostructures prepared through a one-pot template-free strategy and their use as an anode electrocatalyst in direct formic acid fuel cell.

2.4.2 NPs for electrocatalytic reduction of oxygen

The use of proton exchange membrane fuel cells (PEMFCs) could become widespread by improving the performance of the oxygen reduction reaction (ORR), where Pt is the typical electrocatalyst [132]. Critical issues relating to ORR which need to be addressed are: the less catalytic efficiency for ORR, the high material cost and the gradual Pt degradation in the form of Pt dissolution, electrical Ostwald ripening, coalescence, carbon corrosion and Pt particle detachment [133]. In addition, the kinetic limitation of the ORR causes an overpotential loss, associated with the surface adsorption and reductive charge transfer process on the catalyst surface [134]. Therefore, the development of highly active catalysts with low Pt loadings for ORR has always been an important challenge. Pt and Pt alloy NPs have been extensively studied for ORR in acidic solution but ORR researches in base are sometimes found.

The classic work on this topic was published in *Nature* in 2001 [135] describing the

ordered nanoporous arrays of carbon supporting high despersions of PtNPs followed by the removal of the the mesoporous silica template. The resulting Pt cluster diameter can be controlled to below 3 nm, and the high dispersion of these metal clusters gives rise to promising electrocatalytic activity for ORR. This work was a breakthrough in early last decade and has been cited for more than 1000 times so far. After that massive studies have been done to improve the electrocatalytic performance of PtNPs towards ORR [133, 136, 137]. Very recently, Perez-Alonso and co-workers [132] have investigated the effect of size upon the ORR activity of PtNPs with diameters ranging from 2 to 11 nm supported on a planar GC surface. They have shown that the specific activity of the ORR on PtNPs first increases and then decreases with NP size, with a maximum for NPs with a diameter of 3 nm. Other metal NPs such as gold [138] and silver [139] have also been reported.

Similar to methanol oxidation, in the last decades Pt bimetallic NPs catalysts (PtM with M = Co, Cu, Ni, etc.) have shown their importance due to their improved ORR activity, the decreased Pt loading and the resulting reduced cost in materials. All these bimetallic NPs which show an improvement in electrocatalytic activity focus on the modification of the surface composition at the atomic scale [140–142]. The observed surface reactivity brought about by the neighborhood of two different metals in or near the particle surface is associated with ligand effects, ensemble effects and geometric effects [143–145].

More recently, core-shell NPs as particular arrangement of binary metals, have been paid much attention [146–148]. Typical core-shell NPs are composed of a shell of enriched or pure metal A and a core of a different composition (pure B or alloys of A and B) surrounded by the shell. The improved catalytic activity is based on the short-range chemical ligand effects and/or long-range geometric effects such as lattice strain, depending on the shell thickness [149, 150].

2.4.3 Electrocatalysis of other reactions

In addition to electrooxidation of methanol and electroreduction of oxygen, metal NPs or NPs alloys have been used for electrocatalysing other reactions, especially the oxidation of formic acid which is crucial for the development of direct formic acid fuel cell. Nano-scaled Pd islands on highly oriented pyrolytic graphite have been found to be very useful in catalysing hydrogen electroadsorption and desorption and hydrazine oxidation [151]. PtNPs incorporated on gold electrodes have been used to probe the desorption of hydrogen, oxygen and the oxidation of formic acid [152]. The use of AgNPs has been found to enhance the redox activity of organosulfur compounds [153] and that of nanocrystalline Pt particles on the electrooxidation of oxalic acid has been reported [152].

2.4.4 Application to batteries and capacitors

There have been many attempts to utilise nano-scaled materials for battery applications [154–157]. Nanosized alloys of Sn-Sb dispersed on carbon are found to be good anodes for lithium batteries [155]. Through these alloys have been reported to possess high reversible capacities, there is considerable loss in subsequent cycles that is ascribed to the decomposition of surface oxides, formation of solid electrolyte interphases and aggregation of alloy particles during cycling. Dunn and co-workers [158] have prepared nanosized RuNPs supported on carbon aerogels and used them to develop supercapacitors with high capacitances.

2.5 Single nanoparticle-electrode impacts

The study of impact processes between particles and electrode surfaces is less than 20 years old, and has recently added impetus due to the current intense interest in the chemistry of NPs. As this field is the main research interest of this thesis, a separate chapter (Chapter 5) will give a review on the appraisal of the historical results and recent devel-

opments, and the consideration of its potentially wide-ranging applications.

2.6 Conclusions and perspectives

The current efforts on electrochemistry with metal nanoparticles have been reviewed in this chapter with a certain bias towards metal NPs modified electrodes for electroanalysis, metal NPs for catalysis, and single NP-electrode impacts. Of course the study of NPs electrochemistry is far wider than the topics mentioned above with other main research interests including single electron events, spectroelectrochemistry, electron transfer study, enzyme electrochemistry and biosensors. There are many outstanding issues that require the attention of electrochemists in the years to come. Understanding the biological processes, bioassays and the stability of biomolecules under potential control remains an area worth further exploring. Electroanalytical techniques are increasingly expanding, having continuous potential in areas such as bioanalysis, drug delivery and medical devices. NP electrochemistry has been studied for more than a decade in combination with material science and has found its application in many areas. This research interest will remain the focus of many scientists for the coming years.

Recently, the study of thermally-driven nanoparticle impact phenomena has revealed new insights into NP-surface interactions via both indirect (*i.e.* electrocatalytic) and direct electrochemical measurements. This area will keep flourishing in the coming years. The detection of single molecules using NPs has started to attract much attention especially when combined with microfluidic or nanofludic devices [159]. It will be a promising field that is worth immediate attention. The nanoparticle impact study is the main focus of this thesis and will be fully discussed in the later chapters.

Bibliography

[1] M. A. Hayat. *Colloidal Gold: Principles, Methods and Applications*. Academic Press, 1991.

[2] G. Schmid. *Chem. Rev.*, 92:1409, 1992.

[3] M. Faraday. *Philos. Trans.*, 147:145, 1857.

[4] G. Mie. *Ann. Phys.*, 25:377, 1908.

[5] H. S. Halwa, editor. *Handbook of Nanostructured Materials and Nanotechnology, Vol. 1 Synthesis and Processig*. Academic Press, New York, 2000.

[6] J. H. Fendler, editor. *Nanoparticles and Nanostructured Films-Preparation, Characterisation and Applications*. Wiley-VCH, Weinheim, 1998.

[7] C. R. Martin and D. T. Mitchell. *Electroanalytical Chemistry Series*. NY., 1999. Vol.21, p.1.

[8] A. N. Shipway, E. Katz, and I. Willner. *Chem. Phys. Chem.*, 1:18, 2000.

[9] D. Hernandez-Santos, M. B. Gonzalez-Garcia, and A. Costa-Garcia. *Electroanalysis*, 14:1224, 2002.

[10] D. Gerion, W. J. Parak, and S. C. Willians et al. *J. Am. Chem. Soc.*, 12:7070, 2002.

[11] D. E. Cliffel, J. F. Hicks, and A. C. Templeton et al. *in Metal Nanoparticles: Synthesis, Characterisation, and Applications*. New York, 2002, p. 297.

[12] A. Henglein. *J. Phys. Chem.*, 83:2209, 1979.

[13] J. Kiwi and M. Gratzel. *J. Am. Chem. Soc.*, 101:7214, 1979.

[14] O. A. Petrii and G. A. Tsirlina. *Russ. Chem. Rev.*, 11:2887, 2001.

[15] P. Mulvaney. *in Nanoscale Materials in Chemistry*. Wiley-VCH, Weinheim, 2001.

[16] C. M. Welch and R. G. Compton. *Anal. Bioanal. Chem.*, 384:601, 2006.

[17] F. W. Campbell and R. G. Compton. *Anal. Bioanal. Chem.*, 396:241, 2010.

[18] *WebElements periodic table of the elements*. http://www.webelements.com, Winter M (1993-2009).

[19] L. N. Lewis. *Chem. Rev.*, 93:2693, 1993.

[20] O. V. Satata. *L. Nanobiotechnol*, 2:1, 2004.

[21] H. J. Lee and S. H. Jeong. *Text Res J*, 75:551, 2005.

[22] C. J. Murphy, T. K. Sau, and A. M. Gole et al. *J. Phys. Chem. B*, 109:13857, 2005.

[23] C. M. Niemeyer. *Angew. Chem., Int. Ed.*, 40:4128, 2001.

[24] C. Buzea et al. *Biointerphases*, 2:MR17, 2007.

[25] A. Pyatenko, M. Yamaguchi, and M. Suzuki. *J. Phys. Chem. C*, 22:7910, 2007.

[26] C. F. Wang, W. Wang, J. F. Wang, H. Y. Liu, S. F. Jiao, and B. Fang. *Microchim Acta*, 164:149, 2009.

[27] S. T. Dubad and V. Pimpan. *Mater Lett*, 62:2661, 2008.

[28] X. He, X. Zhao, Y. Chen, and J. Feng. *Mater Character*, 59:380, 2008.

[29] A. S. Reddy, C. Y. Chen, S. C. Baker, C. C. Chen, J. S. Jean, C. W. Fan, H. R. Chen, and J. C. Wang. *Mater Lett*, 63:1227, 2006.

[30] C. H. B. Ng, J. Yang, and W. Y. Fan. *J. Phys. Chem. C*, 112:4141, 2008.

[31] B. Hu, S. Wang, K. Wang, M. Zhang, and S. Yu. *J. Phys. Chem. C*, 112:11169, 2008.

[32] O. Domínguez-Renedo, L. Ruiz-Espelt, N. García-Astorgano, and M. J. Arcos-Martínez. *Talanta*, 76:854, 2008.

[33] S. W. Wu, H. Zhao, H. Ju, C. Shi, and J. Zhao. *Electrochem. Commun.*, 8:1197, 2006.

[34] S. J. Guo and E. K. Wang. *Anal. Chim. Acta*, 598:181, 2007.

[35] M. H. Rashid, R. R. Bhattacharjee, A. Kotal, and T. K. Mandal. *Langmuir*, 22:7141, 2006.

[36] G. Frens. *Nature (Phys. Sci.)*, 241:20, 1973.

[37] A. Ullman. *Chem. Rev.*, 96:1533, 1996.

[38] C. Petit, P. Lixon, and M. Pileni. *J. Phys. Chem. B*, 97:12974, 1993.

[39] K. S. Suslick, M. Fang, and T. Hyeon. *J. Am. Chem. Soc.*, 118:11960, 1996.

[40] J. M. Slocik, M. O. Stone, and R. R. Naik. *Small*, 1:1048, 2005.

[41] N. Higash, J. Kawahara, and M. Niwa. *J. Colloid Interface Sci.*, 228:83, 2005.

[42] P. Raveendran, J. Fu, and S. L. Wallen. *J. Am. Chem. Soc.*, 125:13940, 2003.

[43] P. Wasserscheid and W. Keim. *Angew. Chem., Int. Ed.*, 39:3772, 2000.

[44] I. Hussain, S. Graham, Z. X. Wang, B. Tan, D. C. Sherrington, S. P. Rannard, A. I. Cooper, and M. Brust. *J. Am. Chem. Soc.*, 127:16398, 2005.

[45] C. Note, J. Koetz, L. Wattebled, and A. Laschewsky. *J. Colloid Interface Sci.*, 308:162, 2007.

[46] X. Sun, X. Jiang, S. Dong, and E. Wang. *Macromol. Rapid Commnun.*, 24:1024, 2003.

[47] C. S. Love, I. Ashworth, C. Brennan, V. Chechik, and D. K. Smith. *J. Colloid Interface Sci.*, 302:178, 2006.

[48] M. S. El-Deab, T. Okajima, and T. Ohsaka. *J. Electrochem. Soc*, 150:851, 2003.

[49] Y. Ma, J. Di, X. Yan, M. Zhao, Z. Lu, and Y. Tu. *Biosens. Bioelectron.*, 24:1480, 2009.

[50] C. M. Liu, H. B. Cao, Y. P. Li, and Y. Zhang. *J. New Mat. Electrochem. Systems*, 9:139, 2006.

[51] Y. C. Liu and T. C. Chuang. *J. Phys. Chem. B*, 107:12383, 2003.

[52] L. Ting. *Trans Nonferr Met Soc China*, 17:1343, 2007.

[53] X. Dai, G. G. Wildgoose, and R. G. Compton. *Analyst*, 131:1241, 2006.

[54] T. Asefa and R. B. Lennox. *Mater Chem*, 17:2481, 2004.

[55] Y. Kobayashi, Y. Tadaki, D. Nagao, and M Konno. *J. Phys.: Conf. Ser.*, 61:582, 2007.

[56] Y. Kobayashi, Y. Tadaki, D. Nagao, and M. Konno. *J. Colloid Interface Sci.*, 283:601, 2005.

[57] C. Batchelor-McAuley, G. G. Wildgoose, and R. G. Compton. *New J. Chem.*, 32:941, 2008.

[58] Y. G. Zhou, S. Yang, Q. Y. Qian, and X. H. Xia. *Electrochem. Commun.*, 11:216, 2009.

[59] G. G. Couto, J. J. Klein, W. H. Schreiner, D. H. Mosca, A. J. A. de Oliveira, and A. J. G. Zarbin. *J. Colloid Interface Sci.*, 311:461, 2007.

[60] L. Bai, F. Yuan, and Q. Tang. *Mater Lett*, 62:2267, 2008.

[61] J. Cheng, X. Zhang, and Y. Ye. *J. Solid State Chem.*, 179:91, 2006.

[62] Y. Z. Chen, D. L. Peng, D. X. Lin, and X. H. Luo. *Nanotechnology*, 18:1, 2007.

[63] V. Tzitzios, G. Basina, M. Gjoka, V. Alexandrakis, V. Georgakilas, D. Niarchos, N. Boukos, and D. Petridis. *Nanotechnology*, 17:3750, 2006.

[64] D. Kumar, S. J. Pennycook, and A. Lupini. *Appl. Phys. Lett*, 81:4204, 2002.

[65] W. Xu, K. Y. Liew, H. Liu, T. Huang, C. Sun, and Y. Zhao. *Mater Lett*, 62:2571, 2008.

[66] Z. Wu, S. Ge, M. Zhang, W. Li, and K. Tao. *J. Colloid Interface Sci.*, 330:359, 2009.

[67] E. Kauffeldt and T. Kauffeldt. *J Nanopart Res*, 8:477, 2006.

[68] R. G. Compton, G. G. Wildgoose, N. V. Rees, I. Streeter, and R. Baron. *Chem. Phys. Lett.*, 459:1, 2008.

[69] M. E. Hyde, T. J. Davies, and R. G. Compton. *Angew. Chem., Int. Ed.*, 44:6491, 2005.

[70] F. W. Campbell, S. R. Belding, R. Baron, L. Xiao, and R. G. Compton. *J. Phys. Chem. C*, 113:903, 2009.

[71] A. O. Simm, S. Ward-Jones, C. E. Banks, and R. G. Compton. *Anal. Sci.*, 21:667, 2005.

[72] I. Streeter and R. G. Compton. *J. Phys. Chem. C*, 11:18049, 2007.

[73] S. R. Belding, E. J. F. Dickinson, and R. G. Compton. *J. Phys. Chem. C*, 113:11149, 2009.

[74] F. W. Campbell, S. R. Belding, R. Baron, L. Xiao, and R. G. Compton. *J. Phys. Chem. C*, 113:14852, 2009.

[75] F. W. Campbell and R. G. Compton. *ChemPhysChem*, 11:2820, 2010.

[76] Y. G. Zhou, F. W. Campbell, S. R. Belding, and R. G. Compton. *Chem. Phys. Lett.*, 497:200, 2010.

[77] F. W. Campbell, Y. G. Zhou, and R. G. Compton. *New J. Chem.*, 34:187, 2010.

[78] F. W. Campbell and R. G. Compton. *Int. J. Electrochem. Sci.*, 5:407, 2010.

[79] S. E. Ward Jones, F. W. Campbell, R. Baron, L. Xiao, and R. G. Compton. *J. Phys. Chem. C*, 112:17820, 2008.

[80] M. O. Finot, G. D. Braybrook, and M. T. McDermott. *J. Electroanal. Chem.*, 466:234, 1999.

[81] M. S. El-Deab, T. Okajima, and T. Ohsaka. *J. Electrochem. Soc*, 150:A851, 2003.

[82] X. Dai, O. Nekrassova, M. E. Hyde, and R. G. Compton. *Anal. Chem.*, 76:5924, 2004.

[83] E. Majid, S. Hrapovic, Y. Liu, K. B. Male, and J. H. T. Luong. *Anal. Chem.*, 78:762, 2006.

[84] A. A. Isse, S. Gottardello, C. Maccato, and A. Gennaro. *Electrochem. Commun.*, 8:1707, 2006.

[85] S. Thiagarajan, R. F. Yang, and S. M. Chen. *Bioelectrochemistry*, 75:163, 2009.

[86] S. B. Aoun and I. Taniguchi. *Chem. Lett.*, 37:936, 2008.

[87] X. Dai and R. G. Compton. *Anal. Sci.*, 22:567, 2006.

[88] L. Wang, W. Mao D. Ni, J. Di, Y. Wu, and Y. Tu. *Electrochem. Commun.*, 10:673, 2008.

[89] Y. Ma, J. Di, X. Yan, M. Zhao, Z. Lu, and Y. Tu. *Biosens. Bioelectron.*, 24:1480, 2009.

[90] J. Wang, L. Wang, J. Di, and Y. Tu. *Talanta*, 77:1454, 2009.

[91] Y. Zhao, Y. Wu, Y. Zhang, Z. Chen, X. Cao, J. Di, and J. Yang. *Electroanalysis*, 21:939, 2009.

[92] K. E. Toghill and R. G. Compton. *Electroanalysis*, 22:1947, 2010.

[93] A. Safavi, N. Maleki, F. Farjami, and E. Farjami. *J. Electroanal. Chem.*, 626:75, 2009.

[94] Z. Wang, Q. Zhang, D. Kuehner, A. Ivaska, and L. Niu. *Green Chem.*, 10:907, 2008.

[95] R. G. Freeman, K. C. Grabar, K. J. Allison, R. M. Bright, J. A. Davis, A. P. Guthrie, M. B. Hommer, M. A. Jackson, P. C. Smith, D. G. Walter, and M. J. Natan. *Science*, 267:1629, 1995.

[96] G. Chumano, K. Sokolov, B. W. Gregory, and T. M. Cotton. *J. Phys. Chem.*, 67:735, 1995.

[97] Y. Jin, X. Kang, Y. Song, B. Zhang, G. Cheng, and S. Dong. *Anal. Chem.*, 73:2843, 2001.

[98] S. Melzer, R. Resch, B. E. Koel, M. E. Thompson, A. Madhukar, A. A. G. Requicha, and P. Will. *Langmuir*, 17:1713, 2001.

[99] L. Wang and E. Wang. *Electrochem. Commun.*, 6:25, 2004.

[100] M. Brust, M. Walker, D. Bethell, D. J. Schiffrin, and R. Whyman. *Chem. Commun.*, page 801, 1994.

[101] A. C. Templeton, W. P. Wuelfing, and R. W. Murray. *Acc. Chem. Res.*, 33:27, 2001.

[102] M. Tominaga, T. Shimazoe, M. Nagashima, and I. Taniguchi. *Electrochem. Commun.*, 7:189, 2005.

[103] M. Tominaga, T. Shimazoe, M. Nagashima, and I. Taniguchi. *Chem. Lett.*, 34:202, 2005.

[104] M. Tominaga, T. Shimazoe, M. Nagashima, and I. Taniguchi. *J. Electroanal. Chem.*, 615:51, 2008.

[105] W. Chen, J. Kim, S. Sun, and S. Chen. *Langmuir*, 23:11303, 2007.

[106] X. Dai, G. G. Wildgoose, C. Salter, A. Crossley, and R. G. Compton. *Anal. Chem.*, 78:6102, 2006.

[107] J. Qu, H. Chen, and S. Dong. *Electroanalysis*, 20:2410, 2008.

[108] Y. C. Tsai, P. C. Hsu, Y. W. Lin, and T. M. Wu. *Sens. Actuators, B*, 138:5, 2009.

[109] Y. C. Tsai, P. C. Hsu, Y. W. Lin, and T. M. Wu. *Electrochem. Commun.*, 11:542, 2009.

[110] C. Gao, W. Li, Y. Z. Jin, and H. Kong. *Nanotechnology*, 17:2882, 2006.

[111] W. Zhao, H. Wang, X. Qin, X. Wang, Z. Zhao, Z. Miao, L. Chen, M. Shan, Y. Fang, and Q. Chen. *Talanta*, 80:1029, 2009.

[112] X. Chen, Z. Cai, Z. Lin, T. Jia, H. Liu, Y. Jiang, and X. Chen. *Bioelectron.*, 24:2375, 2009.

[113] Y. C. Tsai and Y. H. Hong. *J. Solid State Chem.*, 12:1293, 2008.

[114] J. Kim, S. W. Lee, P. T. Hammong, and Y. Shao-Horn. *Chem. Mater.*, 21:2993, 2009.

[115] F. N. Crespilho, M. E. Ghica, V. Zucolotto, F. C. Nart, O. N. Oliveira Jr., and C. M. A. Brett. *Electroanalysis*, 8:1665, 2006.

[116] E. Yoo, T. Okata, T. Akita, M. Kohyama, J. Nakamura, and I. Honma. *Nano Lett.*, 9:2255, 2009.

[117] C. Xu, X. Wang, and J. W. Zhu. *J. Phys. Chem. C*, 112:19841, 2008.

[118] Y. G. Zhou, J. J. Chen, F. B. Wang, Z. H. Sheng, and X. H. Xia. *Chem. Commun.*, 46:5951, 2010.

[119] R. Baron, G. G. Wildgoose, and R. G. Compton. *J. Nanosci. Nanotechnol.*, 9:2274, 2009.

[120] D. Wen, S. Guo, J. Zhai, L. Deng, W. Ren, and S. Dong. *J. Phys. Chem. C*, 113:13023, 2009.

[121] L. Zhang, L. Wang, S. Guo, J. Zhai, S. Dong, and E. Wang. *Electrochem. Commun.*, 11:258, 2009.

[122] J. O. M. Bockris and S. U. M. Khan. *Surface Electrochemistry*. Plenum Press, New York, 1993.

[123] A. M. Feltham and M. Spiro. *Chem. Rev.*, 71:177, 1971.

[124] J. V. Zoval, J. Lee, and S. Gorer. *J. Phys. Chem. B*, 102:1166, 1998.

[125] S. Wasmus and A. Kuever. *J. Electroanal. Chem.*, 461:14, 1999.

[126] K. Honda, M. Yoshimura, and T. N. Rao. *J. Electroanal. Chem.*, 514:35, 2001.

[127] Y. L. Yao, Y. Ding, L. S. Ye, and X. H. Xia. *Carbon*, 44:61, 2006.

[128] Y. Lou, M. M. Maye, L. Han, J. Luo, and C. J. Zhong. *Chem. Commun.*, 5:473, 2001.

[129] Z. Liu, S. Kang, M. Shamsuzzoha, and D. E. Nikles. *J. Nanosci. Nanotechnol.*, 10:4266, 2010.

[130] J. Prabhuram and R. Manoharan. *J. Appl. Electrochem.*, 28:935, 1998.

[131] C. G. Hu, Y. M. Guo, J. L. Wang, L. Yang, Z. X. Yang, Z. Y. Bai, J. Zhang, K. Wang, and K. Jiang. *ACS Appl. Mater. Interfaces*, DOI: 10.1021/am3013592, 2012.

[132] F. J. Perez-Alonso, D. N. McCarthy, A. Nierhoff, P. Hernandez-Fernandez, C. Strebel, I. E. L. Stephens, J. H. Nielsen, and I. Chorkendorff. *Angew. Chem., Int. Ed.*, 51:4641, 2012.

[133] S. Ci, J. Zou, G. Zeng, S. Luo, and Z. Wen. *J. Mater. Chem.*, 22:16732, 2012.

[134] A. A. Gewirth and M. S. Thorum. *Inorg. Chem.*, 49:3557, 2010.

[135] S. H. Joo, S. J. Choi, I. Oh, J. Kwak, Z. Liu, O. Terasaki, and R. Ryoo. *Nature*, 412:169, 2001.

[136] R. Wlodarczyk, M. Chojak, K. Miecznikowski, A. Kolary, P. J. Kulesza, and R. Marassi. *J. Power Sourses*, 159:802, 2006.

[137] S. Zhang, Y. Shao, G. Yin, and Y. Lin. *J. Mater. Chem.*, 19:7995, 2009.

[138] M. S. El-Deab and T. Ohsaka. *Electrochim. Acta*, 47:4255, 2002.

[139] P. Singh and D. A. Buttry. *J. Phys. Chem. C*, 116:10656, 2012.

[140] H. A. Gasteiger and N. M. Markovic. *Science*, 324:48, 2009.

[141] K. J. J. Mayrhofer, V. Juhart, K. Hartl, M. Hanzlik, and M. Arenz. *Angew. Chem., Int. Ed.*, 48:3529, 2009.

[142] S. Koh, J. Leisch, M. F. Toney, and P. Strasser. *J. Phys. Chem. C*, 111:3744, 2007.

[143] J. R. Kitchin, J. K. Norskov, M. A. Barteau, and J. G. Chen. *Phys. Rev. Lett.*, 93:156801, 2004.

[144] A. Nilsson, L. G. M. Pettersson, B. Hammer, T. Bligaard, C. H. Christensen, and J. K. Norskov. *Catal. Lett.*, 100:111, 2005.

[145] M. Mavrikakis, B. Hammer, and J. K. Norskov. *Phys. Rev. Lett.*, 81:2819, 1998.

[146] S. Sao-Joao, S. Giorgio, J. M. Penisson, C. Chapon, S. Bourgeois, and C. R. Henry. *J. Phys. Chem. B*, 109:342, 2005.

[147] S. Giorgio and C. R. Henry. *Eur. Phys. J. Ap.*, 20:23, 2002.

[148] P. Mani, S. Srivastava, and P. Strasser. *J. Phys. Chem. C*, 112:2770, 2008.

[149] R. Yang, J. Leisch, P. Strasser, and M. F. Toney. *Chemistry of Materials*, 22:4712, 2010.

[150] R. Yang, P. Strasser, and M. F. Toney. *J. Phys. Chem. C*, 115:9074, 2011.

[151] T. Baum, D. Bethell, and M. Brust. *Langmuir*, 15:866, 1999.

[152] S. N. Pron'Kin, A. G. Tsirlina, O. A. Petrii, and S. Y. Vassiliev. *Electrochim. Acta*, 46:2343, 2001.

[153] J. E. Park, O. Hatozaki, and N. Oyama. *Chem. Lett.*, 32:138, 2003.

[154] K. Guo, Q. Pan, and L. Wang. *J. Appl. Electrochem.*, 32:679, 2002.

[155] H. Li, Q. Wang, and L. Shi. *Chem. Mater.*, 14:103, 2002.

[156] H. Li, L. Shi, and W. Lu. *J. Electrochem. Soc*, 148:915, 2001.

[157] H. Li, G. Zhu, and X. Huang. *J. Mater. Chem.*, 10:693, 2000.

[158] J. M. Miller and B. Dunn. *Langmuir*, 15:799, 1999.

[159] M. A. Zevenbergen, P. S. Singh, E. D. Goluch, B. L. Wofrum, and S. G. Lemay. *Nano Lett.*, 11:2881, 2011.

Chapter 3

Thallium underpotential deposition on silver nanoparticles: size-dependent adsorption behaviour

As discussed in the Introduction, electrochemistry at the macro- and nano- scales can exhibit some distinctly different behaviour. In this chapter we investigate the size-dependent adsorption of thallium of silver nanoparticles (AgNPs) in the region of underpotential deposition; the phenomenon is observed for large nanoparticles, and bulk silver, but absent for nanoparticles below 50 nm diameter.

This work was carried out in cooperation with Dr. Fallyn W. Campbell, and has been published in *New Journal of Chemistry*, 2010, 34, 187.

3.1 Introduction

The use of nanoparticles in electrochemistry provides a number of advantages over their corresponding bulk materials. Probably the most subtle difference is enhanced mass transport due to the convergent rather than linear nature of diffusion [1–3]. This in turn can facilitate the study of faster electrode processes. More obviously, nanoparticles provide higher active surface area leading to improved selectivity and signal-to-noise ratio which can be highly advantageous in some electro-analytical applications [4–8], whilst the reduction in size can lead to changed surface and electronic properties. Crystal faces exposed at the nanoscale, and not seen at the macroscale, may lead to improved current responses and catalytic properties; the converse might also be true. Nanoparticles have therefore found extensive use in catalytic [9–11] and sensing [12–14] applications. However, to date little is known on the adsorption behaviour of nanoparticles in the electrochemical environment although the adsorption on macro- and nano-gold supported on carbon nanotubes has been shown to change quantitatively with no adsorption seen on small nanoparticles [15].

Underpotential deposition (UPD) is the deposition of a monolayer, or sub-monolayer, of a metal onto a different substrate metal electrode at potentials more positive than the equilibrium (Nernst) potential for bulk deposition of this metal. It is possible to deposit a wide variety of metals onto an electrode substrate by UPD. Most relevant to this study is UPD of thallium on macro-sized silver electrodes [16–18], which has been extensively reported in the literature. However, the UPD of metals such as lead, bismuth, cadmium, copper, nickel and zinc [19–23] has also been reported in the literature on silver substrates. Studies have also examined the UPD behaviour of two co-depositing species such as Tl and Pb [24, 25]. Thallium UPD has also been reported on gold , platinum and copper electrodes [3]. The potential difference between UPD and bulk deposition can be related to the different work functions associated with substrate material and deposit. This can in turn result in partial charging of the adatoms. Since the work function of nanoparticles

may be size related this offers a further mechanism by which changed electrochemical behaviour may arise at the nanoscale [26–29].

A number of thallium deposition studies have been performed on macro-sized silver single crystal electrodes, each of which displays its own distinct features. The reduction of Tl^+ to an adsorbed layer of Tl metal is represented in ((3.1)).

$$Tl^+ + e^- \rightleftharpoons Tl \text{ (metal)} \tag{3.1}$$

The structure of a surface is seen to control the ease with which thallium can be deposited: Ag(111) > Ag(100) >Ag(110) > polycrystalline Ag [30, 31]. This evidence clearly indicates that the adsorption of Tl is highly sensitive to the detailed surface structure of a silver electrode.

Not many researches can be found in the literature relating to the UPD adsorption of metal atoms such as thallium, on nanoparticulate materials [15, 32], or indeed of the adsorption of molecules in general on nanoparticles. This chapter will compare the deposition of thallium on silver macrodisk electrodes and silver nanoparticles (AgNPs), examining the influence of both nanoparticle size and electrode coverage on the bulk and underpotential deposition of thallium on AgNPs.

The study of UPD is important as it commonly results in the deposition of a monolayer or sub-monolayer of material. Such layers can be highly significant in the mechanisms of electrocatalytic processes. Accordingly the investigation of adsorption effects on nanoparticulate matter is important for the development of these materials for both synthetic and analytical applications.

3.2 Experimental

$TlNO_3$(99.99%, Sigma-Aldrich), KNO_3 (99.99%, Aldrich) and $NaClO_4$ (98-102%, Johnson Mattey) were used as received without further purification. All solutions were pre-

pared using Millipore pure water with resistivity ~ 18.2 MΩcm at 25 °C (Vivendi Water Systems, UK).

All electrochemical experiments were performed using a μAutolab type III potentiostat and desktop PC. A three-electrode set up was used consisting of a working electrode, carbon rod counter electrode and saturated calomel (SCE) reference electrode (Radiometer Analytical). Carbon rods and BPPG were supplied by Le Carbone, Sussex, UK.

The AgNPs were synthesized by a seed mediated citrate reduction of $AgNO_3$ adapted from a procedure by Pyatenko et al. [33, 34], and detailed in our previous publications [35, 36]. Thallium deposition was performed in KNO_3 (1.5 M) + $TlNO_3$ (10 mM) at 50 mV s^{-1} by scanning negatively from −0.2 V and reversing the scan direction.

AgNPs were stripped from the BPPG electrode by LSV in $NaClO_4$ (0.1 M), scanning from 0 V to 0.9 V at 20 mV s^{-1}.

3.3 Results & Discussion

We have chosen to examine the underpotential and bulk deposition of thallium on AgNPs of varying sizes [33, 34]. AgNPs were synthesized by a well documented [33–36] seed mediated citrate reduction process. This method allows us to synthesise AgNPs with the following diameters: 20-40 nm, 50-70 nm and 80-120 nm [35, 36]. The as-synthesized colloidal AgNPs suspension was subsequently evaporated on the surface of a basal plane pyrolytic graphite (BPPG) electrode.

Thallium deposition was carried out in a solution of KNO_3 (1.5 M) + $TlNO_3$ (10 mM) at 50 mV s^{-1}. Figure 3.1 displays the underpotential deposition [E_p = −0.545 V (*vs.* SCE)] and stripping [E_p = −0.440 V (*vs.* SCE)] of Tl on a silver macrodisk (diameter = 0.7 mm) under the same conditions described above. Tl deposition was also examined on a bare BPPG (diameter = 5 mm) electrode and showed no UPD and a bulk deposition taking place at E_p = −0.822 V and corresponding stripping peak at E_p = −0.637 V.

When we compare this with a BPPG electrode modified with AgNPs (20-40 nm) we

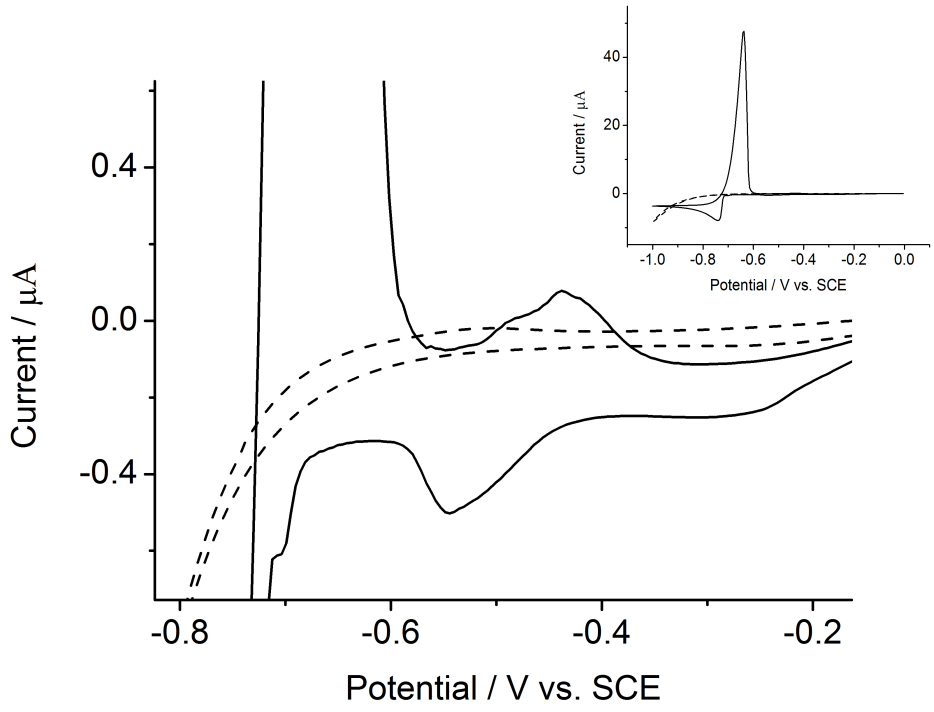

Figure 3.1: Thallium deposition on a silver macrodisk electrode. Experimental conditions: KNO_3 (1.5 M) + $TlNO_3$ *vs.* SEC. Scan rate: 50 mV s^{-1}. (Solid line: 10 mM $TlNO_3$; dashed line: 0 mM $TlNO_3$.)

can see that the bulk deposition peak shifts positively from that of a BPPG bulk deposition to that of silver bulk deposition, as shown in Figure 3.2 (insert). Furthermore, when we closely examine the region of UPD it is clear that on the small AgNPs (20-40 nm), no appreciable UPD or stripping of thallium takes place, while we still observe a bulk deposition wave at $E_p = -0.777$ V (*vs.* SCE) and the corresponding wave at $E_p = -0.633$ V (*vs.* SCE) as shown in Figure 3.2. The same effect is recorded for a range of surface coverages of AgNPs on the BPPG electrode, between 0.5 and 3%. Surface coverage was altered by varying the volume of colloidal suspension dried on the electrode surface *i.e.* by increasing the volume the NP density is increased. Following the deposition and stripping of Tl, the amount of silver on the surface was quantified by linear sweep stripping voltammetry (LSV) in $NaClO_4$ (0.1 M) as shown in Figure 3.3.

When the same experiment was repeated using larger AgNPs (80-120 nm) (Figure 3.4) a similar effect was observed with respect to the shift in position of the bulk deposition

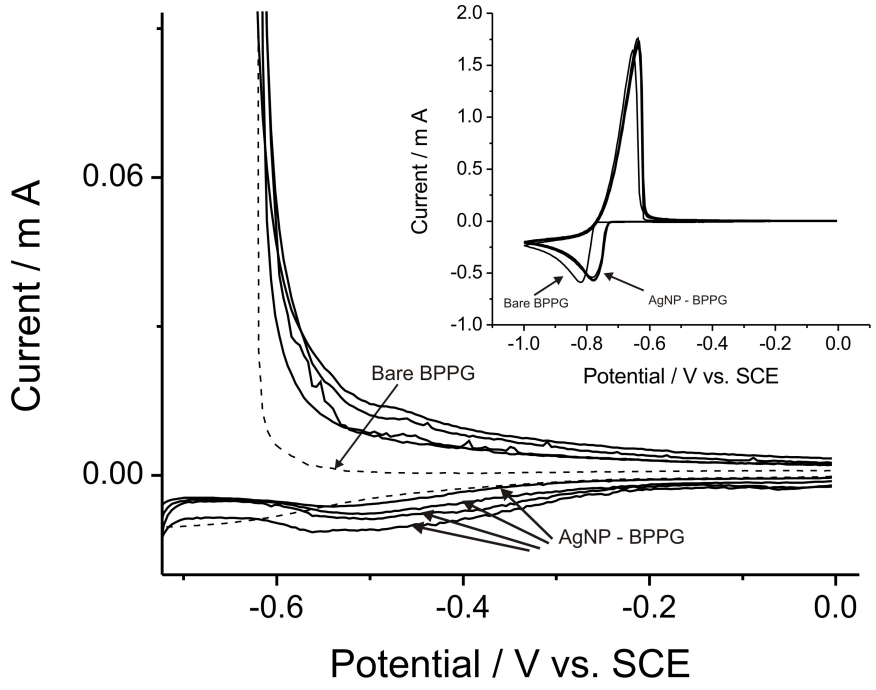

Figure 3.2: Thallium deposition on AgNP-BPPG (20-40 nm) electrode. Experimental conditions: KNO_3 (1.5 M) + $TlNO_3$ *vs*. SEC. Scan rate: 50 mV s^{-1}. (Solid line: AgNP-BPPG (20-40 nm) electrode; dashed line: bare BPPG.)

peak. However, unlike the small AgNPs (20-40 nm), the larger AgNPs (80-120 nm) exhibited distinct deposition and stripping peaks in the thallium UPD region, corresponding to those reported on bulk silver. As no UPD is observed for bare BPPG we can attribute this to the presence of AgNPs (80-120 nm). In this case increased AgNPs density on the electrode surface corresponds to an increase in the thallium deposition and stripping peak heights (Figure 3.4), due to the greater surface area available for thallium adsorption.

3.4 Conclusions

The results reported here indicate clearly that silver nanoparticles show qualitatively different adsorption behaviour from below a size threshold of *ca.* 50 nm with Tl adsorption absent below, but observed above this value. It is evident that metal nanoparticles can show qualitatively different adsorption behaviour from bulk materials and that this may cause marked changes in electrochemical reactivity such as size-dependent changes in electrode mechanism: with clear implication for the investigation of electrocatalysis. The observed behaviour likely arises from size-dependent morphology or electronic (work function) properties [26–29]. In the next chapter another factor that affects voltammetry - surface coverage - will be discussed.

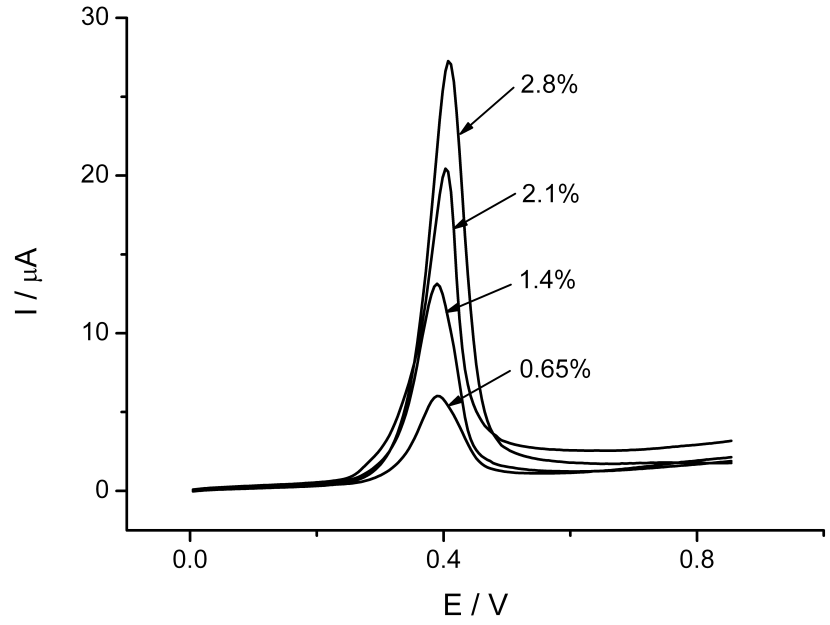

Figure 3.3: Stripping voltammetry recorded for increasing surface coverage of AgNPS (20-40 nm, 0.5 and 3.0%). Experimental conditions: $NaClO_4$ (0.1 M) *vs*. SEC. Scan rate: 20 mV s^{-1}.

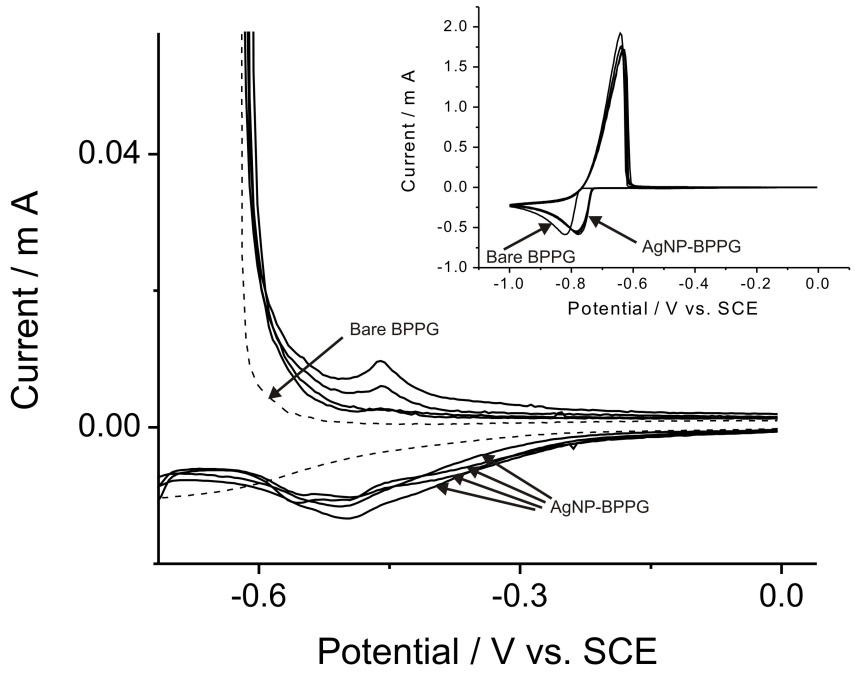

Figure 3.4: Thallium deposition on AgNP-BPPG (80-120 nm) electrode. Experimental conditions: KNO_3 (1.5 M) + $TlNO_3$ *vs.* SEC. Scan rate: 50 mV s^{-1}. (Solid line: AgNP-BPPG (80-120 nm) electrode; dashed line: bare BPPG.)

Bibliography

[1] T. J. Davies, S. Ward-Jones, C. E. Banks, J. del Campo, R. Mas, F. Xavier Mu noz, and R. G. Compton. *J. Electroanal. Chem.*, 585:51, 2005.

[2] T. J. Davies and R. G. Compton. *J. Electroanal. Chem.*, 585:63, 2005.

[3] T. J. Davies, C. E. Banks, and R. G. Compton. *J. Solid State Electrochem.*, 9:797, 2005.

[4] F. W. Campbell and R. G. Compton. *Anal. Bioanal. Chem.*, 396:241, 2010.

[5] C. M. Welsh and R. G. Compton. *Anal. Bioanal. Chem.*, 382:12, 2005.

[6] C. Batchelor-McAuley, Y. Du, G. G. Wildgoose, and R. G. Compton. *Sens. Actuators, B*, 135:230, 2008.

[7] L. Xiao, G. G. Wildgoose, and R. G. Compton. *Anal. Chim. Acta*, 620:44, 2008.

[8] X. Dai, G. G. Wildgoose, C. Salter, A. Crossley, and R. G. Compton. *Anal. Chem.*, 78:6102, 2006.

[9] J. Manso, L. Agüí, P. Yánez-Sede no, and J. M. Pingarrón. *Anal. Lett.*, 37:887, 2005.

[10] H. B. Yildiz, R. Freeman, R. Gill, and I. Willner. *Anal. Chem.*, 80:2811, 2008.

[11] S. W. Wu, H. Zhao, H Ju, C. Shi, and J. Zhao. *Electrochem. Commun.*, 8:1197, 2006.

[12] O. Domínguez-Renedo, L. Ruiz-Espelt, N. García-Astorgano, and M. J. Acros-Martinez. *Talanta*, 76:854, 2008.

[13] K. E. Toghill, L. Xiao, G. G. Wildgoose, and R. G. Compton. *Electroanalysis*, 21:1113, 2009.

[14] M. Gao, H. Qi, Q. Gao, and C. Zhang. *Electroanalysis*, 20:123, 2008.

[15] C. Batchelor-McAuley, G. G. Wildgoose, and R. G. Compton. *New J. Chem.*, 32:941, 2008.

[16] T. C. Girjia and M. V. Sangaranarayanan. *J. Appl. Electrochem.*, 36:531, 2006.

[17] V. Daujotis and E. Gaidamauskas. *J. Electroanal. Chem.*, 446:151, 1998.

[18] E. Herrero, L. J. Buller, and H. D. Abru na. *Chem. Rev.*, 101:1897, 2001.

[19] Y. V. Bokshits, N. P. Osipovich, E. A. Strel'stov, and G. P. Shevchenko. *Colloids Surf., A*, 242:79, 2004.

[20] Y. Bonfil, M. Brand, and E. Kirowa-Eisner. *Anal. Chi*, 464:99, 2002.

[21] K.-O. Thiel ad M. Hintze, A. Vollmer, and C. Donner. *J. Electroanal. Chem.*, 621:7, 2008.

[22] S. Morin, A. Lachenwitzer, F. A. Moller, O. M. Magnussen, and R. J. Behm. *J. Electrochem. Soc.*, 146:1013, 1999.

[23] J. Miragliotta and T. E. Furtak. *Surf. Interface Anal.*, 14:53, 1989.

[24] S. Bharathi, V. Yegnaraman, and G. Prabhakara Rao. *J. Appl. Electrochem.*, 24:981, 1994.

[25] A. M. El-Halim, K. Jüttner, and W. J. Lorenz. *J. Electroanal. Chem.*, 106:193, 1980.

[26] D. M. Kolb, M. Przasnyski, and H. Gerischer. *J. Electroanal. Chem.*, 54:25, 1974.

[27] D. M. Kolb and H. Gerischer. *Surf. Sci.*, 51:323, 1975.

[28] H. Gerischer, D. M. Kolb, and M. Przasnyski. *Surf. Sci.*, 43:662, 1974.

[29] W. J. Plieth. *J. Phys. Chem.*, 86:3166, 1982.

[30] B. M. Mao, Z. Q. Tian, and M. Fleishmann. *Electrochim. Acta*, 37:1767, 1992.

[31] J. X. Wang, R. R. Adžić, O. M. Magnussen, and B. M. Ocko. *Surf. Sci.*, 344:111, 1995.

[32] K. E. Toghill, G. G. Wildgoose, A. Moshar, C. Mulcahy, and R. G. Compton. *Electroanalysis*, 20:1731, 2008.

[33] A. Pyatenko, M. Yamaguchi, and M. Suzuki. *J. Phys. Chem. C*, 111:7910, 2007.

[34] A. Pyatenko, M. Yamaguchi, and M. Suzuki. *J. Phys. Chem. B*, 109:21808, 2005.

[35] F. W. Campbell, S. R. Belding, R. Baron, L. Xiao, and R. G. Compton. *J. Phys. Chem. C*, 113:14852, 2009.

[36] F. W. Campbell, S. R. Belding, R. Baron, L. Xiao, and R. G. Compton. *J. Phys. Chem. C*, 113:9053, 2009.

Chapter 4

Surface coverage effects in voltammetry showing the transition from convergent to linear diffusion: The reduction of aqueous chromium (III) at silver nanoparticle modified electrodes

The previous chapter has shown the size-dependent adsorption of thallium of AgNPs. In this chapter we explore one electron reduction of Cr^{3+} in aqueous solution at silver nanoparticle modified electrodes of differing nanoparticle coverages and, for comparison, at a silver macroelectrode. The shape and size of the measured voltammograms were found to be extremely sensitive to the nanoparticle coverage and to reflect the transition from convergent to planar diffusion with increased coverage. Parameters inferred from the reduction studied at the macroelectrode were successfully used to model the nanoparticle modified electrodes data and to confirm the expected coverage and geometry dependence of the diffusion to and from the electrode surface.

The experimental part presented in this chapter was carried out in cooperation with Dr. Fallyn W. Campbell. The simulation of nanoparticle arrays was credited to Mr. Stephen R. Belding. This work has been published in *Chemical Physics Letters*, 2010, 497, 200.

4.1 Introduction

Nanoparticle (NP) modified electrodes are widely employed in areas as diverse as fuel cells [1,2] and electrocatalytic sensors or biosensors [3,4]. Whilst the change in scale from the macro to the nano-dimension can lead to altered electroactivity as a result of changed electronic or surface structure, at the same time the current-voltage characteristics vary because of the altered mass-transport regimes between the different scales. Deconvoluting these effects quantitatively is essential in order to assess genuine 'nano-effects'. In this chapter we address the problem of coverage dependent mass-transport at nanoparticle modified electrode.

Transport to a nanoparticle array can be described in terms of the degree of diffusion layer overlap, depending on the distance between adjacent nanoparticles in the array. Diffusional behavior at a NP-array, has been categorized by Davies et al. [5] as Case 1, 2, 3 or 4 (Figure. 4.1)

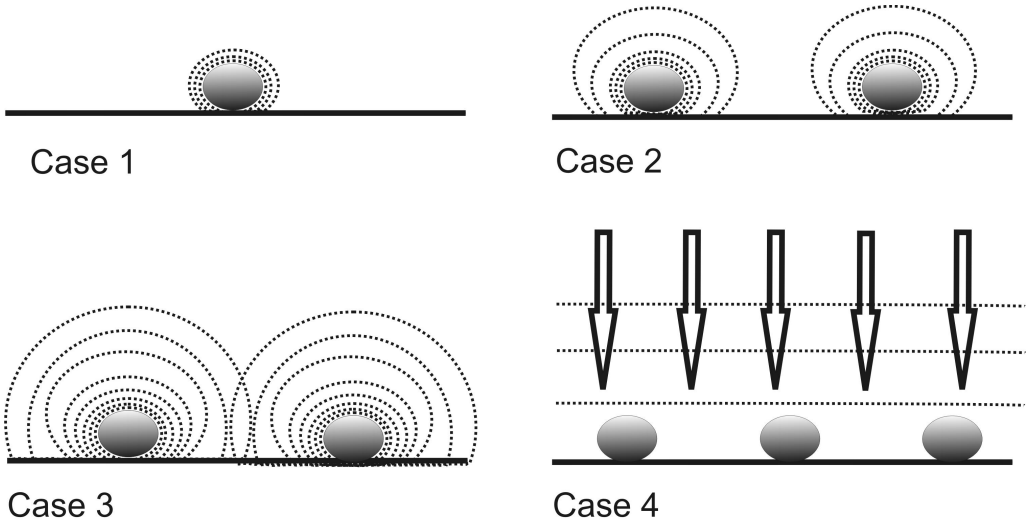

Figure 4.1: Diffusion at a nanoparticle array. Case 1: almost planar diffusion at an isolated nanoparticle where the diffusion layer thickness is small compared to the NP radius. Case 2: convergent diffusion at two adjacent but diffusionally independent nanoparticles. Case 3: partially overlapping diffusion layers at two adjacent nanoparticles. Case 4: heavily overlapping diffusion layers leading effectively to linear diffusion to the array as a whole.

Case 1 describes transient diffusion, at isolated NPs whilst Case 2 sees the expansion

of these isolated diffusion layers over a longer time scale so as to give a quasi steady-state. In Case 1 the timescale is sufficiently short that the diffusion layer around each NP is smaller than the NP radius leading approximately to planar diffusion and 'Cottrellian' diffusional transport. Case 1 gives peak-shaped voltammetry whilst Case 2 gives steady-state current-voltage behaviour. In Case 3, diffusion layers of adjacent particles partially overlap and finally, in Case 4, diffusion layers heavily overlap such that diffusion again appears effectively linear in nature and peak-shaped voltammetry re-emerges. The Case 3 situation has been realized experimentally for some graphite surfaces [6–8] whilst in the Case 4 limit the currents reflect linear diffusion to the geometric area of the array as a whole rather than reflecting the NP surface area. A further example of diffusional behaviour has been described for nanoparticle arrays but of total overall micrometer dimension, referred to as Case 5 [9], such that the entire electrode will behave as a microelectrode with sigmoidal shaped voltammetry; in this situation the array is not approximately infinite in extent but rather of dimensions such that convergent diffusion to the array as a whole can be realized in experimental timescales.

Previous studies carried out in our laboratory have demonstrated that both nanoparticle size and density of nanoparticles on the substrate electrode, play a crucial role in determining the nature of the voltammetry [6–8]. The mass-transport regime changes as a function of the nanoparticle density. At low coverage nanoparticles can effectively be considered as isolated particles experiencing fully convergent diffusion whilst at high coverage, diffusion layers will overlap tending towards a planar diffusion regime as described above. Consequently, the shape of the voltammetry will change accordingly, with steady-state behaviour exhibited at low coverage (Case 2), tending to peak-shaped voltammetry at high coverage (Case 4). Whilst these limits have been investigated theoretically, few if any clear cut examples of the corresponding experimental observations have been made. In this chapter we use the well-defined one electron reduction [10] of Cr^{3+} in aqueous solution (14.1) to show the transition from Case 1 to Case 4.

$$Cr^{3+}(aq) + e^- \rightleftharpoons Cr^{2+}(aq) \tag{4.1}$$

We report measurements using random arrays of silver nanoparticles and, for comparison, corresponding data recorded using a silver macroelectrode.

4.2 Theory

4.2.1 Simulation of isolated nanoparticles

We consider a simple one electron reduction:

$$A + e^- \rightleftharpoons B \tag{4.2}$$

The numerical simulations are based on a nanoparticle, approximately as a circular disc electrode, inlaid on an insulating support as shown in Figure 4.2

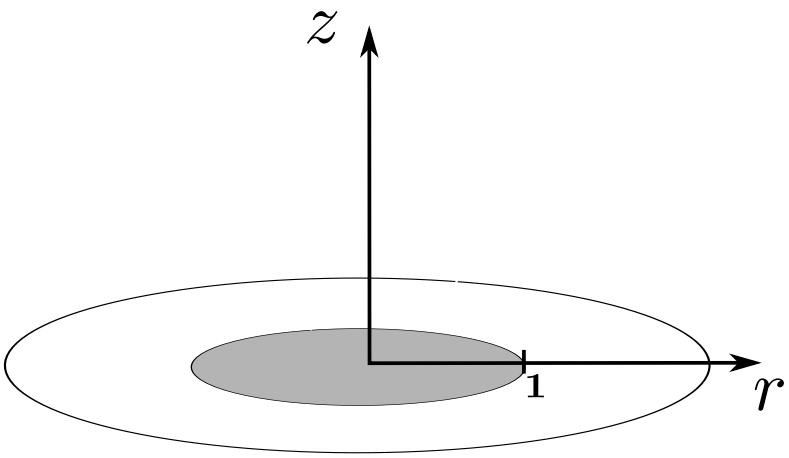

Figure 4.2: Circular disc electrode inlaid on an insulating support.

When solving numerical problems it is standard practice to express equations only in terms of dimensionless parameters such that the solutions are more general owing to the removal of (known) scaling factors. The dimensionless parameters used in this work are defined in Table 10.3:

Dimensionless parameter	Definition
R	r/r_e
Z	z/r_e
τ	$D_A t/{r_e}^2$
a	$[A]/[A]_{bulk}$
b	$[B]/[A]_{bulk}$
a^0	$[A]_0/[A]_{bulk}$
b^0	$[B]_0/[A]_{bulk}$
J	$i/(nF[A]_{bulk}D_A r_e)$
k^0	$k^0 r_e/D_A$
θ	$(F/RT)(E - E_f^0)$
r_e	Electrode radius (m)
F	Faraday constant (C mol^{-1})
R	Universal gas constant (J K^{-1} mol^{-1})
T	Temperature (K)
A	Electrode area (m^2)
$[A]_0$	Concentration of species A at the electrode surface (mol m^{-3})
$[B]_0$	Concentration of species B at the electrode surface (mol m^{-3})
$[A]_{bulk}$	Concentration of species A in bulk solution (mol m^{-3})
$[B]_{bulk}$	Concentration of species B in bulk solution (mol m^{-3})
α	Transfer coefficient (unitless)
k^0	Electrochemical rate constant (m s^{-1})
E^0	Applied potential (V)
E_f^0	Formal reduction potential (V)
D_A	Diffusion coefficient of species A (m^2 s^{-1})
D_B	Diffusion coefficient of species B (m^2 s^{-1})
j	Flux across the electrode (mol m^2 s^{-1})
i	Current (A)
m	i/i_{lim} on a steady-state voltammogram (unitless)

Table 4.1: Definitions of parameters used in the numerical simulation of a nanoparticle array.

The problem amounts to solving Fick's second law:

$$\frac{\partial a}{\partial \tau} = \frac{\partial^2 a}{\partial R^2} + \frac{1}{R}\frac{\partial a}{\partial R} + \frac{\partial^2 a}{\partial Z^2}, \tag{4.3}$$

where, in order to account for the symmetry of the situation, cylindrical coordinates are used. This equation is solved subject to several boundary conditions. The behaviour of the system at the interface between electrode and solution is quantified by the Butler-Volmer equation:

$$J = k^0 a_0 \exp\left[-\alpha\theta\right] - k^0 b_0 \exp\left[(1-\alpha)\theta\right]. \tag{4.4}$$

At very large distances from the electrode surface $a = 1$ and $b = 0$. The values of $Z_{\max}$ and $R_{\max}$ are chosen so as to contain the entire diffusion layer. The expressions used here are [11]

$$\begin{aligned} Z_{\max} &= 6\sqrt{\tau_{\text{total}}} \\ R_{\max} &= 1 + 6\sqrt{\tau_{\text{total}}} \end{aligned} \tag{4.5}$$

In addition, there is zero flux through the symmetry axis or through the insulating surface surrounding the electrode. The boundary conditions are summarised below:

$$\begin{aligned} &R = 0 \quad \frac{\partial a}{\partial R} = 0 \quad \frac{\partial b}{\partial R} = 0 \\ &R = R_{\max} \quad \frac{\partial a}{\partial R} = 0 \quad \frac{\partial b}{\partial R} = 0 \\ &Z = Z_{\max} \quad \frac{\partial a}{\partial R} = 0 \quad \frac{\partial b}{\partial R} = 0 \\ &Z = 0 \quad R \leq 1 \quad \text{Equation (4)} \\ &Z = 0 \quad R > 1 \quad \frac{\partial a}{\partial Z} = 0 \quad \frac{\partial b}{\partial Z} = 0 \end{aligned}$$

The problem is solved numerically using the Alternating Direct Implicit method (ADI) [12, 13]. This required discretization in both space and time. The simulation efficiency is increased by using an expanding spatial mesh. The mesh is chosen so as to leave a

high density at the singularities, i.e. the edge of the electrode and the symmetry axis. An exponentially expanding mesh is used.

The nature of the expansion is identical to that used by Gavaghan [14]. Once the simulation is run across a 2D spatial segment, the flux over the entire electrode is calculated using (11.5)

$$J_{\text{total}} = \pi \int_0^1 J_{\text{segment}} R \partial R \tag{4.6}$$

The integral is solved numerically using the trapezium rule [15].

4.2.2 Simulation of nanoparticle arrays

The simulation procedure for a nanoparticle in array is identical to that described above except the value of R_{max} must be chosen so as to characterise the separation of the electrodes of the array. The electrode separation is calculated assuming a regular square grid. Each nanoparticle can be considered as being at the centre of a unit cell as shown in Figure 4.3a.

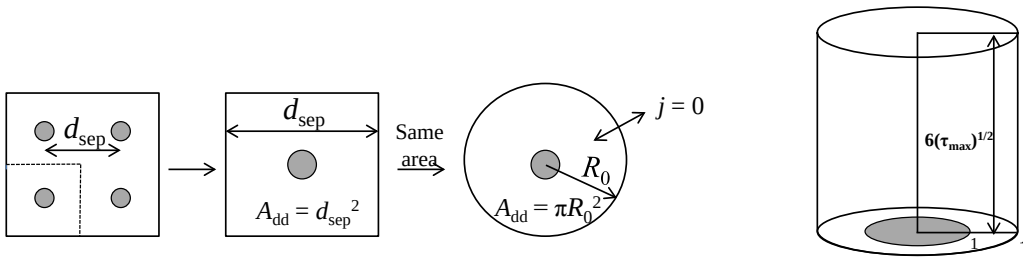

Figure 4.3: The diffusion domain approximation.

Each cell is diffusionally independent. The square base of each cell is taken to be equivalent to a circle of equal area. This is called the diffusion domain approximation and is shown in Figure 4.3. The relationship between R_{max} and the surface coverage, Θ, is:

$$\Theta = \frac{1}{R_{max}^2} \tag{4.7}$$

The current over the entire array is calculated by summing together the contribution from each nanoparticle.

4.2.3 Computation

All programs were written in C++ and compiled using a Borland compiler. The simulations were run on a desktop PC with a 3.4 GHz Pentium processor and 2 GB of RAM. Approximately 2 min of CPU time were required to simulate a single voltammogram. The integrity of the source code and efficiency of the program were investigated by comparing simulations for an isolated disc at steady-state with the Saito equation [16]. The program was converged to yield < 0.1% accuracy.

In this study we explore the redox behaviour of the Cr^{3+}/Cr^{2+} redox couple at silver macro-disk (Ag_{macro}) and silver nanoparticle (AgNP) arrays with varying nanoparticle densities. Studies were carried out in sodium perchlorate ($NaClO_4$) electrolyte solutions. The mass-transport model described above was then used to fit our experimental data.

4.3 Experimental

4.3.1 Chemical and reagents

All chemicals and reagents were used as received without further purification. All solutions were prepared with Millipore deionized water, with a resistivity ~ 18.2 MΩcm at 25 °C (Vivendi Water Systems, UK). All glassware was cleaned with a 'piranha' solution (4:1 H_2SO_4 and H_2O_2) prior to use. Silver nitrate salt (99%, $AgNO_3$) was supplied by BHD and trisodium citrate (99%, $C_6H_5Na_3O_7$) supplied by Sigma-Aldrich. Chromium (III) chloride (99%, $CrCl_3 \cdot 6\,H_2O$) and sodium perchlorate (98-102%, $NaClO_4$) were sup-

plied by Sigma-Aldrich. Hydrochloric acid (37%, Fisher Scientific) was added to 1 M $NaClO_4$ solutions to achieve a pH of 2.0.

Colloidal silver nanoparticles (AgNPs) of 80-120 nm diameter were synthesised by a seed-mediated citrate reduction of $AgNO_3$. This method was adapted from syntheses by Pyatenko [17, 18] and has been outlined in detail in our previous publications [6–8]. These AgNPs were subsequently used to modify a basal plane pyrolytic graphite (BPPG, Le Carbone Ltd., Sussex, UK) electrode by drying a volume of the suspension on the electrode surface. The loading could be increased or decreased with volume of colloidal suspension.

4.3.2 Instrumentation

The electrochemical cell used was a standard 3-electrode set-up using saturated calomel (SCE) reference electrode and a carbon rod as the counter electrode. The working electrode was a silver macro-disk (0.5 mm diameter) or a AgNP-modified BPPG electrode (5 mm diameter). All electrochemical measurements were performed using an Eco Chemie PGSTAT20 potentiostat connected to a desktop computer.

4.3.3 Experiments

These electrodes (Ag_{macro}/AgNP-BPPG) were then applied to the reduction of Cr^{3+}. Experiments were performed for Cr^{3+} (10 mM) in $NaClO_4$ (1 M, pH of 2) electrolyte solutions. AgNP-BPPG electrodes with surface coverage ranging from 0% to 20%, were employed. The potential was scanned negatively from 0 to -0.9 V (vs. SCE) at 50 mV s^{-1}. In the case of the AgNP-BPPG electrodes, silver loading was then quantified by stripping from the surface in $NaClO_4$ (0.1 M), by scanning positively from 0.1 to 1.0 V (vs. SCE) [19].

4.3.4 Linear diffusion simulation

The cyclic voltammetry of the silver macro-disk undergoing linear diffusion was carried out using the commercially available DIGISIM™ [20] program.

4.4 Results and discussion

Silver electrodes are known to display electrocatalytic activity towards the reduction of chromium species in solution, displaying a distinct reversible redox wave [10]. When we compare the macro-disk behaviour to a AgNP-modified BPPG electrode we see some distinct differences in the nature of the voltammetry. We first consider Figure 4.4, which shows the voltammetry of 10 mM Cr^{3+} in a 1 M $NaClO_4$ electrolyte solution at a 5 mm diameter silver macro-disk electrode ($E_{p,c} = -0.581$ V and $E_{p,a} = -0.451$ V (vs. SCE)).

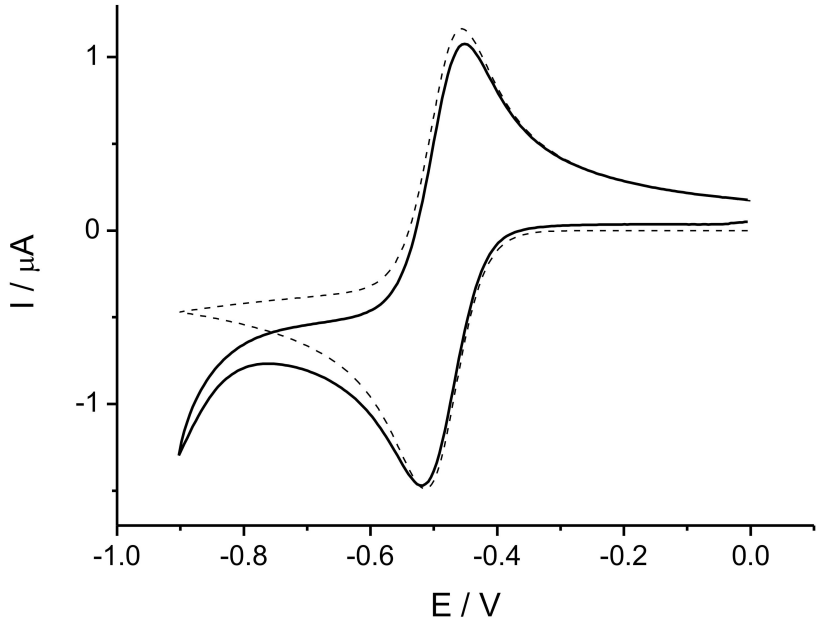

Figure 4.4: Silver macro-disk voltammetry in 1M $NaClO_4$ + 10 mM Cr^{3+} (pH 2). Scan rate: 50 mV s^{-1}. Solid line: experiment; dashed line: DIGISIM™ simulation.

Variable scan rate experiments showed a linear plot of current vs. square root of the

Silver macro-disk fitting DIGISIM™ fitting parameters	
E_f^0 (V) vs. SCE	−0.485
D (m^2 s^{-1})	1.6×10^{-10}
k^0 (m s^{-1})	1.0×10^{-3}
α	0.5

Table 4.2: Silver macro-disk fitting parameters.

scan rate ($\sqrt{v}$), implying a diffusion-controlled process. By applying the Randles-Sevčik equation [21], an experimentally measured diffusion coefficient of 1.5×10^{-10} m^2 s^{-1} was extracted. Using $D_{IGISIM™}$ we were able to model the redox behaviour at the silver macro-disk as shown in Figure 4.4. This allowed us to determine the kinetic parameters for this process based on the one electron reduction of Cr^{3+} to Cr^{2+} ($Cr^{3+} + e^- \rightleftharpoons Cr^{2+}$). In a solution of 1 M $NaClO_4$, the kinetic parameters were optimized as shown in Table 4.2.

The next step was to examine the behaviour of a AgNP-modified BPPG electrode towards the reduction of Cr^{3+} in $NaClO_4$ electrolyte solution. Figure 4.5 shows the experimentally obtained voltammetry for several AgNP-modified BPPG electrodes, with varying NP densities, towards the reduction of Cr^{3+}.

The voltammetry displays a clear relationship between degree of surface coverage and the voltammetric wave shape. The recorded current increases as we increase the active surface area of silver on the electrode. we also observe an increase in the apparent reversibility of the system with increasing NP coverage as the oxidation peak becomes more well-defined and peak-to-peak separation decreases. Furthermore, we also report a small positive shift in reduction potential (~0.15 V from 0.3% to 10.2%) as previously reported in the literature, for the reduction of hydrogen peroxide [9], protons [10] and 4-nitrophnol [11] at AgNP arrays. This occurs at least in part due to the change in diffusion regime experienced at the NP-array as we increase the surface coverage from 0.3% to 10.2%.

This experimental data in the range of 0.3-10.2% nanoparticle coverage, was then first

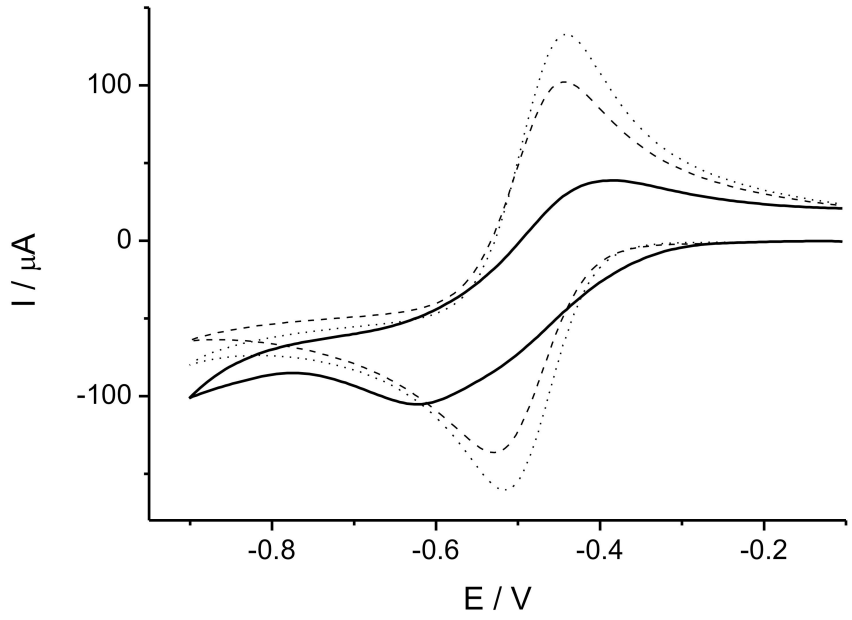

Figure 4.5: Silver nanoparticle modified BPPG electrode (1 M $NaClO_4$ + 10 mM Cr^{3+}, scan rate :50 mV s^{-1}) with increasing surface coverage. Solid line: 0.3% coverage; dashed line: 3.5%; dotted line: 10.2%. The percentage coverage (%) is defined by the area of the projection of the NP as a disc on the electrode surface as a fraction of the total geometric area of the substrate electrode.

approximately fitted using DIGISIM™ . This fitting approximates the mass-transport to the array as linear. The data was fitted by varying the values of Butler-Volmer parameters, k_{apparent} and α where k_{apparent} is the apparent rate constant describing the fit between theory and experiment. The result was a linear relation between apparent rate constant (k_{apparent}) ascertained from the approximate DIGISIM™ fittings and the degree of surface coverage as shown in Figure 4.6.

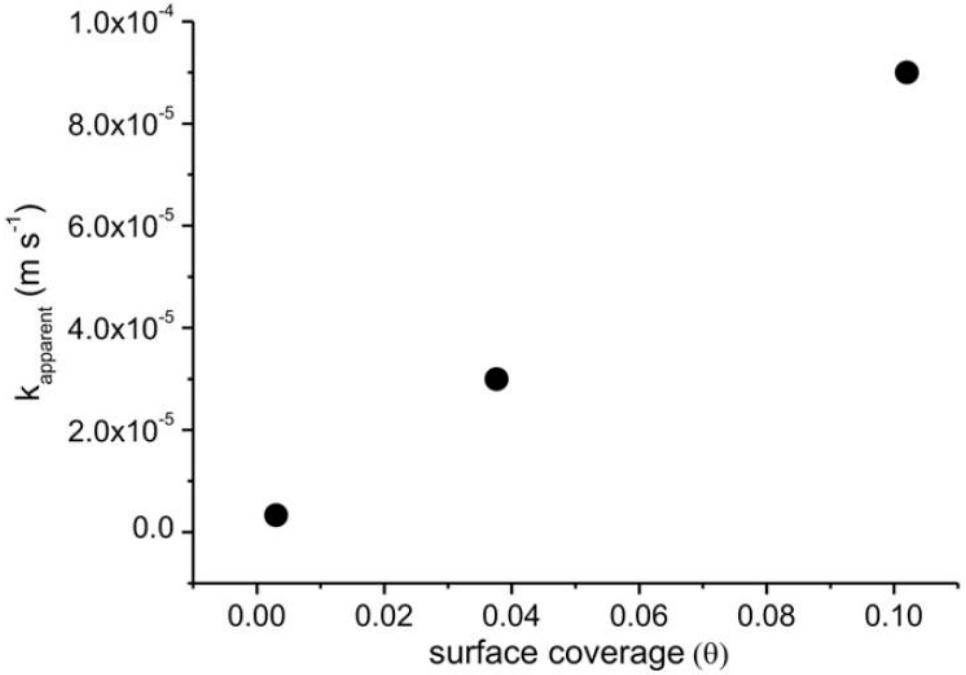

Figure 4.6: Linear plot of (k_{apparent}) vs. surface coverage as obtained from the approximate fitting of AgNP voltammetry using DIGISIM™

We refer to this value of rate constant as k_{apparent} due to the fact that it has been claimed assuming the diffusion to the surface is considered to be linear rather than a mixture of convergent and linear diffusion as actually occurs at arrays of nanoparticles and also that the entire electrode surface is uniformly electro-active. Extrapolation of this linear plot estimated k_{apparent} for full coverage ($\theta = 1$) as $\sim 0.9 \times 10^{-3}$ ms^{-1}, based on the relation shown in (4.8):

$$k_{\text{apparent}}(\text{ms}^{-1}) = k^0(\text{ms}^{-1})\theta \tag{4.8}$$

	Silver nanoparticle surface coverage, θ		
	0.003	0.035	0.102
Fitting parameters			
E_f^0 (V)	-0.485	-0.485	-0.485
D (m^2s^{-1})	1.6×10^{-10}	1.6×10^{-10}	1.6×10^{-10}
k^0 (ms^{-1})	1.0×10^{-3}	1.0×10^{-3}	1.0×10^{-3}
α	0.5 ± 0.1	0.4 ± 0.1	0.4 ± 0.1
$[Cr^{3+}]$(mM)	10 ± 1	10 ± 1	10 ± 1

Table 4.3: Fitting parameters for AgNP-BPPG with varying surface coverage

k^0 is the intrinsic rate constant for the silver macroelectrode. Note that the extrapolation gives a value close to that recorded experimentally for the silver macroelectrode, which was 1.0×10^{-3} ms^{-1}.

In order to account more precisely for the different diffusional behaviour at an array of nanoparticles, the AgNP voltammetry was then fitted using a diffusional model based on a regular array of discs, as developed above [22]. The values of D, E_f^0 and k^0 were taken to be equal to the macro-disk values. The surface coverage (θ) is also inputted into the model in order to define the diffusion domain. It was therefore possible to fit the experimental data as shown in Figure 4.7. Note that at 0.3% coverage simulation does not quite fit the experimental data due to the background current.

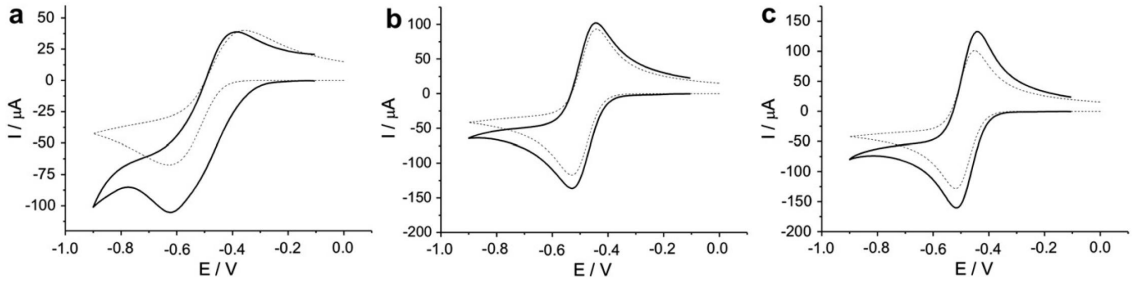

Figure 4.7: Disc simulation fitting for AgNP-BPPG electrode coverage. (a) 0.3%, (b) 3.5%, and (c) 10.2%. Solid line: experimental voltammetry; dashed line: disc simulation.

The optimized parameters for AgNP fitting obtained from this model are shown in Table 4.3.

In summary, an increase in the extent of surface coverage alters the mass-transport

regime, resulting in a transition from convergent to linear diffusional behaviour. At 10.2% surface coverage the electrode exhibits near-macro-disk behaviour due to greatest degree of diffusional overlap.

4.5 Conclusions

In conclusion we discuss in this chapter the reduction of $Cr^{3+}$to Cr^{2+} at an array of silver nanoparticle (80-120 nm diameter) arrays. A relationship exists between the degree of surface coverage (θ) and the nature of the voltammetry. Increasing the coverage, results in an increase in the apparent reversibility of the process as well as an increased current due to the greater surface area available for the reaction to take place. This is due to the transition from convergent diffusion to linear diffusion with increasing surface coverage. By increasing the nanoparticle density the electrode kinetics tend towards those of a macro-disk electrode.

Bibliography

[1] J. Shi, X. Li, Y. Hu, and Y. Hua. *J. Solid State Electrochem.*, 12:1555, 2008.

[2] Z. Wang and K. Qiu. *Electrochem. Commun.*, 8:1075, 2006.

[3] C. M. Welch, C. E. Banks, Ao .O. Simm, and R. G. Compton. *Anal. Bioanal. Chem.*, 382:601, 2005.

[4] F. W. Campbell and R. G. Compton. *Anal. Bioanal. Chem.*, 396:241, 2010.

[5] T. J. Davies, C. E. Banks, and R. G. Compton. *J. Solid State Electrochem.*, 396:241, 2005.

[6] F. W. Campbell, S. R. Belding, R. Baron, and R. G. Compton. *J. Phys. Chem. C*, 113:14852, 2009.

[7] F. W. Campbell, S. R. Belding, and R. G. Compton. *ChemPhysChem*, 11:2820, 2010.

[8] F. W. Campbell, S. R. Belding, R. Baron, and R. G. Compton. *J. Phys. Chem. C*, 113:9053, 2009.

[9] N. Godino, X. Borissé, F. X. Muñoz, and F. J. del Campo. *J. Phys. Chem. C*, 113:11119, 2009.

[10] L. M. Yudi, A. M. Baruzzi, and V. M. Solos. *J. Appl. Electrochem.*, 18:417, 1988.

[11] I. B. Svir, A. I. Oleinick, and R. G. Compton. *Radiotekhnika*, 116:114, 2001.

[12] J. J. Heinze. *Electroanal. Chem.*, 124:73, 1981.

[13] D. J. J. Gavaghan. *Electroanal. Chem.*, 456:25, 1998.

[14] D. J. J. Gavaghan. *Electroanal. Chem.*, 456:1, 1998.

[15] G. Stephenson. *Mathematical Methods for Science Students*. Springer, 1973.

[16] Y. Saito. *Rev. Polarography*, 15:177, 1968.

[17] A. Pyatenko, M. Yamaguchi, and M. Suzuki. *J. Phys. Chem. C*, 111:7910, 2007.

[18] A. Pyatenko, M. Yamaguchi, and M. Suzuki. *J. Phys. Chem. B*, 109:21608, 2005.

[19] S. E. Ward-Jones, F. W. Campbell, R. Baron, L. Xiao, and R. G. Compton. *J. Phys. Chem. C*, 112:17820, 2008.

[20] M. Rudolph, D. P. Reddy, and S. W. Feldberg. *Anal. Chem.*, 66:589A, 1994.

[21] A. J. Bard and L. R. Faulkner. *Electrochemical Methods Fundamentals and Applications*. John Wiley and Sons, 2001.

[22] S. R. Belding, E. J. F. Dickinson, and R. G. Compton. *J. Phys. Chem. C*, 113:11149, 2009.

Chapter 5

Making contact: charge transfer during particle-electrode collisions

The study of impact processes between particles and electrode surfaces is less than 20 years old, and has recently received added impetus due to the current intense interest in the chemistry of nanoparticles. In this chapter, we briefly appraise the historical results and recent developments in this field, and consider its potentially wide-ranging applications. Included in the overview are new results that will be presented more fully in later chapters.

This review was in cooperation with Dr. Neil V. Rees and has been published in *RSC Advances*, 2012, 2, 379.

5.1 Introduction

The electrochemical study of particle impacts on electrodes has been an active research area for less than twenty years [1–4], mirroring the wider interest in nanoscience where very substantial advances have been seen over the last few years [5, 6].

The earliest work was carried out by Heyrovský *et al*. [1–4], considering the voltammetry of colloidal solutions of the semiconducting oxides SnO_2, TiO_2, and Fe_2O_3. They were able to show that the voltammograms measured for a colloidal suspension of polydisperse nanoparticles (NPs) could be rationalised as a summation of the voltammetric responses of a series of homodisperse NPs (see Figure 5.1). Further, using a Hg electrode, they identified catalytic proton reduction occurring on the surface of the TiO_2 particles as part of the overall reduction of TiO_2 particles in acidic solution [3]. In ref. [4], Heyrovský *et al*. studied mixed Fe_2O_3 / TiO_2 NPs of different size ranges and were able to determine approximate composition: smaller NPs were more iron-rich than larger ones.

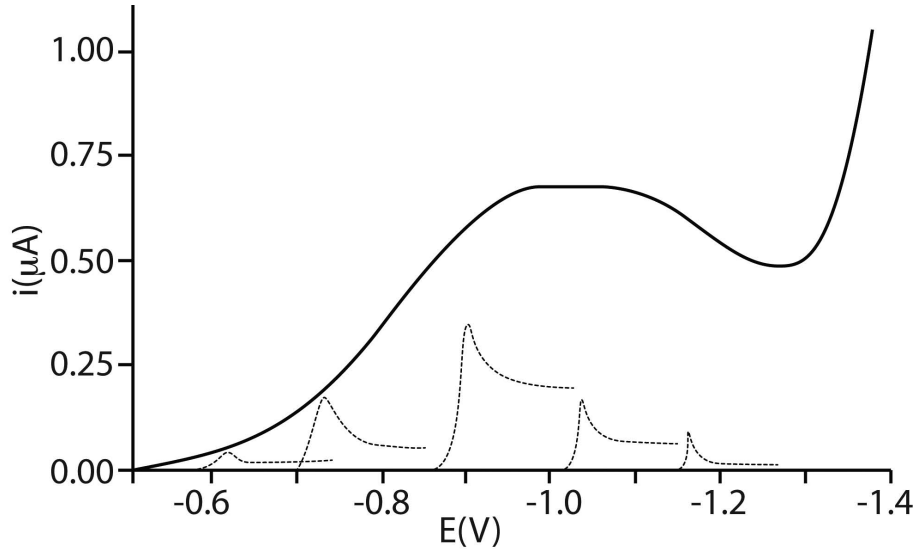

Figure 5.1: Voltammetric curve of a colloidal polydisperse solution of 10^{-2} M TiO_2 in 2×10^{-2} M HClO4 with a schematic indication of contributions by groups of homodisperse particles of different sizes to the total current (not to scale) [1].

Subsequently, Scholz studied the collisions of liposomes, formed by mixing the lecithin molecules phosphatidylcholines with fatty acids in phosphate buffer at pH7, at a

mercury electrode [7]. Sharp current transients were observed as the liposomes contacted, burst and spread on the mercury surface. Integration of the areas under these current spikes enabled the number of lecithin molecules per liposome to be determined. The frequency of spikes was found to increase either side of the potential of zero charge (pzc) the of mercury electrode, with no detectable spikes at the pzc. It was concluded that these non-faradaic spikes were caused by charge transfer that was capacitative in nature [7]. The kinetics of liposome adhesion events were then explored in a subsequent study [8], and then in [9] the methodology was used to consider montmorillonite clay particles adhering onto a mercury electrode (see Figure 5.2).

The importance of Scholz's work in discovering that impacts could be detected directly as sharp current-time transients and that these spikes could be interpreted quantitatively to gain information about the impact process and the colliding materials, led to subsequent studies to investigate the extent that non-faradaic signals could arise and be detected.

Departing from Scholz's experimental design of having liposomes bursting, or particles adhering to mercury (i.e. a physically and chemically soft) surface under thermal motion, the Compton group investigated impacts of hard particles and oil droplets with Pt and Au electrodes under ultrasonically-driven motion [10–13]. It was found that in all cases, current transients of microsecond duration could also be observed during the impacts. These transients were 3 orders of magnitude shorter than the 1-20ms spikes reported by Scholz, and this was ascribed to the higher velocity of the impacting particles leading to a substantially shorter contact-time [10, 11]. As with Scholz, the Compton group found that the impact transients gave information about the electrode as well as the particle: first, the amount of charge passed in the transient (q) scaled with the size and conductivity of the impacting particle [12, 13], but second, the sign of the current transients inverted at the potential of zero charge (pzc) of the substrate electrode, as shown in Figure 5.3 [12, 13]. The charge passed was deemed to be either transferred between the particle and the elec-

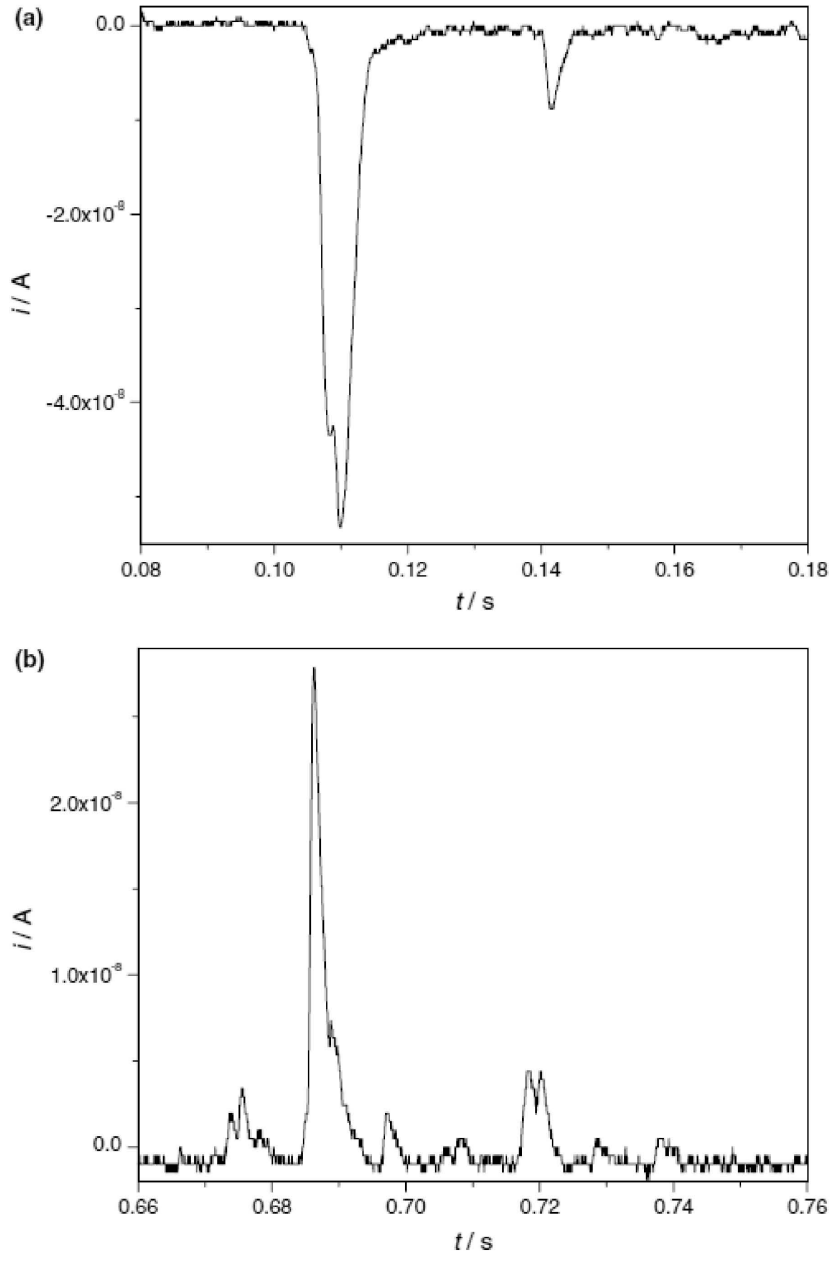

Figure 5.2: Single montmorillonite particle adhesion events at a Hg electrode in 10mM KCl(aq) at a) -0.02V and b) 0.25V. Reproduced from [7].

trode, or between the (deformed) double layer and the electrode, but no conclusion could be made as to if one or both mechanisms were dominant (see Figure 5.4).

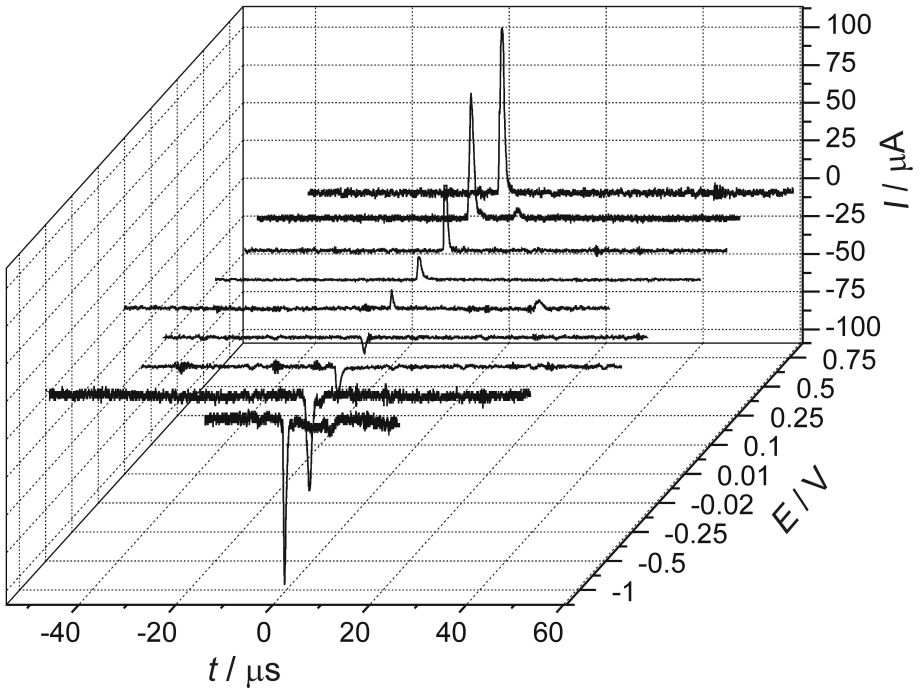

Figure 5.3: Current transients due to impacts of graphite microparticles at a polycrystalline gold electrode in 0.10 M perchloric acid showing polarity inversion at the pzc. Reproduced from [12] with permission.

However, using particles in the size range 30-300 μm made of oxidisable metals or graphite particles chemically-modified with electroactive molecules, Compton's group concluded that faradaic charge transfer could not be observed on the timescale of these ultrasonically-driven impacts [13]. This observation would later be explained in terms of the effects of contact time and particle size.

In a revisitation of his earlier work, Heyrovský published in 2006 a paper on the voltammetry of metallic nanopowder suspensions on mercury electrodes [14]. In it, he described the cyclic voltammetry of suspensions of Cu, Fe, Ni, Mo, and W nanopowders and observed "elementary instantaneous flares of cathodic current" which were ascribed to the reduction of the oxide coatings on the NPs during contact with the Hg electrode (see Figure 5.5). This work is the forerunner of contemporary studies as detailed next.

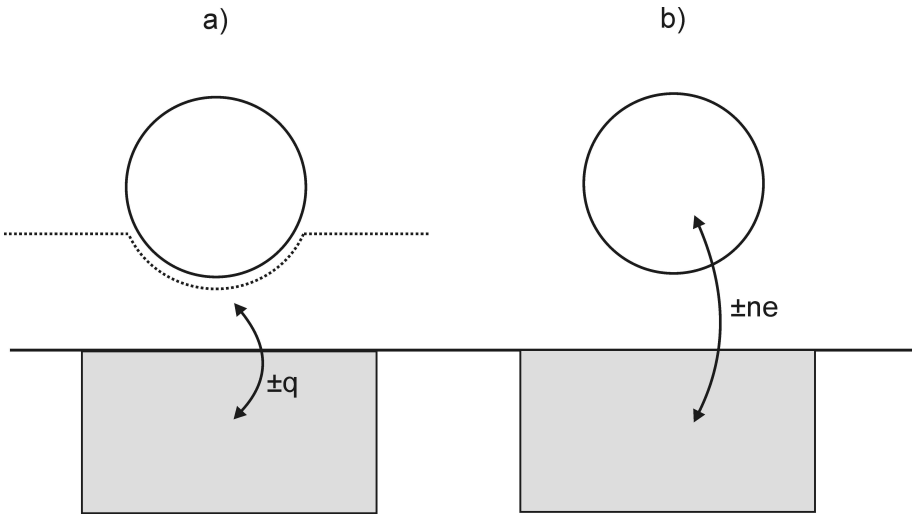

Figure 5.4: Schematic diagram showing particle collision with electrode to illustrate: (a) non-faradaic charge transfer occurring (see text) when an electroinactive particle rapidly deforms the double layer, and (b) faradaic charge transfer occurring where the electrode is held at a sufficiently positive/negative potential to render the particle electroactive.

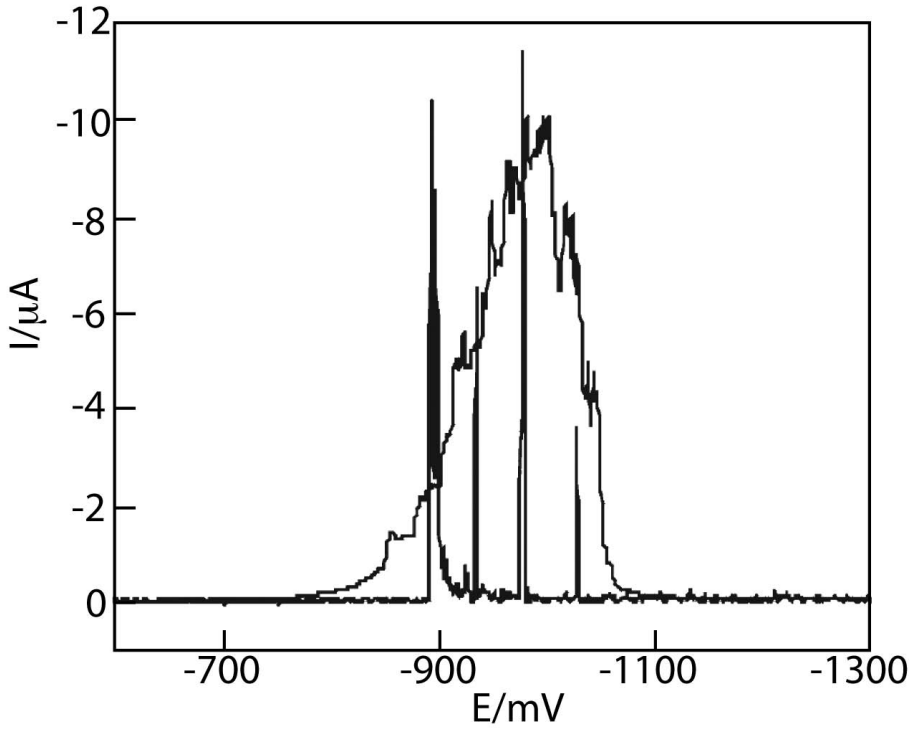

Figure 5.5: Linear DC voltammogram of 10 g copper powder in 10 mL deaerated 0.1 M NaOH, recorded at v =10 mV s^{-1} (needle-form spikes) and at v =100 mV s^{-1} (broad peak). Curve of blank solution merges with potential axis. Reproduced from [14] with permission.

5.2 Recent activity and future possibilities

5.2.1 Electrocatalytic (indirect) voltammetry during NP impacts

There has been substantial renewed interest in particle-electrode collisions with the observation of faradaic charge transfer during nanoparticle (NP)-electrode impacts as a result of work published in 2007-8 by Bard *et al*. [15, 16]. In an experiment that combined aspects of both the earlier work by Heyrovský and Scholz [1–4, 7–9, 14], they succeeded in observing single nanoparticle collisions with an electrode *via* electrocatalytic amplification (see Figure 5.6). To successfully use this method, the NP and electrode materials must be chosen such that the electrocatalysis occurs only on the NP and not on the electrode substrate. Using an acidified suspension of PtNPs with a carbon microelectrode target, the collisions (under thermal motion) were identified as current transients caused by the hydrogen evolution reaction occurring only at the surface of the PtNPs when contact was made with the carbon electrode [15]. In ref. [16], Bard subsequently demonstrated the difference in activity of PtNPs compared to AuNPs for hydrazine oxidation.

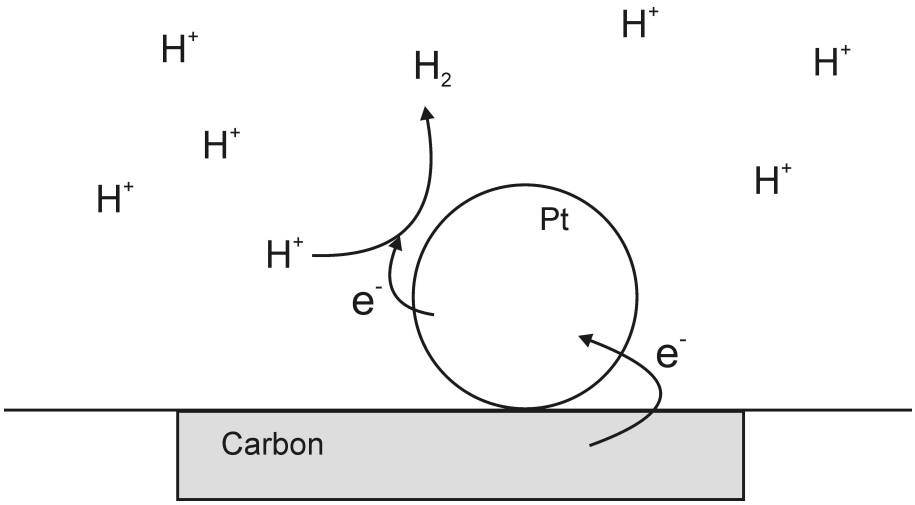

Figure 5.6: Schematic diagram showing the Bard electrocatalytic experiment, where the redox process does not proceed on the substrate electrode but does on the surface of the metal NP.

In 2009, Bard extended his impact studies by first investigating the effects on the current transients by surface monolayers of thiols - thereby limiting the closest distance of

approach of the NP to the electrode surface. Secondly, by demonstrating that iridium oxide (IrOx) NPs could be observed colliding with Pt microelectrodes (pre-treated with $NaBH_4$) [17]. Using IrOx NPs of mean diameter 28 nm to electrocatalyse water oxidation, single current spikes were observed for each collision. The collisions were typically shorter than 1s, in contrast to the longer duration contacts in his earlier work which were often characterised by "staircase" rather than "spike" current responses (see Figure 5.7). The charge passed in the IrOx NP spikes was of the order of 10^{-11}-10^{-12} C, and the collision frequency was found to be proportional to the NP concentration, and in general in the order of *ca*. 0.07 s^{-1} per pM of NP concentration [18]. In [19], Bard developed a stochastic model to explain the frequencies for both "staircase" and "spike" type transients. In the latter case, based on kinetic theory, the result was derived that the average collision frequency could be expressed as:

$$(f) = \frac{AC_{np}}{4}\sqrt{\frac{3k_BT}{m}}, \tag{5.1}$$

where C_{np} and m refer to the concentration of NPs and NP mass respectively and T and k_B are absolute temperature and the Boltzmann constant. However, Bard asserted that the calculated collision frequency was unlikely to be the observed collision frequency, due to such factors as (i) not all collisions may result in an experimentally observable current transient, (ii) some particles may undergo multiple collisions, and (iii) the proportion of particles experiencing multiple collisions is likely to increase with increasing NP concentration.

Within their model, Bard *et al*. considered separately the two distinctive transient shapes that they have previously reported [19]. The "staircase" response has been interpreted as an irreversible adsorption of the NPs with the electrode surface (or else adsorption followed by irreversible deactivation of the NP surface). "Spike" responses occur when the contact time between NP and electrode is shorter. The factors which determine which response is observed were identified as being: the nature of the electrode surface

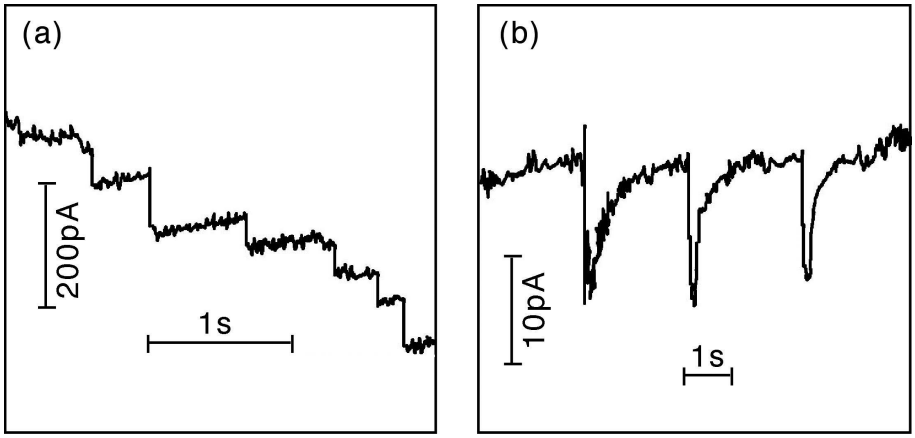

Figure 5.7: Examples of the current transients identified by Bard et al as due to NP collisions: (a) staircase response of PtNP/Au electrode/hydrazine oxidation, and (b) spike response of IrOx NP/Pt electrode/water oxidation. Reproduced from [19].

(including any pre-treatments), the nature of the NP surface including capping agents and ionic adsorption, and finally any process that may deactivate the electrocatalytic reaction occurring. Results showed that the staircase response could be successfully modelled by a diffusion-controlled movement of the NPs to the electrode surface, whereas spike impacts due to transient sticking of the NP to the surface could be described *via* a random walk model also assuming diffusion-control.

5.2.2 Direct oxidation of NPs during impacts

Very recently, the present authors have explored the direct electrochemistry of NPs that can occur during the NP collisions with electrodes, *via* anodic particle coulometry (APC) [20–22]. This work is presented fully in Chapter 6-10.

Initial investigations considered the oxidation of AgNPs during collisions with a glassy carbon electrode (see figures 5.8 and 5.9): only when the electrode was potentiostatted at potentials more positive than the redox potential for the Ag/Ag^+ couple were the spike transients observed [20, 21]. That is, the process occurring during the impact is due to:

$$Ag(NP) - ne^- \rightarrow nAg^+(aq) \tag{5.2}$$

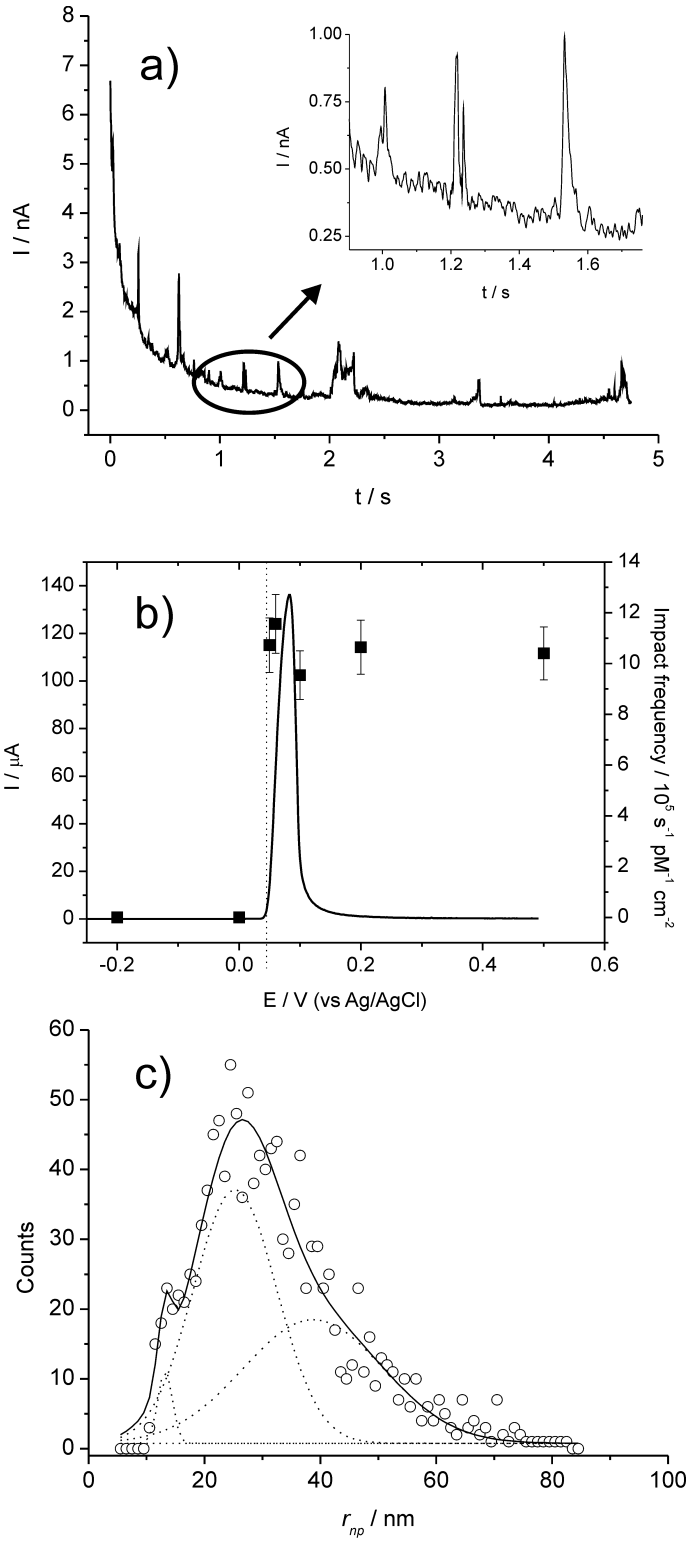

Figure 5.8: a) Chronoamperometric profiles showing oxidative Faradaic collisions of AgNPs in citrate solution. The inset shows detailed impact spikes. b) Overlay plot of a stripping voltammogram for a AgNP-modified GC electrode (left axis) and the impact frequency (right axis) showing the onset potential of the spikes; and c) distribution of AgNP radii inferred from current spikes. Reproduced from [20].

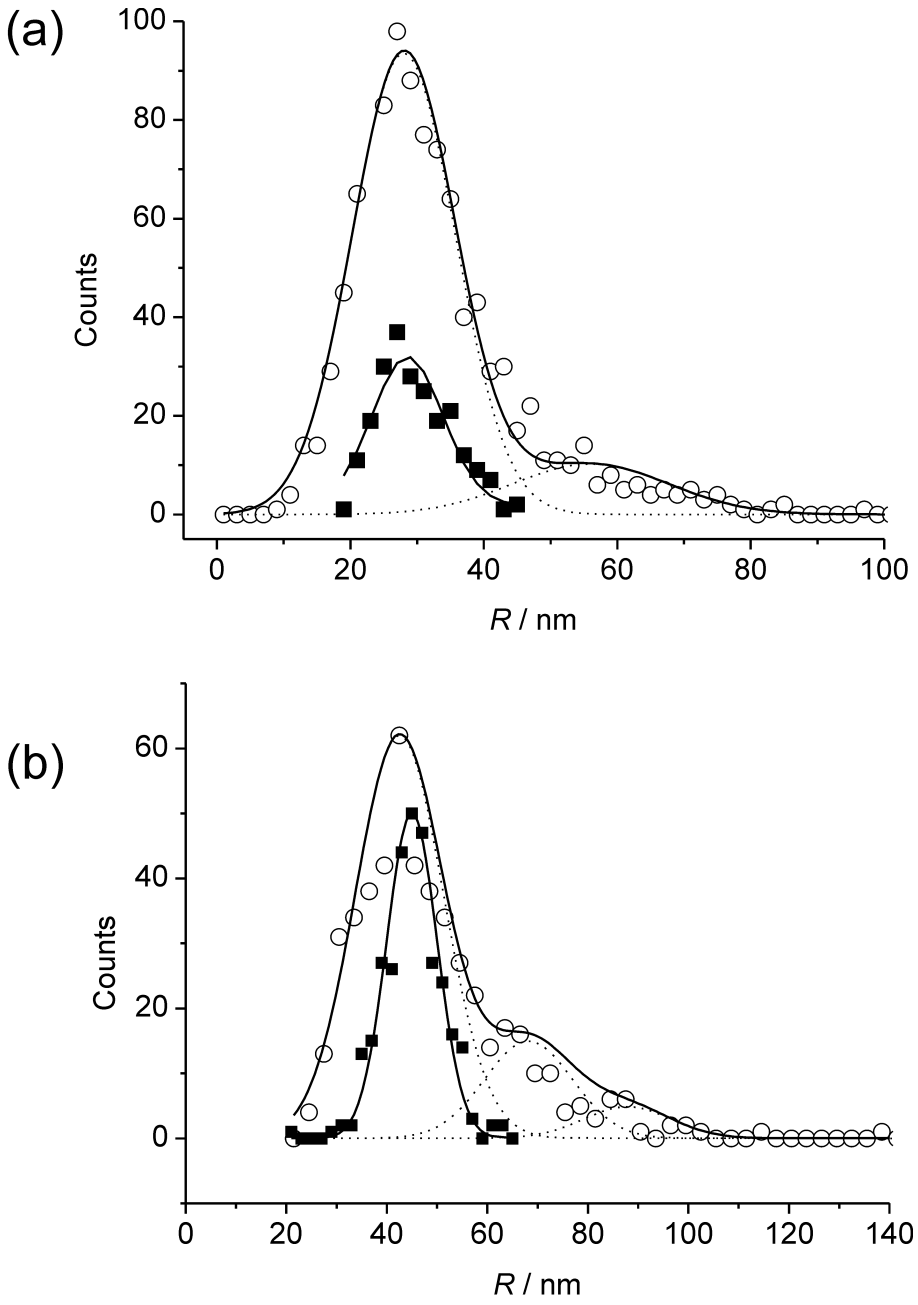

Figure 5.9: Comparison of distributions derived from APC (○) and SEM (■) analysis for AgNPs of nominal radii (a) 29nm, and (b) 45nm. Reproduced from [21].

Figure 5.8 shows a typical chronoamperometric trace with multiple impact transients. In Figure 5.8(b), the sharp"switch on" of the transients at the precise redox potential of the Ag /Ag^+ couple provides confirmation of the faradaic process in (5.2).

Further, it was found that the charge passed during the spike response was quantitatively linked to the size of the NP and therefore size distributions could be extracted from the spike transients (see Figure 5.8(c)).

The ability to determine size distributions was shown to be useful in following the aggregation kinetics of Ag NPs suspended in acidic solutions, and key cluster sizes could be identified with those corresponding to 4, 8, and 27 NPs the most prevalent [21]. It was confirmed that for a range of radii of 14-45 nm, and under the range of overpotentials studied, the oxidation of AgNPs in this size range was exhaustive and a size distribution could be obtained that agreed with independent SEM analysis, as shown in Figure 5.9 [21].

In these studies, only spike-type responses were observed with a duration of 1-10 ms, roughly two orders of magnitude shorter in contact that those reported by Bard, but similar to those first spike observations reported by Scholz [7–9].

Further, this methodology has been very recently shown to be applicable for the characterisation of AuNPs *via* analysis of impact spikes [22]. this work is discussed in Chapter 8. It was demonstrated that the chloride-assisted dissolution of Au at oxidative potentials due to the complexation equilibria (5.3) and (5.4) [5, 6, 23–25] enables the identification of AuNPs as well as determining size information about them (and revealing aggregation of NPs into larger clusters). These results are illustrated in Figure 5.10 and 5.11, which show how the onset of spikes correspond to the AuNP voltammetry in chloride solutions and the resulting size distributions that can be so obtained. It is anticipated that this method should be extendable to other oxidisable metals: for example, Pumera *et al*. has recently published results on the electrochemical detection of molybdenum NPs *via* pulse voltammetry [26], and so MoNPs would appear ideal candidates for a APC-type

analysis.

$$Au + 4Cl^- \rightleftharpoons AuCl_4^- + 3e^- \tag{5.3}$$

$$AuCl_4^- + 2Au + 2Cl^- \rightleftharpoons 3AuCl_2^- \tag{5.4}$$

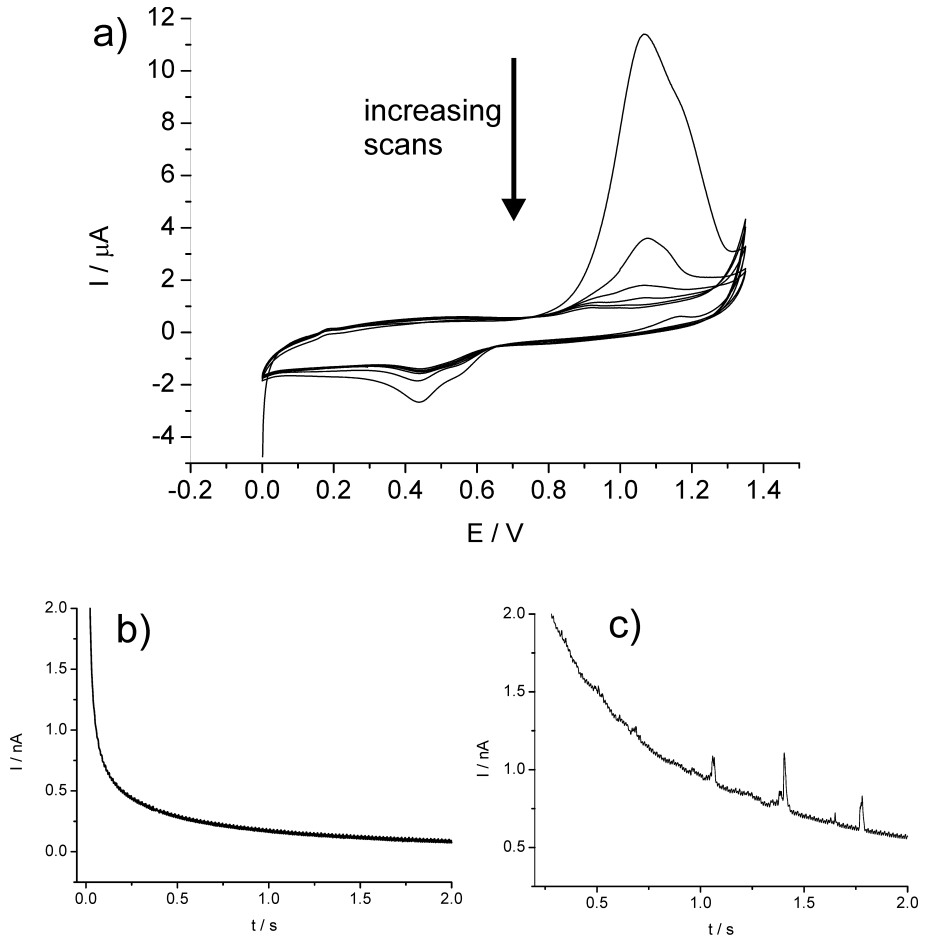

Figure 5.10: (a) Repeat CVs showing the first 6 scans of a AuNP-modified glassy carbon electrode in 0.10 M HCl. Chronoamperometric profiles showing oxidative faradaic transients of AuNPs at potentials of (b) 0.8 V and (c) 1.1V. Reproduced from [22].

Supporting evidence for the transient nature of the NP-electrode encounter suggested by the observation of the "spike" rather than "staircase" shape of the impact current-transients was provided when collision experiments were used to calculate sticking probabilities for the AgNP-glassy carbon impact: a value of 0.16 was determined that was essentially independent of electrode potential or NP size [27]. Higher sticking coefficients

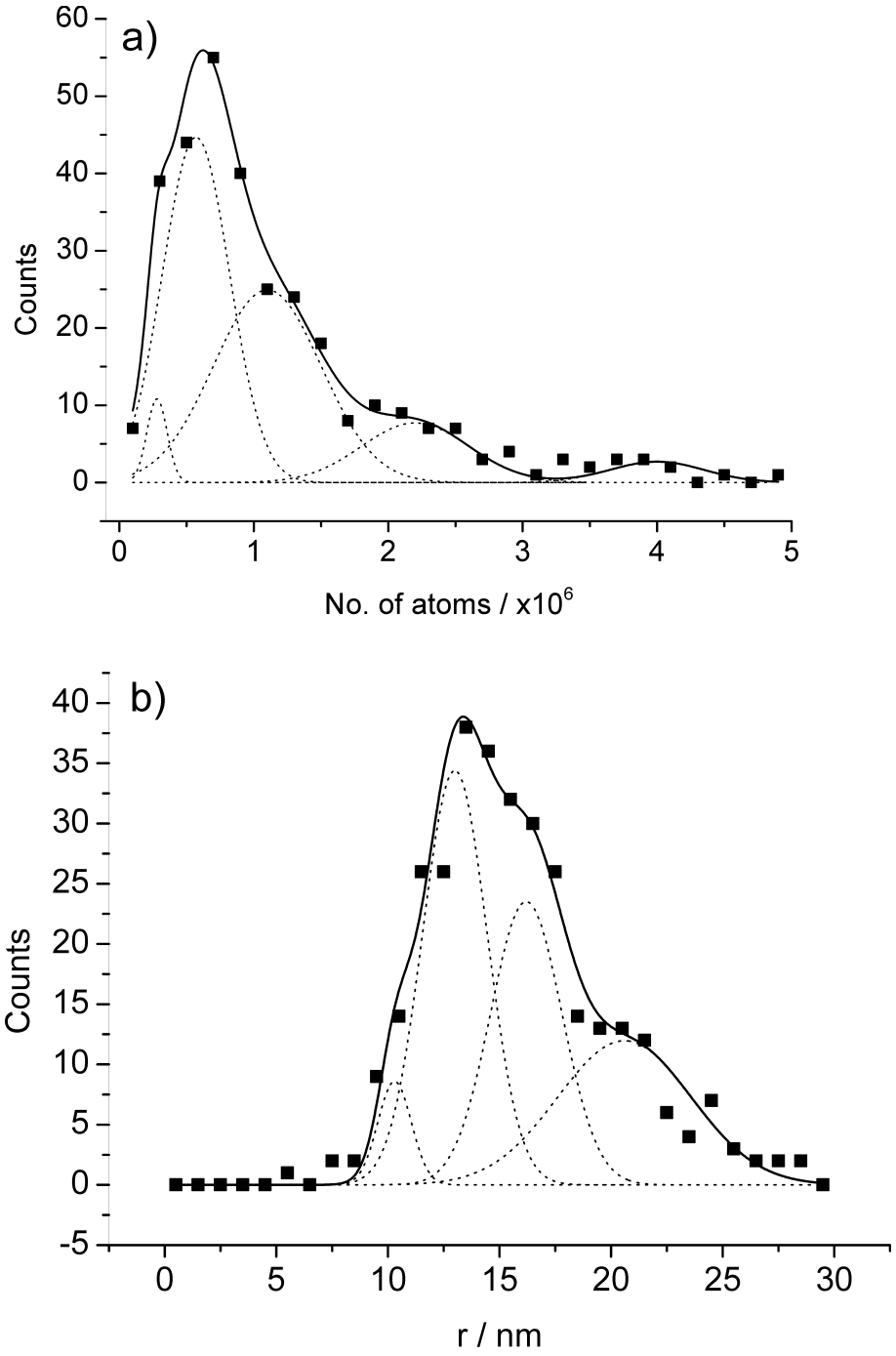

Figure 5.11: APC distributions for the AuNP impact experiments held at a potential of +1.1 V displayed in terms of (a) no. of atoms oxidised, and (b) the inferred NP size. Reproduced from [22].

would account for the "staircase" transients observed by Bard in some cases, which may differ from that of the AgNP-carbon system reported in [27] by factors such as NP and substrate electrode materials, capping agents, electrolytes, *etc*.

5.2.3 Electrodeposition onto NPs during impact

In addition to these detection and sizing experiments, the Compton group have demonstrated that NP collisions may have synthetic potential, by studying the underpotential deposition (upd) of thallium and bulk electrodeposition of cadmium onto AgNPs, forming bimetallic core-shell NPs (denoted Ag@Tl and Ag@Cd respectively) [28, 29]. This work is demonstrated in Chapter 11 and 12. For the upd of thallium, it was shown that up to a monolayer could be deposited onto AgNPs whereas for the electroplating of cadmium onto AgNPs, the average number of layers deposited was 19. In both cases, deposition occurs only during NP-electrode contact, which as before lasts approximately 1-10ms.

$$\mathrm{Ag(NP) + mTl^{+}(aq) + me^{-} \rightarrow Ag@Tl_{m}} \tag{5.5}$$

$$\mathrm{Ag(NP) + mCd^{2+}(aq) + 2me^{-} \rightarrow Ag@Cd_{m}} \tag{5.6}$$

These observations were possibly in contrast to those reported previously [13] which found that faradaic processes were not clearly observable when impacts were studied using micron-sized particles driven under ultrasound such that the impact transients were of microsecond duration. Cutress *et al*. adapted a random walk model to investigate the contact time required to electrodeposit a monolayer of metal onto an NP during collision, and found this to be on the order of 10^{-4} s for a 45 nm radius NP in 10 mM solution of analyte (and longer for larger particles) [30]. This provided confirmation that the NP thermally-driven impacts were of a sufficient duration to allow experimentally-observable faradaic process to occur, whereas the earlier ultrasound experiments were not [13]. In addition, understanding of the contact time required for different degrees of charge transfer to occur

should enable the finer control of electroplating processes described above [29], so that core-shell NPs could be synthesised to precise specification *via* impact processes.

5.3 Conclusions

This chapter has reviewed the study of thermally-driven nanoparticle impact phenomena via electrochemical measurements. The NP detection methods outlined above have wide application. For example, both metal NPs and metal oxide NPs have been shown to be detectable *via* direct [2–4, 20–22] as well as indirect [15–18] faradaic processes. Provided the interplay of factors such as (a) particle-electrode contact time, (b) size of NP, and (c) kinetics of the desired faradaic process are favourable, the impact environment should, in principle, provide the same possibilities for experimental design and development as any other electrochemical reaction environment.

Bibliography

[1] M. Heyrovský and J. Jirkovský. *Langmuir*, 11:4288, 1995.

[2] M. Heyrovský, J. Jirkovský, and B. R. Müller. *Langmuir*, 11:4293, 1995.

[3] M. Heyrovský, J. Jirkovský, and M. Štruplová Bartáčková. *Langmuir*, 11:4300, 1995.

[4] M. Heyrovský, J. Jirkovský, and M. Štruplová Bartáčková. *Langmuir*, 11:4309, 1995.

[5] M. Pumera, M. Aldavert, C. Mills, A. Merkoci, and A Alegret. *Electrochim. Acta*, 50:3702, 2005.

[6] A. Bonanni, M. Pumera, and Y. Miyahara. *Phys. Chem. Chem. Phys.*, 13:4980, 2011.

[7] D. Hellberg, F. Scholz, F. Sshauer, and W. Weitschies. *Electrochem. Commun.*, 4:305, 2002.

[8] F. Scholz, D. Hellberg, F. Harnisch, A. Hummel, and U. Hasse. *Electrochem. Commun.*, 6:929, 2004.

[9] D. Hellberg, F. Scholz, F. Schubert, M. Lovric, D. Omanovic, V. A. Hernanberg, and R. Thede. *J. Phys. Chem. B*, 109:14715, 2005.

[10] C. E. Banks, N. V. Rees, and R. G. Compton. *J. Electroanal. Chem.*, 535:41, 2002.

[11] C. E. Banks, N. V. Rees, and R. G. Compton. *J. Phys. Chem. B*, 106:5810, 2002.

[12] N. V. Rees, C. E. Banks, and R. G. Compton. *J. Phys. Chem. B*, 108:18391, 2004.

[13] A. D. Clegg, N. V. Rees, C. E. Banks, and R. G. Compton. *ChemPhysChem*, 7:807, 2006.

[14] A. V. Korshunov and M. Heyrovský. *Electroanalysis*, 18:423, 2006.

[15] A. J. Bard and X. Y. Xiao. *J. Am. Chem. Soc.*, 129:9610, 2007.

[16] A. J. Bard, X. Y. Xiao, F. R. F. Fan, and J. P. Zhou. *J. Am. Chem. Soc.*, 130:16669, 2008.

[17] A. J. Bard, X. Y. Xiao, S. L. Pan, J. S. Jang, and F. R. F. Fan. *J. Phys. Chem. C*, 113:14978, 2009.

[18] S. J. Kwon, F. R. F. Fan, and A. J. Bard. *J. Am. Chem. Soc.*, 132:13165, 2010.

[19] S. J. Kwon, H. Zhou, F. R. F. Fan, V. vorobyev, B. Zhang, and A. J. Bard. *Phys. Chem. Chem. Phys.*, 13:5394, 2011.

[20] Y. G. Zhou, N. V. Rees, and R. G. Compton. *Angew. Chem., Int. Ed.*, 50:4219, 2011.

[21] N. V. Rees, Y. G. Zhou, and R. G. Compton. *ChemPhysChem*, 12:1645, 2011.

[22] Y. G. Zhou, N. V. Rees, J. Pillay, R. Tshikhudo, S. Vilakazi, and R. G. Compton. *Chem. Commun.*, 48:224, 2012.

[23] A. Kolics, A. E. Thomas, and A. Wieckowski. *J. Electroanal. Chem.*, 92:3727, 1996.

[24] M. A. Dias, G. H. Kelsall, and N. J. Welham. *J. Electroanal. Chem.*, 361:25, 1993.

[25] B. S. Brook, M. I. Pozina, and E. I. Pozenfel'd. *Zh. Analit. Khim.*, 34:1095, 1979.

[26] M. Giovanni and M. Pumera. *Electrochem. Commun.*, 13:203, 2011.

[27] Y. G. Zhou, N. V. Rees, and R. G. Compton. *Chem. Phys. Lett.*, 514:291, 2011.

[28] Y. G. Zhou, N. V. Rees, and R. G. Compton. *ChemPhysChem*, 12:2085, 2011.

[29] Y. G. Zhou, N. V. Rees, and R. G. Compton. *Chem. Phys. Lett.*, 511:183, 2011.

[30] I. J. Cutress, N. V. Rees, Y. G. Zhou, and R. G. Compton. *Chem. Phys. Lett.*, 514:58, 2011.

Chapter 6

The electrochemical detection and characterization of silver nanoparticles in aqueous solution

In this chapter we outline a new detection strategy, based on the Faradaic charge transfer when AgNPs strike an electrode, for the detection of nanoparticles. We show for the first time that the direct electrooxidation of AgNPs colliding with an electrode is both viable and quantitative, and can be used for characterization and NP identification.

This work was carried out in cooperation with Dr. Neil V. Rees, and has been published in *Angewandte Chemie International Edition*, 2011, 50, 4219.

6.1 Introduction

Nanoparticles (NPs) have become ubiquitous with an estimated 1600 commercial products available [1], but they are inevitably released into the environment either by intention, manufacture, or disposal [2, 3]. The commonest metal NPs are Ag (26%), Ti, C, Si, Zn, and Au (all <10%) [4]. Of particular interest are AgNPs, which have powerful antibacterial properties, occuring in many commercial products from clothing (ca.50% of AgNPs leach out per washing cycle [5] to medical dressings. Their biocidal activity is due to the high affinity of Ag^+ for thiols, leading to disruption of enzyme function responsible for nutrient uptake, and cellular energy production/storage processes [6]. AgNPs cause endocrine disruption in amphibians [7] and are toxic to many mammalian organs [8]. An estimated 65t of AgNPs are released into global river systems alone [9]. To characterize the risk posed to ecosystems by increased exposure to AgNPs and their environmental fate, the development of detection techniques is urgently required [10].

In this chapter we outline a new detection strategy, based on the faradaic charge transfer when AgNPs strike an electrode. The direct detection of particle collisions at electrodes is a recent field [11–27] with early work concerned with the adhesion of colloidal particles on Hg [11–18]. Of most relevance are studies into the collisions of micron-sized droplets or particles at potentiostatted electrodes [19–23]. For electroinactive oil droplets and particles driven by ultrasound onto an electrode surface, non-faradaic current transients of microsecond duration occur whose polarity inverts at the potential of zero charge of the electrode-electrolyte system [20, 21]. The transients can also be used for sizing the particles [22]. However, faradaic charge transfer between an electrode and phenylenediamine-modified graphite powder was not observed during collisions under sonication [23]. Recently, Bard and co-workers have applied these concepts to observe electrochemical reactions on the surface of impacting NPs [24–28].

In this chapter, we show for the first time that the direct electro-oxidation of AgNPs colliding with an electrode is both viable and quantitative, and can be used for character-

ization and NP identification.

6.2 Experimental

AgNPs of diameter ranges 20-50 nm and 80-120 nm were synthesized according to the literature [29–31]. Sodium dihydrogen citrate ($NaC_6O_7H_7$, Aldrich, >99.5%) and KCl (Riedel-de-Haan, >99.5%) were used as received. All solutions (10 mM $NaC_6O_7H_7$ and 90 mM KCl unless stated) were made using ultrapure water of resistivity $\sim$ 18.2 MΩcm (Millipore) and degassed thoroughly with N_2 (oxygen-free, BOC Gases plc) and an atmosphere of N_2 maintained during the experiment. Experiments were conducted at (293±2) K within a faraday cage using GC working electrodes (BASI), Ag/AgCl or calomel reference electrode (Radiometer, Copenhagen), and a graphite rod counter electrode. The potentiostat was a μAutolab III (Metrohm-Autolab BV, Utrecht, Netherlands). Impact spikes were analysed using Origin v.8.1 (www.OriginLab.com) for spike identification and integration, and gaussian deconvolution of radius distribution. Electrical noise was removed by applying Fourier transform filtering (within Origin software) at 50Hz and multiples up to 200Hz. Spikes were automatically identified by the same software at a threshold of 15% of the highest spike.

6.3 Results and Discussion

Initial experiments on AgNP-electrode collisions were conducted by observing the hydrogen evolution reaction (HER) in citrate solution (see Experimental). HER kinetics on bare glassy carbon (GC) are slow, with no significant currents before the onset of solvent breakdown in aqueous solutions. Any spikes observed were due to the HER at the surface of AgNPs during contact with the electrode (compare the electrocatalytic amplification observed for PtNPs [28]).

First, cyclic voltammetry was performed using a AgNP-modified GC electrode (dia-

meter 3 mm) to observe the reduction potential for the HER (see Figure 6.1). Next, a 11 μm radius bare GC electrode was potentiostatted in the solution, and no current spikes were observed. The experiment was repeated with dispersed AgNPs, and reductive current spikes were observed in the current-time trace (see Figure 6.2). Repeat experiments at different potentials yielded current spikes which are analyzed in Figure 6.3. The charge passed during each spike (Q) varies with potential for both NP size ranges: the onset potential of spikes is in excellent agreement with the formal potential of the HER on AgNPs (see Figure 6.1). The collision frequency was found to vary linearly with the number concentration of AgNPs up to 40 pM (see Figure 6.3b) according to 3.9×10^4 s^{-1} pM^{-1}; this is in good agreement with the collision rates for PtNPs of 0.012-0.02 s^{-1} cm^{-2} pM^{-1} (10 and 25 μm diameter electrodes) reported by Bard and co-workers [28]. Q was also found to increase linearly with the concentration of citrate (see figure 6.1c).

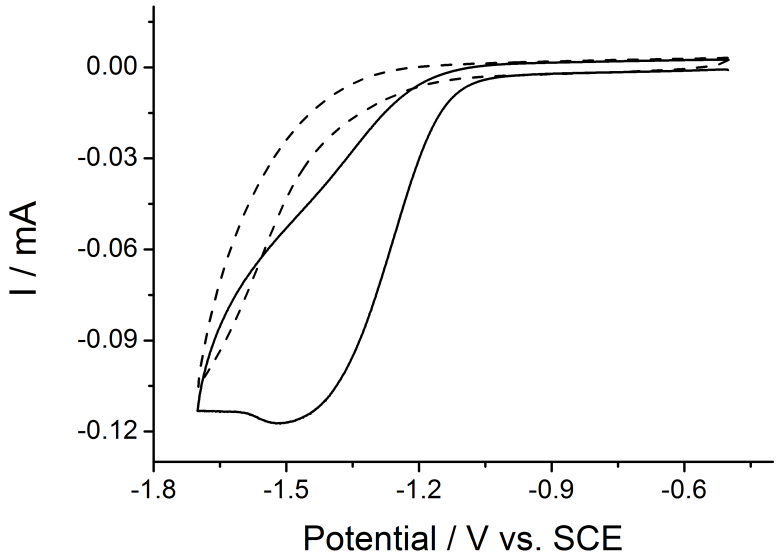

Figure 6.1: Cyclic voltammetry performed using a bare GC electrode (dashed line) and a AgNP-modified GC electrode (solid line) in a solution of 10 mM citrate and 90 mM KCl.

We next investigated the direct characterization of AgNPs via instantaneous oxidation during collisions.

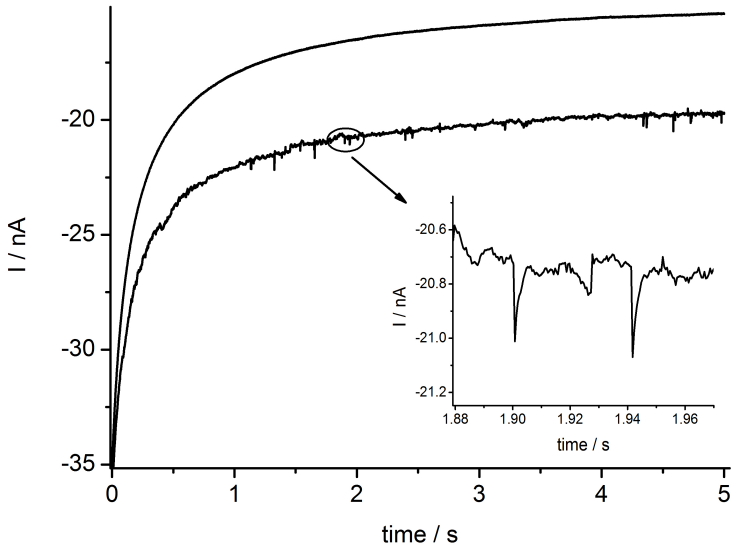

Figure 6.2: Chronoamperometric profiles recorded before (top) and after (bottom) the injection of AgNPs into the citrate solution.

$$\mathrm{Ag(NP)} - \mathrm{e}^- \rightarrow \mathrm{Ag}^+\mathrm{(aq)} \tag{6.1}$$

First, a AgNP-modified GC electrode was scanned anodically in the citrate solution to observe the stripping voltammogram. Next, the GC microelectrode was placed in citrate solution and dispersed AgNPs (diameter 20-50 nm) added. Under potentiostatted conditions (from 50-500 mV vs Ag/AgCl), oxidative (faradaic) current spikes were observed (see Figure 6.4a), showing for the first time that direct oxidation of metal NPs during collision events is both observable and quantitative. The onset of these faradaic spikes was found to vary with potential (see Figure 6.4b), and the collision frequency is in good agreement with the HER results above confirming that NP collisions are the source of the oxidative transients. Assuming that the NPs are spherical (radius rnp), the maximum charge passed due to complete oxidation of the AgNP is given by:

$$Q = \frac{4F\pi\rho r_{np}^3}{3A_r}, \tag{6.2}$$

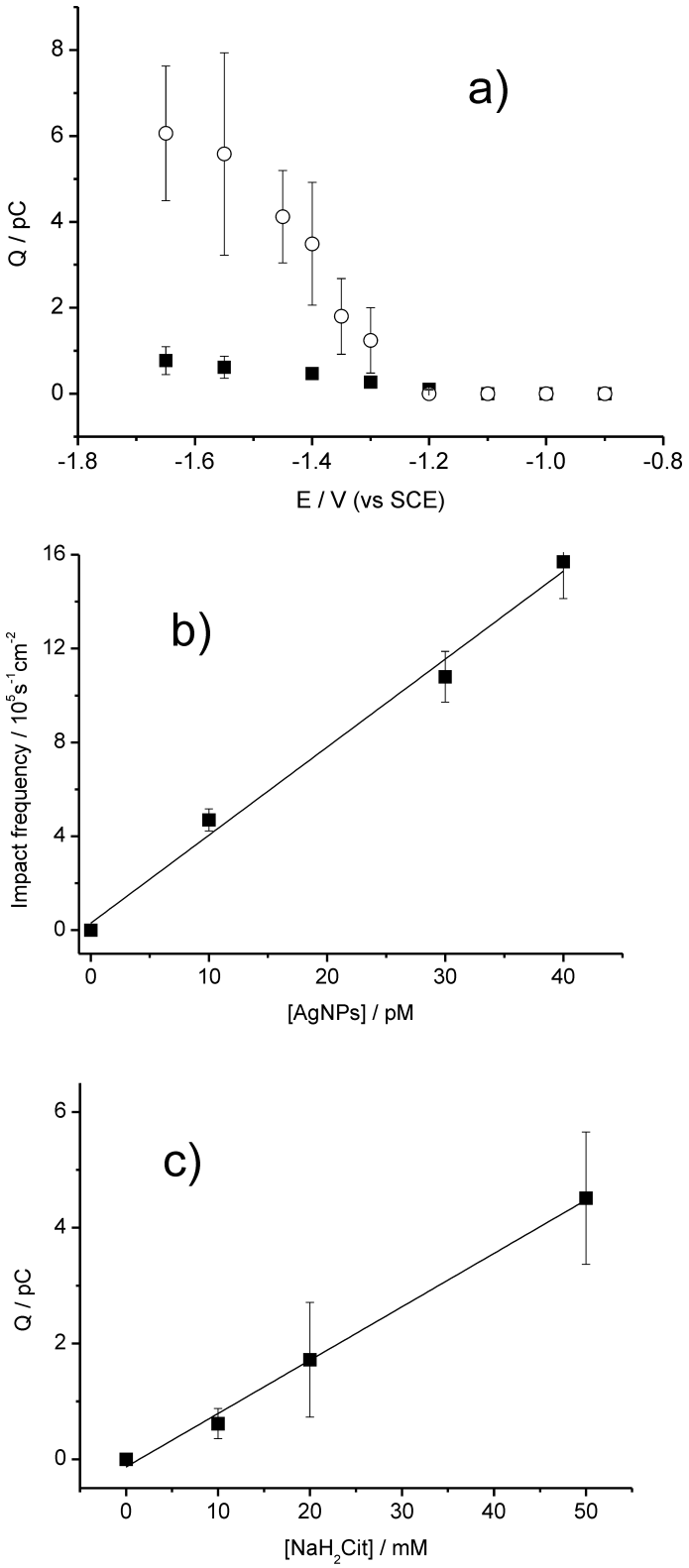

Figure 6.3: Plots the variation of: a) the charge passed, Q, during each spike with potential for 20-50 nm (■) and 80-120nm (○) AgNPs; (b) the frequency of spikes (F) as a function of number concentration of AgNPs; and (c) Q with citrate concentration.

where ρ is the bulk density, and A_r is the relative atomic mass. Figure 6.4c shows the distribution of radii obtained from the analysis of over 1500 impacts, which can be deconvoluted into sub-distributions of radii 13, 26, and 39 nm, corresponding to single NPs and agglomerates.

These results demonstrate that this method can be used as a means to identify AgNPs (via comparison of the onset potential of spikes and the known anodic stripping voltammetry of AgNPs) as well as simultaneously determining their size range by analysis of the charge passed per current spike.

6.4 Conclusions

In this work we have shown for the first time the quantitative detection and characterization of AgNPs in aqueous solution via nanoparticle-electrode collision process. The direct characterisation of gold and nickel NPs as well as the aggregation study using the same method is discussed in the following chapters.

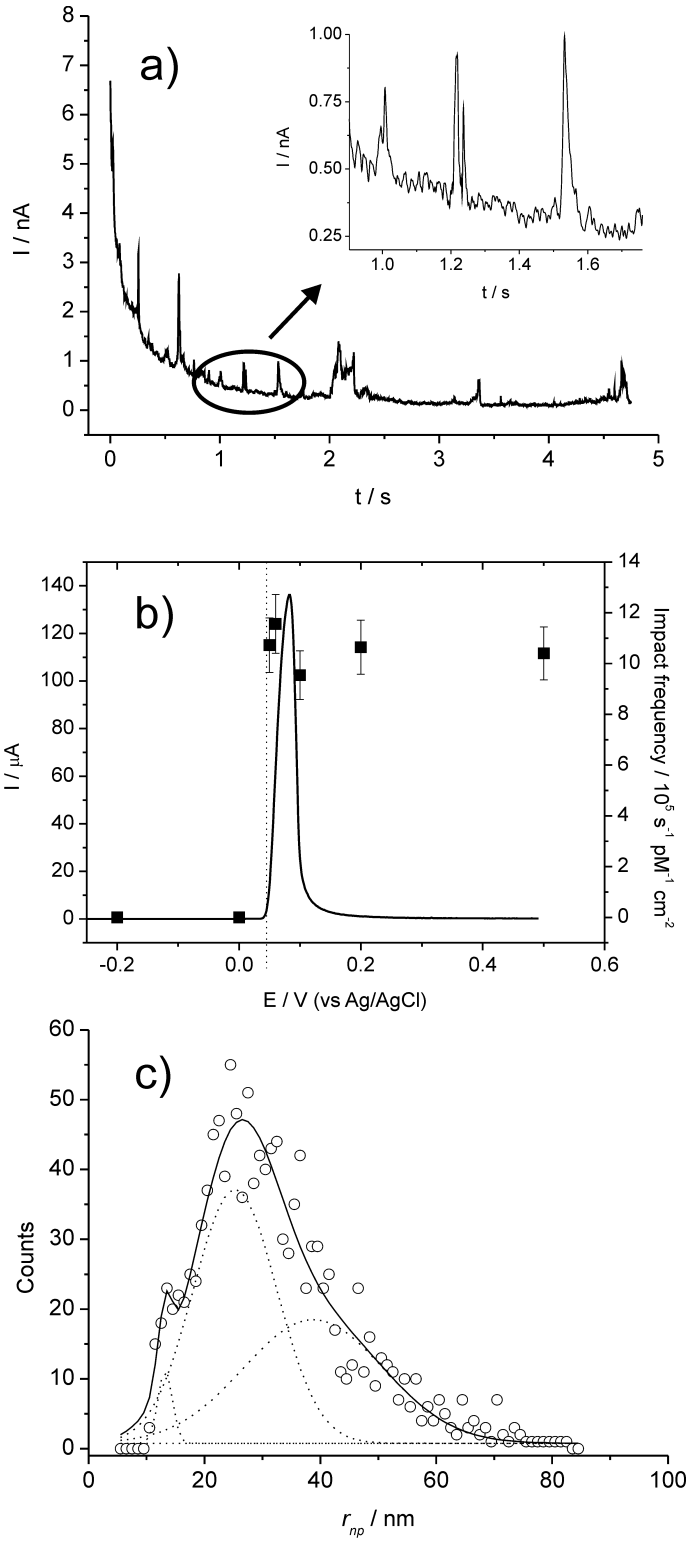

Figure 6.4: a) Chronoamperometric profiles showing oxidative faradaic collisions of Ag-NPs in citrate solution. Inset shows detailed impact spike. b) Overlay plot of stripping voltammogram for a AgNP-modified GC electrode (left axis) and the impact frequency (right axis) showing the onset potential of spikes; and c) distribution of NP radii inferred from Q via Eq.(2) with deconvolution.

Bibliography

[1] *Project on Emerging Nanotechnologies*. www.nanotechproject.org/news/archive/8277/.April 29, 2009, 2009.

[2] R. D. Handy, R. Owen, and E. Valsami-Jones. *Ecotoxicology*, 17:315, 2008.

[3] R. D. Handy, F. Von der Kammer, J. R. Lead amd M. Hassellöv, R. Owen, and M. Crane. *Ecotoxicology*, 17:287, 2008.

[4] X. Chen and H. Schluesener. *Toxicol. Lett.*, 176:1, 2008.

[5] T. M. Benn and P. Westerhoff. *Environ. Sci. Technol.*, 42:4133, 2008.

[6] J. Klein. *Proc. Natl. Acad. Sci. USA*, 104:2029, 2007.

[7] A. Hinther, S. Vawda, R. C. Skirrow, N. Veldhoen, P. Collins J. T. Cullen, G. van Aggelen, and C. C. Helbing. *Environ. Sci. Technol.*, 44:8314, 2010.

[8] M. Ahamed, M. S. Alsalhi, and M. K. J. Siddiqui. *Clin. Chim. Acta*, 411:1841, 2010.

[9] S. A. Blaser amd M. Scheringer, M. Macleod, and K. Hungerbühler. *Sci. Total Environ.*, 390:396, 2008.

[10] H. Weinberg, A. Galyean, and M. Leopold. *TrAC Trends Anal. Chem.*, 30:72, 2011.

[11] M. Heyrovský, J. Jirkovský, and B. R. Müller. *Langmuir*, 11:4293, 1995.

[12] M. Heyrovský, J. Jirkovský, and M. Struplova-Bartackova. *Langmuir*, 11:4300, 1995.

[13] M. Heyrovský, J. Jirkovský, and M. Struplova-Bartackova. *Langmuir*, 11:4309, 1995.

[14] I. D. Charlton and A. P. Doherty. *J. Phys. Chem. B*, 104:8061, 2000.

[15] I. D. Charlton and A. P. Doherty. *Anal. Chem.*, 72:687, 2000.

[16] D. Hellberg, F. Scholz, F. Schauer, and W. Weitschies. *Electrochem. Commun.*, 4:305, 2002.

[17] F. Scholz, D. Hellberg, F. Harnisch, A. Hummel, and U. Hasse. *Electrochem. Commun.*, 6:924, 2004.

[18] D. Hellberg, F. Scholz, F. Schubert, M. Lovric, D. Omanovic, V. A. Hernandez, and R. Thede. *J. Phys. Chem. B*, 109:14715, 2005.

[19] C. E. Banks, N. V. Rees, and R. G. Compton. *J. Electroanal. Chem.*, 535:41, 2002.

[20] C. E. Banks, N. V. Rees, and R. G. Compton. *J. Phys. Chem. B*, 106:5810, 2002.

[21] N. V. Rees, C. E. Banks, and R. G. Compton. *J. Phys. Chem. B*, 108:18391, 2004.

[22] N. V. Rees and R. G. Compton. *Analyst*, 132:635, 2007.

[23] A. D. Clegg, N. V. Rees, C. E. Banks, and R. G. Compton. *ChemPhysChem*, 7:807, 2006.

[24] X. Xiao, S. Pan, J. S. Jang, F. R. F. Fan, and A. J. Bard. *J. Phys. Chem. C*, 113:14978, 2009.

[25] X. Xiao and A. J. Bard. *J. Am. Chem. Soc.*, 129:9610, 2007.

[26] A. J. Bard, H. Zhou, and S. J. Kwon. *Isr. J. Chem.*, 50:267, 2010.

[27] S. J. Kwon, F. R. F. Fan, and A. J. Bard. *J. Am. Chem. Soc.*, 132:13165, 2010.

[28] X. Xiao, F. R. F. Fan, J. Zhou, and A. J. Bard. *J. Am. Chem. Soc.*, 130:16669, 2008.

[29] F. W. Campbell, S. R. Belding, R. Baron, L. Xiao, and R. G. Compton. *J. Phys. Chem. C*, 113:9053, 2009.

[30] A. Pyatenko, M. Yamaguchi, and M. Suzuki. *J. Phys. Chem. C*, 111:7910, 2007.

[31] A. Pyatenko, M. Yamaguchi, and M. Suzuki. *J. Phys. Chem. B*, 109:21608, 2005.

Chapter 7

The aggregation of silver nanoparticles in aqueous solution investigated via Anodic Particle Coulometry (APC)

The previous chapter has showed the use of anodic particle coulometry (APC) method for the direct detection and sizing of AgNPs in aqueous solution. In this chapter we extend this theme to monitor the aggregation of AgNPs over time, and identify stable clusters. We also demonstrate that AgNPs can be quantitatively measured by APC up to a size of at least 150nm in diameter.

This work was carried out in cooperation with Dr. Neil V. Rees, and has been published in *ChemPhysChem*, 2011, 12, 1645.

7.1 Introduction

The rapid rise in the use of nanoparticles (NPs) has caused an increased awareness of their hazardous potential, as they are inevitably released either by intention, during manufacture or disposal [1, 2]. With a lack of general strategies for the detection and characterisation of metal NPs [3], we have recently reported the Anodic Particle Coulometry (APC) method based on faradaic charge transfer during NP collisions with electrode surfaces [4].

The impacts between particles and electrode surfaces have been measured for some years [5–12], most notably through non-faradaic charge transfer transients [13–17]. Recently, electrocatalytic processes occurring on the surface of NPs during collisions have been noted [18–21]. We have introduced APC based on the quantitative and exhaustive electro-oxidation of AgNPs at an electrode: capable of providing detection, characterisation, and identification of AgNPs [4].

$$\mathrm{Ag(NP)} - \mathrm{e^-} \rightarrow \mathrm{Ag^+(aq)} \tag{7.1}$$

In this chapter, we use APC to monitor the aggregation of AgNPs over time, and identifying stable clusters. We also demonstrate that AgNPs can be quantitatively measured by APC up to a size of at least 150nm in diameter.

7.2 Experimental

AgNPs of three different diameter ranges (referred to as samples A, B, and C respectively) were synthesised according to the method of Pyatenko *et al*. [22–24], and characterised via SEM imaging to have mean radii of 14 ± 2 nm (A), 29 ± 2 (B), and 45 ± 3 nm (C). AgNPs were dispersed by ultrasound prior to adding to the solution. Sodium dihydrogen citrate $NaC_6O_7H_7$, Aldrich, >99.5%) and KCl (Riedel-de-Haan, >99.5%) were used as received. All solutions (10 mM $NaC_6O_7H_7$ and 90 mM KCl) were made using ultrapure water of resistivity ~ 18.2 MΩcm (Millipore) and degassed thoroughly with N_2 (oxygen

free, BOC Gases plc) and an atmosphere of N_2 maintained during the experiment. Experiments were conducted within a faraday cage using a μAutolab III potentiostat with a time resolution shorter than 0.1 ms (Metrohm-Autolab BV, Utrecht, Netherlands) and three-electrode arrangement: a 11 μm radius glassy carbon (GC) working electrode (BASi Inc), a graphite counter electrode, and a Ag/AgCl reference electrode (Radiometer, Copenhagen). Impact spikes were analysed using Origin v.8.1 (www.OriginLab.com) for spike identification and integration, electrical noise reduction and Gaussian deconvolution of size distributions [4].

7.3 Results and Discussion

The glassy carbon (GC) microelectrode was placed in degassed citrate solution and a known concentration of sample A pre-dispersed AgNPs added. After a period of 10 minutes post-dispersion, the solution was agitated by bubbling with N_2, the electrode potential held at +0.5 V (relative to Ag/AgCl) and oxidative impact transients recorded (the oxidation of bulk Ag occurs at +0.05 V vs Ag/AgCl [4]. Several hundred impact transients were recorded for analysis. This procedure was repeated at defined times of 19, 28, 35, 60, 90, and 120 minutes after the AgNPs had been dispersed.

The analysis of data was as previously described [4]. The charge passed per impact transient, Q, is related to the number of atoms in the cluster, N, via the electronic charge according to

$$Q = eN \tag{7.2}$$

It can be useful to make a spherical approximation for the NP cluster (radius R), which in general is comprised of n individual NPs of mean radius r, we can see that the charge passed per spike, Q is

$$Q = \frac{4F\pi\rho R^3}{3A_r} \tag{7.3}$$

with

$$n = \left(\frac{R}{r}\right)^3 \tag{7.4}$$

where F is the Faraday constant, ρ is the density of the NP (assumed that of the bulk material), and Ar the relative atomic mass.

Figure 7.1 shows some typical NP cluster distributions obtained from these experiments, illustrating the deconvolution into sub-distributions. The distribution obtained after 10 minutes shows contributions from a wide range of cluster sizes: with particularly significant contributions from those with mean radii of 13, 21, and 27 nm. As time progresses, the contributions from larger clusters become more apparent, as the overall mean radius, R_{mean}, of the cluster increases (shown in Figure 7.2a).

Figure 7.2b shows the time-evolution of each of the principal cluster sizes identified. Based on a minimum cluster radius R of 13nm, and supported by SEM data (see Experimental), we postulate that this corresponds to a single AgNP. Using equation (7.3), we note that the cluster radii detected in Figure 7.1 of R = 13, 21, 27, 39, and 52 nm correspond to cluster numbers, n = 1, 4, 8, 27, and 64 respectively. In turn we speculate that these particular clusters are observed due to the stability of the likely geometries implied by these cluster numbers (i.e. tetrahedral or cubic) [25]. In principle, such data may be useful in investigating the kinetics of aggregation, as for example, the depletion of single AgNPs follows a second-order process with a rate constant of approximately 6×10^{-3} pM^{-1} s^{-1}.

$$(AgNP)_1 + (AgNP)_1 \rightarrow (AgNP)_2 \tag{7.5}$$

As part of this study, it was necessary to determine whether there was an upper limit to the mean cluster size reliably undergoing exhaustive oxidation during collisions. By

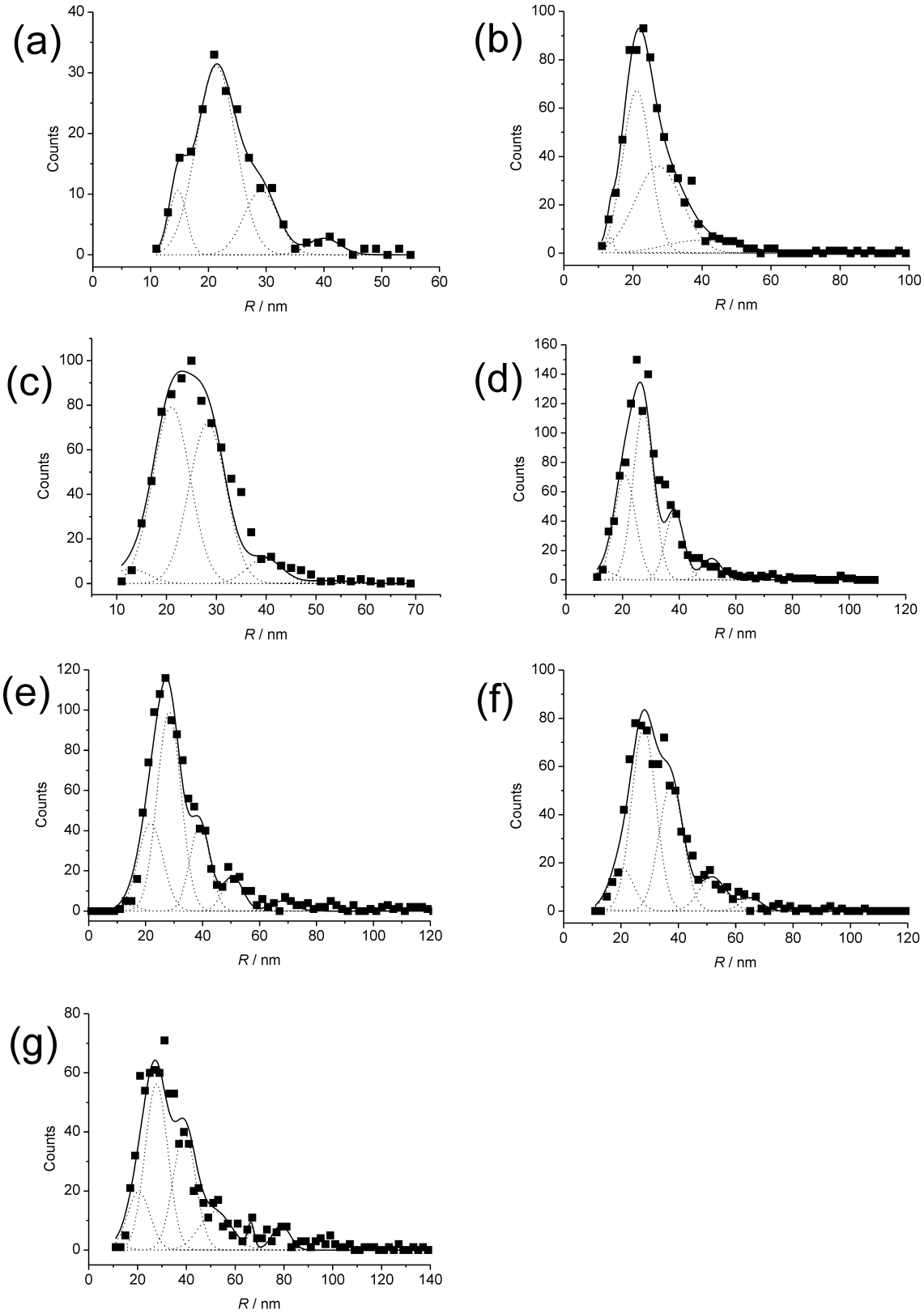

Figure 7.1: APC distributions of AgNPs (sample A) recorded at the following times (in minutes) following dispersion: (a) 10, (b) 19, (c) 28, (d) 35, (e) 60, (f) 90, and (g) 120.

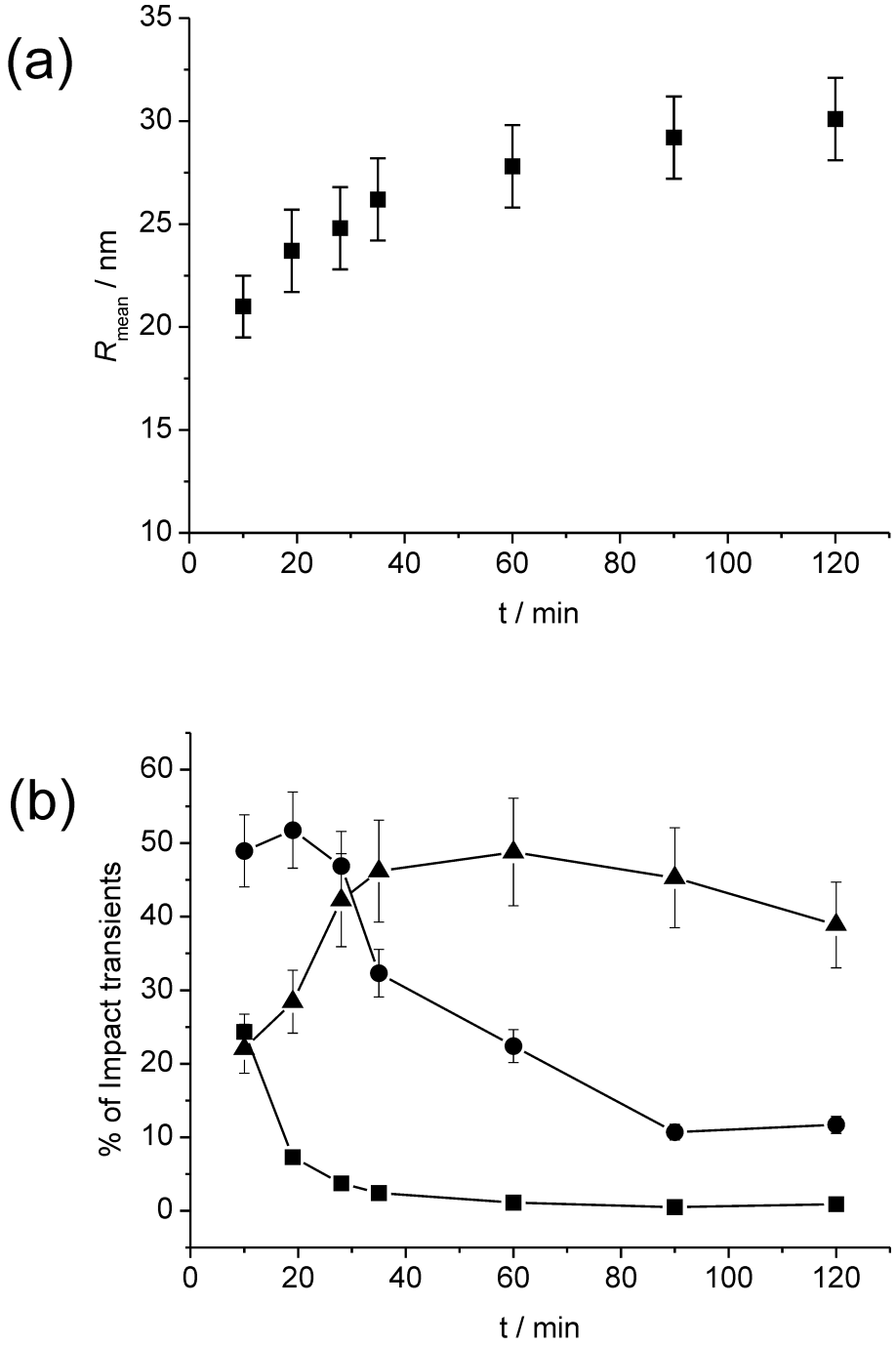

Figure 7.2: Plots showing the time evolution of the AgNP aggregates as (a) the mean cluster radius, R_{mean}, and (b) the individual clusters. The symbols used in (b) correspond to the following cluster sizes (n): 1 (■), 4(●), and 8(▲).

conducting APC experiments on AgNP samples B and C at a time of 20-30 mins post-dispersion, Figure 7.3 shows overlaid SEM and APC distributions for these samples. In Figure 7.3a, the APC data suggests that clusters of radii 28 and 56 nm (n = 1 and 8 respectively) are readily identifiable in good agreement with the SEM data suggesting a mean AgNP radius of 29 nm. Figure 7.3b shows analogous data for sample C, where the APC distribution suggests clusters of radii 43, 68, and 86 nm (n = 1, 4 and 8), against an SEM result of AgNP mean radius of 45 nm. In addition, the APC data (see Figure 7.1) clearly indicates that clusters considerably greater than 50 nm radius are detectable, and we therefore conclude that the APC method can be reliably and quantitatively used for NPs of diameters up to and including 150 nm (ca. 10^8 atoms).

7.4 Conclusions

The APC method has been shown to be reliable in sizing AgNPs to mean radii of 28 and 43 nm in excellent agreement with SEM measurements. The aggregation of AgNPs can be clearly observed and monitored, with some clusters identifiable.

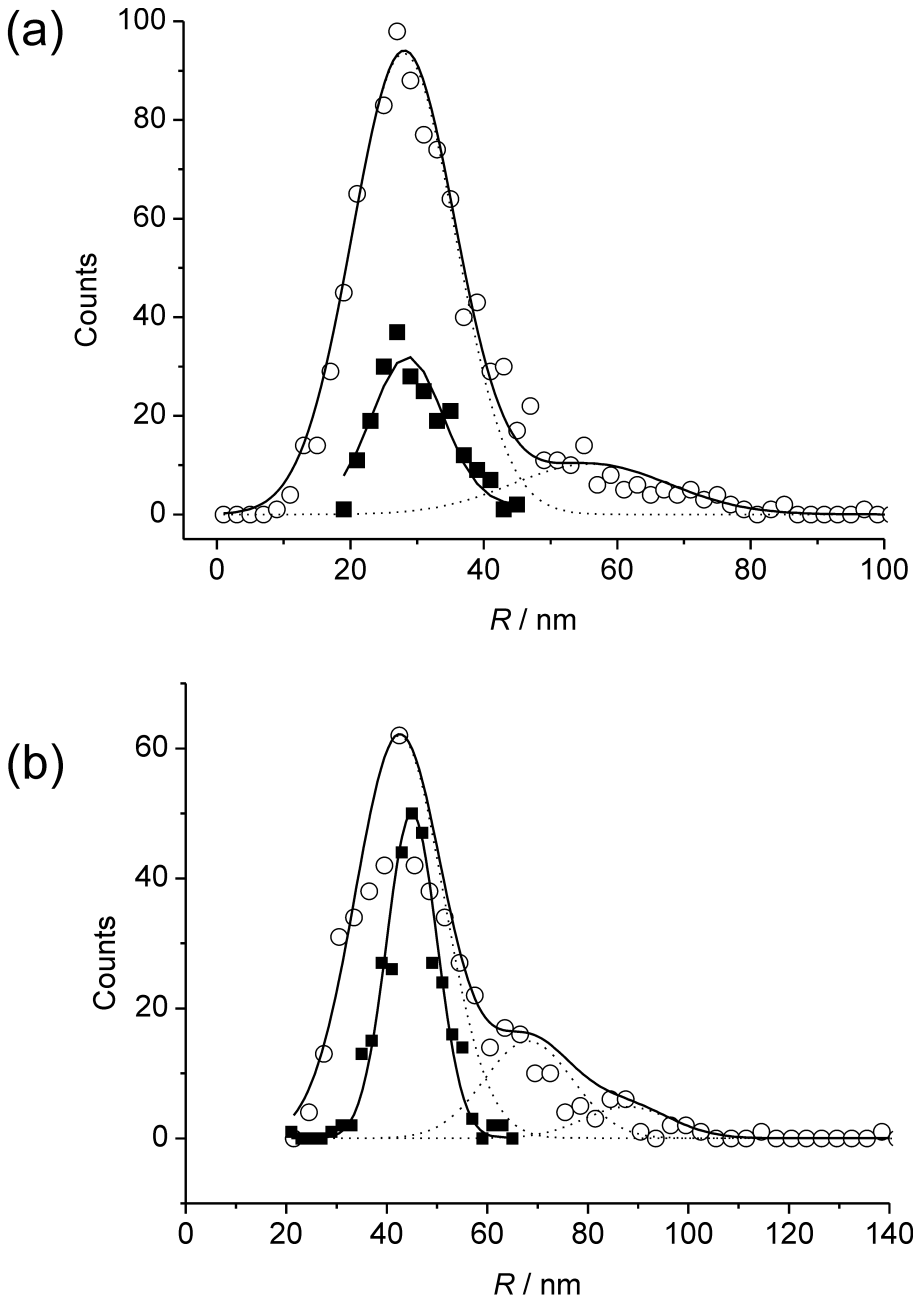

Figure 7.3: Comparison of APC (○) and SEM (■) distributions for (a) sample B, and (b) sample C of AgNPs.

Bibliography

[1] R. D. Handy, R. Owen, and E. Valsami-Jones. *Ecotoxicology*, 17:315, 2008.

[2] R. D. Handy, F. Von der Kammer, J. R. Lead, M. Hassellov, R. Owen, and M. Crane. *Ecotoxicology*, 17:287.

[3] H. Weinberg, A. Galyean, and M. Leopold. *TrAC Trends Anal. Chem.*, 30:72, 2001.

[4] Y. G. Zhou, N. V. Rees, and R. G. Compton. *Angew. Chem., Int. Ed.*, 50:4219, 2011.

[5] M. Heyrovský, J. Jirkovský, and B. R. Müller. *Langmuir*, 11:4293, 1995.

[6] M. Heyrovský, J. Jirkovský, and M. Struplova-Bartackova. *Langmuir*, 11:4300, 1995.

[7] M. Heyrovský, J. Jirkovský, and M. Struplova-Bartackova. *Langmuir*, 11:4309, 1995.

[8] I. D. Charlton and A. P. Doherty. *Anal. Chem.*, 72:687, 2000.

[9] I. D. Charlton and A. P. Doherty. *Anal. Chem.*, 72:687, 2000.

[10] D. Hellberg, F. Scholz, F. Schauer, and W. Weitschies. *Electrochem. Commun.*, 4:305, 2002.

[11] F. Scholz, D. Hellberg, F. Harnisch, A. Hummel, and U. Hasse. *Electrochem. Commun.*, 6:929, 2004.

[12] D. Hellberg, F. Scholz, F. Schubert, M. Lovric, D. Omanovic, V. A. Hernandez, and R. Thede. *J. Phys. Chem. B*, 109:14715, 2005.

[13] C. E. Banks, N. V. Rees, and R. G. Compton. *J. Phys. Chem. B*, 535:41, 2002.

[14] C. E. Banks, N. V. Rees, and R. G. Compton. *J. Phys. Chem. B*, 106:5810, 2002.

[15] N. V. Rees and R. G. Compton. *Analyst*, 132:635, 2007.

[16] N. V. Rees, C. E. Banks, and R. G. Compton. *J. Phys. Chem. B*, 108:18391, 2004.

[17] A. D. Clegg, N. V. Rees, C. E. Banks, and R. G. Compton. *ChemPhysChem*, 7:807, 2006.

[18] X. Xiao, S. Pan, J. S. Jang, F. R. F. Fan, and A. J. Bard. *J. Phys. Chem. C*, 113:14978, 2009.

[19] X. Xiao and A. J. Bard. *J. Am. Chem. Soc.*, 129:9610, 2007.

[20] S. J. Kwon, F. R. F. Fan, and A. J. Bard. *J. Am. Chem. Soc.*, 132:13165, 2010.

[21] X. Xiao, F. R. F. Fan, J. Zhou, and A. J. Bard. *J. Am. Chem. Soc.*, 130:16669, 2008.

[22] A. Pyatenko, M. Yamaguchi, and M. Suzuki. *J. Phys. Chem. C*, 111:7910, 2007.

[23] A. Pyatenko, M. Yamaguchi, and M. Suzuki. *J. Phys. Chem. B*, 109:21608, 2005.

[24] F. W. Campbell, S. R. Belding, R. Baron, L. Xiao, and R. G. Compton. *J. Phys. Chem. C*, 113:9053, 2009.

[25] L. F. Pease III, D. H. Tsai, J. L. Hertz, R. S. Zangmeister, M. R. Zachariah, and M. J. Tarlov. *Langmuir*, 26:11384, 2010.

Chapter 8

Gold nanoparticles show electroactivity: the counting and sorting of nanoparticles upon impact with electrodes

The previous two chapters describe the application of anodic particle coulometry (APC) to characterise of AgNPs and to monitor AgNPs aggregation. In this chapter, we extend the APC method for the detection and characterisation AuNPs. AuNPs in aqueous 0.10 M HCl are shown to be electroactive at oxidising potentials greater than 1.0V (vs Ag/AgCl) by means of the voltammetric monitoring of AuNP-electrode collisions.

This work was carried out in cooperation with Dr. Neil V. Rees and Mintek (Randburg, South Africa), and has been published in *Chemical Communications*, 2012, 48, 224.

8.1 Introduction

Gold nanoparticles (AuNPs) have been extensively studied in recent years for many applications ranging from electrocatalysis, electroanalysis, in-situ surface spectroscopies, as substrates for modification, *etc*. [1, 2]. The changed catalytic behaviour of gold at the nanoscale has been demonstrated, for example in the hydrochlorination of acetylene, the low-temperature oxidation of CO on nanogold, nucleophilic addition to acetylenes, selective hydrogenation of N-O bonds, the oxidation of alcohols to aldehydes and acids, and the direct formation of hydrogen peroxide [3–9]. The electrochemical properties and uses of AuNPs have been extensively studied, for example, the kinetics of the electro-reductions of oxygen and hydrogen peroxide on AuNPs have been reported [10–12], as well as their use in investigating long-range electron transfer [13] and the ability of AuNPs to cross cellular membranes [14–16].

However, despite their ubiquity in nanoparticulate research, AuNPs have in general proved to be difficult to directly analyse and characterise using simple methods [17, 18].

Anodic coulometry has recently been applied to the impacts of silver nanoparticles (AgNPs) with inert, glassy carbon electrodes through anodic particle coulometry (APC). In those experiments the impacts of individual nanoparticles were detected as short-duration current transients, which allowed the identification, characterisation, and even aggregation of the AgNPs to be determined [19–21]. Similar transient signals have been used to follow electrocatalytic reactions on NPs [22–25], and even mitochondria [26]. In this chapter, we report the use of APC to monitor collisions of AuNPs with carbon electrodes as a general means to identify and characterise AuNPs.

8.2 Experimental

Citrate-capped AuNPs from Mintek (Randburg, South Africa) were characterised via SEM imaging to have mean radii of 10 ± 2 nm. Hydrochloric acid (HCl, Sigma-Aldrich,

37%, AR) and nitric acid (HNO_3, Aldrich, 70%, AR) were used as received. All solutions (0.1 M HCl and 0.1 M HNO_3) were made using ultrapure water of resistivity ~ 18.2 MΩcm at 298K (Millipore). Experiments were conducted within a faraday cage using a μAutolab III (Metrohm-Autolab BV, Utrecht, Netherlands) and a 3-electrode arrangement: a glassy carbon (GC) macroelectrode (3 mm diameter) and carbon microelectrode (11 μm diameter) as working electrodes, Ag/AgCl as reference (Radiometer, Copenhagen), and a graphite rod as counter. To modify the GC electrode, 2 μL of the suspension of AuNPs was drop-cast on the GC electrode and left to dry under a gentle N_2 atmosphere. The concentration of the AuNP suspension was determined to be 5.1×10^{14} particles dm^{-3} from the UV-vis absorption spectrum, using the literature extinction coefficient value of 8.8×10^8 mol^{-1} cm^2 for citrate-capped AuNPs of diameter 20 nm [27].

8.3 Results and Discussion

Cyclic voltammograms (CVs) were recorded for a GC macroelectrode modified with AuNPs immersed in 0.10 M HNO_3, yielding a broad, ill-defined oxidation feature associated with gold oxide formation and a sharp oxide-reduction peak as shown in Figure 8.1 The charge associated with the oxidation of the AuNPs was obtained by integrating the reduction peak of the corresponding gold oxide. As only passivation occurs to gold in HNO_3 solution [28] and a monolayer film of gold oxide is reportedly formed under such conditions [29,30], we calculate the number of electrons transferred per surface gold atom from Figure 8.1b to be 1.6 ± 0.1, indicating that a mixed gold oxide of Au (I) and Au (III) has formed, in accordance with the literature [31–38].

The anodic oxidation of gold in acidic media results in the formation of gold oxide layers on the electrode surface, with thicknesses varying from a mono- to multilayers [31–33]. Au_2O_3, AuOOH and $Au(OH)_3$ are known to be chemically stable compounds [33], which may be formed via precursors consisting of dipolar species $Au^{\delta+}{\cdot}OH^{\delta-}$ (formally Au(I) oxide) on gold surfaces [34, 35]. Despite some claims to the contrary

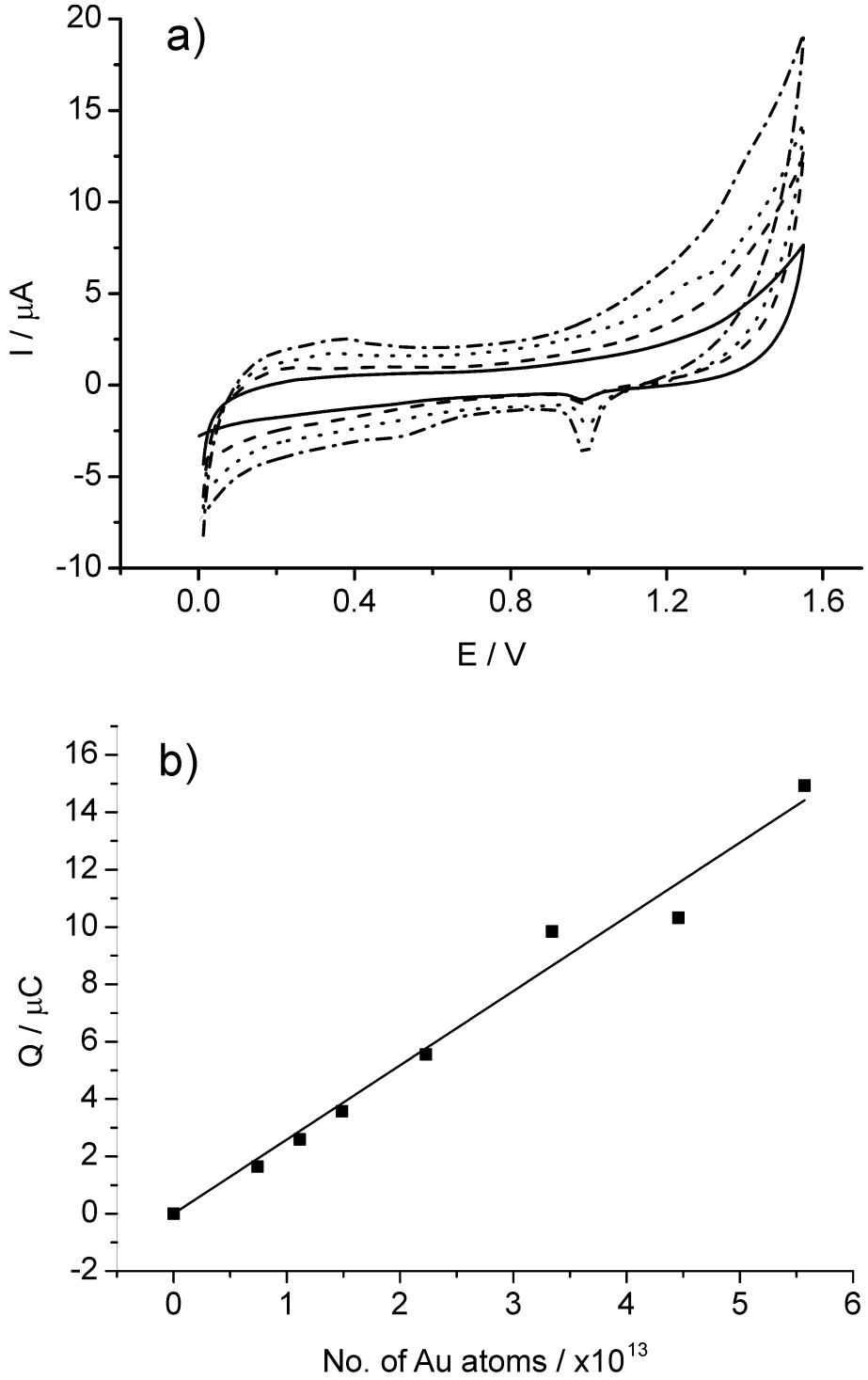

Figure 8.1: a) CVs of a AuNP-modified GC electrode in 0.10 M HNO_3 at a scan rate of 20 mV s^{-1} with different gold atom loadings of: 8.25×10^{13} (dotted line); 1.23×10^{14} (dashed line); 2.47×10^{14} (dotted line); and 4.94×10^{14} (dash-dotted line). b) Plot of charge passed per cathodic peak versus number of surface gold atoms.

[32,36,37], Au(II) oxide is widely regarded as non-existent and the apparent stoichiometries of surface gold oxides between 1 and 3 are generally accepted to be due to mixed oxide phases of Au(I) and Au(III) [38] (see equation 8.1).

$$\begin{aligned} Au + H_2O &\rightarrow Au^{\delta+} \cdot OH^{\delta-} + H^+ + e^- \\ 2Au + 3H_2O &\rightarrow Au_2O_3 + 6H^+ + 6e^- \end{aligned} \tag{8.1}$$

Next, we scanned a AuNP-modified GC macroelectrode in 0.10 M HCl, obtaining a well-defined stripping peak at *ca.* +1.0 V and a considerably smaller reductive wave (see Figure 8.2). By varying the gold loadings on the GC surface, the anodic peak charge (obtained from the integration of the peak area) increases linearly as plotted in Figure 8.2. The gradient of this plot indicates that 1.9 ± 0.1 electrons are transferred per Au atom. The electrochemistry of gold in aqueous solutions in the presence of complex-forming anions has been studied, and chloride found to facilitate its electrodissolution via formation of $AuCl_2^-$ and $AuCl_4^-$ complex ions, with the latter species predominating [39–41], involving the following two equilibria:

$$\begin{aligned} Au + 4Cl^- &\rightleftharpoons AuCl_4^- + 3e^- \\ AuCl_4^- + 2Au + 2Cl^- &\rightleftharpoons 3AuCl_2^- \end{aligned} \tag{8.2}$$

We therefore suggest that the majority of the oxidative signal is due to the dissolution of gold in the form of $AuCl_2^-$ and $AuCl_4^-$ complexes. Repeated voltammetric scans show a rapid decay of both anodic and cathodic peaks (see Figure 8.3). The position of the cathodic (reductive) peak is indicative of the reduction of a Au(III) species [42], and we propose that it is most likely a surface oxide. The understanding of the anodic behaviour of AuNPs in HCl enables us to explore the electro-oxidation of single AuNPs in the same media via the anodic particle coulometry (APC) method through nanoparticle-electrode collisions. In this work, a radius 11 μm GC microelectrode was placed in 0.10 M HCl solution and a known concentration of pre-dispersed AuNPs added.

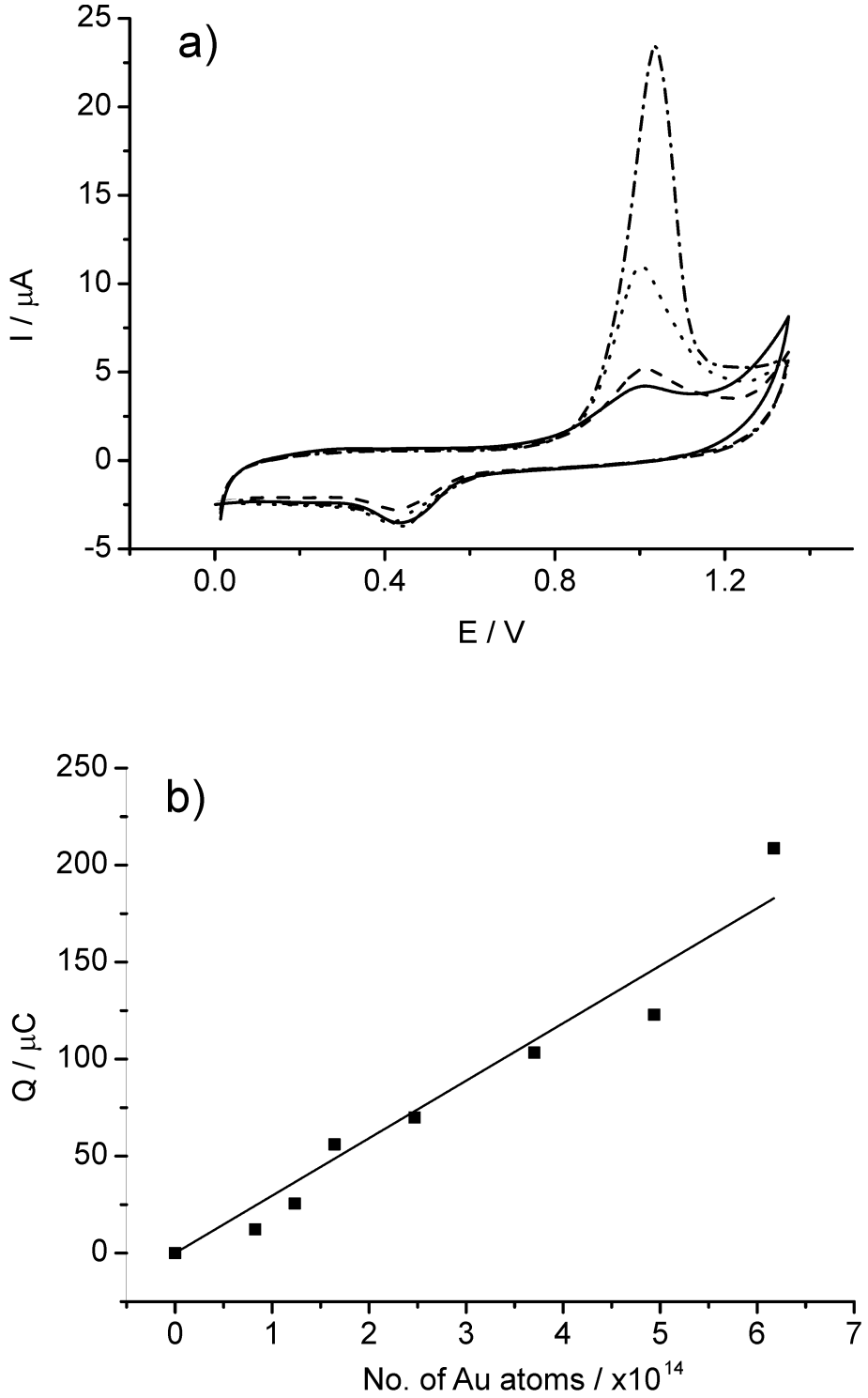

Figure 8.2: a) CVs of a AuNPs modified GC electrode in 0.10 M HCl at a scan rate of 20 mV s^{-1} with different Au atom loadings of (all $\times 10^{14}$): 0.83 (dotted line), 1.23 (dashed line), 2.47 (dotted line), and 4.94 (dash-dotted line). b) Plot of charge passed per anodic peak vs. different Au loadings.

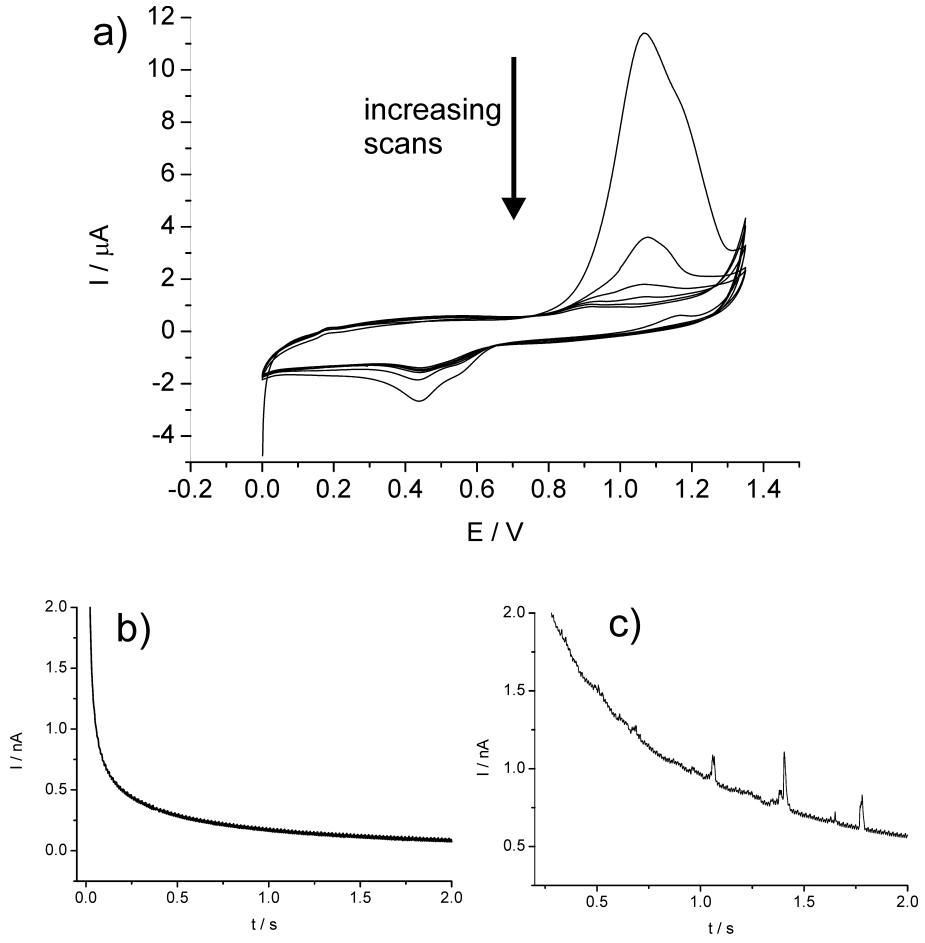

Figure 8.3: a)Repeat CVs showing the first 6 scans of a AuNP-modified GC electrode in 0.10 M HCl. Chronoamperometric profiles showing oxidative Faradaic transients of AuNPs at potentials of (b) 0.8 V and (c) 1.1 V

The electrode potential was held at a series of potentials between 0.8 V and 1.3 V with a sample time of 0.5 ms. Impact transients were not observed at potentials less than +1.0 V, but were recorded above this threshold potential, as shown in Fig 8.4a. The spike frequency was found to be in the range expected for thermally-driven collisions from previous work [19–21].

The APC method is therefore capable of identifying AuNPs in this medium, by virtue of the clear threshold potential for the onset of impact transients and its coincidence with the oxidation peak in the stripping voltammetry. Results for the use of APC in sizing AuNPs in the same way as has been reported for AgNPs [19,20] has been given in figures 8.4b and 8.4c: good agreement is found with the size of single AuNPs (10.5 ± 1.0 nm), it is also clear that aggregation of AuNPs into clusters (particularly containing 2, 4, 8 NPs) occurs on the experimental timescale in a similar way to that found for AgNPs [20].

8.4 Conclusions

In this work AuNPs have been shown to be detected by using the APC method to monitor impacts between NPs and electrodes. Sizing and aggregation information has been demonstrated to be measurable.

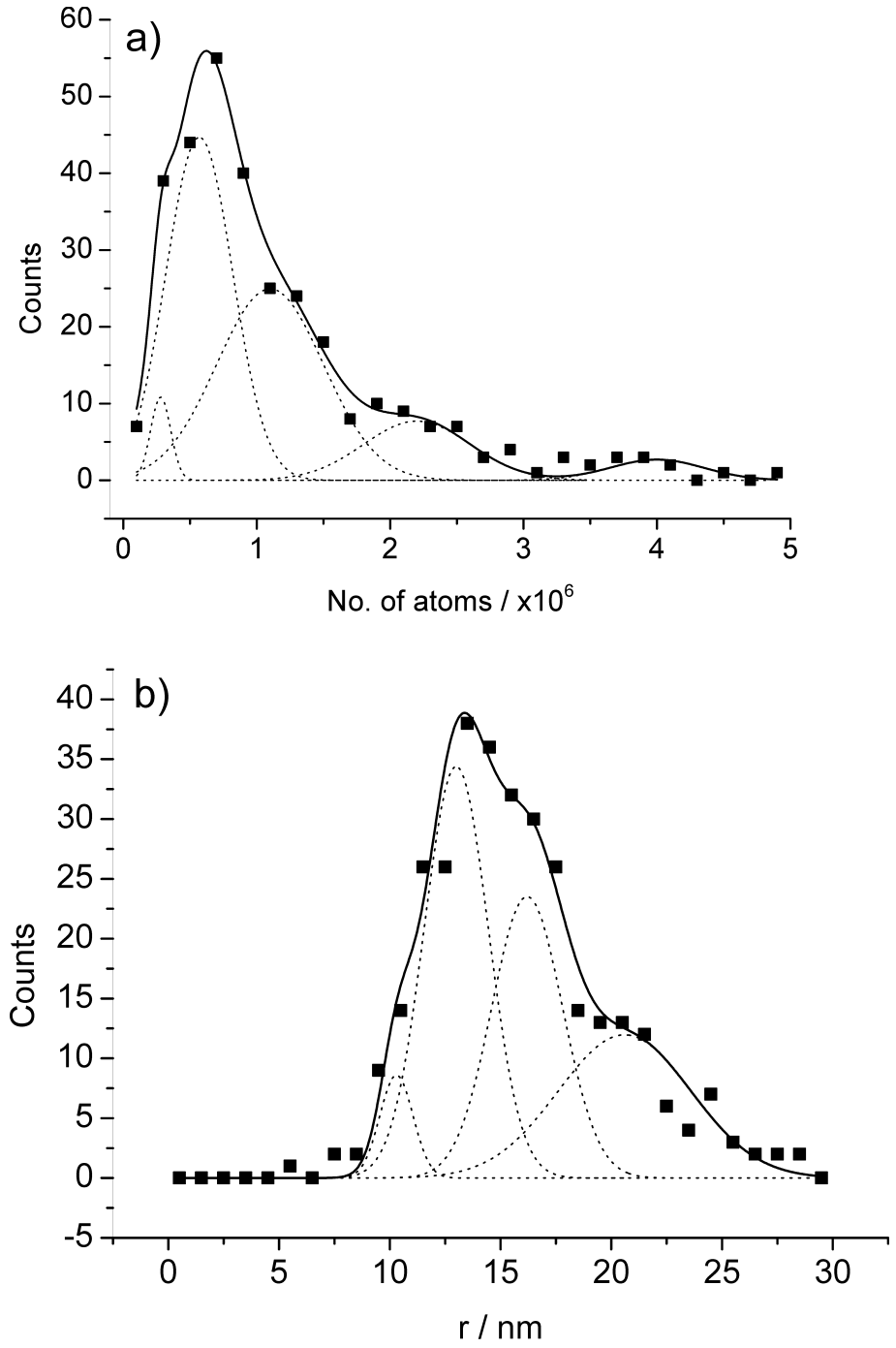

Figure 8.4: APC distributions for the AuNP impact experiments held at a potential of +1.1 V displayed in terms of (a) no. of atoms oxidised, and (b) the inferred NP size.

Bibliography

[1] G. J. Hutchings, M. Brust, and H. Schmidbaur. *Chem. Soc. Rev.*, 37:1759, 2008.

[2] D. Bethell, D. J. Schiffrin, and M. Brust. *Chem. Commun.*, 7:801, 1994.

[3] G. J. Hutchings. *J. Catal.*, 96:292, 1985.

[4] M. Haruta, T. Kobayashi, H. Sano, and N. Yamada. *Chem. Lett.*, 2:405, 1987.

[5] J. H. Teles, S. Brode, and M. Chabanas. *Angew. Chem., Int. Ed.*, 37:1415, 1998.

[6] A. Corma and P. Serna. *Science*, 313:332, 2006.

[7] L. Prati and M. Rossi. *J. Catal.*, 176:552, 1998.

[8] A. Abad, P. Concepcion, A. Corma, and H. Garcia. *Angew. Chem., Int. Ed.*, 44:4066, 2005.

[9] P. Landon, J. Ferguson, B. E. Solsona, T. Garcia, A. F. Carley, A. A. Herzing, C. J. Kiely, S. E. Golunski, and G. J. Hutchings. *Chem. Commun.*, 24:3385, 2005.

[10] F. Mirkhalaf and D. J. Schiffrin. *Langmuir*, 26:14995, 2010.

[11] J. S. Jirkovsky, M. Halasa, and D. J. Schiffrin. *Phys. Chem. Chem. Phys.*, 12:8042, 2010.

[12] F. Mirkhalaf, K. Tammeveski, and D. J. Schiffrin. *Phys. Chem. Chem. Phys.*, 11:3463, 2009.

[13] P. S. Jensen, Q. Chi, F. B. Grumsen, J. M. Abad, A. Horsewell, D. J. Schiffrin, and J. Ulstrup. *J. Phys. Chem. C*, 111:6124, 2007.

[14] Z. Krpetic, P. Nativo, I. A. Prior, and M. Brust. *Small*, 7:1982, 2001.

[15] Z. Krpetic, S. Saleemi, I. A. Prior, V. See, R. Qureshi, and M. Brust. *ACS Nano*, 5:5195, 2011.

[16] P. Nativo, I. A. Prior, and M. Brust. *ACS Nano*, 2:1639, 2008.

[17] M. Pumera, M. Aldavert, C. Mills, A. Merkoci, and A. Alegret. *Electrochim. Acta*, 50:3702, 2005.

[18] A. Bonanni, M. Pumera, and Y. Miyahara. *Phys. Chem. Chem. Phys.*, 13:4980, 2001.

[19] Y. G. Zhou, N. V. Rees, and R. G. Compton. *Angew. Chem., Int. Ed.*, 50:4219, 2011.

[20] N. V. Rees, Y. G. Zhou, and R. G. Compton. *ChemPhysChem*, 12:1645, 2011.

[21] Y. G. Zhou, N. V. Rees, and R. G. Compton. *ChemPhysChem*, 12:2085, 2011.

[22] X. Xiao, S. Pan, J. S. Jang, F. R. F. Fan, and A. J. Bard. *J. Phys. Chem. C*, 113:14978, 2009.

[23] X. Xiao and A. J. Bard. *J. Am. Chem. Soc.*, 129:9610, 2007.

[24] S. J. Kwon, F. R. F. Fan, and A. J. Bard. *J. Am. Chem. Soc.*, 132:13165, 2010.

[25] X. Xiao, F. R. F. Fan, J. Zhou, and A. J. Bard. *J. Am. Chem. Soc.*, 130:16669, 2008.

[26] M. Hermes, F. Scholz, C. Hardtner, R. Walther, L. Schild, C. Wolke, and U. Lendeckel. *Angew. Chem., Int. Ed.*, 50:6872, 2011.

[27] X. Liu, M. Atwater, J. Wang, and Q. Huo. *Colloids Surf., B*, 58:3, 2007.

[28] S. G. D. Shackleford, C. Boxall, S. N. Port, and R. J. Taylor. *J. Electroanal. Chem.*, 538:109, 2002.

[29] L. D. Burke and P. F. Nugent. *Gold Bull*, 30:43, 1997.

[30] L. D. Burke and M. E. G. Lyons. *Mordern Aspects of Electrochemistry*. Plenum, New York, 1986, vol. 18, P. 169.

[31] G. Tremiliosi-Filho, L. H. Dall'Antonia, and G. Jerkiewicz. *J. Electroanal. Chem.*, 578:1, 2005.

[32] H. Angerstein-Kozlowska, B. E. Conway, A. Hamelin, and L. Stoicoviciu. *Electrochim. Acta*, 31:1051, 1986.

[33] L. D. Burke, D. T. Buckley, and J. A. Morrissey. *Analyst*, 119:841, 1994.

[34] P. Kuhlkamp, H. G. Raubenheimer, J. S. Field, and M. S. Desmet. *J. Organomet. Chem.*, 552:69, 1998.

[35] U. Koelle and A. Lanuna. *Inorg. Chim. Acta*, 290:44, 1999.

[36] F. A. Cotton and G. Wilkinson. *Advanced Inorganic Chemistry, 5th edn*. Wiley, New York, 1988.

[37] J. Herrera Gallego, C. E. Castellana, A. J. Calandra, and A. J. Arvia. *J. Electroanal. Chem.*, 66:207, 1975.

[38] D. H. Evans and J. J. Lingane. *J. Electroanal. Chem.*, 4:173, 1964.

[39] A. Kolics, A. E. Thomas, and A. Wieckowski. *J. Chem. Soc., Faraday Trans.*, 92:3727, 1996.

[40] M. A. Dias, G. H. Kelsall, and N. J. Welham. *J. Electroanal. Chem.*, 361:25, 1993.

[41] B. S. Brook, M. I. Pozina, and E. I. Rozenfel'd. *Zh. Analit. Khim.*, 34:1095, 1979.

[42] A. M. Bond, S. Kratsis, S. Mitchell, and J. Mocak. *Analyst*, 122:1147, 1997.

Chapter 9

Determining unknown concentrations of nanoparticles: the particle-impact electrochemistry of nickel and silver

Another successful application of anodic particle coulometry (APC) method is shown in this chapter to characterise nickel NPs (NiNPs) and, for the first time, a mixture of nanoparticles: nickel and silver. In addition, we describe a novel method for the determination on unknown concentrations of nanoparticles by fitting with the integrated flux equation.

This work was carried out in cooperation with Dr. Neil V. Rees, and has been published in *RSC Advances*, 2012, 2, 6879.

9.1 Introduction

Metallic nanoparticles such as nickel are extensively studied in the areas of catalysis, sensing, and electronic applications. However, their interactions with biological systems as well as their environmental and health effects are largely ignored. A number of recent studies report the significant toxicity of metal nanoparticles, such as nickel (NiNPs) and silver (AgNPs) to human lung cells [1, 2], and a damaging effect on aquatic organisms [3]. Every year, a large amount of engineered metal NPs are released into global water systems raising concerns regarding the environment and public health. Therefore it is highly desirable to urgently develop new techniques to monitor metal NPs in aqueous solution, with a particular need for the characterisation of mixtures of NPs.

The electrochemistry of nanoparticles (NPs) during their collisions with electrodes is a rapidly developing field [4]. Recent advances include the utilisation of particle impacts to directly characterize and quantify a sample of AgNPs via the anodic particle coulometry (APC) method [5]: the extension of APC to characterising AuNPs [6] suggests that it may also provide a means for the detection of NiNPs. The electrochemical oxidation of nickel in both alkaline [7–9] and acidic solution [10, 11] has been well studied, as have NiNPs themselves [12, 13]. In alkaline media, the anodic behavior of nickel results in the production of NiO and $Ni(OH)_2$, while in acidic media, especially in concentrated solutions [11], nickel tends to be dissolved into solution and forms $Ni^{2+}(aq)$.

In this chapter, we report the sizing and quantification of NiNPs using the APC method in pH 2 solutions of perchloric acid and sodium perchlorate. In addition, we show for the first time the simultaneous detection of mixed metal NP system by monitoring the impact frequency as a function of potential using a model system of a AgNP/NiNP mixture. We also develop a reliable new method to determine the metal NP concentration in aqueous solution by fitting with the integrated flux equation, and demonstrate its use for NiNPs (which are not observed to aggregate over the timescale of the experiment).

9.2 Experimental

Nickel nanoparticles (NiNPs) of radii range 15-30 nm were purchased from Nanostructured & Amorphous Materials, Inc. (Houston, Texas, USA), and have a NiO shell of between 2-8 nm thick [14]. Citrate-capped AgNPs of mean radius 13 ± 2 nm were synthesized according to the method of Pyatenko *et al*. [15, 16]. NP sizes were confirmed via SEM imaging. Sodium perchlorate (≥98%, $NaClO_4$), sodium dihydrogen citrate ($NaC_6O_7H_7$, >99.5%),and potassium chloride (>99.5% Riedel-de-Haan) were supplied by Sigma-Aldrich and used as received. Perchloric acid (70%, $HClO_4$) was purchased from Fisher Chemicals. All solutions were made using ultrapure water of resistivity ~ 18.2 MΩcm at 298K (Millipore).

The electrochemistry experiments were conducted within a faraday cage using a μAutolab III (Metrohm-Autolab BV, Utrecht, Netherlands) and a three electrode arrangement. Working electrodes used were: a bare glassy carbon (GC, 3 mm in diameter) electrode, or a NiNPs-modified GC electrode, or 6.9 μm radius carbon fibre microelectrode (BASiInc, Stareton, Warks. UK). Ag/AgCl(saturated KCl) was used as reference electrodes (specified in text), and graphite rod as counter electrode. To modify the GC electrode, an aliquot of the suspension of NiNPs was drop-cast on the GC electrode and left to dry under a gentle argon atmosphere. To avoid the aerial oxidation of NiNPs, they were handled in an argon atmosphere at all stages: from transfer out of the sealed sample provided by the supplier, to suspension in deaerated aqueous solution. All experiments were conducted under an argon atmosphere. Spike analysis and fitting was performed using Origin v.8.5 (Microcal Inc).

9.3 Results and Discussion

9.3.1 The particle-impact voltammetry of NiNPs

Voltammograms were recorded for a bare GC electrode and the same GC electrode modified with NiNPs in a solution of 10 mM $HClO_4$ and 100 mM $NaClO_4$, shown in Figure 9.1. At a ding to the oxidation of carbon surface. At NiNPs modified GC electrodes, there are no oxidative features until the onset of anodic dissolution at 1.4 V (vs. Ag/AgCl) which is consistent with the presence of the layer of surface NiO. The oxidation of NiO then occurs [17–21] forming NiO_2 [22]. We postulate that NiO_2 dissolves rapidly oxidising the underlying Ni to NiO, possibly according to the following mechanism:

$$NiO_2(s) + 2H^+(aq) \rightarrow Ni^{2+}(aq) + \frac{1}{2}O_2(g) + H_2O(l) \tag{9.1}$$

$$Ni + \frac{1}{2}O_2(g) \rightarrow NiO(s) \tag{9.2}$$

That is, overall

$$NiO_2(s) + 2H^+(aq) + Ni(s) \rightarrow NiO(s) + Ni^{2+}(aq) + H_2O(l) \tag{9.3}$$

Therefore, there's an overall 2 electron transfer in this process.

We next investigated the electro-oxidation of single NiNPs in the same media via the anodic particle coulometry (APC) method through the nanoparticle-electrode collision process. In this experiment, a carbon fibre microelectrode (radius 6.9 μm) was placed in a degassed solution of 10 mM $HClO_4$ and 100 mM $NaClO_4$, and a known concentration of pre-dispersed NiNPs added. The electrode potential was held at +1.7 V (relative to Ag/AgCl) where there is no expected faradaic processes occurring on the carbon surface, with a data sampling time of 0.5 ms. The oxidative transients were recorded as shown in Figure 9.2(a). Collisions were observed as sharp spikes with durations of 2-10 ms. The procedure was repeated at the potential of 1.0 V and no oxidative spikes were observed,

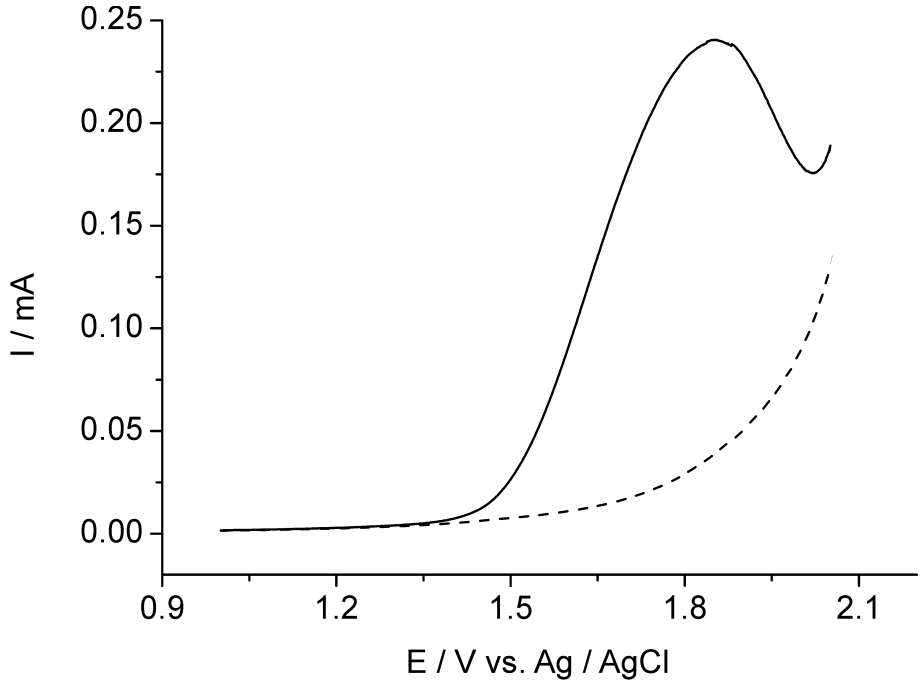

Figure 9.1: Voltammograms of a NiNPs modified GC electrode (solid line) and a bare GC electrode (dashed line) recorded in a solution of 10 mM $HClO_4$ and 100 mM $NaClO_4$ at a scan rate of 20 mV s^{-1}.

confirming that the faradaic oxidation is the source of the transients. The collision frequency was found to increase linearly with the concentration of NiNPs shown in Figure 9.2(b), with a rate of 0.22 s^{-1} pM^{-1}.

Assuming that the NiNPs are spherical (radius r_{np}), the maximum charge passed resulting from the complete (2 electrons per atom) oxidation of the NiNPs is given by:

$$Q = \frac{8F\pi\rho r_{np}^3}{3A_r}, \tag{9.4}$$

where ρ is the bulk density, A_r is the relative atomic mass, r_{np} is the radius of the NP, and F the Faraday constant. Figure 9.3 shows the distribution of radii obtained from the anodic particle coulometry (APC) analysis of more than 1000 impacts, of charges ranging from 1.2×10^{-13} to 2.6×10^{-11} C (corresponding to 3.8×10^5 to 4.0×10^7 Ni atoms) showing excellent agreement with the SEM-derived size distribution. This result demonstrates that NiNPs can be fully oxidized at the potential of 1.7 V, and in contrast

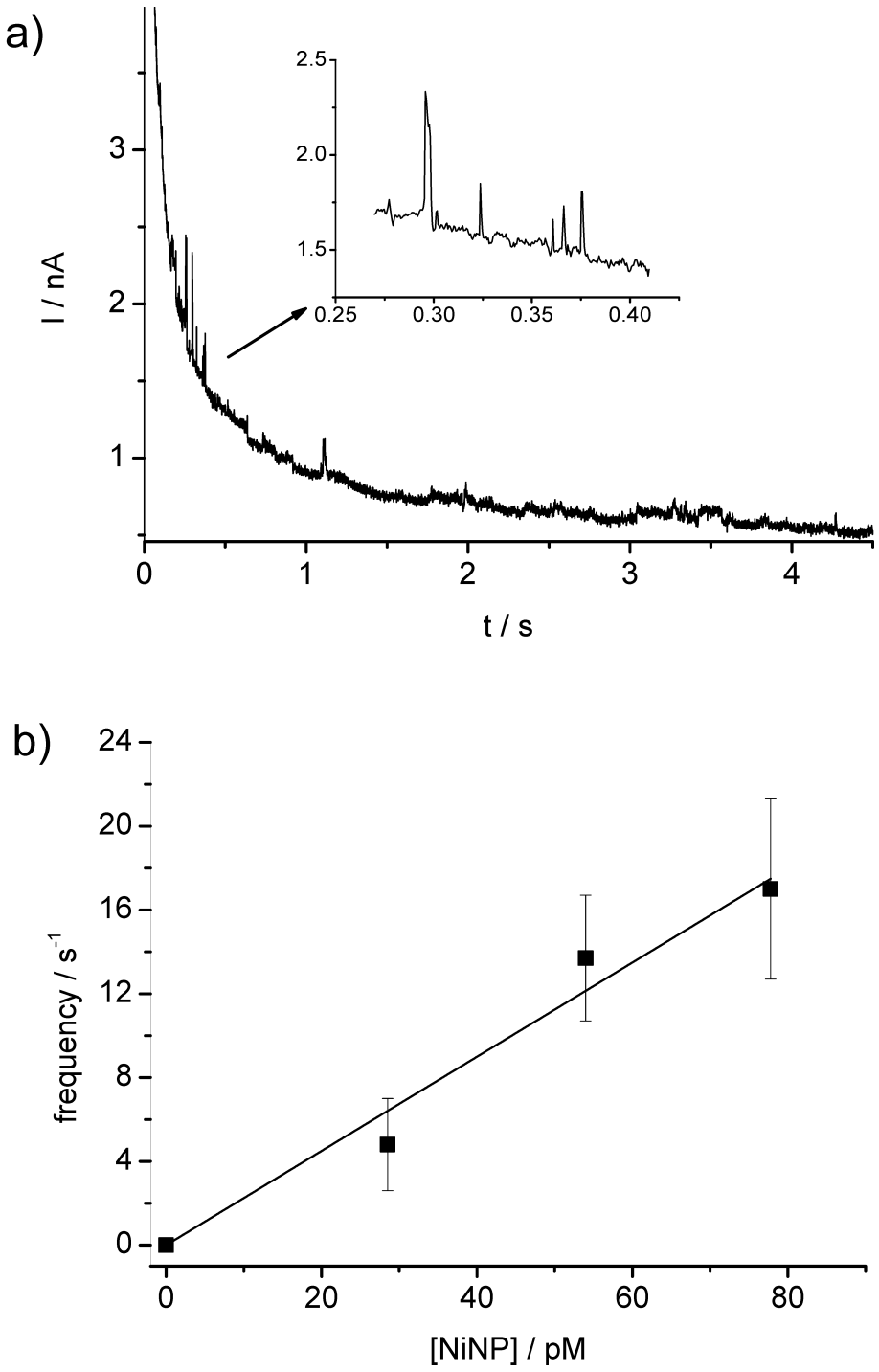

Figure 9.2: (a) Typical oxidative Faradaic transients of NiNPs in perchlorate solution at the potential of 1.7 V. The inset shows detailed impact spikes. (b) The frequency of spikes as a function of NiNP concentration.

with previous studies on AgNPs and AuNPs [5, 6, 23], NiNPs do not show aggregation in the perchlorate solutions at pH 2, with no change in distribution over the experimental timescale of 2 hours.

9.3.2 APC of mixed nanoparticle systems

The APC of AgNPs has been reported previously [5, 24, 25]. A carbon fibre microelectrode (radius 6.9 μm) was placed in a degassed solution of 10 mM $HClO_4$ and 100 mM $NaClO_4$, and a known concentration of pre-dispersed AgNPs added. The average size of the AgNPs had previously been determined to be 13±2 nm (corresponding to ca. 6×10^5 atoms). The electrode potential was held at +0.5 V (relative to saturated Ag/AgCl) beyond the onset potential for impact spikes [5].

Next, a known concentration of AgNPs-NiNPs mixture was added into the cell and a range of potentials were applied from +0.2 V to +1.8 V and at each potential the impact frequency recorded. We can see from Figure 9.4 that the frequency switches on at the potential of 0.45 V and 1.55 V, corresponding to the direct oxidation of AgNPs and the mixed NPs, respectively. This measurement allows us to simultaneously detect and identify mixed NPs: application of the methodology outlined above also enables the determination of the respective concentrations.

9.3.3 Determination of unknown concentrations of nanoparticles

The steady-state current transient at a microdisk electrode of radius r, assuming a simple n electron oxidation, is given by

$$I = 4nFcDrf(\tau), \tag{9.5}$$

where n is the number of electrons transferred, F is the Faraday constant (C mol^{-1}), c is bulk concentration (mol cm^{-3}), D is diffusion coefficient (cm^2 s^{-1}) and $f(\tau)$ is a function

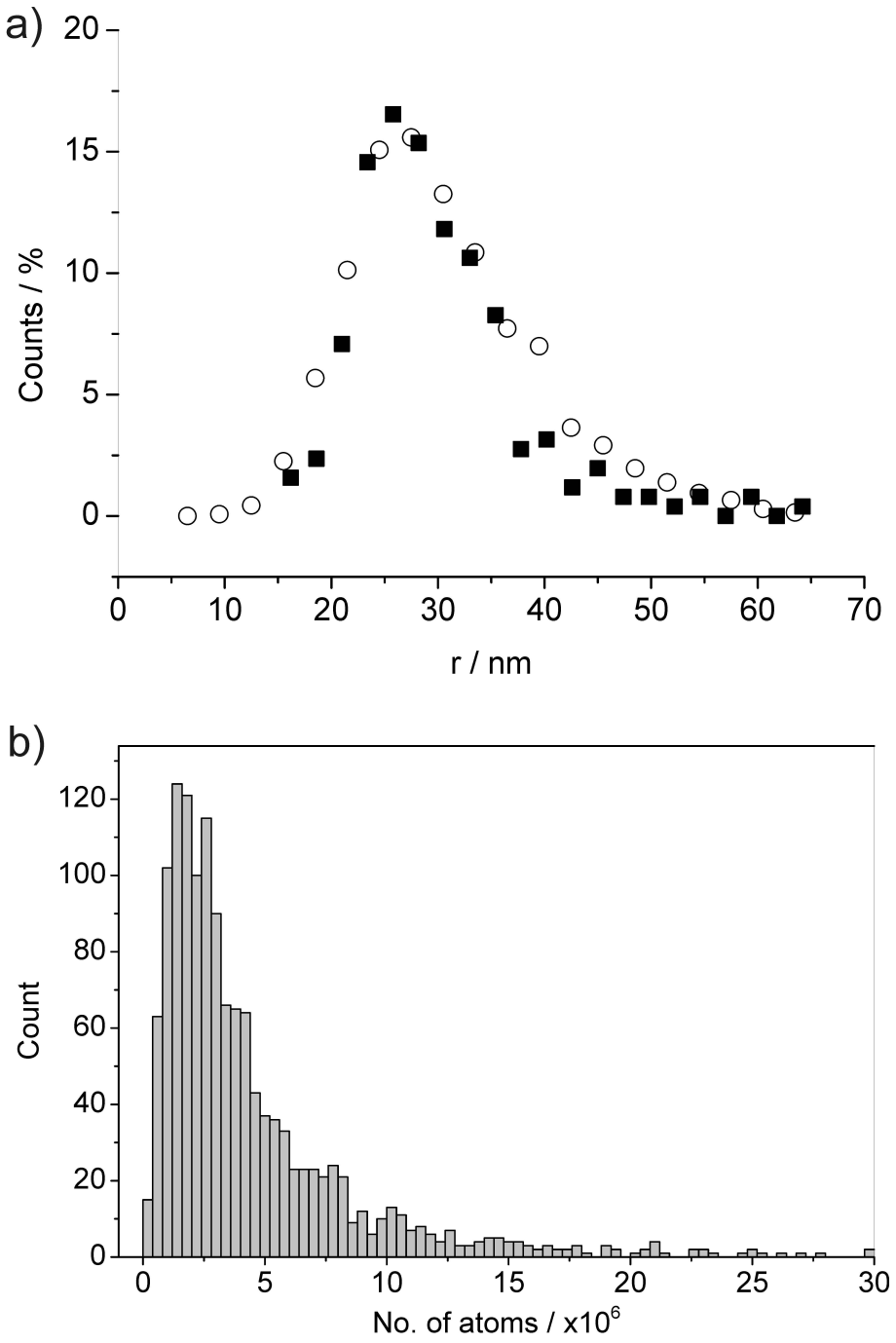

Figure 9.3: (a) Size distributions for NiNPs obtained from APC (○) and SEM (■) data, yielding a most likely radius of 26 nm, and (b) APC data expressed in the no. of Ni atoms oxidised per nanoparticle impact.

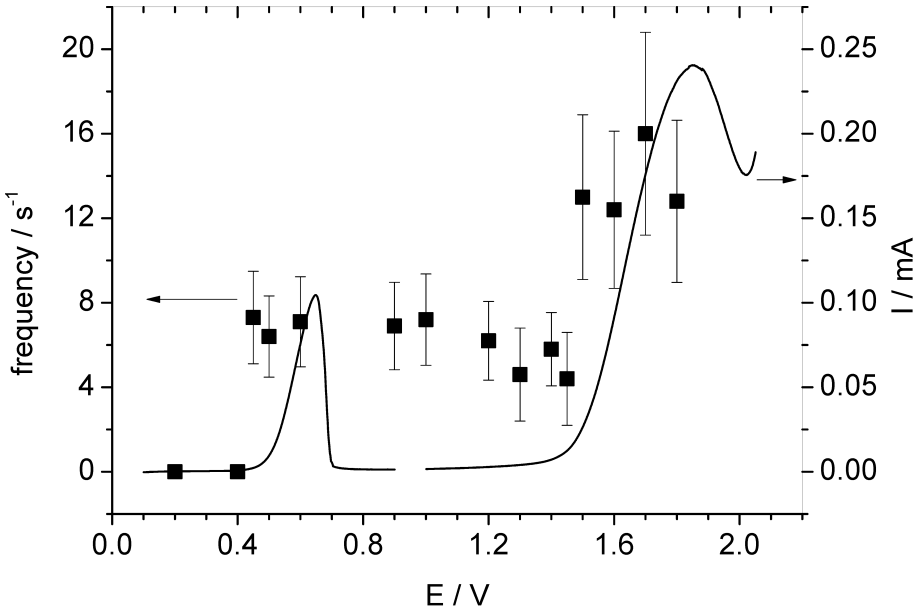

Figure 9.4: Overlay plot of stripping voltammograms for a AgNP-modified GC electrode and a NiNP-modified GC electrode (right axis) and the impact frequency (left axis).

of time, t (s). A convenient single expression for $f(\tau)$ has been obtained from simulation by Shoup and Szabo [26] and shown to correctly predict the current over the entire time domain with a maximum error of less than 0.6%. The Shoup and Szabo expression is

$$f(\tau) = 0.7854 + 0.8863\tau^{-1/2} + 0.2146exp(0.7823\tau^{-1/2}), \tag{9.6}$$

where $\tau = 4Dt/r^2$. At short times, the flux to the electrode is 1-dimensional and Cottrellian behaviour is observed with $I \propto r^2(D/t)^{1/2}$. As t $\rightarrow \infty$, however, the steady-state limit is reached and $I \propto rD$.

The experimental observation illustrated in Figure 9.2a that impact spikes are more frequent at the start of the chronoamperograms is consistent with this model.

Equation (9.6) can also be used to calculate the flux of nanoparticles to the microdisk electrode. For ease of comparison with experimental data, we convert the flux (impacts per second) to the cumulative number of impacts by integrating equation (9.6), simplifying the exponential term via a series expansion to 5 terms and introducing electrode area and the Avogadro constant to scale for the number of particle impacts for our electrode

area.

$$N = N_A c r^3(\tau+1.427\tau^{1/2}+6.57\times10^{-2}ln\tau-3.35\times10^{-3}\tau^{-1}+3.43\times10^{-3}\tau^{-1/2}+3.49\times10^{-4}\tau^{-3/2}) \tag{9.7}$$

This enables the fitting of experimental data to obtain the nanoparticle concentration, c, by fixing r and D, where r is the radius of the microelectrode (determined by independent electrochemical calibration) and D is calculated from the Stokes-Einstein equation [27].

$$D = \frac{k_B T}{6\pi\eta r_{np}}, \tag{9.8}$$

where k_B is the Boltzmann constant, η the solution viscosity and r_{np} the nanoparticle radius. The use of equation (9.8) is appropriate due to the large size (r_{np}= 10-30 nm) of the NPs, since it is based on Stokes' Law (i.e. the macro-scale). Therefore this analysis would not be suitable for molecules.

As a model system for testing this methodology we selected NiNPs due to the absence of aggregation over the experimental timescale as noted above. Figure 9.5 shows data of cumulative number of impacts versus time from three separate APC experiments (as described above) using known particle concentrations of 28±4 pM, 54±8 pM and 77±11 pM, with the theoretical lines obtained from optimising equation (9.7). The plots give optimised NiNPs concentrations of 30 pM, 60 pM and 80 pM, respectively, in excellent agreement with the known values, demonstrating the usefulness of this method to determine unknown concentrations of nanoparticles. It should be noted that in this methodology, there are no adjustable parameters apart from concentration: the diffusion coefficient of the NP, D is fixed by the NP radius (derived from the APC distribution).

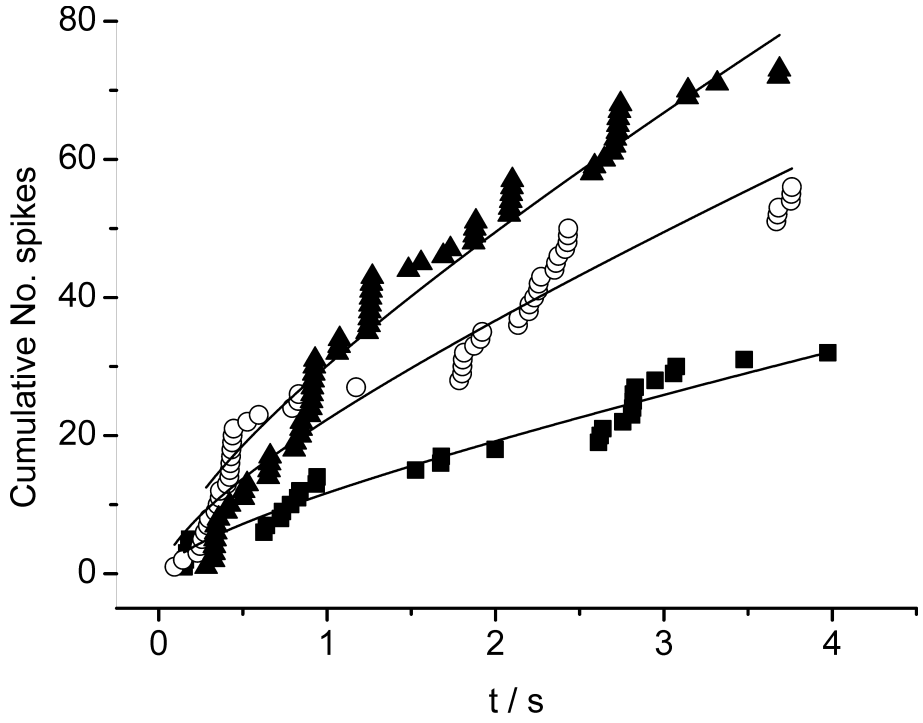

Figure 9.5: Integrated Shoup-Szabo fit for the accumulative number of spikes against time at varying NiNPs concentrations of (■)28, (○)54, and (▲)77 pM, respectively. The dotted lines show the experimental data and theoretical fit.

9.4 Conclusions

We have shown that the method of particle-impact voltammetry can be used successfully to characterise nickel nanoparticles, and introduced a new methodology for the determination of unknown concentrations of non-aggregating particles. The use of these methods for mixtures of nickel and silver nanoparticles has been demonstrated, proving the feasibility of particle-impact electrochemistry for real-world applications such as environmental monitoring and chemical analysis.

Bibliography

[1] M. Ahamed. *Toxicol. in Vitro*, 4:930, 2011.

[2] D. D. Guo, C. H. Wu, X. M. Li, H. Jiang, X. H. Wang, and B. A. Chen. *J. Nanosci. Nanotechnol.*, 5:2301, 2008.

[3] R. J. Griffitt, J. Luo, J. Gao, J. C. Bonzongo, and D. S. Barber. *Environ. Toxicol. Chem*, 9:1972, 2008.

[4] N. V. Rees, Y. G. Zhou, and R. G. Compton. *RSC Adv.*, 2:379, 2012.

[5] Y. G. Zhou, N. V. Rees, and R. G. Compton. *Angew. Chem., Int. Ed.*, 50:4219, 2011.

[6] Y. G. Zhou, N. V. Rees J. Pillay, R. Tshikhudo, S. Vilakazi, and R. G. Compton. *Chem. Commun.*, 48:224, 2012.

[7] A. Seghiouer, J. Chevalet, A. Barhoun, and F. Lantelme. *J. Electroanal. Chem.*, 442:113, 1998.

[8] J. C. Harfield, K. E. Toghill, C. Batchelor-McAuley, C. Downing, and R. G. Compton. *Electroanalysis*, 23:931, 2011.

[9] W. Visscher and E. Barendrecht. *Electrochim. Acta*, 25:651, 1980.

[10] P. Gonzalez, V. A. Cortinez, and C. A. Fontan. *Talanta*, 58:679, 2002.

[11] M. Bojinov. *J. Electroanal. Chem.*, 405:15, 1996.

[12] A. Ambrosi and M. Pumera. *Chem. Eur. J.*, 7:702, 2012.

[13] M. Giovanni, A. Ambrosi, and M. Pumera. *Chem. Asian J.*, 7:702, 2012.

[14] Q. Xu. *Nanostructured & Amorphous Materials Inc, Houston, USA. Pricate communication.*

[15] A. Pyatenko, M. Yamaguchi, and M. Suzuki. *J. Phys. Chem. C*, 111:7910, 2007.

[16] A. Pyatenko, M. Yamaguchi, and M. Suzuki. *J. Phys. Chem. B*, 109:2160, 2005.

[17] M. Cid, A. Jouanneau, D. Nganga, and M. C. Petit. *Electrochim. Acta*, 23:945, 1978.

[18] M. Zamin and M. B. Ives. *J. Electrochem. Soc*, 126:470, 1979.

[19] K. Nii. *Corr. Sci.*, 10:571, 1970.

[20] L. V. Volkov and M. I. Kalashnikova. *Tsvetnye Metally*, 8/9:101, 2011.

[21] F. T. Wagner and T. E. Moylan. *J. Electrochem. Soc.*, 136:2498, 1989.

[22] D. Zuili, V. Maurice, and P. Marcus. *J. Electrochem. Soc.*, 147:1393, 2000.

[23] Y. G. Zhou, N. V. Rees, and R. G. Compton. *ChemPhysChem*, 12:2085, 2011.

[24] Y. G. Zhou, N. V. Rees, and R. G. Compton. *Chem. Phys. Lett.*, 511:183, 2011.

[25] N. V. Rees, Y. G. Zhou, and R. G. Compton. *ChemPhysChem*, 12:1645, 2011.

[26] R. G. Compton and C. E. Banks. *Understanding Voltammetry 2nd Edition*. Imperial College Press, 2011.

[27] K. A. Dill and S. Bromberg. *Molecular Driving Forces*. Garland Science, 2002.

Chapter 10

Electrode-nanoparticle collisions: the measurement of the sticking coefficient of silver nanoparticles and nickel nanoparticles on a glassy carbon electrode

In this chapter, we demonstrate another application of the anodic particle coulometry (APC) method - measurement of the sticking coefficient of nanoparticles while their collisions with an electrode. The measurement is achieved by combining APC with anodic stripping voltammetry, using AgNPs in collision with glassy carbon electrode. Sticking coefficients are reported for AgNP radii of 14, 29, and 45 nm, measured at electrode biases ranging from OCV to -0.2 to -1.2 V (vs Ag/AgCl). No significant systematic trends were found in either case. The same study was performed on nickel nanoparticles (NiNPs). We suggest that this methodology may be widely applicable to measuring the sticking coefficient of any oxidisable metal nanoparticle on an electrode surface in solution.

This work was carried out in cooperation with Dr. Neil V. Rees, and has been published in *Chemical Physics Letters*, 2011, 514, 291.

10.1 Introduction

The impacts between particles and electrode surfaces have been known to be electrochemically measurable for over a decade [1–8]: through non-faradaic [9–13] and faradaic charge transfer transients [14–20]. Amongst the latter faradaic processes that have been reported between nanoparticles (NPs) and inert electrode surfaces are: electrocatalytic processes occurring on the surface of NPs [14–17], anodic particle coulometry (APC) based on the quantitative and exhaustive electro-oxidation of silver NPs (AgNPs) [18], and the underpotential deposition (UPD) of thallium onto AgNPS [20].

Sticking coefficients or probabilities are routinely measured in gas-solid surface science: classically for the adsorption of gas-phase atoms and molecules onto catalyst or well-defined crystal surfaces [21–23]. These experiments typically use molecular beams and ultra-clean surfaces under UHV, and can be far from straightforward. Molecular sticking coefficients have been found to vary widely depending on surface (both crystal face and substance), temperature and coverage. For example, at 300 K the sticking coefficients of N_2 on tungsten surfaces range from 0.09 to 0.59 to 0.64 for the (111), (100) and polycrystalline surfaces [23].

Collisions between small particles and surfaces have been investigated for many years, primarily by those interested in extra-terrestial research [24–26] considering impact velocities ranging from $101 - 103$ m s^{-1}. Of most interest is perhaps the theoretical work by Jung *et al*. [26] who produced molecular dynamics calculations to predict adhesion probabilities of a single nanocluster containing 1055 atoms with a weakly attractive static surface using a Lennard-Jones model. They concluded that for both low and high collision velocities the sticking probability was greater than 0.5, whereas for intermediate collision velocities, the sticking probability was less than 0.5.

Of the work reported to date on solution-based particle-wet surface collisions, there is no clear indication of the likely sticking coefficient for the collisions, defined as

$$s = \frac{\text{Rate of NPs sticking to surface}}{\text{Rate of NP collisions with surface}} \tag{10.1}$$

The early work in the field by Scholz, considered adhesion events of colloidal particles on mercury surfaces [6–8], and more recent studies by Bard *et al*. [14–17] have asserted that the faradaic electrocatalytic processes they observe at Pt and IrOx NPs occur at adsorbed NPs based on the qualitative shape of the current transients.

In this chapter, we combine APC with anodic stripping voltammetry, to quantify the proportion of NP impacts that result in adsorbed NPs. Using AgNPs in collision with glassy carbon electrode, we find that $s = 0.15 \pm 0.02$. The same study was performed on NiNPs with s close to 0. We suggest that this methodology may be widely applicable to measuring the sticking coefficient of any oxidisable metal nanoparticle on an electrode surface in solution.

10.2 Experimental

Three different sizes of AgNPs were synthesised according to the method of Pyatenko *et al*. [27, 28] and characterised *via* SEM imaging to have mean radii of 14 ± 2 nm, 29 ± 2 nm, and 45 ± 3 nm respectively. NiNPs of radii range 15 - 30 nm (average 26 nm) were purchased from Nanostructured & Amorphous Materials, Inc. (Houston, Texas, USA). AgNPs and NiNPs were dispersed by ultrasound prior to adding to the stripping solution. Sodium dihydrogen citrate ($NaC_6O_7H_7$, Aldrich, >99.5%), KCl (Riedel-de-Haan, >99.5%) and sodium perchlorate ($NaClO_4$, Johnson Matthey, 98-102%) were used as received. Solutions were made using ultrapure water of resistivity ~ 18.2 MΩcm (Millipore) and degassed thoroughly with N_2 (oxygen free, BOC Gases plc) and an atmosphere of N_2 maintained during the experiment. Experiments were conducted within a faraday cage using a μAutolab III potentiostat with a time resolution shorter than 0.1 ms (Metrohm-Autolab BV, Utrecht, Netherlands) and three-electrode arrangement: a 11 μm

radius glassy carbon (GC) working electrode (BASi Inc), a graphite counter electrode, and a saturated Ag/AgCl reference electrode (Radiometer, Copenhagen). Impact spikes were analysed using Origin v.8.1 (www.OriginLab.com) for spike identification and integration, and electrical noise reduction [18].

10.3 Results and Discussion

First, the potential of the oxidation of AgNPs with a mean radius of 14 nm was determined by modifying a glassy-carbon electrode (diameter 3 mm) with a small quantity of AgNPs, and measuring the anodic stripping voltammogram in a solution of 10 mM citrate and 90 mM KCl, in a repeat of the procedure detailed in [29]. The modification was carried out by drop-casting 2 μL of an aqueous suspension of AgNPs onto the electrode, and allowing the solvent (water) to evaporate.

Next, the collision frequency was determined by potentiostatting the glassy carbon (GC) electrode at a potential positive of the Ag oxidation potential, in this case +0.50 V (vs satd. Ag/AgCl), adding AgNPs to the level of 7.2×10^{12} particles dm^{-3} in a solution of 10 mM citrate and 90 mM KCl and measuring APC transients over a period of 35 minutes (see Figure 10.1b). More than 200 such transients were recorded, and these were then analysed for the signature collision spikes according to our previous method [18–20], yielding a total number of spikes as well as an average charge passed per spike, Q_s = 6.1×10^{-12} C. A collision frequency of $f_s = (114 \pm 8)$ min^{-1} was found in good agreement with previously reported values [14–20].

In order to determine the number of adhered NPs, the following procedure was used. First, the GC electrode was cleaned by mechanical polishing followed by oxidative scanning in 0.10 M $NaClO_4$ solution to ensure no pre-adsorbed material. Then the "exposure potential" was set to a fixed value (E_{exp}), the AgNPs were added (7.2×10^{12} particles dm^{-3}) to the solution and a stopwatch started. After 3 minutes' exposure to AgNP collisions, an anodic stripping voltammogram was recorded, as shown in Figure 10.2, and the charge

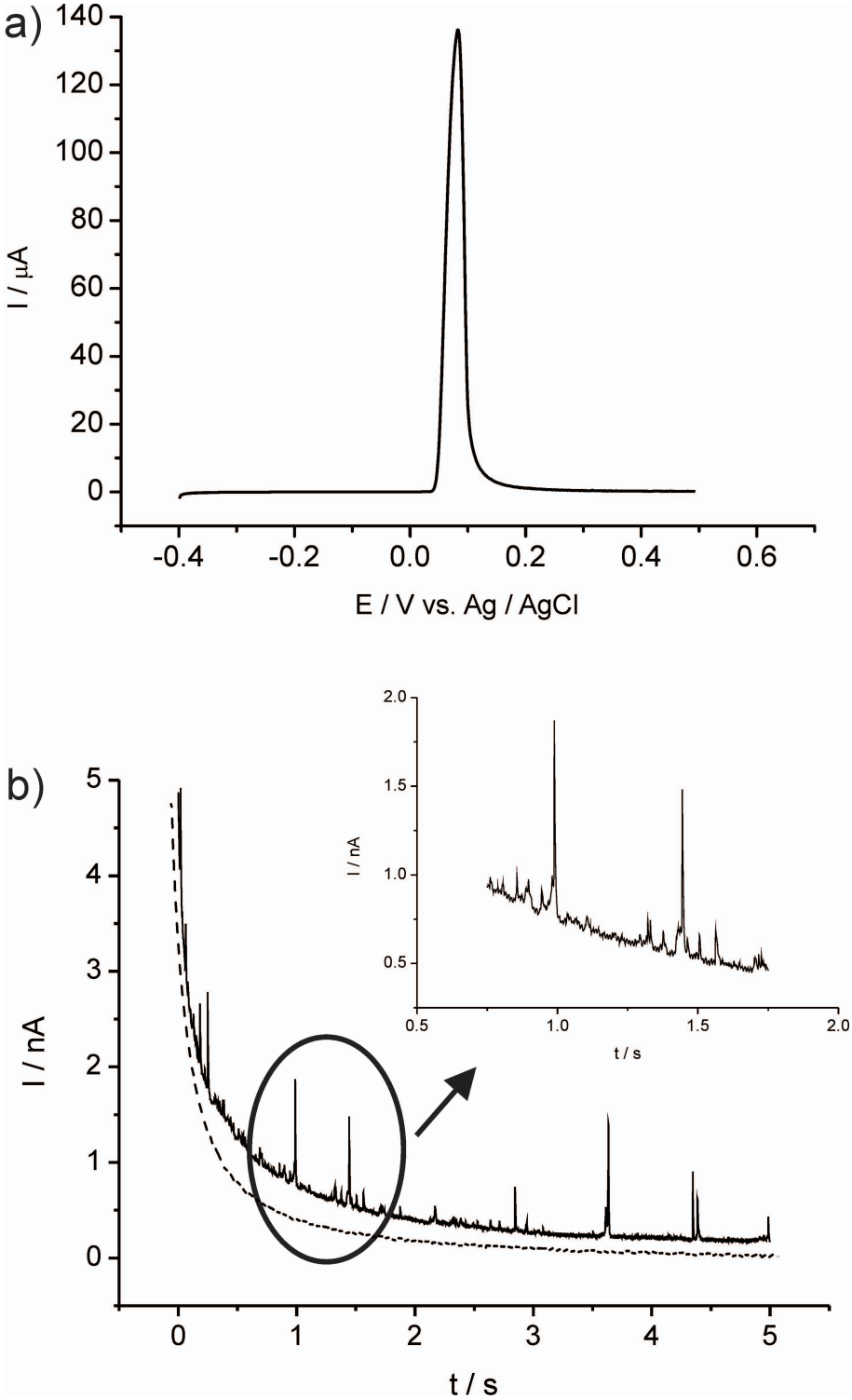

Figure 10.1: a) a typical anodic stripping voltammogram for AgNP-modified GC electrode in a solution of 10 mM citrate and 90 mM KCl, and b) APC transients showing oxidation spikes due to collisions of AgNPs at the GC electrode (radius 11 μm, E = +0.50 V vs Ag/AgCl, supporting electrolyte 10 mM sodium citrate / 90 mM potassium chloride). The chronoamperogram in the dotted line (....) is recorded under the same conditions except without AgNPs present.

relating to the Ag stripped from the electrode surface, Q_{ads}, calculated. Whilst stripping voltammetry in principle detects the net effect of adsorption and desorption events, the nature of the AgNP-electrode system in quiescent solution is such that the desorption rate is not significant. The electrode was then removed and cleaned as before, the solution and glassware changed, and repeat experiments performed for different periods of exposure to AgNP collisions (t_{exp}). Figure 10.2 shows that as exposure time increases, the stripping peak moves to less positive potentials before stabilising at *ca*. 0.2 V. This is expected since, as at short exposure times the adsorbed NPs are essentially isolated, and as time progresses the degree of aggregation of NPs increases [19] until the stripping voltammetry approximates to bulk silver.

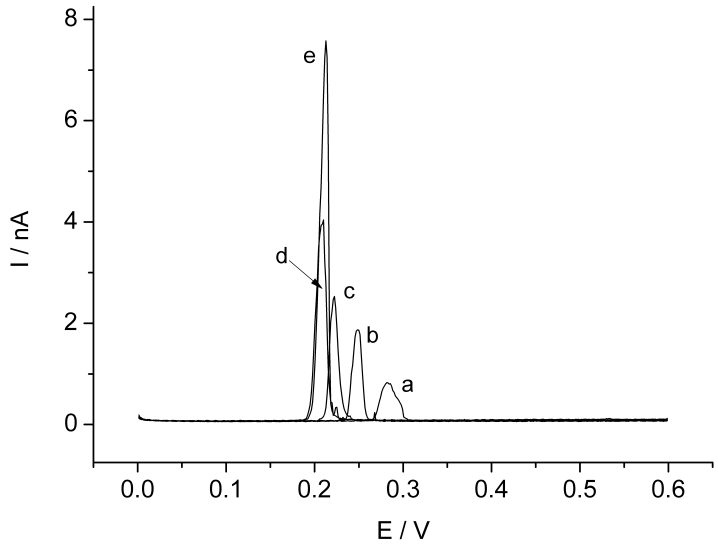

Figure 10.2: Anodic stripping voltammograms of the GC electrode measured after different exposure times (t_{exp}) to the AgNPs in 0.10 M $NaClO_4$: (a) 6.5, (b) 12, (c) 20, (d) 36, and (e) 50 minutes. AgNP radius was 45 nm, and E_{exp} = -0.2 V. The voltage scan rate was 20 mV s^{-1} for all cases, and the shift in oxidation potential compared to Figure 10.1 is due to the differences in electrolyte [30].

Figure 10.3 illustrates the linear variation of Q_{ads} with exposure time (the gradient is 8.9 ± 10^{-11} C min^{-1}), for the case of 45 nm radius AgNPs and an exposure potential of -0.2 V. The number of Ag atoms adsorbed per minute can thus be determined from the

gradient of Figure 10.3 and the relation:

$$Q_{\text{ads}} = N_{\text{ads}} e \tag{10.2}$$

Since an analogous relationship holds between the average charge passed per spike, Q_{s}, and the average number of Ag atoms in a colliding NP, N_{s}, the number of adsorbed NPs per minute (P_{ads}) can be found by

$$P_{\text{ads}} = \frac{N_{\text{ads}}}{N_{\text{s}}} \tag{10.3}$$

The sticking coefficient is then found by rewriting equation (10.1) as

$$s = \frac{P_{\text{ads}}}{f_{\text{s}}} = 0.15 \pm 0.02 \tag{10.4}$$

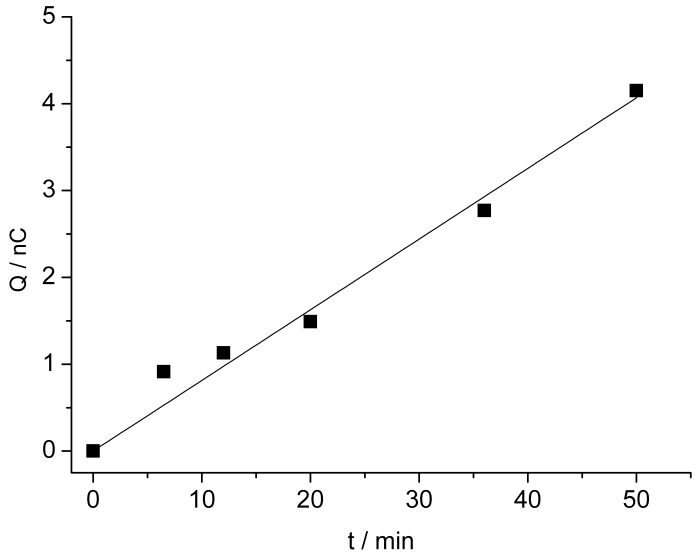

Figure 10.3: Integration of stripping peaks in Figure 10.2 showing linear variation of Q_{ads} with t_{exp} (gradient = 8.1×10^{-11} C min^{-1}, $R^2 = 0.991$), from which $s = 0.15$ was derived (see text)

Given that the point of zero charge (pzc) of glassy carbon is close to 0.0 V vs. Ag/AgCl in aqueous solution at pH 7 [31], and of Ag is *ca.* -0.9 V [32], a simple Coulombic ap-

proach suggests that the sticking probability may be influenced by the exposure potential (E_{exp}). We therefore conducted analogous experiments to those described above for E_{exp} = -0.20, -0.50, -0.90, and -1.20 V (all vs. saturated Ag/AgCl), for exposure times of up to 50 mins (positive exposure potentials were not used due to the proximity of the oxidation potential of silver). For completeness, this was repeated for all three sizes of AgNPs, to determine if there was a size effect on the sticking probability, and all results are given in Table 10.1. It is noteworthy that, within error, very similar values for the sticking coefficient are found for all sizes and exposure potentials, indicating that neither size nor electrode potential has a significant effect on the sticking coefficient, although it appears that the sticking probabilities at the most negative potentials are slightly lower than those measured at the least negative potentials. The apparent invariance of sticking probability with variations in size and especially electrode potential may be surprising. Detailed experimental work is currently in progress, to understand the behaviour of the sticking coefficient with respect to other physical aspects of the system; namely temperature, solvent and electrolyte (both identity and concentration), electrode surface, etc. We anticipate the results of these investigations will shed more light on the factors that do influence the sticking coefficient, and therefore the nature of the NP-electrode interaction.

AgNP radius/nm	E_{exp}/V (vs. satd. Ag/AgCl)				
	OCV	−0.2	−0.5	−0.9	−1.2
14	–	0.13	0.09	0.12	0.09
29	–	0.13	0.14	0.09	0.10
45	0.16	0.15	0.13	0.15	0.13

Table 10.1: Sticking coefficients (error ±0.02 in all cases) determined for different sizes of AgNPs size and exposure potentials.

Next, analogous experiments were performed with nickel nanoparticles (NiNPs) with mean radii of 26 nm. The impact frequency was determined to be 13.2 $pM^{-1}min^{-1}$. Accumulation experiments were performed at three different exposure potentials: E_{exp} = 0.50 V, 0.80 V and 1.20 V at which NiNPs cannot be oxidized due to the NiO surface layer

[33]. Figure 10.4 shows the cyclic voltammetry of these NiNPs adsorbed onto a glassy carbon electrode in confirmation of this, where full oxidation of the NiNP only occurs at potentials above +1.5 V where the oxidative dissolution of the NiO layer commences [33]. Figure 10.5 shows the stripping voltammetry recorded after various exposure times at the potential of 0.50 V. We notice that the sticking amount of Ni onto GC electrode is very tiny (see voltammogram of a bare micro GC electrode for comparison) even after very long exposure time of 200 min. The stripping peak goes up very slowly with time. The linear variation of Q_{ads} with exposure time yields a gradient of 7.4×10^{-12} C min^{-1}, corresponding to a sticking rate of 0.05 $\text{pM}^{-1}\text{min}^{-1}$. This result enables the calculation of a sticking coefficient, s, of 0.4 %. Repeat experiments at 0.8 V and 1.2 V both show s less than 1%.

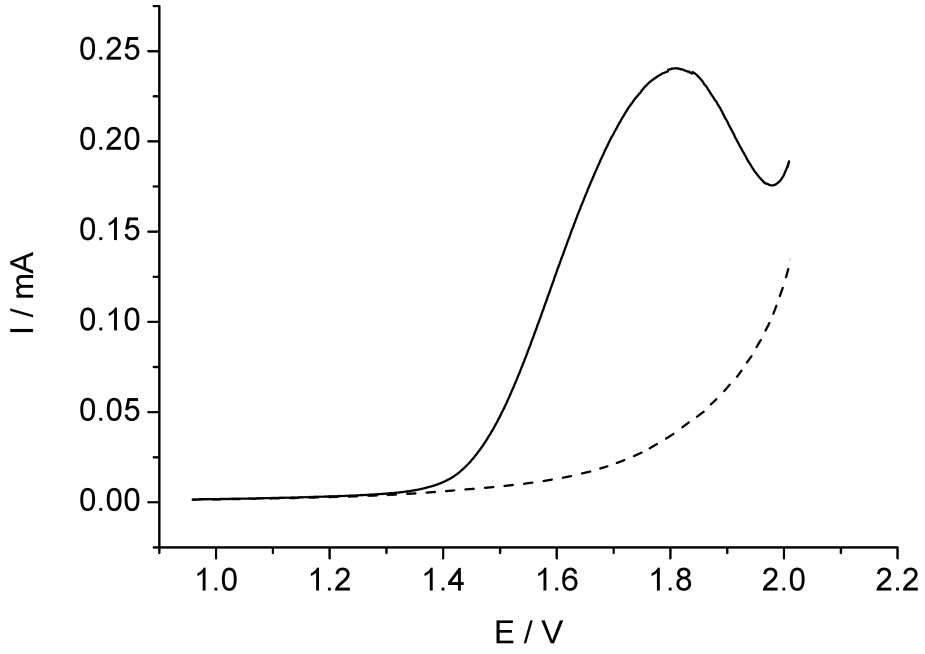

Figure 10.4: Cyclic voltammogram of bare GC (dashed line) and NiNP modified GC (solid line) electrodes in pH 2 $HClO_4/NaClO_4$ solution.

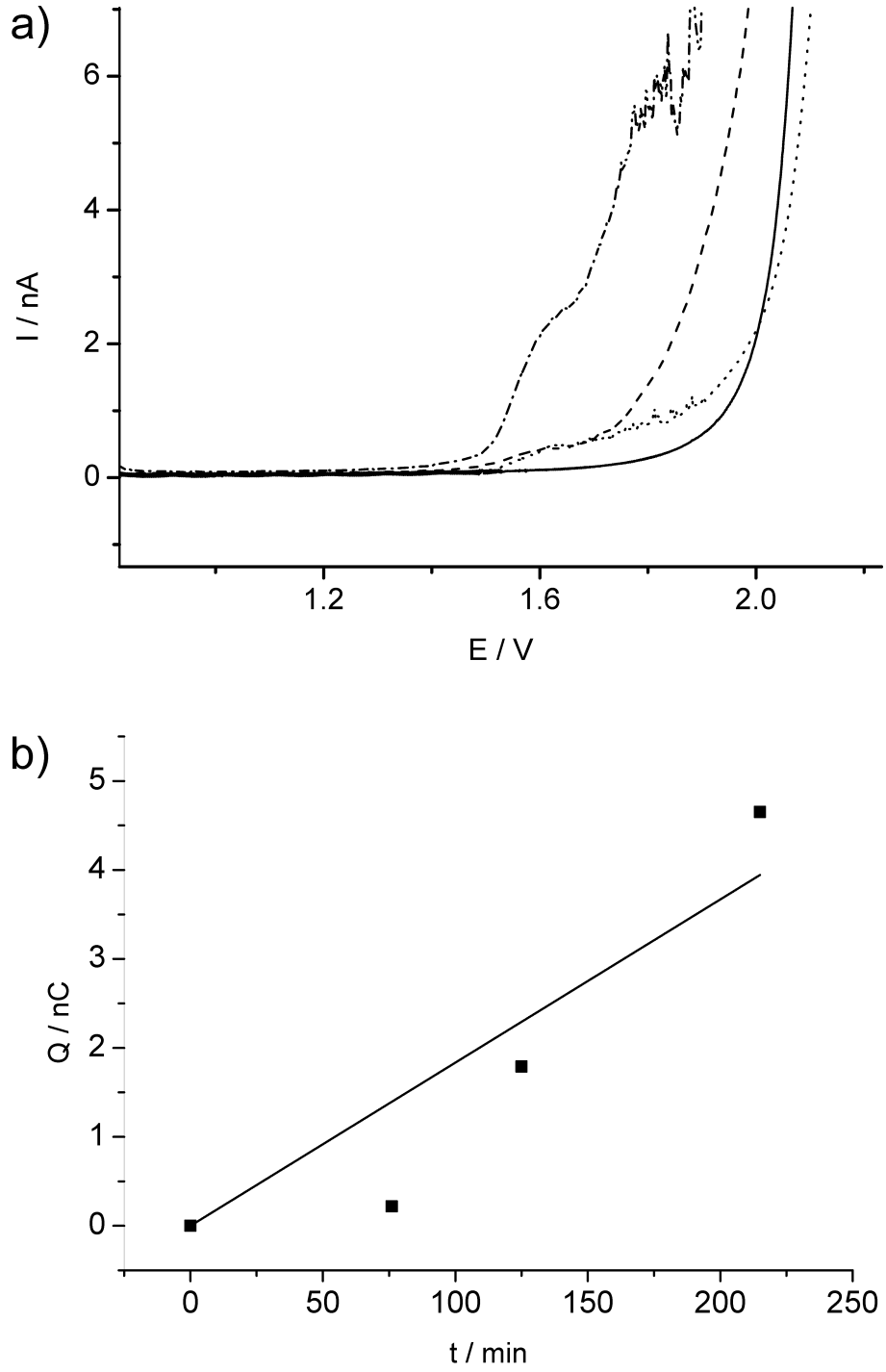

Figure 10.5: a) Anodic stripping voltammograms of the GC electrode measured after different exposure times (t_{exp}) to the NiNPs at E_{exp} = +0.50 V: 70(dotted line), 100(dashed line), and 200 (dash dotted line) minute, with the response of the bare GC (solid line) also shown. b) Integration of stripping peaks in Figure 10.4 showing linear variation of Q_{ads} with t_{exp} (gradient of 7.4×10^{-12} C min^{-1}), from which s = 0.04 was derived (see text)

10.4 Conclusions

The sticking coefficient for AgNPs of radii 14, 29, and 45 nm on GC electrode surface has been determined using a combination of anodic particle coulometry and anodic stripping voltammetry at a range of potentials. No significant trends were observed and an overall average sticking coefficient was found to be $s = 0.12 \pm 0.02$. The sticking coefficient for NiNPs of mean radius of 26 nm was determined using the same method to be below 1% at three different potentials, showing the NiNPs do not stick to GC in aqueous solution.

Bibliography

[1] M. Heyrovský, J. Jirkovský, and B. R. Müller. *Langmuir*, 11:4293, 1995.

[2] M. Heyrovský, J. Jirkovský, and M. Struplova-Bartackova. *Langmuir*, 11:4300, 1995.

[3] M. Heyrovský, J. Jirkovský, and M. Struplova-Bartackova. *Langmuir*, 11:4309, 1995.

[4] I. D. Charlton and A. P. Doherty. *J. Phys. Chem. B*, 104:8061, 2000.

[5] I. D. Charlton and A. P. Doherty. *Anal. Chem.*, 72:687, 2000.

[6] D. Hellberg, F. Scholz, F. Schauer, and W. Weitschies. *Electrochem. Commun.*, 4:305, 2002.

[7] F. Scholz, D. Hellberg, F. Harnisch, A. Hummel, and U. Hasse. *Electrochem. Commun.*, 6:929, 2004.

[8] D. Hellberg, F. Scholz, F. Schubert, M. Lovric, D. Omanovic, V. A. Hernandez, and R. Thede. *J. Phys. Chem. B*, 109:14715, 2005.

[9] C. E. Banks, N. V, and R. G. Compton. *J. Electroanal. Chem.*, 535:41, 2002.

[10] C. E. Banks, N. V. Rees, and R. G. Compton. *J. Phys. Chem. B*, 106:5810, 2002.

[11] N. V. Rees and R. G. Compton. *Analyst*, 132:635, 2007.

[12] N. V. Rees, C. E. Banks, and R. G. Compton. *J. Phys. Chem. B*, 108:18391, 2004.

[13] A. D. Clegg, N. V. Rees, C. E. Banks, and R. G. Compton. *ChemPhysChem*, 7:807, 2007.

[14] X. Xiao, S. Pan, J. S. Jang, F. R. F. Fan, and A. J. Bard. *J. Phys. Chem. C*, 113:14978, 2009.

[15] X. Xiao and A. J. Bard. *J. Am. Chem. Soc.*, 129:9610, 2007.

[16] S. J. Kwon, F. R. F. Fan, and A. J. Bard. *J. Am. Chem. Soc.*, 132:13615, 2010.

[17] X. Xiao, F. R. F. Fan, J. Zhou, and A. J. Bard. *J. Am. Chem. Soc.*, 130:16669, 2008.

[18] Y. G. Zhou, N. V. Rees, and R. G. Compton. *Angew. Chem., Int. Ed.*, 50:4219, 2011.

[19] N. V. Rees, Y. G. Zhou, and R. G. Compton. *ChemPhysChem*, 12:1645, 2011.

[20] Y. G. Zhou, N. V. Rees, and R. G. Compton. *ChemPhysChem*, 12:2085, 2011.

[21] G. A. Attard and C. Barnes. *Surfaces*. Oxford University Press, Oxford, 1994.

[22] K. Oura, V. G. Lifshits, A. A. Saranin, A. V. Zotov, and M. Katayama. *Surface Science*. Springer-Verlag, Berlin, 2003.

[23] D. A. King and M. G. Wells. *Proc. R. Soc. London A*, 339:245, 1974.

[24] C. L. Cleveland and U. Landman. *Science*, 257:355, 1992.

[25] P. Reissaus, T. Waldemarsson, J. Blum, D. Clement, I. Llamas, H. Mutschke, and F. Giovane. *J. Nanopart. Res.*, 8:693, 2006.

[26] S. C. Jung, D. Suh, and W. S. Yoon. *J. Aerosol Sci.*, 41:745, 2010.

[27] A. Pyatenko, M. Yamaguchi, and M. Suzuki. *J. Phys. Chem. C*, 111:7910, 2007.

[28] A. Pyatenko, M. Yamaguchi, and M. Suzuki. *J. Phys. Chem. B*, 109:21608, 2005.

[29] S. E. Ward Jones, F. W. Campbell, R. Baron, L. Xiao, and R. G. Compton. *J. Phys. Chem. C*, 112:17820, 2008.

[30] Ch. Labar and L. Lamberts. *Talanta*, 1997:733, 44.

[31] R. Cisternas, E. Munoz, R. Henriquez, R. Cordova, H. Kahlert, U. Hasse, and F. Scholz. *J. Solid State Electrochem.*, 15:2461, 2011.

[32] R. E. White, J. O'. M. Bockris, and B. E. Conway, editors. *Modern Aspects of Electrochemistry*. Kluwer Academic Press, New York, 1999, P. 70.

[33] Y. G. Zhou, B. Haddou, N. V. Rees, and R. G. Compton. *Phys. Chem. Chem. Phys.*, accepted, 2012.

Chapter 11

Nanoparticle-electrode collision processes: the underpotential deposition (UPD) of thallium on silver nanoparticles in aqueous solution

The previous chapters focused on the direct oxidation of metal NPs. From this chapter on we will leave this topic and discuss the work on the indirect electrochemistry of NPs - electroactive species reacting on the surfaces of NPs during collisions with electrode without reaction of the nanoparticles themselves. This chapter outlines the underpotential deposition (UPD) of thallium onto silver nanoparticles (AgNPs) during NP-electrode collisions. The analysis of the charge passed during these UPD events correspond to a UPD layer coverage of the NPs.

This work was carried out in cooperation with Dr. Neil V. Rees and has been published in *ChemPhysChem*, 2011, 12, 2085.

11.1 Introduction

The impacts between particles and electrode surfaces have been known and measured for several years [1–8], often through non-faradaic charge transfer transients [9–13]. Recently, electrocatalytic processes occurring on the surface of nanoparticles (NPs) during collisions have been noted, giving rise to faradaic charge transfer [14–17]. In Chapter 6 and 7 we introduced anodic particle coulometry (APC) based on the quantitative and exhaustive electro-oxidation of AgNPs at an electrode [18, 19]:

$$\mathrm{Ag(NP)} - \mathrm{e^-} \rightarrow \mathrm{Ag^+(aq)} \tag{11.1}$$

These two chapters demonstrated that this method enables the detection, characterisation, and identification of AgNPs, and is also capable of monitoring aggregation processes and identifying multiple NP clusters [18, 19].

The underpotential deposition of Tl onto Ag [20–22], and in particular AgNPs has been thoroughly investigated in recent years [23]. The difference in potential between the onsets of UPD and bulk deposition can be related to different work functions associated with substrate material and deposit (i.e. silver and thallium respectively). This can result in partial charging of the adatoms [24–27].

In this chapter, we report the first observation of underpotential deposition (UPD) of a metal onto metal NPs during NP-electrode impacts, and demonstrate that the UPD of Tl onto AgNPs occurs during collisions between AgNPs and an electrode.

11.2 Experimental

AgNPs were synthesised according to the method of Pyatenko *et al*. [28–30], and characterised via SEM imaging to have a mean radius of 45 ± 3 nm. AgNPs were dispersed by ultrasound prior to adding to the solution. Thallium (I) nitrate (Aldrich, >99.5%) and potassium nitrate (Aldrich, >99.5%) were used as received. All solutions were made using

ultrapure water of resistivity ~ 18.2 MΩcm (Millipore) and degassed thoroughly with N_2 (oxygen free, BOC Gases plc) and an atmosphere of N_2 maintained during the experiment. Experiments were conducted within a faraday cage using a μAutolab III potentiostat with a time resolution shorter than 0.1 ms (Metrohm-Autolab BV, Utrecht, Netherlands) and three-electrode arrangement: a 11 μm radius glassy carbon (GC) working electrode (BASi Inc), a graphite counter electrode, and a Ag/AgCl reference electrode (Radiometer, Copenhagen). Impact spikes were analysed using Origin v.8.1 (www.OriginLab.com) for spike identification and integration, and electrical noise reduction [18, 19].

11.3 Results and Discussion

First, the voltammetry of thallium was recorded on a bare glassy carbon (GC) electrode (radius of 3 mm) and the same GC electrode modified with AgNPs [23] immersed in a 10 mM solution of $TlNO_3$ (aq) and 1.0 M KNO_3, as shown in Fig. 11.1. On bare GC a single cathodic deposition peak was observed at -0.62 V (vs Ag/AgCl), whereas on the AgNP-modified GC electrode the same peak was observed in addition to an UPD peak at -0.46 V [23]. Fig. 11.1 shows these results verifying that the UPD occurs solely on the AgNPs [23]. Having confirmed the clear separation of UPD and bulk deposition potentials and determined their values, we turn to the observation of UPD on AgNPs during collisions with a bare GC electrode.

Second, the GC microelectrode was placed in degassed thallium (I) nitrate solution and a known concentration of pre-dispersed AgNPs added. After a period of 10 minutes post-dispersion, the solution was agitated by bubbling with N_2, the electrode potential held at -0.50 V (relative to Ag/AgCl) and impact transients recorded as shown in Fig. 11.2. The potential of zero charge (pzc) for polycrystalline silver is in the order of -0.90 to -0.98 V (vs. Ag/AgCl) [31] and the electrode is therefore potentiostatted at potentials more positive than the surface charge of the NPs. The impact transients were observed as sharp, reductive spikes of duration 1-10 ms and peak heights of up to 1 nA, similar

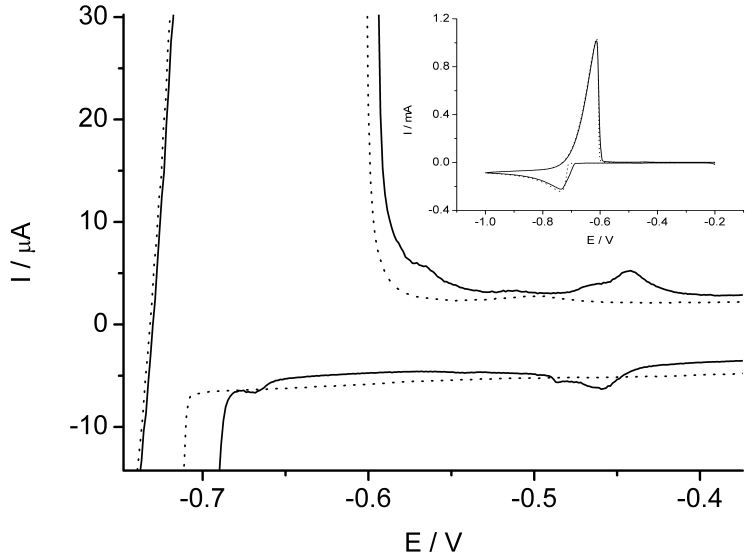

Figure 11.1: Thallium deposition on bare GC (....) and AgNP-modified GC (—) electrodes, showing the UPD feature at ca -0.47 V on the latter. Inset shows the complete deposition-stripping voltammogram.

to those reported previously for NP impact events [18, 19]. The longer duration features sometimes observed (as in Figure 11.3 around t = 3 s) are thought to be possibly due to multiple near-coincident collisions with AgNPs and NP clusters. Several hundred impact transients were recorded for analysis. This procedure was repeated at potentials of -0.30 V, and -0.60 V: no UPD spikes were observed at the former (as shown in Figure 11.3) whilst they were clearly observed at the latter, thus confirming that the potential of the onset of transient spikes coincides with the potential of UPD for thallium [23].

Further control experiments were performed where first, Tl^+ ions, and second, AgNPs were omitted from the reaction cell. In both cases no transient spikes were observed at the potential of -0.50V, confirming that the reductive transients were indeed due to the UPD of thallium on the AgNPs during the collisions with the GC electrode surface:

$$Tl^+(aq) + e^- \rightarrow Tl(NP) \tag{11.2}$$

Variation of the added concentration of AgNPs, was found to cause an increase in the

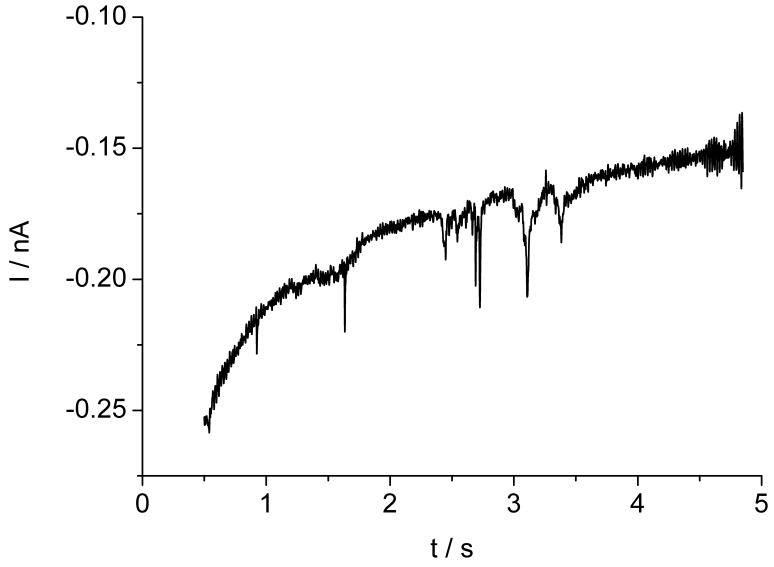

Figure 11.2: Typical cathodic UPD transients occurring at AgNP collisions with the GC electrode potentiostatted at -0.50 V.

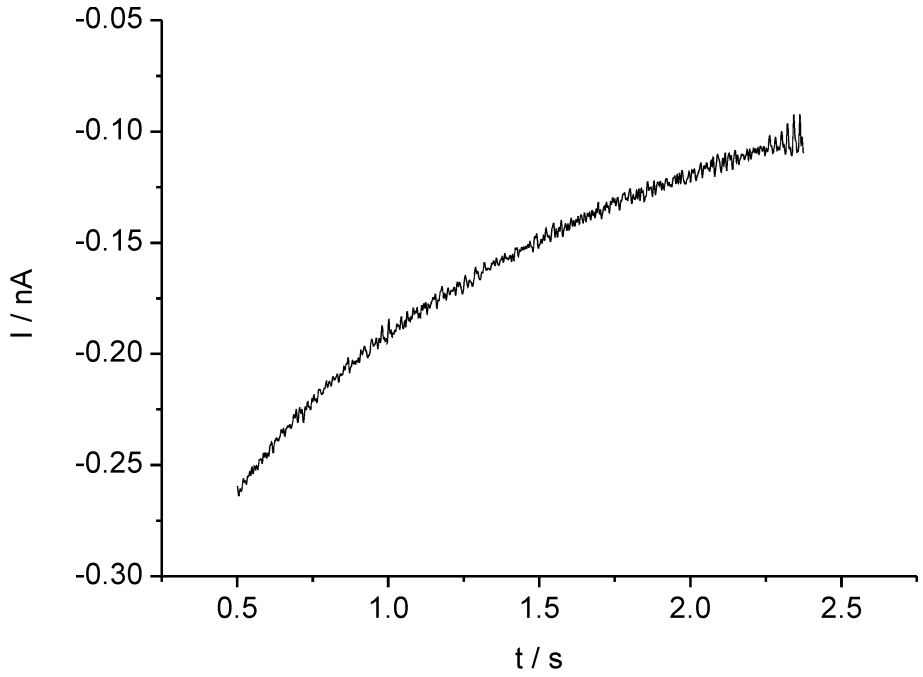

Figure 11.3: Current-time transient for AgNP collisions with the GC electrode potentiostatted at -0.30 V. No impact transients are observed.

impact frequency as has been noted previously [14–19]. Increasing the Tl^+ concentration was found to have no effect on the charge passed per spike (Q) as illustrated in Fig. 11.4. This result implies that even at 10 mM Tl^+ an UPD layer of Tl can be deposited on a AgNP during an impact with the electrode.

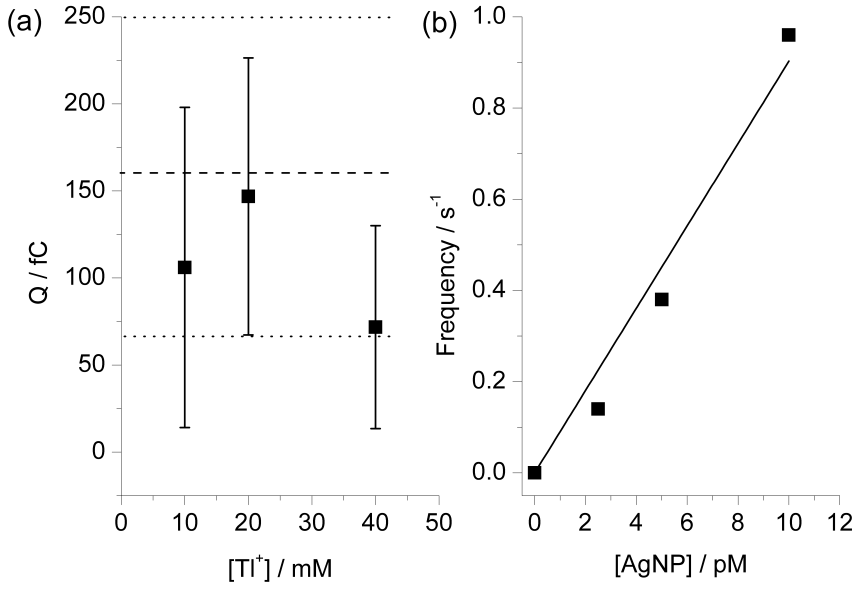

Figure 11.4: Plots showing: (a) the variation in Q with $[Tl^+]$, showing the Q ($\theta = 1$) values for an average AgNP (- - - -) with upper and lower limits of AgNP size (....) as described in text. The variation in impact frequency with [AgNP] is shown in (b) with a rate of 0.09 s^{-1} pM^{-1} for this electrode.

The APC analysis of this exact batch of AgNPs has been previously described [18,19], and yielded a mean Q of 6.1×10^{-12} C. The charge passed per impact transient, Q, is related to the number of electrons passed, N, via the electronic charge according to

$$Q = eN \tag{11.3}$$

Given that bulk Ag is known to adopt a fcc structure, assuming a cubic packing arrangement within the NP, a surface area (S) can be calculated with knowledge of the atomic radius, r_A by using Equation (11.4):

$$S = 24{r_A}^2 N^{2/3} \tag{11.4}$$

This therefore allows monolayer coverage of Tl atoms ($\theta = 1$) to be calculated for a mean AgNP, and hence is included in Fig. 11.4 and Fig. 11.5.

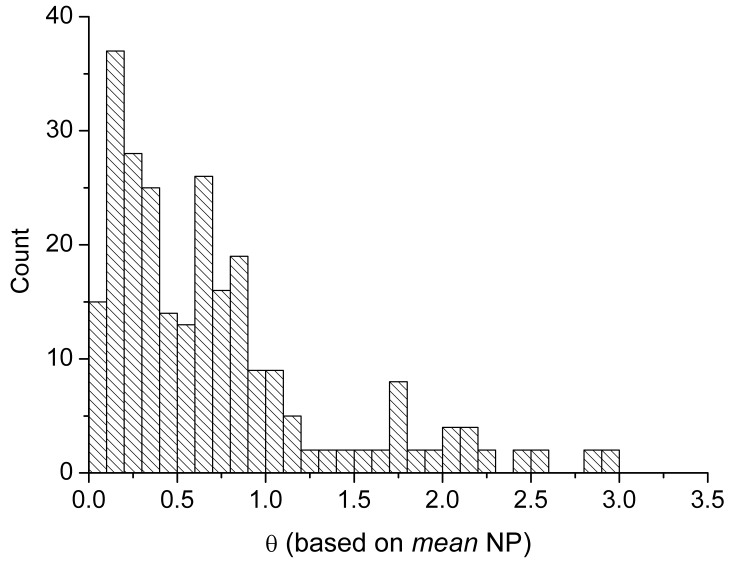

Figure 11.5: UPD spikes analysed in terms of fractions of a monolayer (θ) on a mean single AgNP (see text for a discussion on the implications of NP aggregation).

The agreement of the experimental data to approximately monolayer coverage is very good: remembering that at these ionic strengths, agglomeration of AgNPs is rapid to the point where after 20 mins less than 20% of the AgNP species present are in the form of single dispersed NPs, the remainder being larger cluster species [19]. To put Fig. 11.5 in the context of clustered NP species, the most common clusters observed in [19] were of 4 and 8 NPs. These have surface areas of 3 and 4 times greater than the single NP used as the basis for the scale in Fig. 11.5 (where the surface areas have been calculated using a simple "building block" model of arranging cubes into clusters). In other words, monolayers on clusters of 4 and 8 NPs would correspond to $\theta = 3$ and 4, respectively, in Fig. 11.4.

Finally, the above experiments for Tl UPD were repeated using a sample of dispersed AgNPs of average radius 14 nm. No reductive spikes were observed. This is in agreement with previous reports of the effects on Tl UPD on the size of AgNPs [23], where no UPD was found to occur on AgNPs less than about 50 nm in diameter.

11.4 Conclusions

In this chapter, we have for the first time, demonstrated that UPD can occur at nanoparticles during their collisions with an inert electrode, in this case the UPD of Tl onto AgNPs:

$$Tl^{+}(aq) + e^{-} \rightarrow Tl(NP) \tag{11.5}$$

The onset of reductive spikes was observed at the UPD potential, and the charge passed during these UPD events correspond very well to sub-monolayer to monolayer coverage of the NPs, using a simple model of a single AgNP. Where there is apparent deposition of more than a single monolayer using this model, it is noted that the rapid aggregation of AgNPs [19] means that NP clusters increasingly become the dominant species in the reaction cell and larger UPD currents probably correspond to submonolayer deposition on these clustered species.

Bibliography

[1] M. Heyrovský, J. Jirkovský, and B. R. Müller. *Langmuir*, 11:4293, 1995.

[2] M. Heyrovský, J. Jirkovský, and M. Struplova-Bartackova. *Langmuir*, 11:4300, 1995.

[3] M. Heyrovský, J. Jirkovský, and M. Struplova-Bartackova. *Langmuir*, 11:4309, 1995.

[4] I. D. Charlton and A. P. Doherty. *J. Phys. Chem. B*, 104:8061, 2000.

[5] I. D. Charlton and A. P. Doherty. *Anal. Chem.*, 72:687, 2000.

[6] D. Hellberg, F. Scholz, F. Schauer, and W. Weitschies. *Electrochem. Commun.*, 4:305, 2002.

[7] F. Scholz, D. Hellberg, F. Harnisch, A. Hummel, and U. Hasse. *Electrochem. Commun.*, 6:929, 2004.

[8] D. Hellberg, F. Scholz, F. Schubert, M. Lovric, D. Omanovic, V. A. Hernandez, and R. Thede. *J. Phys. Chem. B*, 109:14715, 2005.

[9] C. E. Banks, N. V. Rees, and R. G. Compton. *J. Electroanal. Chem.*, 535:41, 2002.

[10] C. E. Banks, N. V. Rees, and R. G. Compton. *J. Phys. Chem. B*, 106:5810, 2002.

[11] N. V. Rees and R. G. Compton. *Analyst*, 132:635, 2007.

[12] N. V. Rees, C. E. Banks, and R. G. Compton. *J. Phys. Chem. B*, 108:18391, 2004.

[13] A. D. Clegg, N. V. Rees, C. E. Banks, and R. G. Compton. *ChemPhysChem*, 7:807, 2006.

[14] X. Xiao, S. Pan, J. S. Jang, F. R. F. Fan, and A. J. Bard. *J. Phys. Chem. C*, 113:14978, 2009.

[15] X. Xiao and A. J. Bard. *J. Am. Chem. Soc.*, 129:9610, 2007.

[16] S. J. Kwon, F. R. F. Fan, and A. J. Bard. *J. Am. Chem. Soc.*, 132:13165, 2010.

[17] X. Xiao, F. R. F. Fan, J. Zhou, and A. J. Bard. *J. Am. Chem. Soc.*, 130:16669, 2008.

[18] Y. G. Zhou, N. V. Rees, and R. G. Compton. *Angew. Chem., Int. Ed.*, 50:4219, 2001.

[19] N. V. Rees, Y. G. Zhou, and R. G. Compton. *ChemPhysChem*, 12:1645, 2011.

[20] T. C. Girjia and M. V. Sangaranarayanan. *J. Appl. Electrochem.*, 36:531, 2006.

[21] V. Daujotis and E. Gaidamauskas. *J. Electroanal. Chem.*, 446:151, 1998.

[22] E. Herrero, L. J. Buller, and H. D. Abruna. *Chem. Rev.*, 101:1897, 2001.

[23] F. W. Campbell, Y. G. Zhou, and R. G. Compton. *New J. Chem.*, 34:187, 2010.

[24] D. M. Kolb, M. Przasnyski, and H. Gerischer. *Surf. Sci.*, 54:25, 1974.

[25] D. M. Kolb and H. Gerischer. *Surf. Sci.*, 51:323, 1975.

[26] H. Gerischer, D. M. Kolb, and M. Przasnyski. *Surf. Sci.*, 43:662, 1974.

[27] W. J. Pleth. *J. Phys. Chem.*, 86:3166, 1982.

[28] A. Pyatenko, M. Yamaguchi, and M. Suzuki. *J. Phys. Chem. C*, 111:7910, 2007.

[29] A. Pyatenko, M. Yamaguchi, and M. Suzuki. *J. Phys. Chem. B*, 109:21608, 2005.

[30] F. W. Campbell, S. R. Belding, R. Baron, L. Xiao, and R. G. Compton. *J. Phys. Chem. C*, 113:9053, 2009.

[31] R. E. White, J. O' M. Bockris, and B. E. Conway, editors. *Modern Aspects of Electrochemistry*. Kluwer, New York, 1999, P. 69.

Chapter 12

Nanoparticle-electrode collision processes: The electroplating of bulk cadmium on impacting silver nanoparticles

Following the previous chapter, we report in this chapter, for the first time, the *bulk* deposition (electroplating) of a metal onto nanoparticles during collisions with electrode. Experiments show that for silver nanoparticles, multiple layers of Cd atoms can be electroplated onto the silver nanoparticles (AgNPs) from aqueous Cd^{2+} during collisions with a glassy carbon electrode held at a suitably reducing potential, and an average of 19 atomic layers of cadmium are found to be deposited in the few milliseconds that the NP is in contact with the electrode. For comparison, results are also presented for the underpotential deposition of Cd onto AgNPs under similar conditions.

This work was carried out in cooperation with Dr. Neil V. Rees and has been published in *Chemical Physics Letters*, 2011, 511, 183.

12.1 Introduction

The electrochemical signatures of impacts between particles and wet electrode surfaces were first reported in 1995 [1–5]. Since then several studies have investigated the non-faradaic [6–13] and faradaic charge transfer transients [14–21] that can arise during such impacts. Faradaic processes have been identified relatively recently; Bard *et al*. have identified electrocatalytic processes occurring on the surface of NPs during collisions [14–17]. Chapter 6 demonstrated the exhaustive electro-oxidation of AgNPs [18] during collisions enabling a sample of AgNPs to be sized and identified. Use of this anodic particle coulometry (APC) method has also enabled measurement of NP aggregation effects and sticking coefficients of AgNPs with wet electrode surfaces [19, 32]. In addition, the underpotential deposition (UPD) of thallium onto AgNPs has been observed [20].

In this chapter, we extend our metal deposition investigations to report the first confirmed bulk deposition of multilayers of metal atoms onto a metal NP during NP-electrode impacts, by electroplating cadmium onto AgNPs. Comparison is made with UPD of Cd on the same AgNPs. The deposition has synthetic application in the facile formation of metal NPs with different core and shell metallic compositions.

12.2 Experimental

AgNPs were synthesised according to the method of Pyatenko *et al*. [21–23] and characterised *via* SEM imaging to have a mean radius of 45 ± 3 nm. AgNPs were dispersed by ultrasound prior to adding to the solution. An aliquot of AgNPs was determined to give a particle density of 9×10^{12} particles dm^{-3} in the volume of electrolyte used in the reaction cell. Cadmium chloride and sodium chloride (Aldrich, >99%) were used as received. Deposition solutions were made of 1 mM $CdCl_2$ and 0.10 M NaCl, using ultrapure water of resistivity ~ 18.2 MΩcm (Millipore) and degassed thoroughly with N_2 (oxygen free, BOC Gases plc) and an atmosphere of N_2 maintained during the experiment. Experiments were

conducted within a faraday cage using a μAutolab III potentiostat with a time resolution shorter than 0.1 ms (Metrohm-Autolab BV, Utrecht, Netherlands) and three-electrode arrangement: a 11 μm radius glassy carbon (GC) working electrode (BASi Inc), a graphite counter electrode, and a Ag/AgCl reference electrode (Radiometer, Copenhagen). Impact spikes were analysed using Origin v.8.1 (www.OriginLab.com) for spike identification and integration, and electrical noise reduction [18].

12.3 Results and Discussion

First, the voltammetry of cadmium was recorded at a scan rate of 50 mV s^{-1} on a bare glassy carbon (GC) electrode (diameter of 3 mm) and the same GC electrode covered with immobilised AgNPs [24–27] immersed in a 1 mM solution of $CdCl_2$ (aq) and 0.10 M NaCl, as shown in Figure 12.1. On bare GC a single cathodic deposition peak was observed at -0.82V (vs Ag/AgCl), whereas on the AgNP-modified GC electrode the same peak was observed at -0.75 V, along with a cathodic UPD feature at -0.46 V which is in good agreement with the literature [28]. We note that the significant reductive features reported for the desorption and discharge of chloride ions on Ag(111) [29] are not apparent under our experimental conditions and do not present interference with the UPD peak.

Second, a GC microelectrode (radius 11 μm) was placed in a degassed solution of 1 mM $CdCl_2$ and 0.1 M KCl and the potential held at -0.55 V (the potential where underpotential deposition is found to occur). An aliquot of dispersed AgNPs were then added to the solution which was then agitated by bubbling with N_2. Impact transients were recorded as shown in Figure12.2. The impact transients were observed as sharp, reductive spikes of duration 1-10 ms and peak heights of several nA, similar to those reported previously for NP impact events [18–20]. Over one hundred impact spikes were recorded and analysed according to a previously published procedure [18]. The frequency of collisions is consistent with previous measurements of *ca.* 1.8 collisions s^{-1} at this size electrode with the same concentration of NPs (9×10^{12} particles dm^{-3}). No spikes were

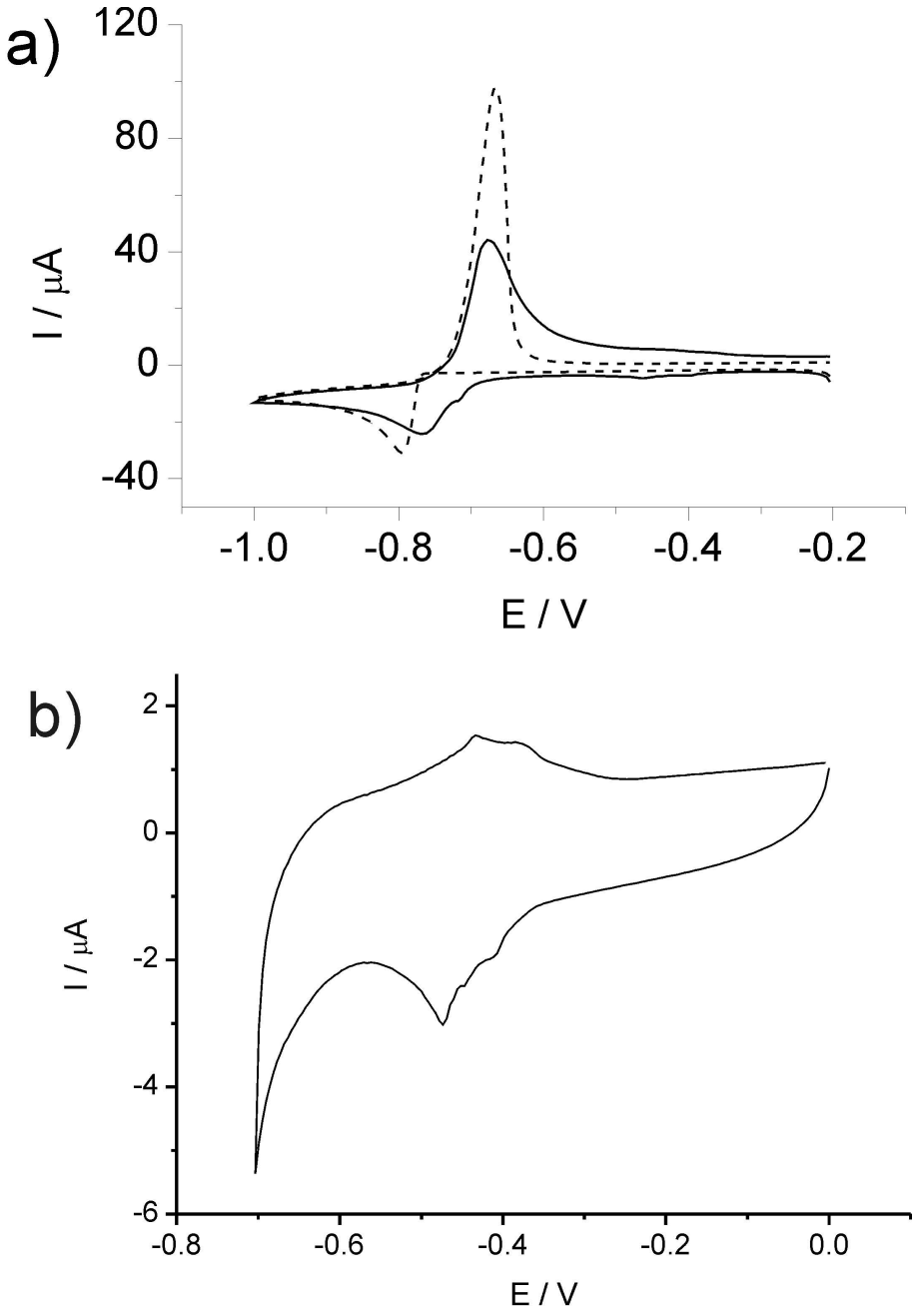

Figure 12.1: Cadmium deposition on bare GC (- - -) and AgNP-modified GC (—) electrodes: (a) full voltammograms, and (b) underpotential deposition region. Experimental details are given in the text.

found to occur when the electrode was potentiostatted at potentials more positive than the UPD feature (e.g. at -0.30 V), confirming that the reductive transients were due to the deposition of cadmium on the AgNPs during the collisions with the GC electrode surface:

$$Cd^{2+}(aq) + 2e^{-} \rightarrow Cd(NP) \tag{12.1}$$

Analysis of the spikes according to a previously described method [20], enables the charge passed per impact spike to be converted into an approximate coverage of an average single nanoparticle, since the charge passed per impact transient, Q, is related to the number of electrons passed, N, *via* the electronic charge according to

$$Q = eN \tag{12.2}$$

and a surface area (S) can be calculated for a single, fcc geometry AgNP with knowledge of the Ag atomic radius, r_A.

$$S = 24{r_A}^2 N^{2/3} \tag{12.3}$$

This therefore allows monolayer coverage of Cd atoms ($\theta = 1$) to be calculated to be 9.1×10^5 atoms for a mean AgNP. Figure 12.2 shows that in the case of Cd UPD, the agreement of the experimental data to approximately monolayer coverage is very good: at these ionic strengths, agglomeration of AgNPs is rapid to the point where after 20 mins less than 20% of the AgNP species present are in the form of single dispersed NPs, the remainder being larger cluster species [19]. The most common clusters observed in [19] were of 4 and 8 NPs, which have surface areas of 3 and 4 times greater than the single NP used as the basis for the scale in Figure 12.2.

Next, the bulk deposition of cadmium onto AgNPs was investigated by first verifying the deposition of Cd onto bare GC. The GC microelectrode was placed in a degassed solution of 1 mM $CdCl_2$ and 0.10 M NaCl, and the potential held at -0.74 V for 5 seconds

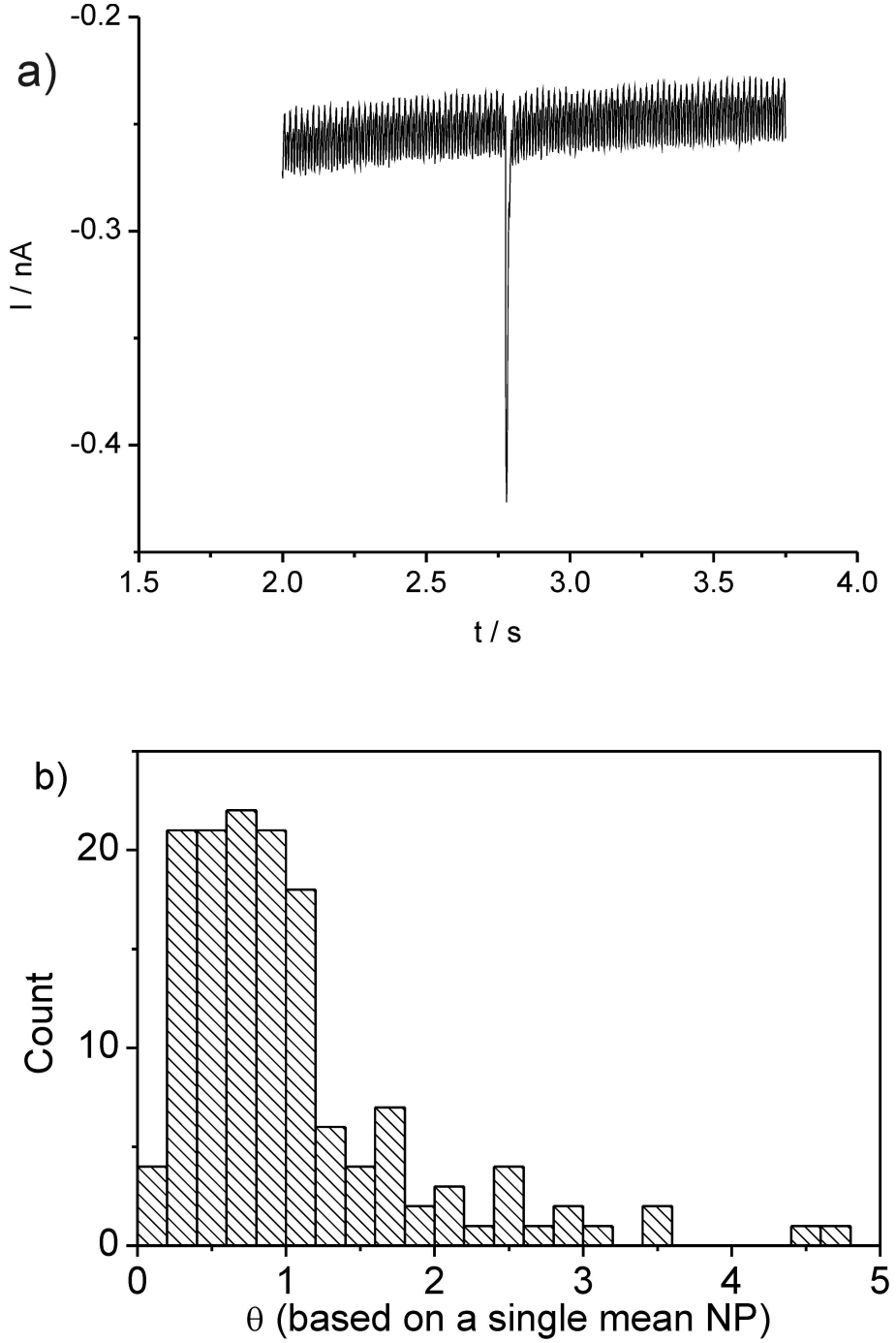

Figure 12.2: a) A typical impact transient at -0.55 V, and b) a histogram showing the number of impacts in terms of layer coverage of an average AgNP, see text for comments on the effect of aggregation.θ represents monolayer coverage.

and then smoothly swept back to +0.5 V at a scan rate of 20 mV s^{-1} in order to observe the anodic stripping of any deposited metals. As shown in Figure 12.3, no direct deposition of Cd onto GC was observed (Figure 12.1 indicates the Cd stripping peak commences at -0.70 V).

Additions of aliquots of AgNPs under the same conditions resulted in numerous reductive collision spikes being recorded, as illustrated in Figure 12.4. These spikes were considerably larger than those observed for UPD processes and were of the order of 10^{-12} C per spike. In this case, Cd has clearly been deposited, due to the clear cadmium stripping peak observed in the anodic sweep. The charge passed under the Cd stripping peak was found to be *ca*. 6.5×10^{-10} C (an average of 5 experiments): 6-60 times greater than the total charge passed under the impact spikes, leading to the conclusion that at -0.74 V the majority of the Cd bulk deposition occurs at adsorbed AgNPs. Analysis of the Ag stripping peak at +0.05 V indicates that an average of 5.2×10^{-10} C charge is passed, corresponding to *ca*. 168 single AgNPs.

Next, the same experiments were performed at a potential of -0.73 V, and analogous "step-sweep" plots are given in Figure 12.5. However, at this potential, no discernible Cd stripping feature is observed in the presence of AgNPs despite there being significant deposition impact spikes (average charge = 4.4×10^{-12} C). The frequency of collisions is consistent with previous measurements of ca. 1.8 collisions s^{-1} at this size electrode with the same concentration of NPs (9×10^{12} particles dm^{-3}). We speculate that there is in fact some Cd deposition on adsorbed AgNPs (formed by sticking collisions between the NPs and the electrode), but that the stripping feature is too small and broad due to surface alloying [29–31] to be reliably measured above the baseline.

Analysis of the deposition spikes at -0.73 V yields a distribution of charges passed per impact, which can be converted into an approximate coverage of an average single nanoparticle using equations (12.2) and (12.3) (as described above for the UPD impacts). Figure 12.6 shows the distribution of NP coverages confirming that multilayers of Cd are

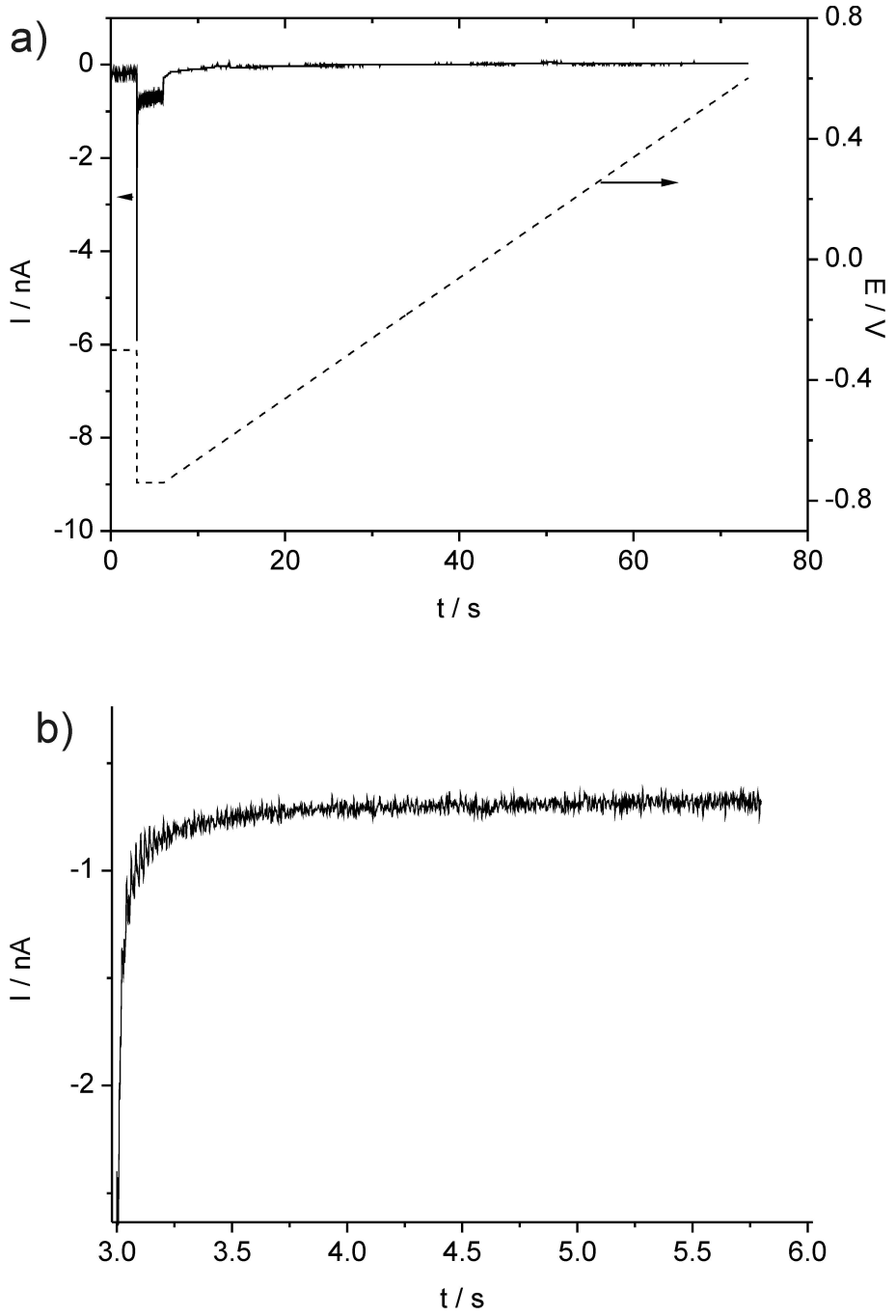

Figure 12.3: a) Potential step-sweep experiment of GC electrode (r = 11 μm) in 1 mM $CdCl_2$ in 0.10 M NaCl. Potential held at -0.74 V (vs Ag/AgCl) and scanned positive at 20 mV s^{-1}. b) shows an enlargement of the "transient" region after noise reduction to confirm no spikes.

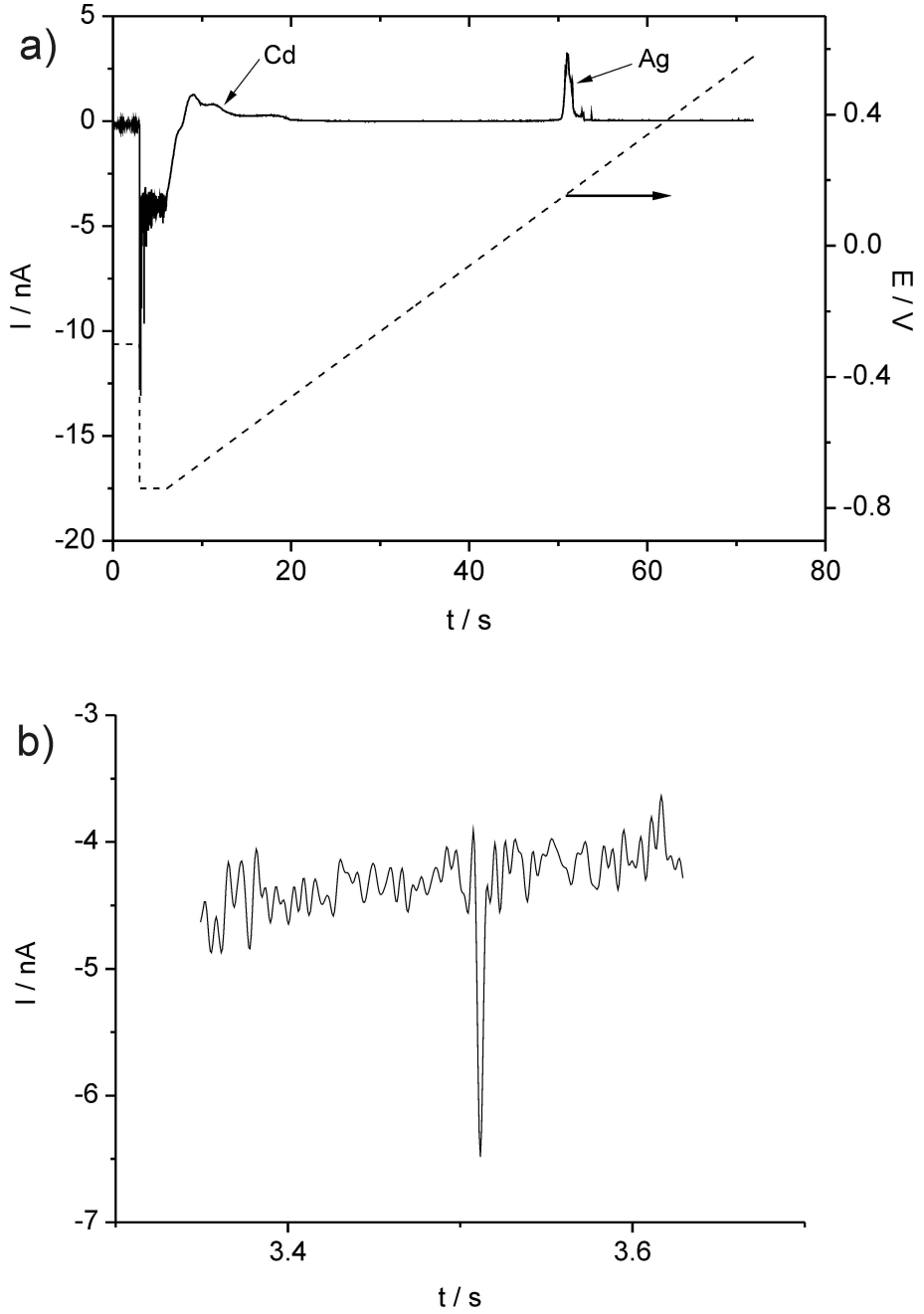

Figure 12.4: As for Figure 12.3 except for 9×10^{12} particles dm^{-3} of AgNPs are present. Details of charges passed are given in the text. b) shows an enlargement of the "transient" region post-noise reduction.

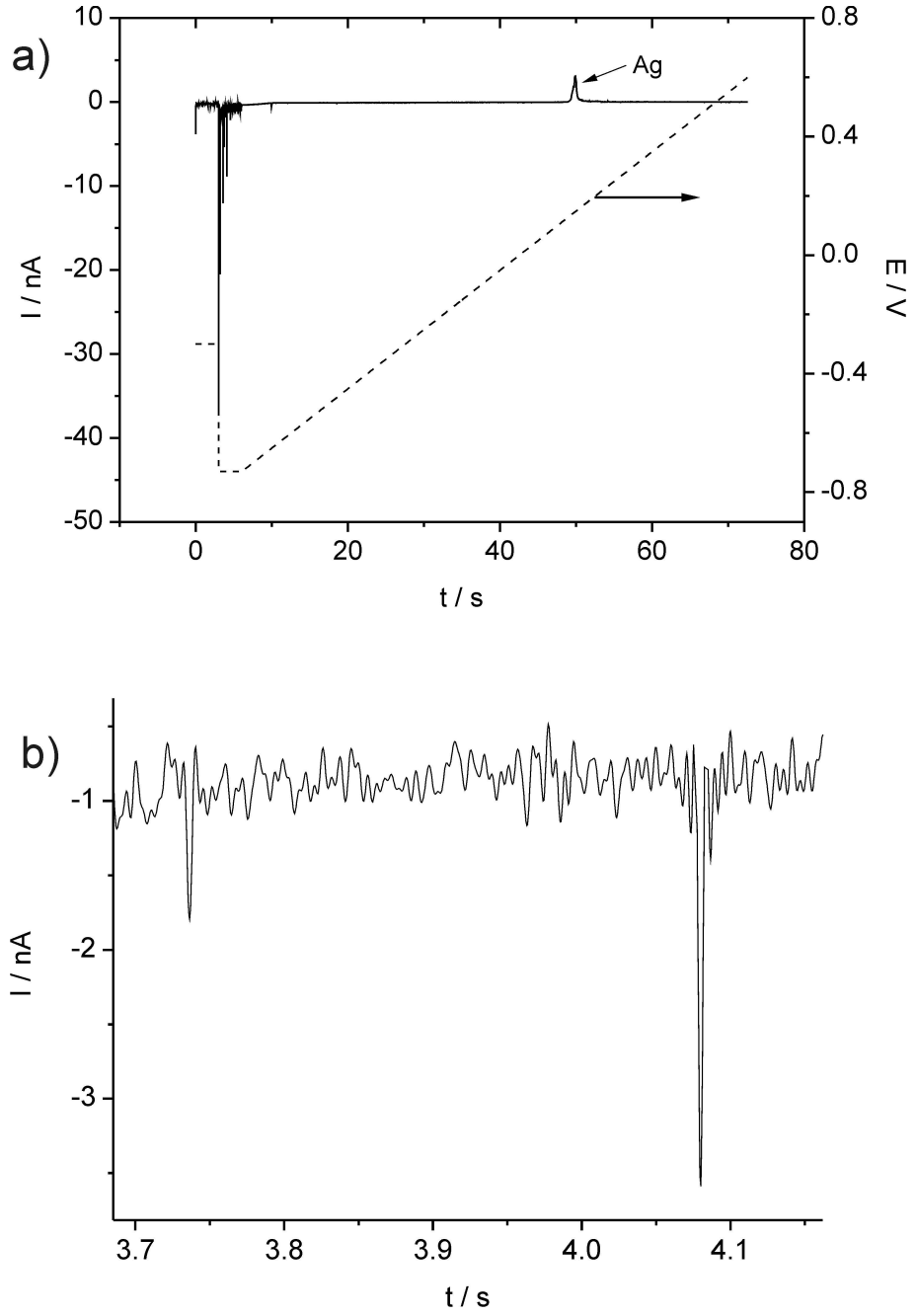

Figure 12.5: a) Potential step-sweep experiment of GC electrode (r = 11 μm) in 1 mM $CdCl_2$ in 0.10 M NaCl. Potential held at -0.73 V (vs Ag/AgCl) and scanned positive at 20 mV s^{-1}. No Cd stripping feature is observed. b) shows an enlargement of the "transient" region after noise reduction showing spikes.

deposited onto the AgNPs during collision.

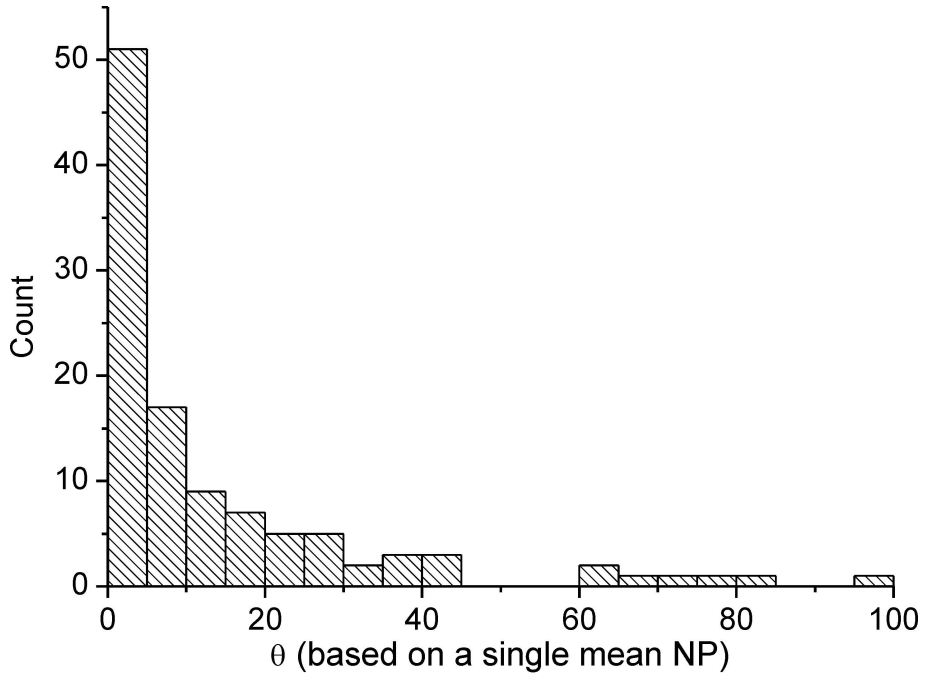

Figure 12.6: Histogram showing the number of impacts in terms of layer coverage of an average AgNP. θ represents monolayer coverage.

12.4 Conclusions

We therefore conclude that for the first time, electroplating has been demonstrated to occur at nanoparticles during their collisions with an inert electrode, in this case the bulk deposition of Cd onto AgNPs ((14.1)). The UPD and electroplating of metal onto NPs also suggest possible synthetic route for core-shell NPs.

Bibliography

[1] M. Heyrovský, J. Jirkovský, and B. R. Müller. *Langmuir*, 11:4293, 1995.

[2] M. Heyrovský, J. Jirkovský, and M. Struplova-Bartackova. *Langmuir*, 11:4300, 1995.

[3] M. Heyrovský, J. Jirkovský, and M. Struplova-Bartackova. *Langmuir*, 11:4309, 1995.

[4] I. D. Charlton and A. P. Doherty. *J. Phys. Chem. B*, 104:8061, 2000.

[5] I. D. Charlton and A. P. Doherty. *Anal. Chem.*, 72:687, 2000.

[6] D. Hellberg, F. Scholz, F. Schauer, and W. Weitschies. *Electrochem. Commun.*, 4:305, 2002.

[7] F. Scholz, D. Hellberg, F. Harnisch, A. Hummel, and U. Hasse. *Electrochem. Commun.*, 6:929, 2004.

[8] D. Hellberg, F. Scholz, F. Schubert, M. Lovric, D. Omanovic, V. A. Hernandez, and R. Thede. *J. Phys. Chem. B*, 109:14715, 2005.

[9] C. E. Banks, N. V. Rees, and R. G. Compton. *J. Electroanal. Chem.*, 535:41, 2002.

[10] C. E. Banks, N. V. Rees, and R. G. Compton. *J. Phys. Chem. B*, 8:5810, 2002.

[11] N. V. Rees and R. G. Compton. *Analyst*, 132:635, 2007.

[12] N. V. Rees, C. E. Banks, and R. G. Compton. *J. Phys. Chem. B*, 108:18391, 2004.

[13] A. D. Clegg, N. V. Rees, C. E. Banks, and R. G. Compton. *ChemPhysChem*, 7:807, 2006.

[14] X. Xiao, S. Pan, J. S. Jang, F. R. F. Fan, and A. J. Bard. *J. Phys. Chem. C*, 113:14978, 2009.

[15] X. Xiao and A. J. Bard. *J. Am. Chem. Soc.*, 129:9610, 2007.

[16] S. J. Kwon, F. R. F. Fan, and A. J. Bard. *J. Am. Chem. Soc.*, 132:13615, 2010.

[17] X. Xiao, F. R. F. Fan, J. Zhou, and A. J. Bard. *J. Am. Chem. Soc.*, 130:16669, 2008.

[18] Y. G. Zhou, N. V. Rees, and R. G. Compton. *Angew. Chem., Int. Ed.*, 50:4219, 2011.

[19] N. V. Rees, Y. G. Zhou, and R. G. Compton. *ChemPhysChem*, 12:1645, 2011.

[20] Y. G. Zhou, N. V. Rees, and R. G. Compton. *ChemPhysChem*, 12:2085, 2011.

[21] A. Pyatenko, M. Yamaguchi, and M. Suzuki. *J. Phys. Chem. B*, 111:7910, 2007.

[22] A. Pyatenko, M. Yamaguchi, and M. Suzuki. *J. Phys. Chem. B*, 109:21608, 2005.

[23] F. W. Campbell, S. R. Belding, R. Baron, L. Xiao, and R. G. Compton. *J. Phys. Chem. C*, 113:9053, 2009.

[24] D. M. Kolb, M. Przasnyski, and H. Gerischer. *J. Electroanal. Chem.*, 54:25, 1974.

[25] D. M. Kolb and H. Gerischer. *Surf. Sci.*, 51:323, 1975.

[26] H. Gerischer, D. M. Kolb, and M. Przasnyski. *Surf. Sci.*, 43:662, 1974.

[27] W. J. Plieth. *J. Phys. Chem.*, 86:3166, 1982.

[28] F. W. Campbell and R. G. Compton. *Int. J. Electrochem*, 5:407, 2010.

[29] V. D. Jovic and B. M. Jovic. *Electrochim. Acta*, 47:1777, 2002.

[30] R. Vidu, N. Hirai, and S. Hara. *PhysChemChemPhys*, 3:3320, 2001.

[31] S. G. Garcia, D. R. Salinas, and G. Staikov. *Surf. Sci.*, 576:9, 2005.

[32] Y. G. Zhou, N. V. Rees, and R. G. Compton. *Chem. Phys. Lett.*, 514:291, 2011.

Chapter 13

The electrochemical detection and non-destructive sizing of tagged nanoparticles via particle-electrode collisions: tag-redox coulometry (TRC)

In the previous two chapters we showed UPD and bulk deposition of metal onto AgNPs during collisions. In this work, AgNPs are tagged with electroactive molecules prior to the impacts. The use of particle-impact coulometry in identifying and quantifying nanoparticles tagged (or labelled) with electroactive molecules is demonstrated via the detection of 1,4-nitrothiophenol-tagged silver nanoparticles in aqueous dispersion at potentials more negative than -0.17 V (vs Ag/AgCl, the reduction potential of nitrothiophenol) via monitoring of particle-electrode collisions. Using this method, we for the first time, realise non-destructive sizing and detection of nanoparticles. Tag-redox coulometry (TRC) thus significantly expands the scope of nanoparticle sizing by particle-impact methods.

This work was carried out in cooperation with Dr Neil V. Rees and has been published in *Chemical Communications*, 2012, 48, 2510 and *Chemical Physics Letters*, 2012, 525-526, 69.

13.1 Introduction

Tagged nanoparticles (NPs) have become increasingly used in sensing and biosensing applications. In one class of applications, modified silver or gold NPs are used to detect molecules binding to the modifier via surface-sensitive spectroscopies such as SPR and SERS [1–6]. Similarly, fluorescent and colour-coded tags have also been used to enable rapid optical detection of target molecules [7–10]. Of particular interest has been the use of electrochemical methods to detect the tagged NPs: typically square wave or cyclic voltammetry [11–15]. Other methods for detecting tagged NPs include ICP-MS [16], and electrochemiluminescence [17]. In these applications, the tagged NPs have been immobilised onto the electrode before the voltammetric or electrochemical measurement.

The recently growing field of particle-electrode collisions [18] has, amongst other results, demonstrated the ability to detect electrochemical processes occurring at the surface of naked NPs during their impacts with inert electrode surfaces [19–26]. On the other hand, anodic particle coulometry (APC) has recently been developed and investigated as a means of characterising metal nanoparticles (NPs) such as silver and gold [26–28]. In this method, collisions between individual NPs and an inert electrode are observed as current spikes of approximately millisecond duration, provided the electrode is potentiostatted at a potential more positive than the formal potential for the oxidation of the NP material. In the cases thus far reported (AgNPs and AuNPs), this has resulted in the exhaustive oxidation of the NP: that is, the APC method is quantitative but destructive.

In this chapter we report the first use of particle coulometry to monitor the collisions of tagged NPs, and use AgNPs tagged with 1,4-nitrothiophenol (NTP): the NTP is adsorbed onto the NPs and the NPs are modified prior to dispersion in the electrochemical cell. By potentiostatting the substrate carbon electrode at a sufficiently negative potential, sharp reductive current transients are observed as the tagged NPs collide with the electrode corresponding to reduction of the attached NTP molecules. Using this method, we demonstrate that tagged NPs may be used to achieve the same sizing and detection role as

conventional APC on naked NPs: significantly this tag-redox coulometry (TRC) method is non-destructive and very considerably widens the scope of particle-impact coulometry.

13.2 Experimental

Citrate-capped AgNPs of mean radius 45 ± 5 nm were synthesised according to the method of Pyatenko *et al*. [29, 30]. Sodium perchlorate (≥98%, $NaClO_4$) and NTP (80%) were supplied by Sigma-Aldrich. Perchloric acid (70%, $HClO_4$) was purchased from Fisher Chemicals. All solutions were made using ultrapure water of resistivity ~ 18.2 MΩcm at 298K (Millipore). AgNPs were modified with NTP by mixing AgNPs colloid with 0.5 mM NTP aqueous solution with a volume ratio of 1:1 for 2 to 40 hours. The excess NTP molecules were removed by centrifuging and washing the tagged NPs three times.

The electrochemistry experiments were conducted within a faraday cage using a μAutolab III (Metrohm-Autolab BV, Utrecht, Netherlands) and a three electrode arrangement. Working electrodes used were: a bare silver macro electrode (0.3 mm in diameter), or a bare glassy carbon (GC, 3 mm in diameter) electrode, or a AgNP-modified GC electrode, or a 11 μm diameter GC microelectrode. Reference and counter electrodes were a Ag/AgCl (Radiometer, Copenhagen), and a graphite rod respectively. To modify the GC electrode, 2.5 μL of the suspension of AgNPs was drop-cast on the GC electrode and left to dry under a N_2 atmosphere.

13.3 Results and Discussion

First, control experiments were conducted to confirm the voltammetry of NTP adsorbed on silver and GC electrode surfaces. The Ag macroelectrode was first dipped into a 0.1 mM solution of NTP for 1 hour, then sonicated in water to remove the excess molecules from the electrode surface, and then transferred to a solution of 100 mM $NaClO_4$ and

10 mM $HClO_4$. Cyclic voltammograms (CV) were recorded as shown in Figure 13.1a, which shows the first reduction peak at ca -0.17 V on the silver surfaces and at *ca*. -0.31 V on naked GC: in agreement with the literature [31–33]. The first reduction peak for a NTP-tagged AgNPs modified GC macroelectrode was observed to occur at -0.167 V, corresponding to the four-electron, four-proton reduction to the hydroxylamine (see Figure 13.2). No peaks were observed for the second scan showing that a self-assembled NTP monolayer was formed on AgNPs. In the context of the following impact experiments it is important to note that there is no reduction signal observable on the bare GC macroelectrode at this potential.

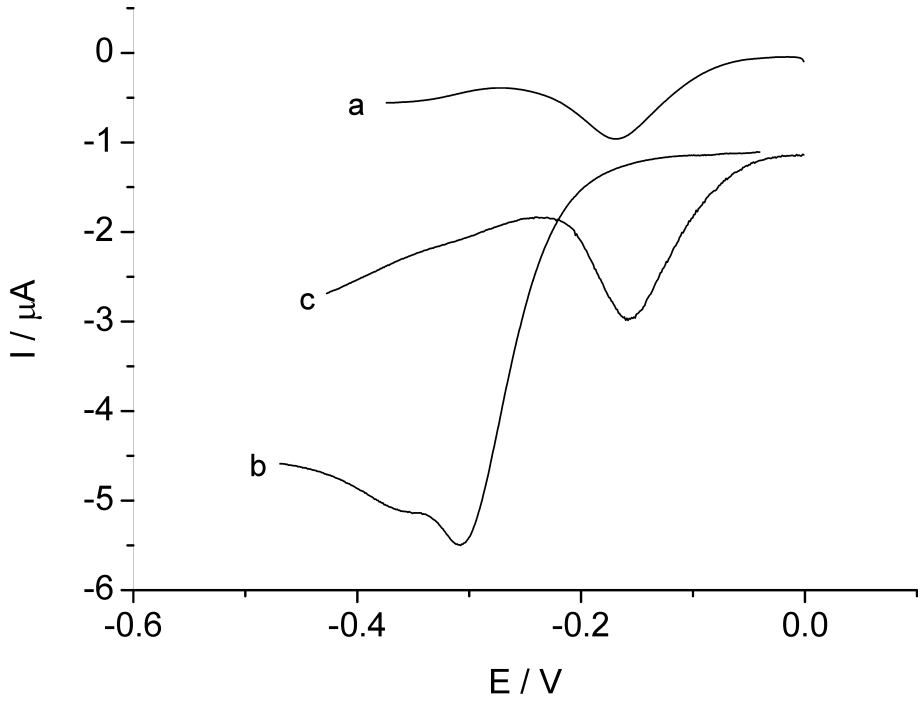

Figure 13.1: Cyclic voltammograms for (a) a NTP-modified Ag macroelectrode, (b) a NTP-modified GC macroelectrode and (c) NTP-tagged AgNPs modified GC macroelectrode. All scans were performed in a solution of 0.1 M $NaClO_4$ and 10 mM $HClO_4$ at a scan rate of 50 mV s^{-1}. Scans have been offset vertically for clarity.

To measure the particle impacts, the cell was assembled with the GC microelectrode, reference and counter electrodes, and with 20 mL of an aqueous solution of 100 mM $NaClO_4$ and 10 mM $HClO_4$ which was thoroughly degassed with nitrogen prior to the experiment. Chronoamperograms were recorded at the potential of -0.17 V in the absence

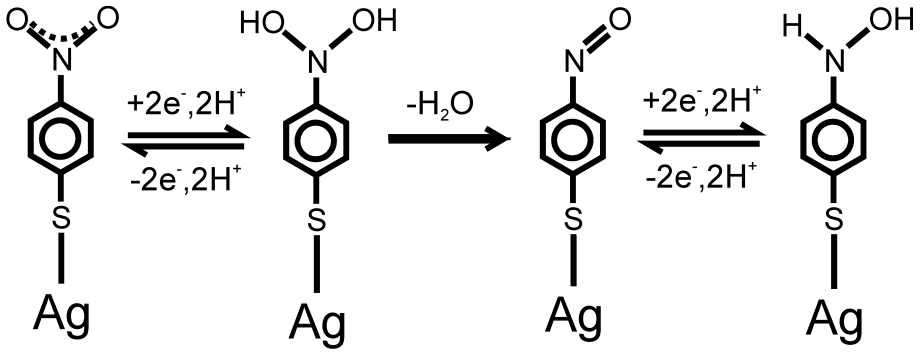

Figure 13.2: The 4-electron, 4-proton reduction of NTP.

of NPs to confirm that no impact spikes could be observed. Next, a known amount of NTP-tagged AgNPs were added, the solution briefly bubbled with nitrogen to evenly disperse NPs and the potential held first at 0 V and then at -0.17 V. No spikes were observed at the former potential whilst they were clearly observed at the latter shown in Figure 13.3(a) due to the reduction of nitro group while NTP-tagged AgNPs were in contact with the substrate GC microelectrode. Another control experiment was done at the potential of -0.17 V with untagged AgNPs in the solution and no spikes were shown (Figure 13.3(b)), confirming again that the reduction of NTP on the surface of NPs is the source of the transients. The collision frequency was found to be in the range of 0.1 s^{-1} pM^{-1} for all NP concentrations studied, which is in good agreement with our previous result for the oxidation of AgNPs [24, 27].

The variation in the average charge passed per transient was found to vary according to the length of time that the AgNPs were immersed in NTP solution during the modification process: the charge passed per impact spikes increases up to 8 h and almost levels off when the immersion time is over 8 h (see Figure 13.4).

For a modification time of 30 hours, the analysis of the obtained several hundred spikes gave a mean charge (Q_t) of 2.72×10^{-13} C passed per impact transient. Q_t, on the other hand, is related to the number of electrons passed, N_t, via the electronic charge according to

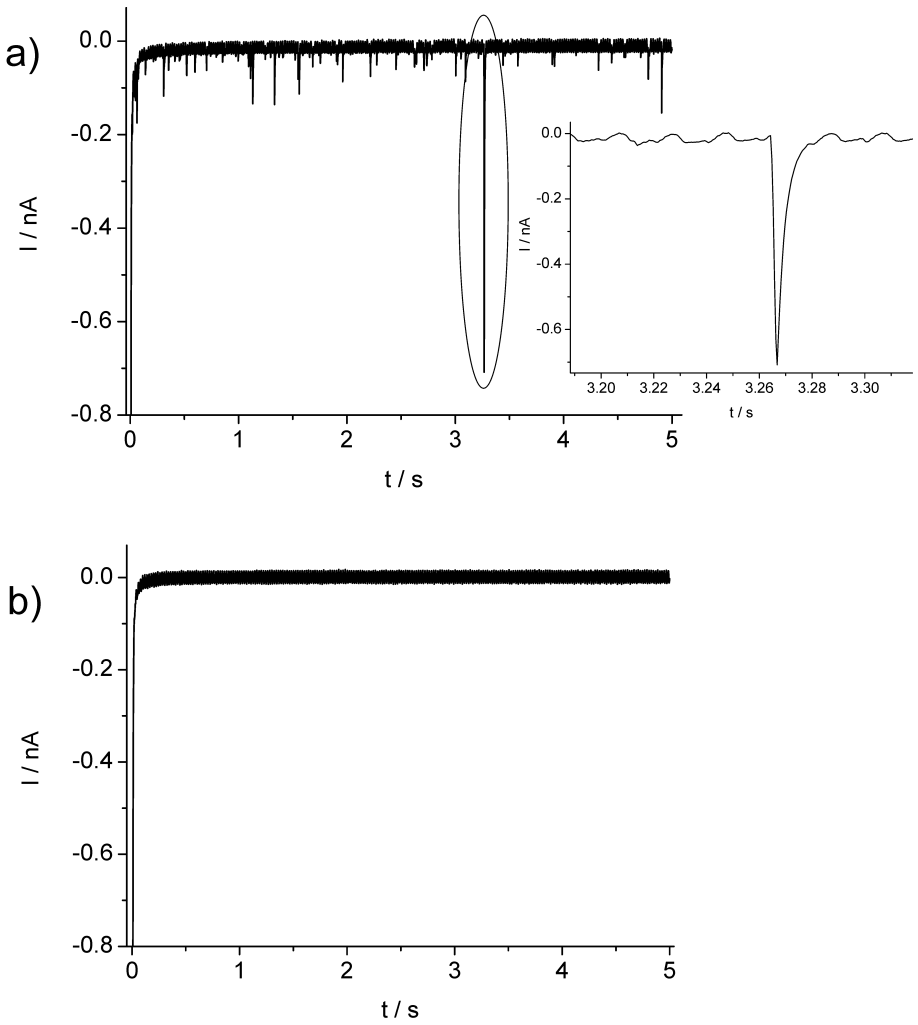

Figure 13.3: Chronoamperometric profiles showing (a) reduction spikes for NTP-tagged AgNPs with zoom of circled transient (inset) and (b) no spikes for untagged AgNPs potentiostatted at -0.17 V.

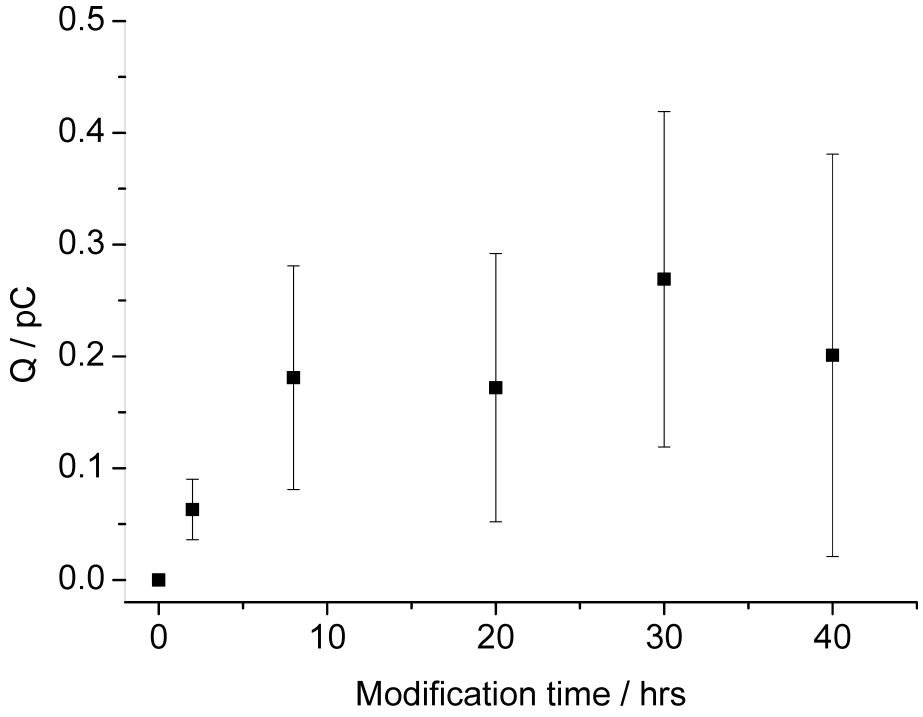

Figure 13.4: The variation of the average charge per impact transient, Q_t, with the time allowed for NTP to adsorb onto AgNPs.

$$Q_t = 4eN_t, \tag{13.1}$$

where the subscripts indicate the parameters refer to the tag molecule(NTP). This allows us to calculate an average number of NTP molecules attached to the surface of single AgNPs of 4.3×10^5. Given the surface area of a single AgNP is

$$S = 4\pi R^2 \tag{13.2}$$

and the size of a NTP molecule, and assuming NTP molecules are vertically aligned on the NPs surface, a number of 5.5×10^5 NTP molecules can be calculated in terms of a full monolayer coverage on the surface of a single AgNP. Therefore, we can conclude that an approximate monolayer of NTP was formed on the surface of AgNPs in our experiment and can be detected during the tagged NPs colliding with the electrode.

Figure 13.5 shows the distribution of charge passed per reduction spike. We note that

the majority of the charges are centred in the range of 1.0 to 4.0×10^{-13} C. The variation in the charges passed will reflect variations in (i) the NTP coverage of the NPs, (ii) the size and degree of aggregation of the NPs, (iii) the contact times between NP and electrode. In addition the contact time required to effect full reduction of the complete NTP coverage of the impacting NP will depend on NP size [34] as well as the kinetics of the NTP reduction: note there are two possible routes for the electron transfer in this scenario, namely direct electron conduction 'through' the metal NP, or a hopping mechanism around the NTP-covered surface [35, 36].

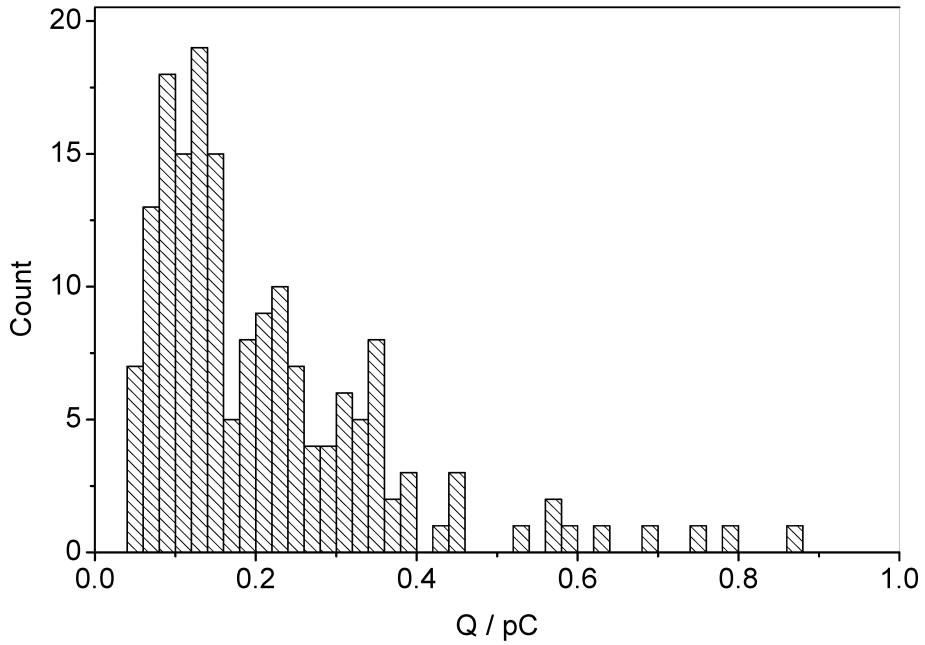

Figure 13.5: Distribution of charge passed per spike during NTP-tagged AgNPs collision with the substrate GC electrode.

Next, we demonstrate that tagged NPs may be used to achieve the same sizing and detection role as conventional APC on naked NPs. First, the APC experiment for AgNPs with a mean radius of 45 ± 5 was repeated as detailed in [26, 27], with the measurement confined to a period confined of 15-20 min. Using the previously illustrated analysis [26, 27], the distribution of the number of Ag atoms oxidised per impact thus obtained is given in Figure 13.6a, showing a dominant NP size of 43 ± 8 nm.

Second, the TRC analysis was performed on tagged AgNPs. Following equation

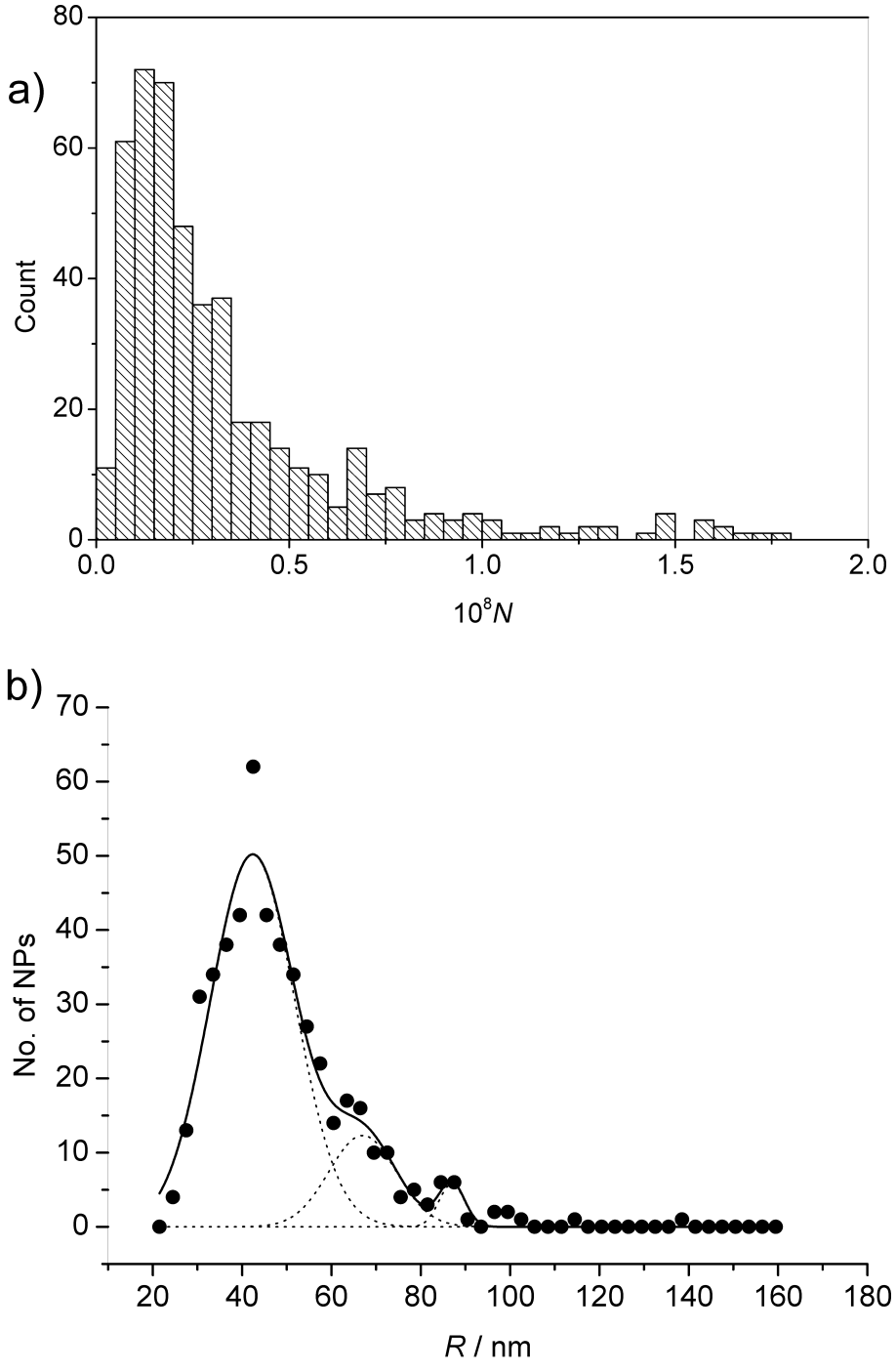

Figure 13.6: Distribution plots derived from APC experiments on bare AgNPs of nominal radius 45 nm in terms of: a) number of Ag atoms oxidised during impact spikes, and b) derived NP sizes yielding a dominant particle size of 43 ± 8 nm.

(13.1), the surface area of the bare AgNPs will be given by

$$S = \frac{N_t S_t}{f} \tag{13.3}$$

with S_t being the two-dimensional area occupied by a tag molecule, and f the fractional filling efficiency assuming optimal close-packing of tag molecules (0.91 for spheres or ellipses on a plane [37]). Combining equation (13.1) and equation (13.3) we find

$$S = \frac{S_t Q_t}{n_t f e} \tag{13.4}$$

and assuming a simple spherical geometry for the AgNP, we derive the following expression for its radius

$$R = \sqrt{\frac{S_t Q_t}{4\pi n_t f e}} \tag{13.5}$$

Calculation of S_t will therefore enable the conversion of the current spikes due to reduction of the NTP tags into a distribution of radii for the underlying AgNP cores. From a simple geometric consideration of the NTP molecule, with typical atomic radii for H, O, and S or 25, 60, and 100 pm respectively and bond lengths for N-O, C-C (aromatic), and C-H of 120, 140, and 100 pm respectively [38, 39], the two-dimensional area occupied by an NTP molecule can be described as an ellipse with major and minor radii of 235 and 155 pm. Consequently $S_t = 1.144 \pm 10^{-19}$ m^2, and together with values of $f = 0.91$ and $n_t = 4$, equation (13.5) simplifies to

$$R = 0.1256\sqrt{Q_t} \tag{13.6}$$

and application of equation (13.6) to the distribution of observed APC charges, Q_t, in Figure 13.5 is found to produce the distribution of AgNP radii in Figure 13.7a, with the dominant AgNP size being 43 ± 8 nm. This is in excellent agreement with the size results from the destructive, exhaustive oxidation APC experiment shown in Figure 13.6

and suggests that the assumption of complete, 4-electron reduction of the entire NTP monolayer is justified. For ease of comparison the two distributions are overlaid in Figure 13.7b.

This result is significant as it extends the range of NPs that can, in principle, be sized using particle-impact coulometry. Whilst APC is restricted to sizing oxidisable metal NPs, this TRC method can be applied to reduction (or oxidation) of any suitably selected electroactive tag molecule on any NP core without destroying the sample. The NP core need not even be conductive, provided that electron transport via hopping [35, 36] is sufficiently fast on the timescale of the particle impact to enable complete reduction (or oxidation) of the tag molecules.

13.4 Conclusions

We have successfully demonstrated the use of particle coulometry to monitor the collisions of tagged NPs with an electrode using AgNPs tagged with NTP. The detected signals are due to the reduction of the adsorbed NTP molecules. This method can be applied generally to identify tagged (or labelled) NPs when the labelling molecule is electroactive. Furthermore, we have successfully demonstrated the use of TRC to non-destructively size the AgNP cores, and excellent agreement is found with the previously reported destructive APC method. This result greatly expands the utility of particle impact coulometry in sizing functionalised NPs. Thus we believe this method has considerably wide application in analytical nanoscience and microfluidics [40]. In addition, the present results have potential use in conjunction with gold NPs in nano-drug formulation and delivery.

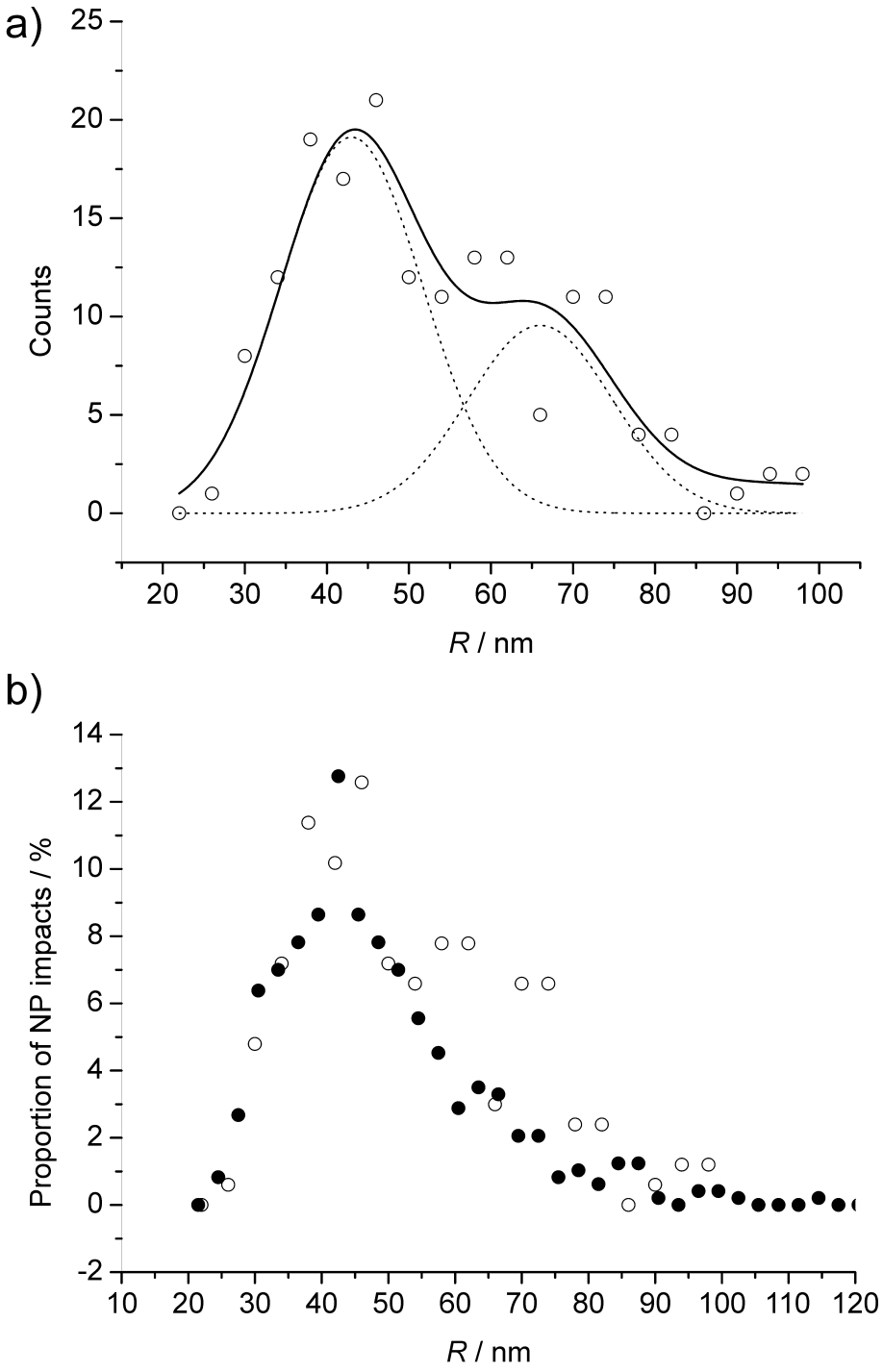

Figure 13.7: a) TRC distribution obtained from application of equation (13.6) onto the charge distribution in Figure 13.5, showing a dominant particle size of radius 43 ± 8 nm, and b) superimposed APC and TRC distributions showing the remarkably close correlation between both methods for nanoparticle sizing.

Bibliography

[1] S. Paul, D. Paul, G. R. Fern, and A. K. Ray. *J. R. Soc. Interface*, 8:1204, 2001.

[2] X. Chen, H. Liu, X. Zhou, and J. Hu. *Nanoscale*, 2:2841, 2010.

[3] L. Sun and J. Irudayaraj. *J. Phys. Chem. B*, 113:14021, 2009.

[4] J. Wang and S. H. Zhou. *Anal. Chem.*, 80:7174, 2008.

[5] L. Sun, C. Yu, and J. Irudayaraj. *Anal. Chem.*, 79:3981, 2007.

[6] S. P. Mulvaney, M. D. Musick, C. D. Keating, and M. J. Natan. *Langmuir*, 19:4784, 2003.

[7] M. Hong, X. Zhou, Z. Lu, and J. Zhu. *Angew. Chem., Int. Ed.*, 48:9503, 2009.

[8] D. R. Bae, W. S. Han, J. M. Lim, S. Kang, J. Y. Lee, D. Kang, and J. H. Jung. *Langmuir*, 26:2181, 2010.

[9] A. Agrawal, R. Deot, G. D. Wang, M. D. Wang, and S. Nie. *Proc. Natl. Acad. Sci. USA*, 105:3298, 2008.

[10] Z. S. Wu, J. H. Jiang, L. Fu, G. L. Shen, and R. Q. Yu. *Anal. Biochem.*, 353:22, 2006.

[11] Z. Dai, A. N. Kawde, Y. Xiang, J. T. La Belle, J. Gerlach, V. P. Bhavanandan, L. Joshi, and J. Wang. *J. Am. Chem. Soc.*, 128:10018, 2006.

[12] M. Ganesana, G. Istarnboulie, J. L. Marty, T. Noguer, and S. Andreescu. *Biosens. Bioelectron.*, 30:43, 2011.

[13] L. D. Li, Z. B. Zheng, H. T. Zhao, L. Guo, and X. Mu. *Sens. Actuators, B*, 149:110, 2010.

[14] J. A. Ho, H. C. Chang, N. Y. Shih, L. C. Wu, Y. F. Chang, C. C. Chen, and C. Chou. *Anal. Chem.*, 82:5944, 2010.

[15] L. J. Lai, Y. W. Yang, Y. K. Lin, L. L. Huang, and Y. H. Hsieh. *Colloids Surf., B*, 68:130, 2009.

[16] S. Hu, R. Liu, S. Zhang, Z. Huang, Z. Xing, and X. Zhang. *J. Am. Soc. Mass Spectrom.*, 20:1096, 2009.

[17] Q. Xu, J. Liu, Z. He, and S. Yang. *Chem. Commun.*, 46:8800, 2010.

[18] N. V. Rees, Y. G. Zhou, and R. G. Compton. *RSC Adv.*, 2:379, 2012.

[19] A. J. Bard and X. Y. Xiao. *J. Am. Chem. Soc.*, 129:9610, 2007.

[20] A. J. Bard, X. Y. Xiao, F. R. F. Fan, and J. P. Zhou. *J. Am. Chem. Soc.*, 1330:16669, 2008.

[21] A. J. Bard, X. Y. Xiao, S. L. Pan, J. S. Jang, and F. R. F. Fan. *J. Phys. Chem. C*, 113:14978, 2009.

[22] S. J. Kwon, F. R. F. Fan, and A. J. Bard. *J. Am. Chem. Soc.*, 132:13165, 2010.

[23] S. J. Kwon, H. Zhou, F. R. F. Fan, V. Vorobyev, B. Zhang, and A. J. Bard. *Phys. Chem. Chem. Phys.*, 13:5394, 2011.

[24] Y. G. Zhou, N. V. Rees, and R. G. Compton. *ChemPhysChem*, 12:2085, 2011.

[25] Y. G. Zhou, N. V. Rees, and R. G. Compton. *Chem. Phys. Lett.*, 511:183, 2011.

[26] N. V. Rees, Y. G. Zhou, and R. G. Compton. *ChemPhysChem*, 12:1645, 2011.

[27] Y. G. Zhou, N. V. Rees, and R. G. Compton. *Angew. Chem., Int. Ed.*, 50:4219, 2011.

[28] Y. G. Zhou, N. V. Rees, J. Pillay, R. Tshikhudo, S. Vilakazi, and R. G. Compton. *Chem. Commun.*, 48:224, 2012.

[29] A. Pyatenko, M. Yamaguchi, and M. Suzuki. *J. Phys. Chem. C*, 111:7910, 2007.

[30] A. Pyatenko, M. Yamaguchi, and M. Suzuki. *J. Phys. Chem. B*, 109:21608, 2005.

[31] H. Tsutsumi, S. Furumoto, M. Morita, and Y. Matsuda. *J. Colloid Interface Sci.*, 171:505, 1995.

[32] I. Rubenstein. *J. Electroanal. Chem.*, 183:379, 1985.

[33] P. Abiman, G.G. Wildgoose, and R. G. Compton. *Electroanalysis*, 19:437, 2007.

[34] I. J. Cutress, N. V. Rees, Y. G. Zhou, and R. G. Compton. *Chem. Phys. Lett.*, 514:58, 2011.

[35] C. Amatore, Y. Bouret, E. Maisonhaute, J. I. Goldsmith, and H. D. Abru na. *ChemPhysChem*, 2:130, 2001.

[36] C. Amatore, Y. Bouret, E. Maisonhaute, J. I. Goldsmith, and H. D. Abru na. *Chem.-Eur. J.*, 7:2206, 2001.

[37] T. Matsumoto and W. Nowacki. *Zeitsch. Kristall*, 12:401, 1996.

[38] J. C. Slater. *J. Chem. Phys.*, 41:3199, 1964.

[39] D. R. Lide, editor. *CRC Handbook of Chemistry and Physics, eightysixth edn.* CRC Press, Boca Raton, USA, 1993.

[40] M. Pumera. *Chem. Commun.*, 47:5671, 2011.

Chapter 14

The charge transfer kinetics of the oxidation of silver and nickel nanoparticles via particle-electrode impact electrochemistry

Earlier chapters have discussed the direct electrooxidation of silver and nickel nanoparticles in aqueous solution via their collisions with a carbon electrode. In this chapter, the average charge passed per impact in a variation with potential is analysed, showing that AgNPs display an electrochemically fast ("reversible") one-electron oxidation, whilst the NiNPs exhibit slow ("irreversible") 2-electron kinetics.

This work was carried out in cooperation with Dr. Neil V. Rees, and has been accepted by *PhysChemChemPhys*, 2012, 14, 14354.

14.1 Introduction

The collisions between metal nanoparticles (NPs) and an inert electrode held at a suitably oxidising potential such that the nanoparticle becomes completely oxidised have been shown to be a valuable source of information via the method of anodic particle coulometry (APC): quantities such as size distributions, concentrations, degree of aggregation, and nanoparticle identity have been shown to be obtainable [1–10]. Very recently, we have been able to show that by considering both partial and full oxidation of the nanoparticles, the charge transfer kinetics of the oxidation of the metal nanoparticles can also be determined by this method [11].

In this chapter we investigate the behaviour of both silver and nickel nanoparticles (AgNPs and NiNPs) in collision with carbon electrodes using APC, to extract quantitative information on their charge transfer kinetics.

14.2 Experimental

Nickel nanoparticles (NiNPs) of mean radii 26 nm were purchased from Nanostructured & Amorphous Materials, Inc. (Houston, Texas, USA), and have a NiO shell of between 2-8 nm thick [12]. Citrate-capped AgNPs of mean radius 13 ± 2 nm were synthesized according to the method of Pyatenko *et al*. [13, 14]. NP sizes were confirmed via APC and SEM imaging. Sodium perchlorate (≥98%, $NaClO_4$), sodium dihydrogen citrate ($NaC_6O_7H_7$, >99.5%), and potassium chloride (>99.5% Riedel-de-Haan) were supplied by Sigma-Aldrich and used as received. Perchloric acid (70%, $HClO_4$) was purchased from Fisher Chemicals. All solutions were made using ultrapure water of resistivity ~ 18.2 MΩcm at 298K (Millipore). NP suspensions were obtained by adding 1.0 g L^{-1} of NPs to dearated ultrapure water. Prior to adding aliquots to the electrochemical cell, the suspensions were thoroughly dispersed by sonication for several minutes. Experiments were conducted within a double faraday cage using a μAutolab III (Metrohm-Autolab

BV, Utrecht, Netherlands) and a three electrode arrangement. The working electrodes used in this study was a carbon fibre microelectrode (BASi Inc, Stareton, Warks. UK) of radius 6.9 μm. A saturated calomel reference electrode (SCE, Radiometer Ltd, Crawley, UK) was used, with a graphite rod as counter electrode. All experiments were conducted under an argon atmosphere and solutions thoroughly purged with argon.

14.3 Results and Discussion

14.3.1 Charge transfer kinetics of AgNPs

The APC of AgNPs has been reported previously [7, 10]. A carbon fiber microelectrode (radius 6.9 μm) was placed in a degassed citrate solution, and a known concentration of pre-dispersed AgNPs added. The average size of the single AgNPs had previously been determined to be 13 ± 2 nm (corresponding to ca. 6×10^5 atoms), and that due to aggregation effects the average radius of a AgNP cluster over the timescale of the chronoamperometric experiments was 28nm [10]. The electrode potential was held at +0.5 V (relative to saturated Ag/AgCl) beyond the onset potential for impact spikes [7], according to the process

$$\mathrm{Ag(NP)} - \mathrm{e}^- \rightarrow \mathrm{Ag}^+\mathrm{(aq)}. \tag{14.1}$$

Several chronoamperograms were recorded at this electrode potential such that more than 250 impact spikes were obtained. This was repeated at a range of potentials from 0.0 to 0.8 V (vs SCE). The chronoamperograms were analysed according to our published procedure [7] to obtain the charge passed under each impact spike: Figure 14.1 shows how the average charge per impact varies with electrode potential.

We then analysed this data according to the theoretical results recently developed for fully reversible and irreversible charge transfer kinetics during oxidative particle impacts [11]. During the oxidation of the metal NP, the charge passed will be given by

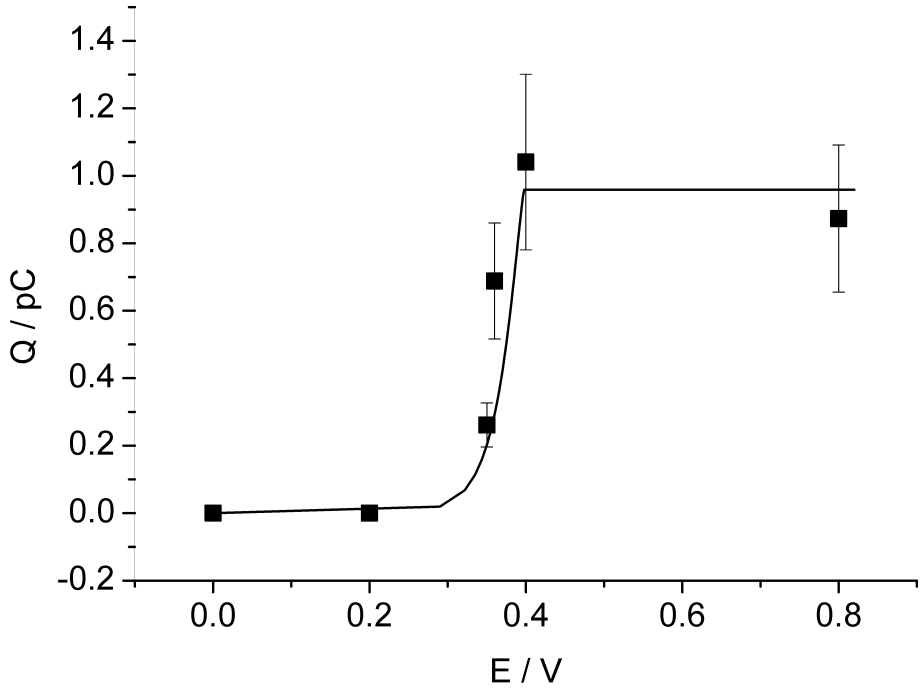

Figure 14.1: The variation of average spike height (i.e. peak current) with potential for the APC experiment of AgNPs (■), and fit of data with equation (14.3) (—) with r = 3 nm and t_L = 20 ms.

$$Q = \frac{4n\pi\rho F}{3M}(r_i{}^3 - r_f{}^3), \tag{14.2}$$

where n is the number of electrons transferred per atom, ρ is the bulk metal density, F the Faraday constant, M the relative atomic mass, r_i the initial NP radius and r_f the final NP radius. Here the 'final radius' means the radius when the NP leaves the vicinity of the electrode after collision such that no further electro-oxidation occurs. Clearly if the electrode potential is positive enough, the NP will be completely oxidised and $r_f = 0$.

For the case of fully reversible charge transfer (fast electrode kinetics relative to mass transport) it is found that

$$E - E_f^0 = \frac{RT}{nF} ln\left(\frac{\rho(r_i^2 - r_f^2)}{(2ln2)MDt_L}\right) \tag{14.3}$$

and

$$E_{1/2} - E_f^0 = \frac{RT}{nF} ln\left(\frac{\rho {r_i}^2}{3.746MDt_L}\right) \tag{14.4}$$

For fully irreversible charge transfer (slow electrode kinetics), the analogous relations are:

$$E - E_f^0 = \frac{RT}{F} \frac{1}{(n' + \beta)} ln\left(\frac{\rho(r_i - r_f)}{Mt_L k_0}\right) \tag{14.5}$$

and

$$E_{1/2} - E_f^0 = \frac{RT}{F(n' + \beta)} ln\left(\frac{\rho r_i}{4.847Mt_L k_0}\right) \tag{14.6}$$

In the above, E_f^0 is the formal potential, $E_{1/2}$ is the 'half-wave potential', the potential at which the impact oxidation charge is half that of the maximum charge (i.e. corresponding to oxidation of half of the atoms in the NP), n' is the number of electrons transferred before the rate determining step (so n'=0 for a 1 electron oxidation and 0 or 1 for a 2-electron process) [15], β is the anodic charge transfer coefficient, k^0 is the electrochemical rate constant (with units in this case of mol cm^{-2} s^{-1}) ,and t_L is the duration of the NP-electrode contact.

Figure 14.1 shows the comparison of equation (14.3) with the experimental data, using the literature value for $E_f^0(Ag/Ag^+)$ = +0.559 V vs SCE [16]. From this Figure it is clear that equation (14.3) provides an excellent fit to the data with no adjustable parameters and from this we infer that the oxidation of AgNPs displays fast (i.e. reversible) electron transfer. The predicted behaviour for irreversible electrode kinetics given by equation (14.5) lies to more positive potentials than that of reversible kinetics described by equation (14.3). It can be seen in Figure 14.1 that $E_{1/2} < E_f^0$, which is caused by the size effect on $E_{1/2}$ and that the nanoparticle dissolves as the measurement proceeds [11]. In this case E_f^0 is the same as that of bulk Ag, therefore there is no nanoeffect.

We believe that this single nanoparticle approach may be more straightforward for the

extraction of thermodynamic and kinetic data than other recently developed methods to study the electro-oxidation of silver nanoparticles [17, 18].

14.3.2 Charge transfer kinetics of NiNPs

First a cyclic voltammogram was recorded at a NiNP-modified glassy carbon macroelectrode (diametre 3 mm) to verify the oxidation potential (see Figure 14.2a). As we have discussed in NiNPs APC chapter, there are no oxidative features until the onset of anodic dissolution at +1.4 V (vs SCE) which is consistent with the presence of the layer of surface NiO. The oxidation of NiO then occurs [19–23] forming NiO_2 [24]. Voltammetry conducted at a Ni rod (diameter 12 mm) is consistent with this, showing oxide formation followed by continuous dissolution at potentials above +1.5 V (vs SCE). On this basis we postulate that NiO_2 dissolves rapidly oxidising the underlying Ni to NiO, possibly according to the following mechanism:

$$NiO_2(s) + 2H^+(aq) \rightarrow Ni^{2+}(aq) + \frac{1}{2}O_2(g) + H_2O(l) \tag{14.7}$$

$$Ni + \frac{1}{2}O_2(g) \rightarrow NiO(s) \tag{14.8}$$

That is, overall

$$NiO_2(s) + 2H^+(aq) + Ni(s) \rightarrow NiO(s) + Ni^{2+}(aq) + H_2O(l) \tag{14.9}$$

Analogous experiments were then conducted with NiNPs (mean radii 26 nm) which have previously been shown to undergo a 2 electron oxidation (and dissolution) at potentials more positive than +1.5 V (vs SCE) with no significant aggregation over experimental times [9].

The NiNPs were dispersed in a solution of 10 mM $HClO_4$ and 100 mM $NaClO_4$, and added to the cell with the carbon fibre microelectrode, and reference (SCE) and counter electrodes. The working electrode was potentiostatted at a range of potentials from +1.4

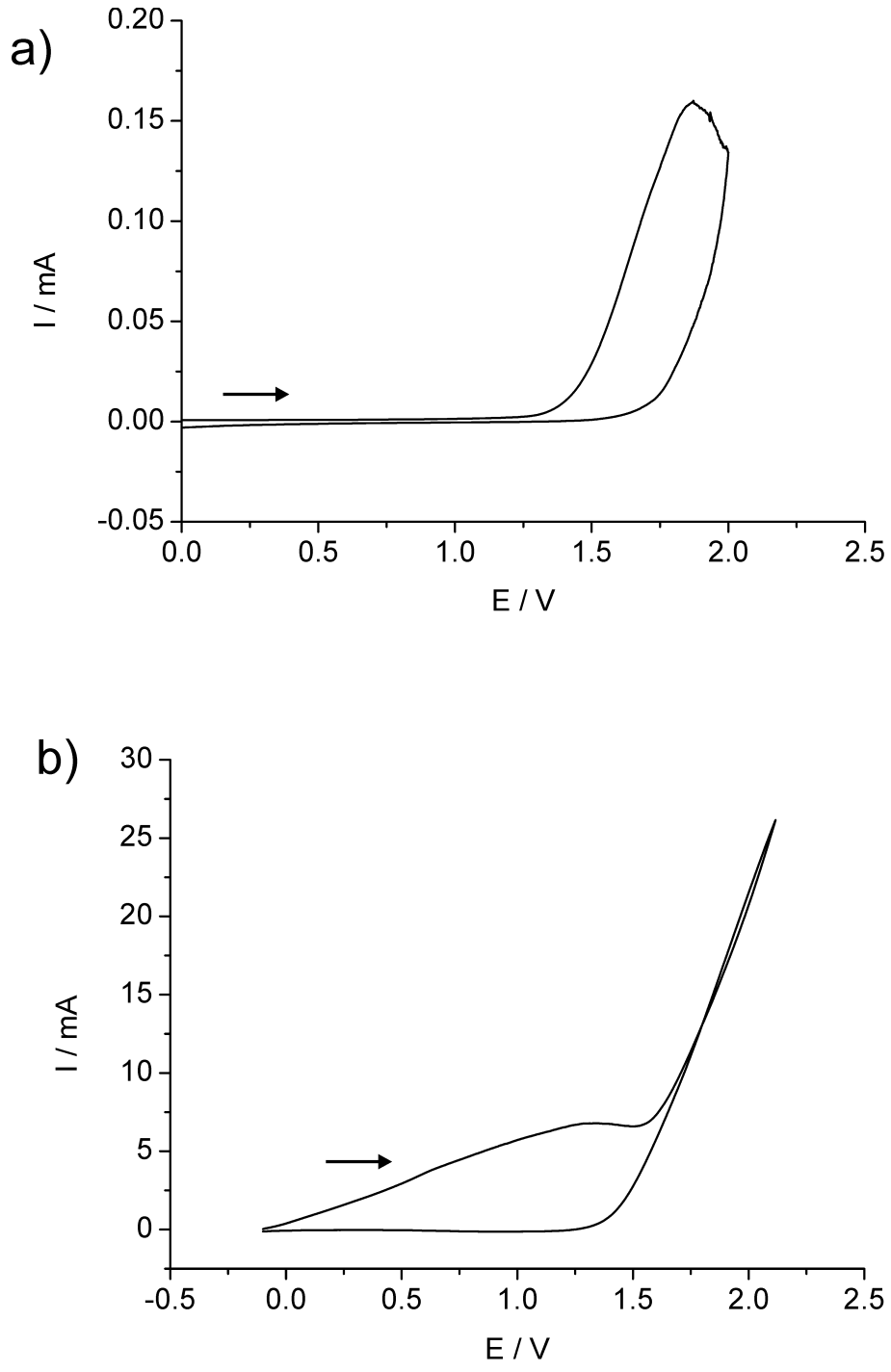

Figure 14.2: Cyclic voltammogram of a) NiNP-modified glassy carbon electrode and b) a Ni rod in 10 mM $HClO_4$ / 0.1M $NaClO_4$ (arrows show direction of scan).

V to +1.8 V and chronoamperograms recorded. As before, oxidative impact spikes were observed from ca. +1.55 V and above. Figure 14.3a shows the variation in the average charge passed per impact spike with potential.

In applying equations (14.3) and (14.5) in Figure 14.3b, the literature value for $E_f^0(NiO/\mathrm{NiO_2})$ = +1.75 V (vs SCE) [16] has been used corrected for pH, yielding a good fit with equation (14.4) for irreversible 2 electron oxidation with $(n' + \beta)$= 1.50 and $k^0 = 5 \times 10^{-4}$ mol cm^{-2} s^{-1}.

14.4 Conclusions

The charge transfer kinetics have been determined for the oxidative dissolution of AgNPs and NiNPs via analysis of the APC experimental methodology, with the former displaying reversible (fast) kinetics, and the latter irreversible (slow) kinetics with $n' + \beta$ =1.50 and $k^0 = 5 \times 10^{-4}$ mol cm^{-2} s^{-1}. We anticipate this will have application in the wider research into metal nanoparticles [25,26], given the advantages of measuring kinetics on individual nanoparticles such as the removal of the requirements of modelling the complex mass transport regime operating with large numbers of deposited nanoparticles.

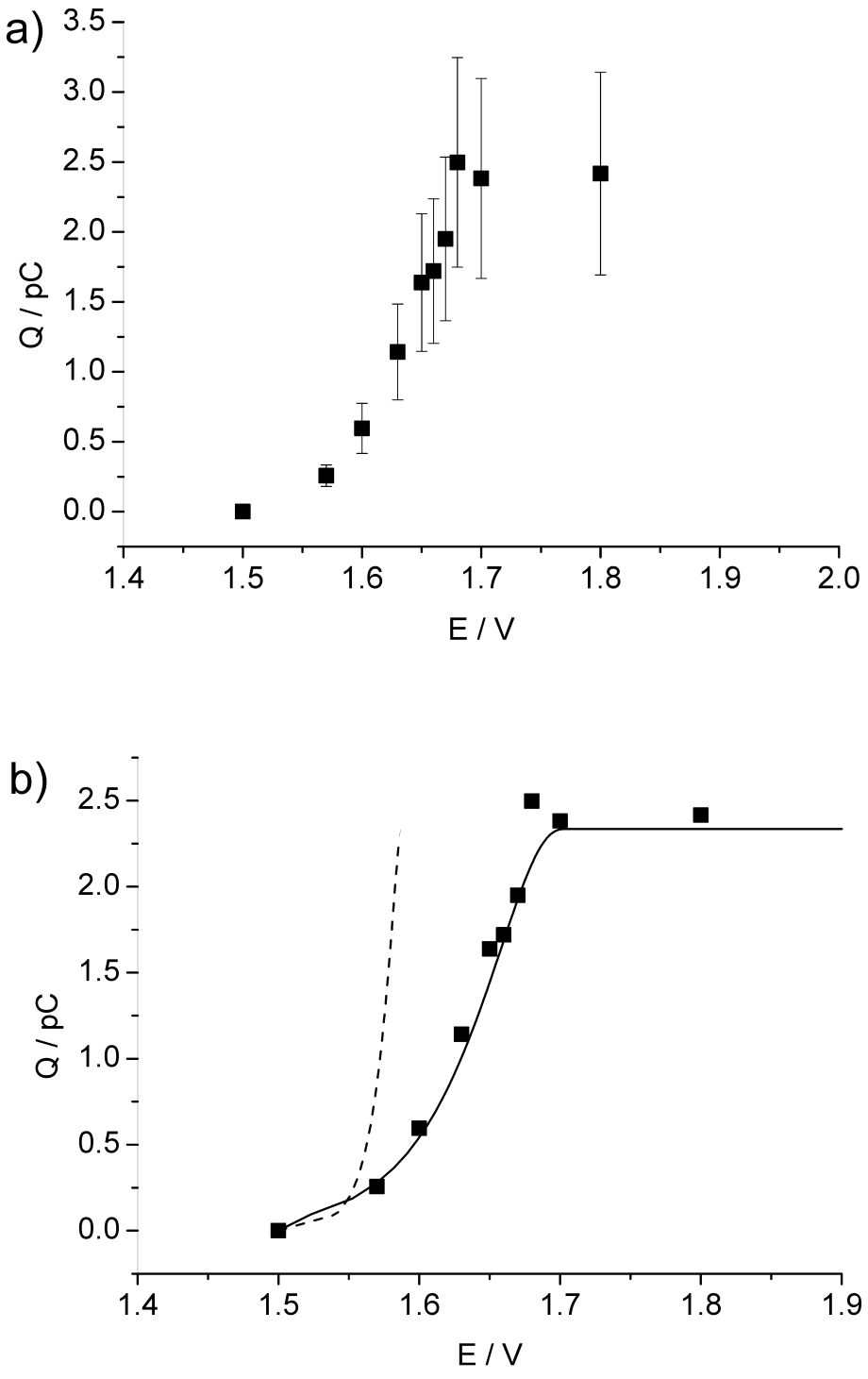

Figure 14.3: a) The variation of average spike height (i.e. peak current) with potential for the APC experiment of NiNPs, and b) fit of data with eqns (3) and (5) where the reversible model is shown in (- - -) and irreversible with $(n' + \beta)$=1.5 and $k^0 = 5 \times 10^{-4}$ mol cm^{-2} s^{-1} by (—).

Bibliography

[1] M. Heyrovský and J. Jirkovský. *Langmuir*, 11:4288, 1995.

[2] M. Heyrovský, J. Jirkovský, and B. R. Müller. *Langmuir*, 11:4293, 1995.

[3] M. Heyrovský, J. Jirkovský, and M. Štruplová Bartáčková. *Langmuir*, 11:4309, 1995.

[4] M. Heyrovský, J. Jirkovský, and M. Štruplová Bartáčková. *Langmuir*, 11:4309, 1995.

[5] A. V. Korshunov and M. Heyrovský. *Electroanalysis*, 18:423, 2006.

[6] N. V. Rees, Y. G. Zhou, and R. G. Compton. *RSC Adv.*, 2:379, 2012.

[7] Y. G. Zhou, N. V. Rees, and R. G. Compton. *Angew. Chem., Int. Ed.*, 50:4219, 2011.

[8] Y. G. Zhou, N. V. Rees, J. Pillay, R. Tshikhudo, S. Vilakazi, and R. G. Compton. *Chem. Commun.*, 48:224, 2012.

[9] E. J. E. Stuart, Y. G. Zhou, N. V. Rees, and R. G. Compton. *RSC Adv.*, 2:6879, 2012.

[10] N. V. Rees, Y. G. Zhou, and R. G. Compton. *ChemPhysChem*, 12:1645, 2011.

[11] B. Haddou, N. V. Rees, and R. G. Compton. *Phys. Chem. Chem. Phys.*, 14:13612, 2012.

[12] Q. Xu. *Nanostructured & Amorphous Materials Inc, Houston, USA. Pricate communication.*

[13] A. Pyatenko, M. Yamaguchi, and M. Suzuki. *J. Phys. Chem. C*, 111:7910, 2007.

[14] A. Pyatenko, M. Yamaguchi, and M. Suzuki. *J. Phys. Chem. B*, 109:21608, 2005.

[15] R. G. Compton and C. E. Banks. *Understanding Voltammetry, 2nd Edition*. World Scientific, Singapore, 2011.

[16] *CRC Handbook of Chemistry and Physics, 86th Edition*. CRC Press, Boca Raton, FL, USA, 2006.

[17] M. Giovanni and M. Pumera. *Electroanalysis*, 24:615, 2012.

[18] Kh. Z. Brainina, L. G. Galerin, T. Yu. Kiryuhina, A. L. Galperin, N. Yu. Stozhko, A. M. Murzakaev, and O. R. Timoshenkova. *J. Solid State Electrochem.*, 16:2365, 2012.

[19] M. Cid, A. Jouanneau, D. Nganga, and M. C. Petit. *Electrochim. Acta*, 23:945, 1978.

[20] M. Zamin and M. B. Ives. *J. Electrochem. Soc.*, 126:470, 1979.

[21] K. Nii. *Corr. Sci.*, 10:571, 1970.

[22] L. V. Volkov and M. I. Kalashnikova. *Tsvetnye Metally*, 8/9:101, 2011.

[23] F. T. Wagner and T. E. Moylan. *J. Electrochem. Soc.*, 136:2498, 1989.

[24] D. Zuili, V. Maurice, and P. Marcus. *J. Electrochem. Soc.*, 147:1393, 2000.

[25] M. Giovanni, A. Ambrosi, and P. Marcus. *Chem. Asian J.*, 7:702, 2012.

[26] M. Giovanni and M. Pumera. *Electrochem. Commun.*, 13:203, 2011.

Chapter 15

Conclusions

The study of thermally-driven nanoparticle impact phenomena has revealed new insights into NP-surface interactions via both indirect (*i.e.* electrocatalytic) and direct electrochemical measurements. Identification and characterisation of metal NPs has been shown to be possible, as well as the synthesis of core-shell structures.

The work discussed in this thesis is based on the investigation of the electrochemistry of both the nanoparticles (NPs) themselves and that of solution species reacting at the NP surface during the collisions of NPs at electrodes. The method is simple and relatively easy to deploy requiring little detailed theory beyond Faraday's 1st Law and conventional three-electrode voltammetric equipment.

The sizing of Ag, Ni, Au nanoparticles using anodic particle coulometry (APC) method has shown excellent agreement with independent SEM measurements whilst the studies of AgNP aggregation in real time provide data which is not easily accessible by other techniques. Sticking coefficients are measured as an extension of this theme. Furthermore, the determination of nanoparticle concentration is realised by integration of the flux equation and finally the charge transfer kinetics of the oxidation of silver and nickel nanoparticles studied. In contrast to the APC method, electrode-particle impacts using surface tagged NPs provides a non-destructive way of sizing the NPs from the charge associated with one monolayer of "tag". In addition to tagged NPs, underpotential de-

position and bulk deposition of metal onto AgNPs are also observed as part of indirect electrochemical measurement.

Currently 3 patents have been filed on this research:

1) Electrochemical detection of silver nanoparticles. UK Patent Application 1103064

2) Electrochemical detection of tagged nanoparticles. UK Patent Application 1121241.2

3) Coated nanoparticles (core-shell) and methods for their production. UK Patent Application 1110654.9

Future directions of research will inevitably involve the synthetic exploitation of some of the above phenomena, for example in controlled core-shell NP synthesis. The use of both direct APC and indirect electrocatalytic detection methods also holds promise for general NP detection and characterisation strategies which are clearly required for regulatory and environmental monitoring of NPs within industrial and environmental contexts.

Appendix: Charge transfer kinetics for nanoparticle oxidation

This theory was presented in *PhysChemChemPhys*, 2012, 14, 13612

reversible kinetics

First we derive the relationship between the formal oxidation potential and the 'half-wave' potential (i.e. the potential at which the measured average spike current is half of the diffusion-limited average spike current) by considering a sphere of radius r in contact with a conducting plate with a surface concentration of electroactive ions given by $[M^{n+}]_0$ as illustrated in Figure 1

The mass-transport limited current to such a sphere on a flat surface is known to be

$$I_{lim} = 4nFC_{bulk}Drln2, \tag{1}$$

where n is the number of electrons transferred, F is the Faraday constant, r the sphere radius, and D and C_{bulk} refer to the diffusion coefficient and bulk concentration of the electroactive species in solution. It follows that the mass transport coefficient, k_{mt}, defined by

$$flux = k_{mt}C_{bulk} \tag{2}$$

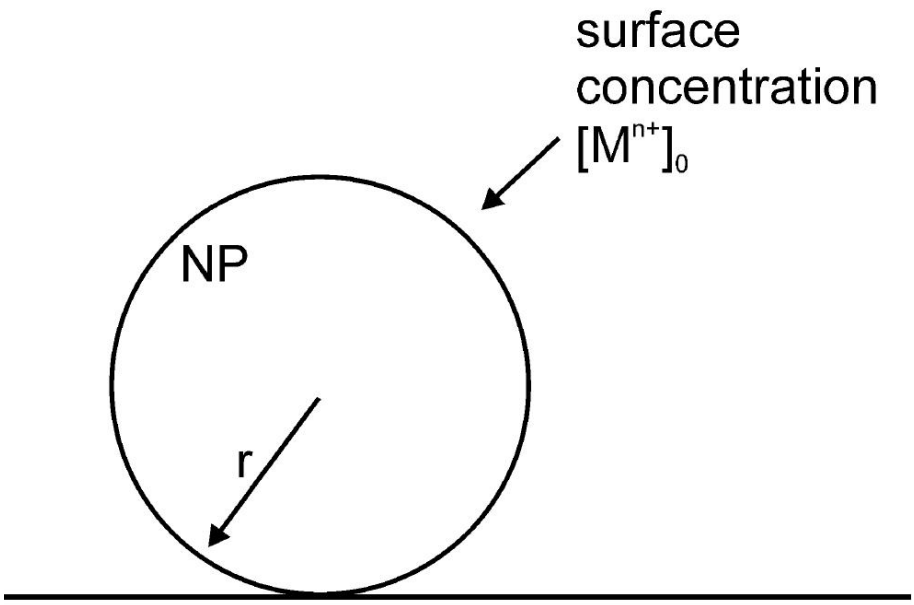

Figure 1: Schematic representation of metal NPs of radius r_{np} in contact with an electrode.

is

$$k_{mt} = \frac{Dln2}{r} \tag{3}$$

The Nernst equation requires

$$E = E_f^0 + \frac{RT}{nF} ln[\mathrm{M^{n+}}]_0, \tag{4}$$

where $[\mathrm{M^{n+}}]_0$ is the concentration of $\mathrm{M^{n+}}(\mathrm{aq.})$ at the NP surface, the pure metal M(s) is assumed to have unit activity, and n is the number of electrons transferred in the oxidation

$$\mathrm{M(s)} - n\mathrm{e^-} \rightarrow \mathrm{M^{n+}(aq.)} \tag{5}$$

and R, T, and F have their usual meanings; E_f^0 is the formal potential of the M / $\mathrm{M^{n+}}$ couple.

After some time, the rate of material (in moles) lost from the NP will be given by

$$\frac{\mathrm{d}N}{\mathrm{d}t} = k_{mt}[\mathrm{M}^{n+}]_0 4\pi r^2 = -\frac{D}{r} ln2 [\mathrm{M}^{n+}]_0 4\pi r^2 \tag{6}$$

whilst the amount of material present in th NP, N (in moles), will be

$$N = \frac{4}{3}\pi r^3 \frac{\rho}{M} \tag{7}$$

where ρ and M are the bulk density and relative atomic mass of element M, respectively.

Differentiating (7) with respect to time, we obtain

$$\frac{\mathrm{d}N}{\mathrm{d}t} = \frac{4\pi\rho r^2}{M}\frac{\mathrm{d}r}{\mathrm{d}t}. \tag{8}$$

Equating (6) and (8), replacing $[\mathrm{M}^{n+}]_0$ by $e^{n\theta} = e^{nF(E-E_f^0/RT)}$ as per (4), and integrating between initial and final NP states (r_i and r_f) we obtain

$$r_f{}^2 - r_i{}^2 = -\frac{2MDte^{n\theta} ln2}{\rho}. \tag{9}$$

Rearrangement then provides

$$E - E_f^0 = \frac{RT}{nF} ln\left(\frac{\rho(r_i^2 - r_f^2)}{(2ln2)MDt_L}\right) \tag{10}$$

Assuming that the average spike contact time (t_L) is independent of potential for a given nanoparticle material, then the charge passed per spike is related to the current passed by

$$Q = It_L \tag{11}$$

Clearly at the half-wave potential, $E_{1/2}$, the charge passed per spike is

$$Q_{1/2} = \frac{1}{2}Q_{max} \tag{12}$$

and therefore consideration of the number of atoms oxidised leads us to

$$r_f = 2^{-1/3} r_i. \tag{13}$$

Combing (10) and (12) we arrive at an expression for $E_{1/2}$ in the case of reversible kinetics of

$$E_{1/2} - E_f^0 = \frac{RT}{nF} ln\left(\frac{\rho {r_i}^2}{3.746 M D t_L}\right), \tag{14}$$

where r_i is the initial NP radius, and r_f is the NP radius at $t = t_L$.

A convenient plot for comparison with experimental data is Q *vs.* E, since the average charge passed per impact at a particular potential , Q, is related to r_f by

$$Q = \frac{4n\pi\rho F}{3M}({r_i}^3 - {r_f}^3) \tag{15}$$

Since the average r_i is known from the APC size distribution, a theoretical plot can be constructed by calculating r_f from (10) and then finding Q *via* (13). The use of the average size (rather than the single NP size) is more appropriate here due to the existence of NP clusters of varying size dependig on the aggregation effects inherent to each particular size and type of NP.

Fully irreversible kinetics

Analogous expressions to (6) and (8) can be expressed as

$$\frac{4\pi r^2 \rho}{M} \frac{\mathrm{d}r}{\mathrm{d}t} = \frac{\mathrm{d}N}{\mathrm{d}t} = -4\pi r^2 k_0 e^{(n' + \beta)\theta}, \tag{16}$$

where k_0 is the electrochemical rate constant (units of mol cm^{-2} s^{-1}), n' is the number of electrons transferred before the rate determining step and β is the anodic transfer coefficient for the rate determining step.

By integrating we obtain the irreversible version of (8):

$$E - E_f^0 = \frac{RT}{F}\frac{1}{(n' + \beta)} ln\left(\frac{\rho(r_i - r_f)}{Mt_L k_0}\right). \tag{17}$$

Including (13) as a condition for the half-wave potential, and simplifying we obtain

$$E_{1/2} - E_f^0 = \frac{RT}{F(n' + \beta)} ln\left(\frac{\rho r_i}{4.847 Mt_L k_0}\right). \tag{18}$$